Doktoretza tesia automatika eta elektronikan

DESIGN METHODOLOGY FOR PERMANENT MAGNET AXIAL FLUX MACHINES

Doktoregaia:
ARITZ EGEA CACERES

Zuzendaria:
GAIZKA ALMANDOZ LARRALDE

Bigarren Zuzendaria:
GAIZKA UGALDE ROSILLO

Mondragon Unibertsitatea
2012ko Urria

LABURPENA

Azken urte hauetan efizientzia energetikoak hartu du protagonismo nagusia. Efizientzia hobetzeak ekologikoki onurak eskaintzeaz gain funtzionamendu kosteak murriztea ere ekartzen du, produktu erakargarriagoak sortzea bideratuz. Honez gain diseinu prozesua arintzea eta fabrikazio kosteak murriztea ere fabrikatzaile ororen jomuga izan dira. Makina elektrikoen munduak bide bera jarraitu du.

Hortaz tesi honen helburu nagusia fluxu axialeko makinak diseinatzeko metodologia oso bat proposatzea izan da. Metodologia hau ondorengo etapa desberdinetan banatzen da. Hasteko aplikazioaren betebehar zein mugak definitzen dira horrela makinaren ezaugarriak zehazteko. Behin ezaugarri hauek izanda makinaren diseinua burutzen da. Diseinu hau lehenik erreminta analitikoen bidez egiten da ondoren numerikoen laguntzaz diseinua fintzeko. Diseinu honetatik eraikiko den makina zehazten da.

Aipatu erreminta hauen definizioa izan da tesiaren muin nagusia. Erreminta analitikoei dagokienez, lehenik lege elektromagnetikoetan oinarritutako oinarrizko dimentsionatze ekuazioak definitu dira. Bestetik Fourier-en serietan oinarrituriko modelo garatua ere planteatu da. Ondoren erreminta numerikoen inguruan elementu finituen metodoa (FEM) aurkeztu da makina axialen diseinura nola bideratu azalduz. FEM plataformek eskaintzen dituzten bi dimentsiotako zein hiru dimentsiotako inguruneak landu direlarik.

Prozesu honen baliagarritasuna frogatzeko igogailu aplikazio batera bideratutako prototipo esperimental bat ere eraiki da. Prototipo hau eraikitzeko, tesian proposatutako metodologia jarraitu da pausuz pausu. Gainera beste prototipo txikiago batzuk ere eraiki dira metodologia bera frogatzeko baino, erremintak balioztatzeko asmoz. Honek gainera ikerketari balio erantsi bat eman ahal izan diolarik.

Funtsezko hitzak: *Iman Iraunkorreko Makinak, Fluxu Axialeko Makinak, Makina Diseinurako Erremintak*

ABSTRACT

In recent years, improving energy efficiency has become a primary concern in not only providing ecological benefits but also lowering operational costs. These benefits would then enable the creation of more attractive products. Thus, simplifying the design process and reducing manufacturing costs are the objectives of manufacturers worldwide. The realm of electric machines has followed the same trend.

The main objective of this thesis is to define a methodology for the design of axial machines. This methodology is divided into the following steps. First, the features and limitations of the application are defined, so the characteristics of the machine to be designed can be specified. Once these specifications are established, the design process can be performed. The design is carried out by first using analytical tools and is then further refined using numerical tools. This design specifies the characteristics of the future machine.

The development of these tools forms the core of this thesis. Sizing equations based on the laws of electromagnetism were developed as analytical tools. An advanced model based on the Fourier series was then constructed. The finite element method (FEM) focused on axial machines is used for the numerical tools. The two environments offered by FEM platforms are examined: two dimensional environments and three dimensional environments.

In order to validate the proposed methodology, a prototype oriented to an elevation application is built. This machine is created following the methodology presented in the thesis. Furthermore, some small prototypes are fabricated to validate the tools in addition to the methodology, which lends added value to the research work.

Keywords*: permanent magnet machines, axial flux machines, machine design tools*

RESUMEN

En los últimos años la eficiencia se ha convertido en un protagonista destacado. No solo la eficiencia energética con motivos ecológicos sino también para reducir costes operacionales. Estos beneficios permiten la producción de productos más atractivos para el mercado. Por ello el simplificar el proceso de diseño y reducir costes de producción se han destacado como meta de los fabricantes. La industria de las máquinas eléctricas no ha escapado de esta tendencia.

El principal objetivo de esta tesis es el definir una metodología de diseño de máquinas de flujo axial. Esta metodología se divide en los siguientes pasos. Primero los requisitos y limitaciones de la aplicación son definidas, para así especificar las características de la máquina a diseñar. Una vez establecidas estas especificaciones el proceso de diseño puede llevarse a cabo. El diseño comienza con la utilización de herramientas analíticas para luego redefinirlo con más precisión mediante herramientas numéricas. Este diseño especifica las características de la futura máquina.

El desarrollo de las citadas herramientas es el cuerpo de esta tesis. Primeros se desarrollaron ecuaciones de dimensionamiento basadas en las leyes de electromagnetismo como parte de las herramientas analíticas. Estas fueron completadas con un modelo avanzado basado en las series de Fourier. El método de elementos finitos (FEM) enfocado a las máquinas axiales es utilizado en las herramientas numéricas. Los dos entornos ofrecidos en FEM son examinados: entorno de 2D y 3D.

Con el objetivo de validar la metodología propuesta un prototipo orientado a un ascensor fue construido. Esta máquina fue fabricada siguiendo la metodología presentada en la tesis. Además, otros pequeños motores fueron construidos para validar las herramientas, lo que da un valor añadido al trabajo realizado.

***Palabras clave**: máquinas de imanes permanentes, máquinas de flujo axial, herramientas de diseño de máquinas*

ESKERRAK-ACKNOWLEDGEMENTS

Lerro hauek urte hauetan zehar beraien laguntza eskaini didaten guztiei eskaini nahiko nizkieke.

Lehenik eta behin unibertsitateko jendearekin gogoratu beharra daukat edo hobe esanda gogoratu nahi dut. Hasteko administrazio kontuetan lagun didaten isileko lana egiten duten horiekin. Garaian dugun giroa beste edonon izatea ez da lan erreza eta zuek guztioi ere eskerrak eman nahi dizkizuet. ”Aula orona”koen inguruan zer esan, Unai ”Txo”, Iraola “old..” eta Aizpuru “kortakesos” a ze taldea! Makinetako taldea ere aipatu nahi dut nigan iraganean izandako konfidantzagatik eta etorkizunerako eginiko eskaintzagatik. Eskerrikasko Javi. Bereziki zuzendari (berari gustatzen ez bazaio ere “jefe”) moduan izan dudan Gaizkari, eginiko lan guztia estimatzen diot. Ikaragarri ikasi dut bere laguntzaz eta tesia bide zuzenetik bideratu du.

Bestalde Orona-EIC ko lagunak ere aipatu nahi ditut. Nere etorkizunerako aukera ederra eman zidaten eta espero dut nire erantzuna eurek jarritako itxaropenen pare egon izana. Ana Escaladak urte hauetan azaldutako interesa eta emandako laguntza bereziki estimatu nahi dut.

I can neither forget about the people in KTH; Shafigh, Nima, Andreas, Shuang, Naveed… thanks for making me feel at home, the discussions we had not only about technical topics but also about life issues where really interesting and enriching. I have to specially thank Juliette and Oskar for the opportunity they gave me to stay in one of the most important universities on the world.

Azkenik, baina noski ez horregatik garrantzia gutxiagorekin, etxekoak. Lehenik gurasoei nire bizitza erreza egin izanagatik, ikasketak eman dizkidazuelako eta zazpi izarretako hotela ere eskaini didazuelako, baina batez ere nigan sinetsi duzuelako, eskerrik asko. Aiton amonekin ere gogoratu nahi dut, batez ere nire aitona zen Alejandrorekin, ziur naiz berak irakatsia bizitzako esparru guztietarako baliagarri izango zaidala. Zutaz ere ez naiz ahaztu “rubita”. Eskerrik asko Saioa aguantatu egin nauzulako eta aguantatu egin beharko nauzulako.

Aritz Egea Caceres

CONTENTS

Chapter 1.

INTRODUCTION

The first chapter provides a brief description of the thesis framework. The background of the design and analysis of axial flux machines is introduced and the different design methodologies for electrical machines found in the literature are discussed.

The main objectives as well as the contribution of the thesis are then presented. Chapter summaries are provided. Finally, the publications generated during the development of the thesis are listed at the end of the chapter.

1.1 Background and Framework of the Thesis

Investigations in the field of electrical machines have included a wide variety of matters and concepts. The design, the control, or thermal aspects are some examples of commonly studied issues. From the first DC machines to the current leading induction machines, there is no doubt that a high level of technological development has been achieved.

Permanent magnet synchronous machines have gained much interest in recent years. The search for more efficient and eco-friendly machines makes this an interesting field of research. Development of new materials and concepts as well as new needs and applications have placed permanent magnet (PM) machines in a prominent position.

The inherent features of PMs, such as high efficiency, high compactness and wide operation speed range, make these machines suitable for direct drive applications. In direct drive applications, the shaft of the machine is directly coupled to the shaft of the application, thus avoiding the gearbox, which leads to more efficient and compact solutions. The high power of current magnet materials may decrease the size of the machine in comparison with the classic induction machines. Furthermore, PM machines have a magnetized motor, so that the consumption of electrical energy is decreased. These machines are able to work at low speed, which is very interesting for direct drive low speed applications; however, high speeds are also reachable, giving the PM machine a wide speed range. However, the capability of flux weakening is not as good as in induction machines.

Depending on the direction of the flux through the air gap, PM machines are divided in three main groups: radial, transversal, and axial flux machines (Figure 1-1).

Mondragon University (MU) has been researching topics in electrical machines for years, in both industrial projects and PhD theses. Some of these theses were related to radial flux permanent magnet machines for elevation applications. This thesis is a continuation of this research line, but in this case, the focus is on the design of axial flux machines.

Several PM machine design methodologies are found in the literature. Generally, these methodologies combine analytical tools with numerical tools based on the finite element method (*FEM*). The development of new software packages in addition to the increase in the capabilities of personal computers have enabled the use of numerical tools in combination with flexible analytical tools, thereby attaining accurate machine designs in far less time consumption than before.

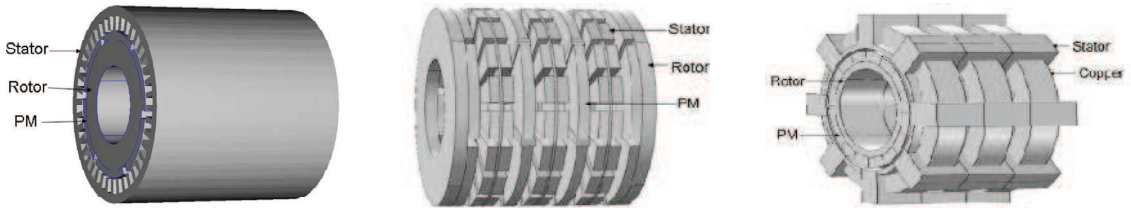

a) *b)* *c)*

Figure 1-1: Permanent magnet synchronous machines a) radial b) axial and c) transversal [1]

For example, in [2] a methodology based in the aforementioned combination of numerical and analytical tools is proposed. In [3], after an iterative analytical and numerical design, *MATLAB-SIMULINK* is used to analyze the machine inside the application. *Leonardi et al.* [4] went a step ahead and included a co-simulation coupling the *FEM* software and time domain electrical circuit. *Almandoz* presented an advanced design methodology for PM radial machines in his thesis [5]. Another example is the complete electromagnetic-thermo-mechanical design methodology proposed in [6]. Finally, [7] explains the design and analysis of an axial flux machine for a flywheel.

1.2 Objectives

The main objective of this thesis is to define an advanced methodology for the design of permanent magnet axial flux machines. This methodology is focused on low speed (<500 rpm) and medium power (≈10 kW) surface mounted magnet machines. In order to achieve this main goal, the sub-objectives are as follows:

- To optimize the design process in terms of cost and time consumption. For that purpose, adequate design tools should be developed and then properly used.
- To identify the most suitable materials and manufacturing techniques in order to achieve cost- and energy-efficient motors.
- Validate the proposed design methodology in a real application.

During the development of this thesis, the following tasks were accomplished:

- Compilation and study of state of the art axial machines, including different topologies for axial flux machines, potential applications, a new generation of magnetic materials, and different manufacturing techniques.

- Research of different materials and manufacturing techniques in order to build an efficient axial machine.
- Development of analytical tools for the sizing of axial flux machines.
- Development of advanced analytical tools based on Fourier series for the design and accurate analysis of axial flux machine performances.
- Development of simulation platforms by *FEM* using the software *FLUX®* by *CEDRAT*. These simulations are carried out in both three- and two-dimensional environments.
- Development of thermal models based on lumped parameter circuits for axial flux machines.
- Design and construction of a machine for application in a real elevator.

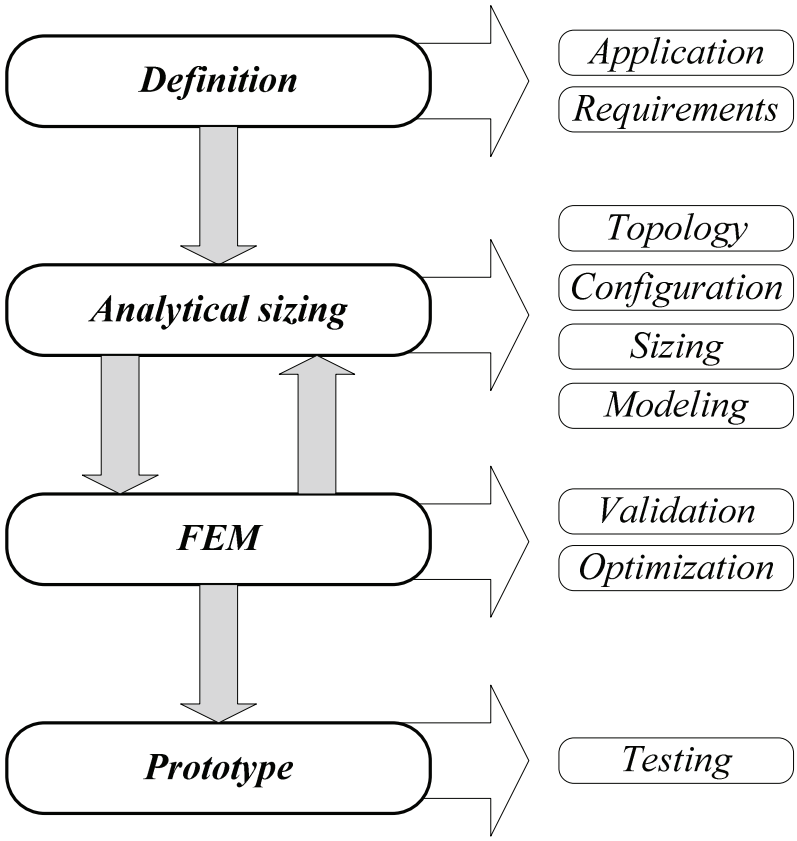

Figure 1-2: Proposed methodology for the design of axial machines

1.3 Thesis Contribution

This thesis is intended to contribute a methodology for the design of axial flux machines. The methodology is divided into four steps as shown in Figure 1-2.

First, the requirements of the application are established. These requirements are bound by both operating needs and geometrical restrictions. In other words, this step defines the operating characteristics and geometrical constraints of the machine.

The analytical sizing then can be performed. Before starting with the sizing, both the topology and configuration of the machine have to be selected. The configuration defines the number of stator and rotor poles and the characteristics of the magnets. The sizing of the machine can then be done and then if necessary, the modeling can be performed.

Once the analytical sizing gives a design this is checked by *FEM*. Here some effects that are not easy to assume in analytical equations, such as saturation, are taken into account. If the design is correct, it can be optimized to achieve a size reduction. However, if the design does not fulfill the requirements, a new analytical design has to be performed. As Figure 1–2 shows, the relation between analytical sizing and *FEM* is linked.

The final step is the fabrication of the prototype, which is then tested to check whether the requirements are fulfilled. In this case, the prototype is also used to validate the design tools.

The proposed methodology was developed combining tools already defined in the literature with new proposed tools in this thesis. Among these new tools the most remarkable ones are the formulation of the model in Fourier series for axial machines and the new proposed method which combines *FEM-2D* and analytical tools.

1.4 Outline

This section presents a brief description of each chapter in the thesis.

Chapter 1

This chapter provides a global view of the thesis. The motivation of this work is presented, defining the framework that is developed. The objectives are also listed. Finally, papers that have been published during this period are reviewed.

Chapter 2

This chapter summarizes the state of the art in axial flux machines. First, a brief introduction is given, emphasizing some historical milestones and describing the current situation of the axial flux machines. In the next section, a general view of the different topologies of the axial flux machines is provided. The applications to which these machines are used are then analyzed. Finally, a study of the different ferromagnetic materials used to build axial flux machines is made, and the fabrication techniques using those materials are summarized.

Chapter 3

After a brief general description of the analytical tools used for the design of axial flux machines, those developed in the thesis are presented. First, the equations used in terms of lumped parameters for a pre-design and sizing are shown. The Fourier series advanced model is then presented.

Chapter 4

This chapter begins with an introduction to the finite element method for the design of electrical machines. A deeper analysis of this method then focuses on axial flux machines. After explaining the process that has to be followed in both two-dimensional (2D) and three-dimensional (3D) *FEM*, a new method in which 2D finite element analysis and analytical tools are combined is presented. Finally, the measurement of magnetic losses in finite element software is explained.

Chapter 5

The fifth chapter is an introduction to the thermal modeling of axial flux machines. First, the different models found in the literature are summarized. Some tests in which the main objective is to provide a general idea of the thermal behavior of axial machines are performed. Finally, the thermal model used in this thesis is presented.

Chapter 6

In this chapter, the steps in the design of an axial flux machine for an elevation are enumerated and explained. First, the specifications and characteristics given by the application are defined. The design process followed is then shown. This process uses the analytical and

numerical tools explained in previous chapters. A brief comparison between axial and radial flux machines is also included. Finally, the resultant real machine is tested.

Chapter 7

The seventh chapter concludes the thesis. First, the main conclusions of the developed project are summarized, followed by recommendations for future research.

1.5 Publications

Five publications were produced during the thesis period. Three were conference publications and the other two were journal publications. One of them was accepted and the other one has been submitted. The following gives information about the publications; the complete papers are collected in the Appendix.

First Publication

"Analytic model of axial flux permanent magnet machines considering spatial harmonics"

Egea, A.; Almandoz, G.; Poza, J.; González, A.

International Symposium on Power Electronics Electrical Drives Automation and Motion (SPEEDAM), 14-16 June 2010

Abstract: This work deals with the development of a complete analytic model for axial flux surface mounted permanent magnet synchronous machines. The magnetic field in the air-gap, the induced electromotive force *EMF*, the linked flux ψ and the electromagnetic torque are represented as sum of spatial-temporal components. Then, the accuracy of the model is evaluated comparing the results with those obtained in numerical analysis by 3D simulations.

Second Publication

"Modelado FEM 3D de Máquinas Síncronas de Imanes Permanentes y Flujo Axial"

Egea, A.; Almandoz, G.; Poza, J.; González, A.

Seminario Anual de Automática, Electrónica Industrial e Instrumentación (SAAEI), 7-9 Julio 2010

Abstract: En los últimos años, debido en gran medida a las mejoras en la calidad de los materiales y en las técnicas de fabricación, las máquinas síncronas de imanes permanentes en general y en concreto la topología de flujo axial está adquiriendo un protagonismo cada vez mayor. Las herramientas numéricas basadas en métodos de elementos finitos (*FEM*) resultan de gran ayuda a la hora de diseñar este tipo de máquinas. Sin embargo debido a la estructura

constructiva de las mismas, para poder hacer un análisis más profundo es necesario llevar a cabo estudios tridimensionales. Cabe destacar la complejidad de este tipo de simulaciones en comparación con las bidimensionales. En este artículo se expone la metodología utilizada para la simulación tridimensional de las máquinas axiales y se hace especial hincapié en detalles o consideraciones inherentes a estas simulaciones.

Third Publication

"Axial flux machines modeling with the combination of 2D FEM and analytic tools"

Egea, A.; Almandoz, G.; Poza, J.; González, A.

XIX International Conference on Electrical Machines (ICEM), 8 Sept. 2010

Abstract: This paper deals with the development of performance analysis tools for axial flux permanent magnet machines. Modeling with 3D finite element method (*FEM-3D*) software could take too much time, and both the definition and the problem solving may be very arduous. In this work an analysis method for axial flux machines is proposed. This method consists in the combination of *FEM-2D* simulations in the average radius plane with analytical models. The obtained results prove that the proposed method could be a very interesting option in terms of time and accuracy.

Fourth Publication

"Axial-Flux-Machine Modeling With the Combination of FEM-2-D and Analytical Tools"

Egea, A.; Almandoz, G.; Poza, J.; Ugalde, G.; Escalada A.

IEEE Transactions on Industry Applications, (Vol. 48 Issue 4)

Abstract: This paper deals with the development of analysis tools for axial-flux permanent-magnet machines. Normally, the study of this kind of machine involves three-dimensional (3-D) finite element method (*FEM*) (*FEM-3D*) due to the 3-D nature of the magnetic problem. As it is widely known, the *FEM-3D* software could take too much time, and both definition and solving processes of the problem may be very arduous. In this paper, a novel analysis procedure for axial-flux synchronous machines is proposed. This method consists in the combination of 2D *FEM* simulations with analytical models based on the Fourier-series theory. The obtained results prove that the proposed method could be a very interesting option in terms of time and accuracy.

Fifth Publication

"Analytical Model of Axial Flux Permanent Magnet Machines Considering Spatial Harmonics"

Egea, A.; Almandoz, G.; Poza, J.; Ugalde, G.; Escalada A.

Submitted to: IEEE Transactions on Industrial Electronics

Abstract: This work deals with the development of a complete analytic model for axial flux surface mounted permanent magnet synchronous machines. The magnetic flux density in the air-gap, the back electromotive force EMF, the linked flux ψ and the electromagnetic torque are represented as sum of spatial-temporal components, and they are defined as function of different design parameters such as mechanical dimensions, magnet properties and so on. Therefore, the proposed model gives a detailed inside view into the behavior of axial flux machines. Finally the accuracy of the model is evaluated comparing the results with those experimentally obtained.

Chapter 2.

STATE OF THE ART IN AXIAL FLUX MACHINES

This chapter aims to provide a global vision of axial flux machines. First, historical milestones of the electrical machines are mentioned. A classification of the different topologies the axial flux machine may acquire is then presented. Next, the main applications in which these machines are used or could be used as a real alternative to radial flux machines are summarized. Finally, a brief examination of the fabrication materials and techniques for axial machines is provided.

2.1 Introduction

From the beginning, human beings have developed systems to take advantage of the power in nature. For example, after the invention of steam and combustion machines, in 1831 Faraday built the first disc generator, which is shown in Figure 2-1-a. This device is considered the first electric generator in history; furthermore, it was based on the axial flux concept. In 1889, Tesla also patented a machine that used the axial flux principle (Figure 2-1-b). However, after the first patent of a radial flux machine in 1937, the axial flux machine was displaced and almost forgotten.

The main reasons, among others, for this neglect were the large attraction forces between the rotor and stator, manufacturing difficulties, and the high cost. Nevertheless, the interest in axial flux machines has increased in recent years because of new materials and manufacturing technologies. Hence, the need for new applications has become a boost for axial flux machines.

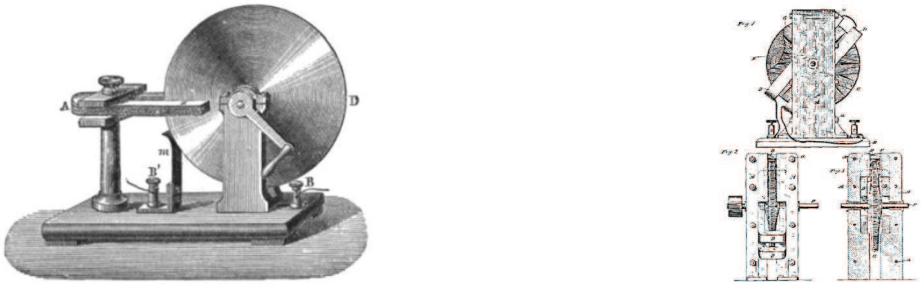

a) *b)*

Figure 2-1: First machines reported in history [8]*: a) disc generator built by Faraday and b) electromagnetic machine with a disc rotor built by Tesla*

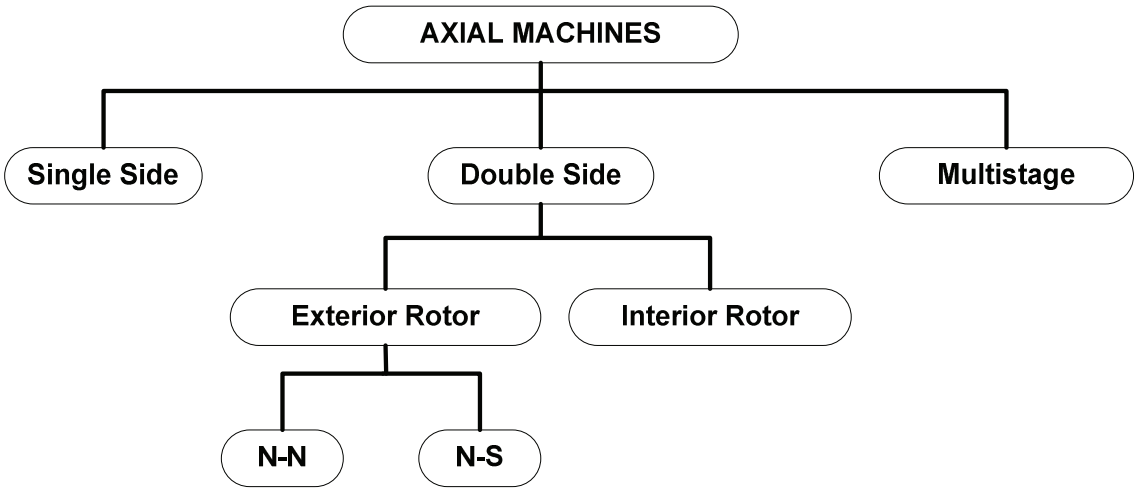

Figure 2-2: Diagram of axial machine topologies

2.2 Topologies of Axial Flux Machines

One of the most interesting aspects of axial flux machines is the wide range of topologies they offer. These different options may fit several applications. In [9] a deep study of the different topologies of axial flux machines is done.

As shown in Figure 2-2, axial flux machines are divided into three main groups: single-side machines (Figure 2-3), double side machines (Figure 2-4 and Figure 2-5) and multistage machines (Figure 2-6). In addition, a variety of configurations can be carried out within each group. This constructive flexibility makes axial machines suitable for different applications and optimizable for the specific requirements of each application.

As in radial flux machines, in axial flux machines the winding may be either concentrated or distributed. In the case of concentrated windings, coils are wound around teeth (Figure 2-3), whereas in the case of distributed windings, coils surround more than one tooth. Furthermore, in some machine configurations it is possible to have a toroidal winding. In this case, the coils are wound in the stator, which results in a toroidal shape (Figure 2-5-b).

2.2.1 Single Side

This is the simplest topology in the axial flux machines range. This kind of machine consists of a single stator and a single rotor, as shown in Figure 2-3. The stator core may be either slotted (Figure 2-3-a) or slotless (Figure 2-3-b).

a) *b)*

Figure 2-3: Single side machine: a) slotted stator and b) slotless stator

In this configuration, the attraction force exerted by the magnets between the rotor and the stator may be a drawback. The axle and the bearings must withstand this force, so they have to be properly dimensioned.

2.2.2 Double Side

Double side machines consist of three elements in two possible configurations:

- Double Stator – Single Rotor: The interior rotor is placed between two stators.
- Single Stator – Double rotor: The interior stator is placed between two rotors.

2.2.2.1 Interior Rotor Axial Flux Machines

In these kinds of machines, an interior rotor is placed between two stators, as shown in Figure 2-4. One of the interesting advantages of this configuration is that the core of the rotor shown in Figure 2-4-a can be avoided to obtain a coreless rotor as shown in Figure 2-4-b. The magnets have to be held in a non-ferromagnetic material to create the rotor structure. In this way, a lighter machine is obtained. It has to be noted that because the rotor is between the two stators and in the case when the distance from the rotor to each stator is equal, the attraction forces are equilibrated, avoiding possible stress in mechanical parts.

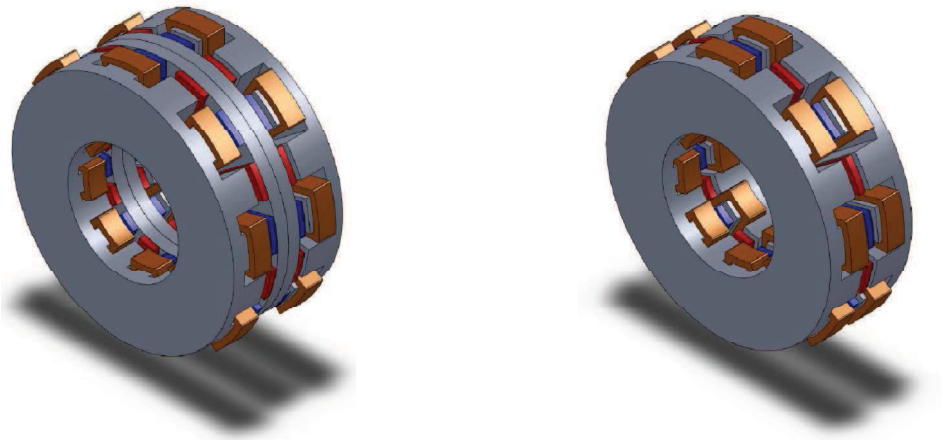

a) *b)*

Figure 2-4: Interior rotor machines: a) with ferromagnetic core in the rotor and b) coreless rotor

Similar to single side machines, the stators can be either slotted or slotless. The electrical connection between the two stators may in series or parallel, taking into account that the characteristics of the machine depend on this connection: that is, higher voltage in a series connection and higher current in a parallel connection.

2.2.2.2 Interior Stator Axial Flux Machines

In this topology, the magnets are usually mounted in a ferromagnetic material to facilitate the magnetic flux flow between adjacent magnets.

There is a wide range of possibilities for the configuration of the stators in these machines. On the one hand, in the configuration known as north-north (*N-N),* magnets with opposite magnetization direction are placed in front of each other, as shown in Figure 2-5-a-b. In this configuration, the path of magnet flux is closed along the stator yoke so that the stator core is needed. The winding may be placed surrounding the teeth, as shown in Figure 2-5-a. This figure shows a slotted stator with concentrated one layer winding. However, a toroidal winding with a slotless stator would be also possible, as shown in Figure 2-5-b. The main disadvantage of slotless machines is that the coils take place in the air gap, which increases the effective air gap length.

Another possible configuration is the north-south (*N-S)* machine. In this case, magnets with the same magnetization direction are placed in front of each other. The magnetic flux passes through the air gap and is then closed through the rotor yoke. Because the path followed by the flux does not use the stator yoke, this part could be avoided, leading to a lighter stator core consisting only of ferromagnetic teeth, as shown in Figure 2-5-c. Moreover, it could even be possible to avoid the whole stator core and place the coils in the air gap as shown in Figure 2-5-d. However, the *N-S* configuration is not feasible with toroidal windings because both side forces would cancel each other, resulting in a null overall torque.

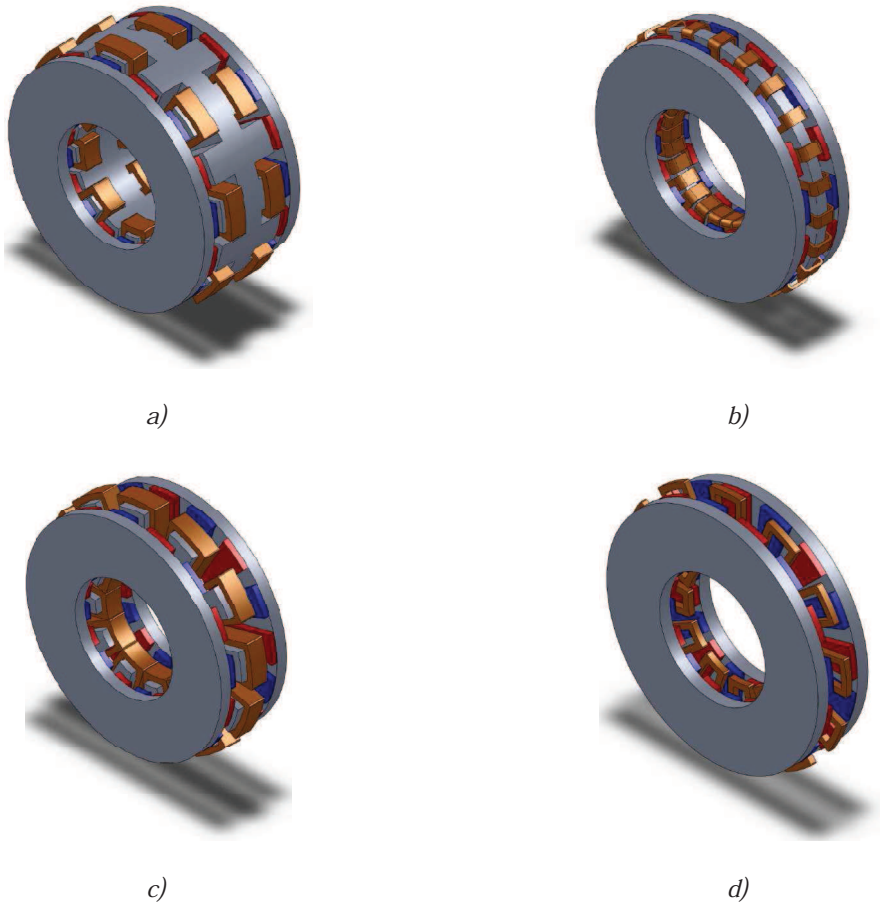

a) *b)*

c) *d)*

Figure 2-5: a) Interior slotted stator N-N machine with lap winding, b) Interior slotless stator N-N machine toroidal winding, c) Interior ferromagnetic core stator N-S machine, and b) Interior coreless stator N-S machine

2.2.3 Multistage

This topology could be defined more accurately as a concept than a type of machine. The idea is to place stators and rotors alternately to obtain a machine with as much sides or stages as desired in order to fulfill the application's requirements. This configuration offers a quite interesting possibility: modularity. Figure 2-6 shows a multistage axial machine with two stators and three rotors. The connection between the winding of different stages could be done in either series or parallel. Furthermore, a connection/disconnection of stages could be done depending on the temporary requirements of the application. This connection may allow fault tolerance as the machine can keep working even if any of the stages is damaged or disconnected.

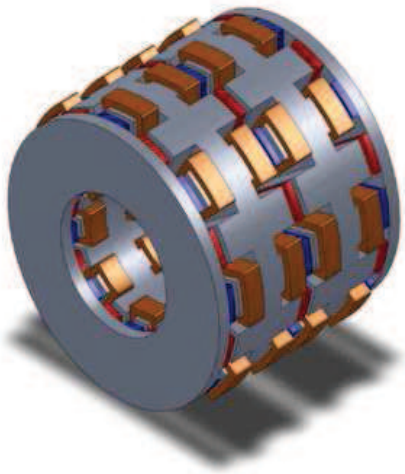

Figure 2-6: Multistage axial flux machine with two stators and three rotors

2.2.4 Conclusions about Topologies

It is not easy to choose a specific topology as the best option. This issue depends on the application to which the machine is suited and the operational requirements of the machine. This section summarizes the advantages and disadvantages of each topology.

The single side machine stands out as the simplest structure. As the literature indicates, this advantage makes it the most often used, but of course, it has drawbacks. The most obvious drawback is the attraction force between the stator and the rotor. Furthermore, it is also remarkable that the slot leakage inductance is greater in a single side machine than in a double side machine with the same characteristics. The reason is that the slot leakage inductance depends on the dimensions of the slot and the number of conductors in it, as shown in expression (3-41). It is proportional to the dimensions of the slot, but it has a square relation to the number of conductors, which increases the inductance considerably.

Although they have common advantages and drawbacks, double-side machines should be considered independently because they entail different possibilities. A common advantage is the possibility of connecting the stators in series or parallel to each other. Another advantage is the lower slot inductance mentioned above. On machines with two stators, the relative position between the stators may be variable, thus increasing the field-weakening capability of the motor [10]. Perhaps the biggest difficulty is a more complex manufacturing and assembly process than in the case of single side machines.

2.3 Suitable Applications for Axial Flux Machines

Throughout history, induction machines have been the most frequently used topologies in common industries. However, in recent years, because of ecological thinking and the rise low-speed applications, permanent magnet synchronous machines have become more popular. Furthermore, the development of new applications, such as electrical vehicles and renewable energy has pushed the development of high-performance, direct-drive electrical machines. The improvement in fabrication techniques and the appearance of new materials have had an important part in this development.

In some of these applications, axial flux machines might be a good choice because of their disk shape, multi stage capability, and characteristic high torque density. These features make axial flux machines a real alternative to classical radial flux machines. In that sense, it is possible to find companies that commercialize axial machines.

Nowadays the majority of applications share the same requirements: high efficiency, saving of space, and economic feasibility, among other characteristics. The role of the electrical machine is of paramount importance in application in general.

Axial flux machines may be used in any kind of application. The literature contains a number of examples:: naval propulsion (Figure 2-7) [11]; the mining industry [12], aeronautics [13]; and small fans, among others [14]. However, three applications may be the most relevant due to the numbers of documents and amount of research a review of the literature reveals in the search for information about axial flux machines: wind power, electric vehicles, and elevation.

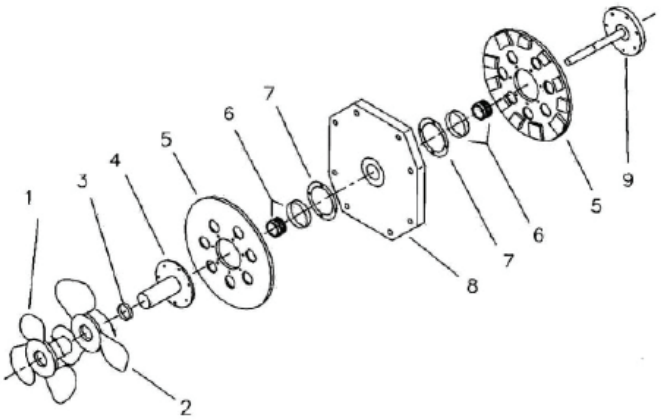

Figure 2-7: Naval propulsion system with axial flux machine [11]

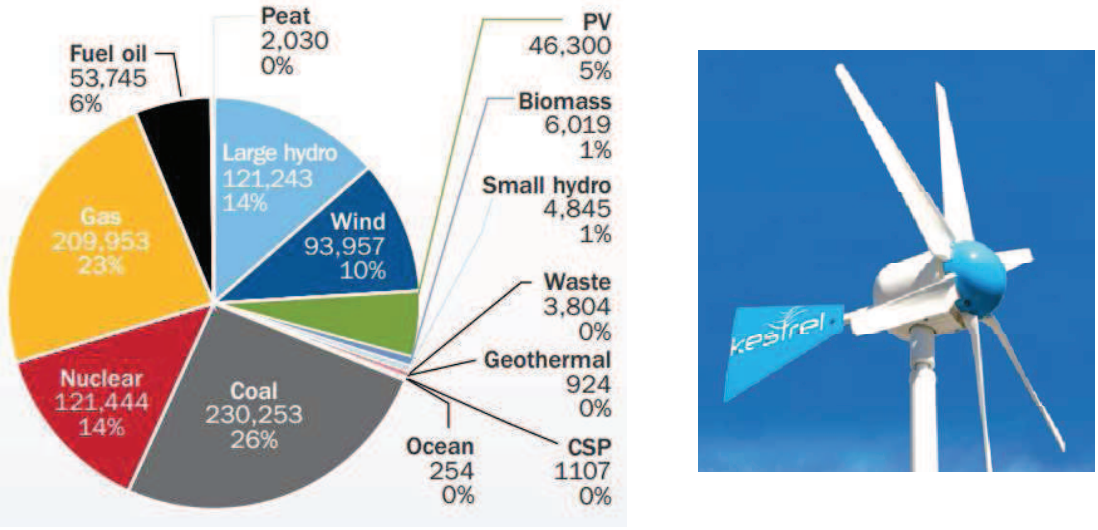

a) *b)*

Figure 2-8: a) EU power capacity 2011 [15] *and b) Kestrel e150 wind turbine*

2.3.1 Wind Power

Because it is highly developed and efficient, wind power has become the leading actor among renewable energies. In fact, in some European countries, such as Denmark, Spain, and Portugal, wind power is among the main energy sources (The European Wind Energy Association [*EWEA*] report 2011). According to the *EWEA* report, wind power has increased from 2% of the total power capacity in 2000 to 10% in 2011 [15]. Historically the induction machine was widely used in wind turbines, but in recent years the use of permanent magnet synchronous machines has increased [16]. The main reason is that by avoiding mechanical coupling and reducing the size of the machine, the system becomes lighter, more efficient, and maintenance free. Most machines used in wind turbines are radial flux machines, but several researches [17–21] have proposed axial machines. There are also commercial solutions, such as those proposed by Kestrel Wind Turbines Ltd. This company offers a range of axial machines between 600 W and 3 KW.

2.3.2 Electrical Traction

Among applications of electrical traction, the electrical vehicle stands out. Hybrid vehicles, which combine a combustion engine with an electrical motor, as well as fully electric vehicles, are a fact nowadays, and there are commercial models on the market. It seems that in the future, the trend will be to develop electrical vehicles with in-wheel machines based on the

concepts shown in Figure 2-9. This will lead to a very sensitive and precise driving. The biggest challenge could be to increase the life of the batteries and decrease their cost.

However, an axial flux machine has not been used in any known commercial electrical vehicle although several researches have focused on this application [22–28]. For example, [22] built an in-wheel axial machine prototype for a solar vehicle (Figure 2-10-a). In [28], an axial machine for an hybrid vehicle was presented (Figure 2-10-b). Furthermore, studies have applied flux weakening to axial flux machines, which is an interesting vehicle application. For example, *Lipo et al.* reviewed different weakening options reported in the literature for both radial and axial machines [27]. In [28], an example of flux weakening used a mechanical system that adjusted the shifting of the two series-connected windings in the stators.

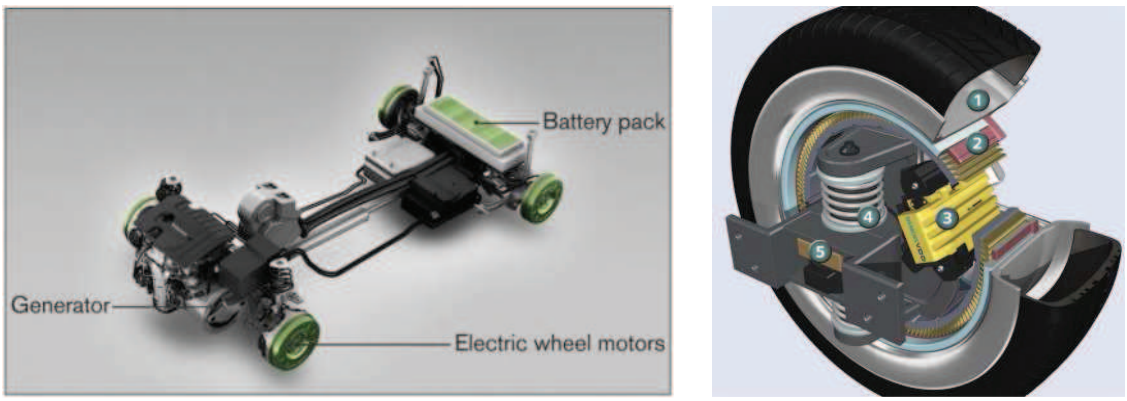

a) *b)*

Figure 2-9: a) Traction system concept for an electrical vehicle by Volvo and b) Built–in wheel by Siemens(Radial flux)

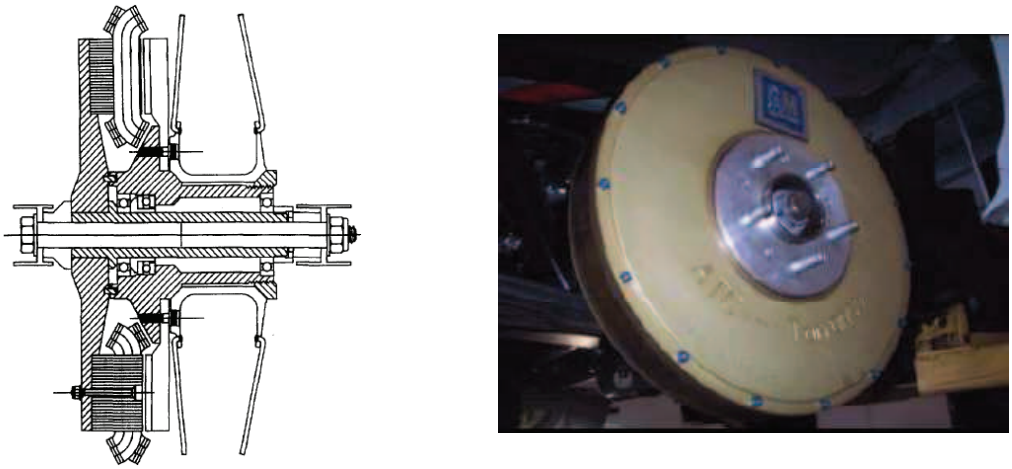

a) *b)*

Figure 2-10: In-wheel axial flux machine a) solar vehicle [22] *and b) hybrid car* [28]

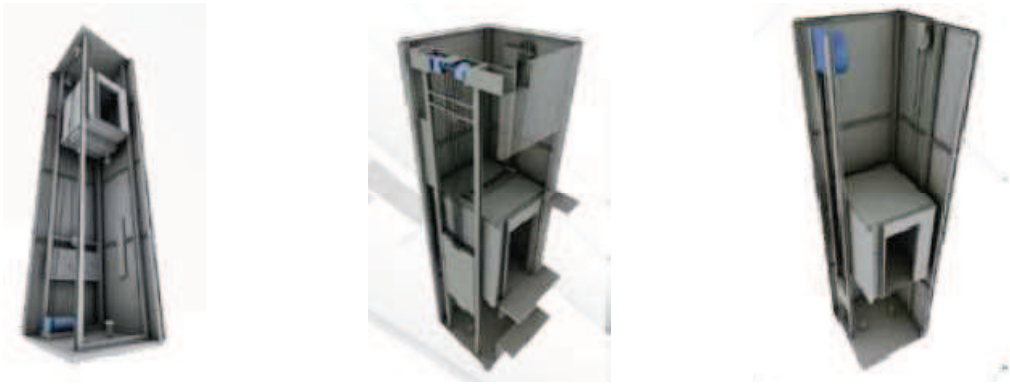

a) b) c)

Figure 2-11: a) Machine on the base, b) machine on the top, and c) machine integrated in the rails [Figures by Kone]

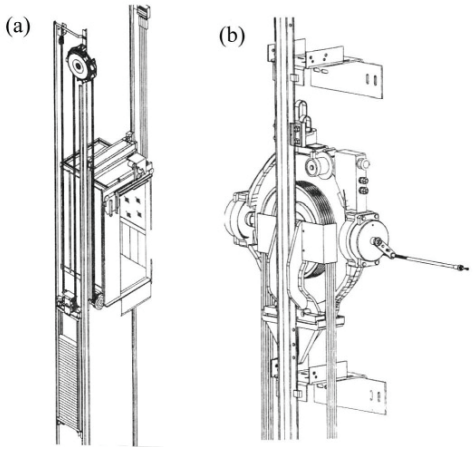

Figure 2-12: MonoSpaceTM elevator by Kone: a) traction system and b) EcoDiscTM machine

2.3.3 Elevation

Another potential sector that may benefit by the characteristics of the axial flux machine is the elevation industry. In 1992, the *Kone Corporation* in Finland was a pioneer of launching elevators with a gearless machine. Subsequently, direct-drive technology was developed quickly and most companies have implemented it in their products, choosing the radial flux machine and placing it in different positions.

Figure 2-11 shows how the machine room is avoided by using direct drive technology and consequently saving space and money. Despite these important improvements, some extra space is needed to house the machine. Due to the shape of axial machines, which are flat and wide, they are a good option for saving space. The machine can be integrated with the rails of the elevator as is done in the *Kone MonoSpace*^{TM} concept, as shown in Figure 2-12. Furthermore, the high torque density of the axial flux machine may reduce their size.

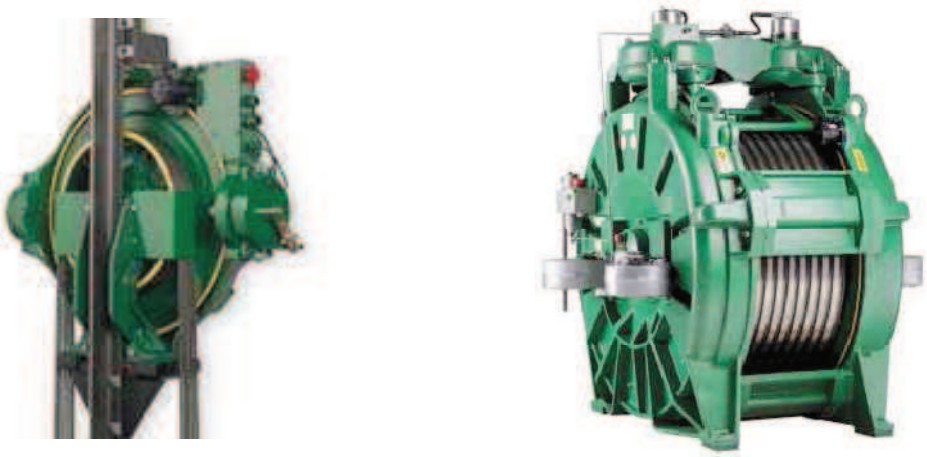

a) b)

Figure 2-13: Kone EcoDisc™: a) MonoSpace™ and b) Alta™

Kone currently uses single side axial machines (*MonoSpace™*) for common buildings and interior rotor machines (*Alta™*) for skyscrapers, where higher torque and speed are needed. Both machines are shown in Figure 2-13. One of the main differences between these machines is that while the *MonoSpace™* machine is integrated with the rails, the *Alta™* is placed on the top of the lift shaft.

The literature search yielded only one study [31] in which the axial machine was applied to elevation. In this work, *SIMINOR Ascenseurs* and a researcher at the University of Rome jointly developed two twin prototypes for a direct-drive elevator system without a machine room. The machines were rated at 5 kW and 95 rpm.

2.4 Fabrication Materials and Techniques of Axial Machines

It is widely known that the main disadvantage of axial flux machines in comparison with radial machines is the complexity of the fabrication. Hence, it is interesting to carry out a study of the materials and fabrication techniques in order to find an easy and economical way to build axial machines. In recent years, several prototypes and even commercial axial machines have been developed, although they are still relatively few.

This section summarizes a study of the materials used in the construction of electrical machines in general and their use in axial flux machines in particular. The manufacturing techniques that are used in axial machines are also analyzed.

2.4.1 Materials for the Construction of Electrical Machines

In the last century, ferromagnetic materials used for the construction of electrical machines were constantly developed. One of the main milestones was the creation of more powerful magnets. At the same time, new ferromagnetic materials with a higher magnetic capacity and lower losses were also developed.

2.4.1.1 Magnets

In the 1940s, *alnico* magnets where used in permanent magnet electrical machines [8]. These magnets have a great remanent flux density, but due to their low coercitivity force, they can be easily demagnetized. In the 1950s, *ferrite magnets* (barium or strontium) were developed. The coercitivity force of these magnets is higher, but the remanent flux density is much lower. The early 1970s saw the beginning of the commercialization of rare earth magnets composed of samarium and cobalt. However, in recent years a new generation of magnets fabricated with neodymium has taken the lead. This magnet family provides both high coercitivity and remanent flux density. Figure 2-14-a shows the *BH* curves of different magnets. The integral $\int_H BdH$, or in other words, the area delimited by each curve represents the energy capacity of each magnet type.

Grain	*Grade*	*Width (mm)*	*Specific losses (W/Kg) 50Hz*	*Magnetic polarization (T)*
Non-oriented	*M210-27A*	*0.27*	*2.10*	*1,49(H=2500 A/m)*
Oriented	*M120-27S*	*0.27*	*0.8*	*1.78(H=800 A/m)*

Table 2-1: Comparison of the electrical sheets by Cogent

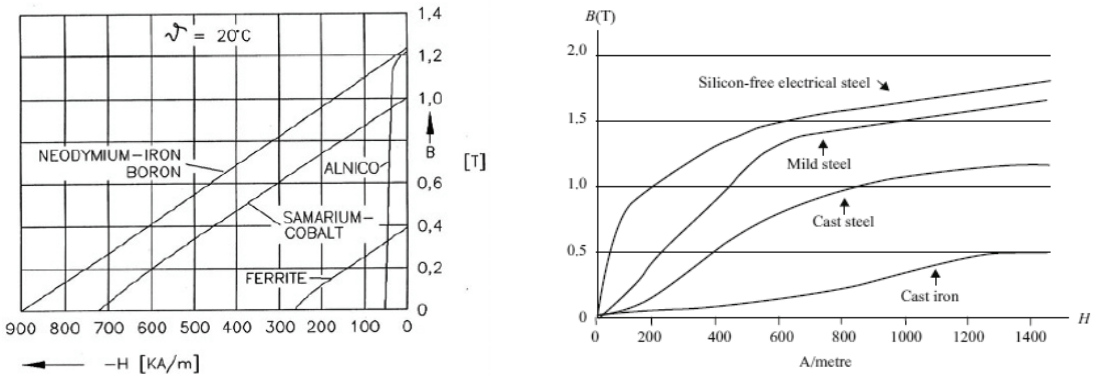

a) *b)*

Figure 2-14: a) BH curve of different magnets [8] *and b) Permeability of different ferromagnetic materials* [32]

2.4.1.2 Electrical Steel

The main objective in building ferromagnetic cores for electrical machines is to obtain high permeability and low losses. In [32] a deep study of the electrical steel used in rotating machines was performed. This study included the history to the manufacturing process of electrical steel and even added experimental results.

In early manufacturing, cast iron was used to build electrical machines. However, the permeability of this material is quite low, as shown in Figure 2-14-b. Higher permeability is reached by using cast steel and mild steel, but the high eddy losses due to the solid core may be a problem. To avoid or at least reduce these losses, the use of electrical steel lamination is essential. These electrical sheets usually have an insulating varnish on their faces, so when they are stacked together, the path for the eddy currents is limited, thus reducing the losses. Depending on the width of the insulation, the effective ferromagnetic material of the stacking is around 95% to 97% of the total length.

The variety of electrical steel available nowadays is immense. Electrical sheets with non-oriented grain are the most commonly used in electrical machines. The non-oriented grain gives the sheets an isotropic characteristic, which means that the magnetic properties are equal in two directions. However, in certain axial flux machines, such as N-S machines, using oriented grain sheets could be possible. These sheets have a better magnetic characteristic in the orientation direction than the non-oriented sheets do. Several studies in the literature have exploited the better magnetic polarization and lower specific losses of oriented grain sheets [33] [34]. Table 2-1 shows the characteristics of both types of electrical sheets.

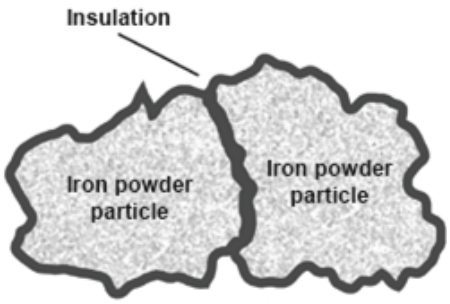

Figure 2-15: Composition of the SMC, Höganäs [35]

2.4.1.3 Soft Magnetic Composites (SMC)

S*oft magnetic composites* (*SMC*) are synthetic materials created from iron powder. The iron powder is coated with a dielectric material (epoxy resin), as shown in Figure 2-15, and then crushed and shaped.

The main advantage of this material compared to electrical sheets is that any shape can be obtained. In contrast, the disadvantages are that the saturation flux density is lower and that even if the eddy losses are very low, the hysteresis losses are higher. This last affirmation depends on the operating electrical frequency of the machine. The higher the frequency is, the higher the eddy currents are, so in this case the *SMC* could be a good option.

The manufacturing process of the *SMC* is divided into several stages. First, the powder is mixed with the insulation and different chemical products needed for the gluing. Once the raw material is obtained, it packed at a pressure of *400-800 Mpa* in the desired shape. Finally, a thermal treatment is used to stabilize the final piece. This molding process is not standard in electrical machinery industry. Only a few companies offer an industrial manufacturing.

Some *SMC* manufacturers fabricate preformed disc shaped *SMC* pieces that can then be machined for prototyping. However, this machining is a difficult process, and the magnetic characteristics of the preformed blocks are not as good as those obtained in the typical manufacturing process. Furthermore, the dimensions of the available discs are quite small.

2.4.2 Fabrication Techniques for Axial Machines

Here the most common materials used in the construction of electrical machines are presented before studying the fabrication processes. In this case, the analysis focuses on axial machines.

2.4.2.1 Construction of the Stator

The complexity and cost of the stator manufacturing process varies depending on the topology of the axial machine. No matter what topology is chosen, the winding process must be taken into account. Depending on the winding type, this process may be more or less difficult, if it is possible to have pre-formed coils. This section provides a global vision of the available possibilities for building a stator core and the winding in it.

- **Lamination**

Using solid cores to build the stator is practically infeasible because of the high eddy losses. Hence, the electrical steel sheets are a good option to avoid or at least attenuate the eddy currents.

In single side machines, interior rotor machines, and *N-N* configuration machines (Figure 2-5) in which the stator yoke is inevitable, the core can be created by rolling the sheets concentrically. This limits the eddy currents while the path of the flux follows the magnetically good direction of the lamination. The easiest way to achieve this concentric lamination is to roll up a long sheet as a spiral, as shown in Figure 2-16. This option has been used in different studies in the literature [36] [38] [39].

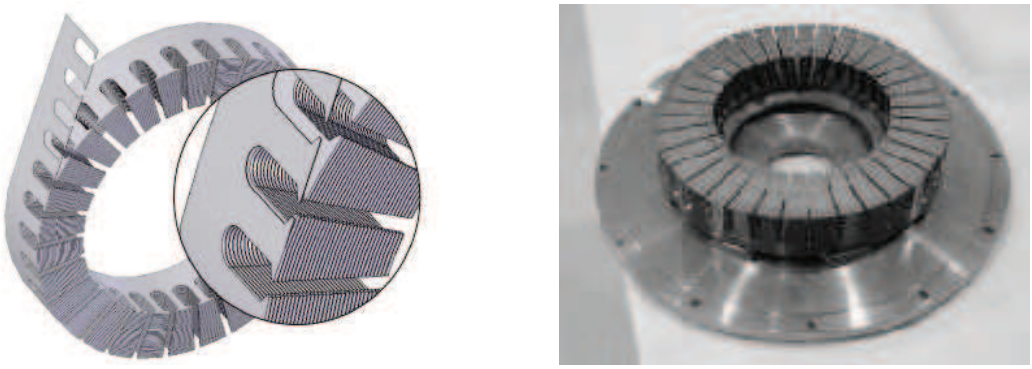

a) *b)*

Figure 2-16: Sheet rolled up in spiral a)method schema[36] *and b) real prototype*[39]

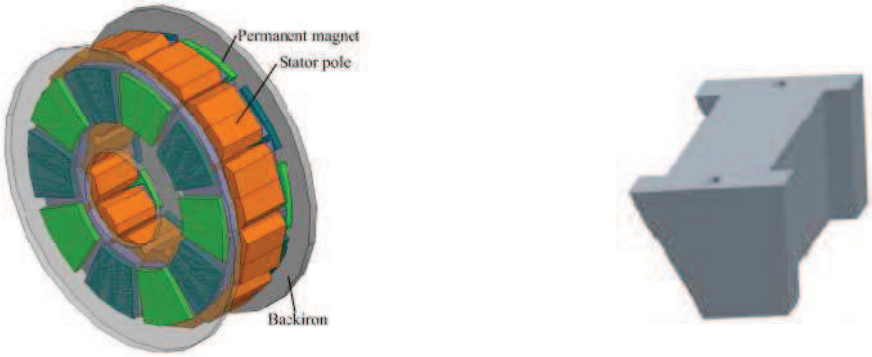

a) *b)*

Figure 2-17: N-S prototype[40] *a) the whole machine and b) detail of a stator pole*

The machining of the slots is another important step. The machining may be done in two ways. The first way is to cut the slots with a variable step and then roll up the sheet. The machining can be done by punching, which is an expensive method and only feasible in mass production or *electrical discharge machining (EDM)*, which is slow. The second option is to machine the slots after rolling up the sheet [38], which is usually done by *EDM*.

In this last technique, a long sheet is first rolled up in spiral. The back of the block is then welded in radial direction. Finally, once the block is thermally stabilized and impregnated with varnish, the slots are created by *EDM*. This last step must be done with extreme care to prevent the sheet from separating in the tooth tips.

In the case of *N-S* machines (Figure 2-5-c-d), it is also possible to use laminations. This configuration does not need a yoke in the core, so it is possible to create the core with independent poles only. In [40] these poles are created by stacking the sheets in a tangential direction, as shown in Figure 2-17. Another option proposed in [34] for this topology is to stack the sheets in a radial direction, as shown in Figure 2-18.

In these last two cases, the flux flows mainly in the axial direction, so using oriented grain electrical steel sheets is possible. However, some of the flux, mostly in the tooth tip vertex, might be distorted with an uncertain path. This distortion might cause some iron loss that is not easy to calculate because the manufactures usually do not give the *BH* curve in the non-oriented direction.

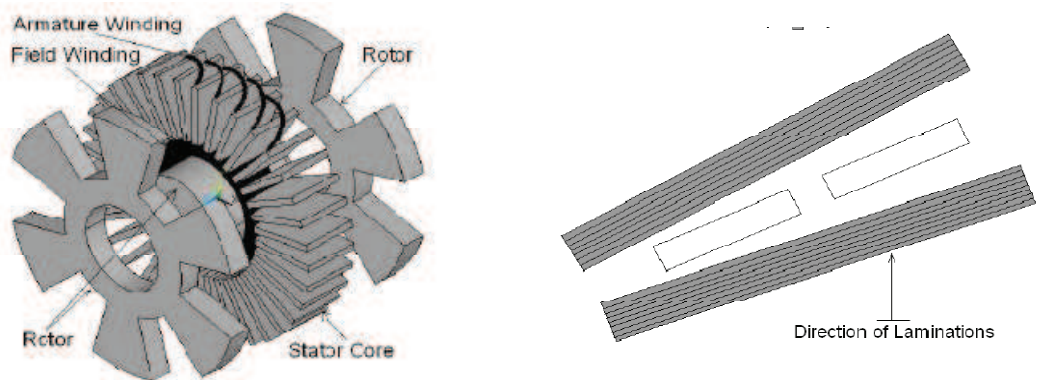

Figure 2-18: Switching reluctance axial machine [34] *a) whole machine and b) detail of a stator pole*

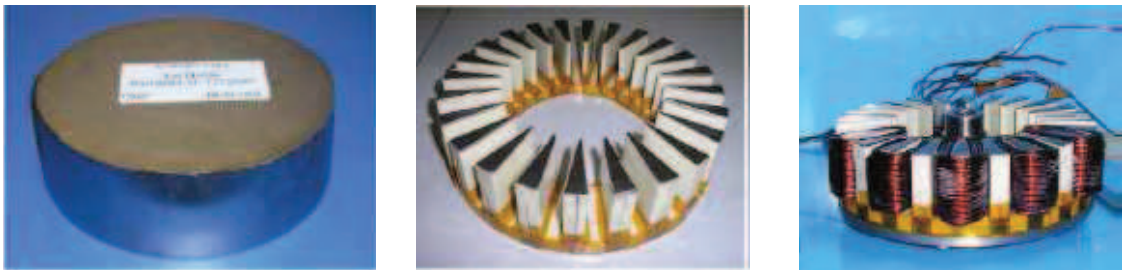

a) *b)* *c)*

Figure 2-19: SMC stator[41]*: a) SMC block b) stator core and c) stator winding*

- ***SMC***

As previously mentioned, the main advantage of the *SMC* is the possibility of obtaining any core shape. However, its cost is a handicap, even if it were a feasible option in mass production [8].

It is not known whether the *SMC* is used in any kind of commercial electrical machine. Nevertheless, it is reported in the literature [19] [41–43] for prototypes using these materials. Typically, these prototypes were created by machining a preformed *SMC* block, as shown in Figure 2-19. On the other hand, it should be emphasized that the highest power obtained in these prototypes is 1.75 kW [41].

Two main problems must be solved when using this material. The preformed pieces are usually quite small (120 mm diameter and 20 mm height for *Höganas*), so it is only useful for small machines. Furthermore, if the core to be built is large, it might be necessary to press the SMC power.

- **Combination of Electrical Sheets and *SMC***

In axial machine configurations where a stator yoke is needed, that is, single side machines, a third option is possible. *SMC* and lamination can be combined to create the stator core. The teeth can be formed with *SMC* and then placed in electrical sheets that are stacked in an axial direction to create the yoke. Some authors implemented this in their prototypes [44] [45], as shown in Figure 2-20. The main advantage of this configuration is the simplicity of the lamination and the moldability of the *SMC*.

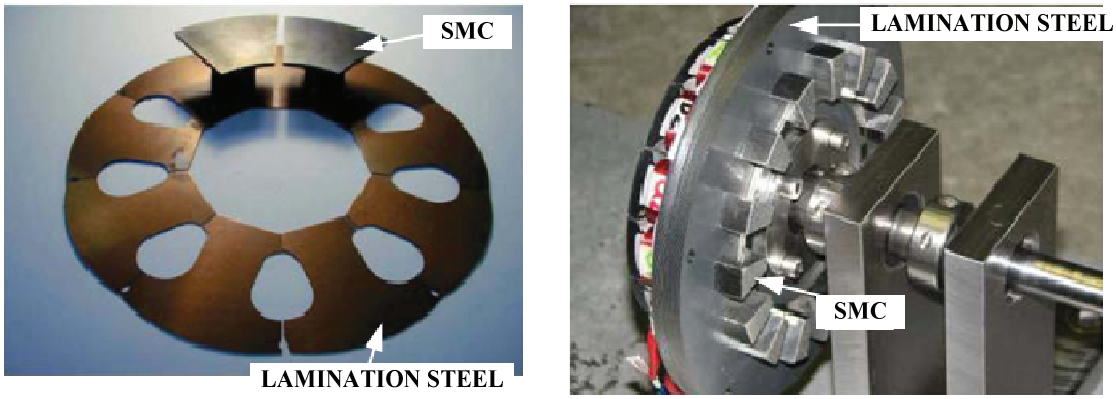

a) *b)*

Figure 2-20: Axial machines with the stator constructed in SMC and lamination: a) 5kW machine[44] *and b) 220 W machine* [45]

- **Coreless**

In *N-S* machines, the stator ferromagnetic core can be avoided and the coils placed in the air gap between the magnets of both rotors. A wide range of research using this method is found in the literature [46–50]. The coils are usually flattened into resin so that the stator is built as is shown in Figure 2-21-a. It is also possible to make the stator with printed circuits [51–53], as in the example shown in Figure 2-21-b.

The main advantage of making the stator with this method is that magnetic losses are avoided. However, because the coils take up space in the air gap, the magnet flux density is attenuated and a higher volume of magnets may be required in order to compensate it. Hence, it is important to find a good compromise between the electrical load and the magnetic load.

a) *b)*

Figure 2-21: Coreless axial machines: a) coils flatten in resin [46] *and b) PCB winding* [53]

2.4.2.2 Construction of the Rotor

The construction of the rotor can vary depending on the concept of the rotor machine: interior or exterior. In both cases, the magnets can be directly glued to a ferromagnetic solid core. In permanent magnet machines, the main flux density in the air gap is created by the magnets, so this field rotates in synchronism with the rotor, making the eddy currents negligible. Nonetheless, in machines with an interior rotor, the magnets can be placed in a non-ferromagnetic structure to create the rotor so that the magnetic losses are negligible [54] [55].

2.5 Conclusions

The following lines sum up the main conclusions regarding the state of the art:

- In those applications where a disc shape is needed, the axial are an interesting fit.
- The wide range of the topologies of axial flux machines makes them polyvalent. It is possible to choose the topology that suits the application best.
- *N-S* and multistage machines allow independent operation of each side of the machine. This could be very useful in faulty situations or instantaneous adjustments to the application's requirements.
- Nowadays some commercial applications use axial flux machines, which indicates increasing interest in them.
- The fabrication of the rotor can be considered simple and relatively inexpensive as it is done with a solid core. The only delicate step is the gluing of the magnets because of the high attraction forces.
- The *SMC* may be a valid option, but it is focused on small machines. Lamination may be the most feasible option. Punching is the best method for mass production, but for prototypes, some suppliers have rolled up blocks that can be machined or even finished.

Chapter 3.

ANALYTICAL DESIGN TOOLS FOR AXIAL FLUX MACHINES

A design methodology for axial flux machines using analytical tools is proposed in this chapter. In the first step, a rough design using electromagnetic equations is described, and in the second step the machine sizing and optimization is carried out. An advanced model in terms of Fourier series is then presented. This model provides very accurate information about the machine in terms of harmonics. Finally, an equivalent electrical circuit is obtained so that the characteristics datasheet can be completed.

3.1 Introduction

Analytical tools for the design of all kinds of electrical machines are still essential although there is a growing trend towards using finite element-based numerical tools. The analytical tools are very useful and a first approximation of the desired machine, both electromagnetic and size characteristics can be obtained easily and quickly. The accuracy of the results obtained by analytical tools varies depending on whether geometrical effects, such as slotting or saturations, are neglected. Despite these limitations, the obtained results are useful in building a more accurate design, which is usually built using finite element methods.

The first step is to design the machine analytically by basic electromagnetic equations. The values of the geometrical and electromagnetic parameters are obtained by these equations, which follow the requirements of the application. These equations give the amplitude of the electromagnetic variables but not the spatial distribution. Nonetheless, the information is sufficient for a first approximation of the dimensions of the machines.

In the second stage, the special distribution of the electromagnetic variables is presented. This method makes possible a deeper view of the machine. Some authors proposed analyses in terms of an equivalent magnetic circuit based in nonlinear reluctance nets [56–58], although there is little research applied directly to axial machines [59].

In contrast, some authors [60–65] chose to analyze the machine by Fourier series, which is in line with this thesis. The Fourier series method yields very detailed information about the analyzed machine because it shows the harmonic spectrum of the electromagnetic variables. Hence, it is possible to identify the link between different variables that cause, for example, torque ripple and to determine whether the design fulfills the requirements.

Finally, the equivalent electrical circuit is obtained to define the characteristic sheet of the machine.

In summary, the analytic design process by which the machine can be easily defined is presented in this chapter. This easy, quick, and effective method is the first step in the whole design process before optimization is achieved by using numerical tools.

3.2 Analytical Sizing

The analytic sizing is divided into two big blocks. First, the electromagnetic equations are presented. These equations, combined with the specifications of the application, allow a first impression of the geometric and electromagnetic characteristics of the machine. In the second step, the sizing of the ferromagnetic cores of the machine is done. Previous studies have presented the general sizing equations in different ways [66–71].

3.2.1 Electromagnetic Equations

An optimized design of the machine is pursued by using electromagnetic equations. The application sets some requirements in terms of torque, size, supply power, and frequency as well as other parameters. The machine is designed according to these requirements. The electromagnetic equations presented here are based on [72].

The first equation considered is the electromagnetic torque T_{em}.

$$T_{em} = \pi \xi_1 \frac{B_{g1}^m}{\sqrt{2}} A k_r (1 - k_r^2) \frac{D_o^3}{8} \tag{3-1}$$

where ξ_1 and B_{g1} are the fundamental harmonics of the winding factor and the magnetic field density induced by the magnets in the air gap. A is the linear electrical load at the inner diameter, k_r is the shape factor and D_o is the outer diameter of the machine. The main dimensions of the machine are shown in Figure 3-1-a.

In most cases, the torque is a requirement of the application, so there are three grades of freedom: electrical, magnetic, and geometric variables. It should be noted that if the expression (3-1) is defined as a function of the shape factor, the maximum torque is reached when $k_r = 1/\sqrt{3}$ as shown in Figure 3-1-b.

The shape factor is the relation between the inner and outer diameters of the machine:

$$k_r = \frac{D_i}{D_o} \tag{3-2}$$

where D_i is the inner diameter of the machine.

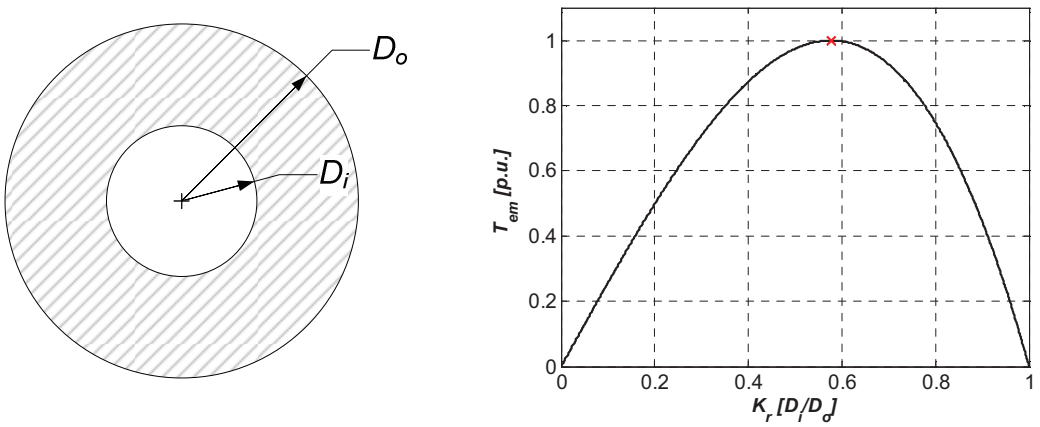

a) *b)*

Figure 3-1: a)Main dimension of the axial flux machines and b) Torque as a function of shape factor

The linear load is defined as the total electrical load in the inner diameter:

$$A = \frac{mI_{rms}N_{ph}}{\pi D_i} \tag{3-3}$$

where m is the number of phases, I_{rms} is the supply *rms* current and N_{ph} is the number of turns per phase.

Although only the value of the fundamental harmonic of the magnet field is needed for this first approximation in general, it is calculated as:

$$B_{g_k}^m = \frac{4}{\pi}\frac{B_r}{(1+g')}\sin(kp\frac{\beta_m}{2}) \tag{3-4}$$

where k is the harmonic number, B_r is the magnet remanent field, β_m is the magnet span angle (Figure 3-2-b) and p is the number of pole pairs in the rotor. Finally g' is the equivalent air gap:

$$g' = \mu_r \frac{g}{h_m} \tag{3-5}$$

where μ_r and h_m are the magnet remanent field and height, respectively. g is the air gap length.

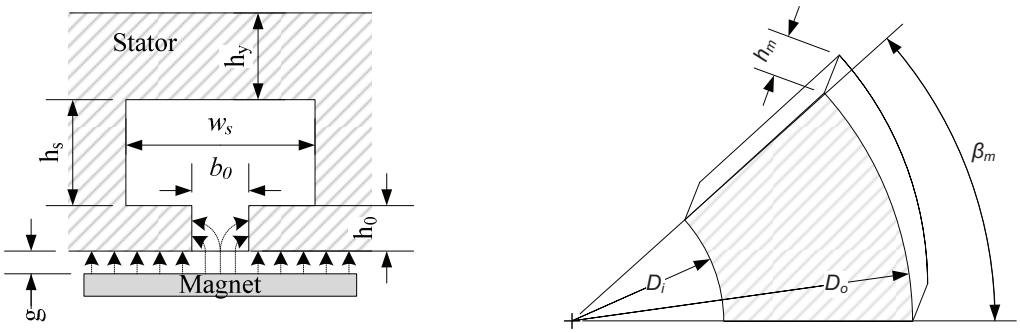

a) *b)*

Figure 3-2: a)Geometry of the slot and b) Dimensions of the magnets

It is possible to consider the slotting effect in the fundamental harmonic by adding the Carter coefficient to the expression (3-4). The Carter coefficient K_c [73] is:

$$K_c = \left[1 - \frac{b_0}{\tau_s} + \frac{4g}{\pi\,\tau_s}\ln\left(1 + \frac{\pi b_0}{4g}\right)\right]^{-1} \tag{3-6}$$

where b_0 is the slot opening and τ_s is the slot span. Both are expressed in Cartesian coordinates. Figure 3-2-a shows the geometry of the slot as well as the path the flux takes in the slot.

Taking into account the effects that happen in the slot is not easy without using numerical tools, so in this stage the assumption of the slot is an approximation.

The winding factor, ξ, is divided into three factors:

- Span factor

The span factor, $\xi_{s,}$ is the span between the negative and positive conductors of a coil. It is defined as the maximal magnet flux linked in the winding:

$$\xi_{s_k} = \sin\left(k t_p \frac{\beta_w(r)}{2}\right) \tag{3-7}$$

where β_w is the span angle between the negative and positive conductors of a coil. t_p is the periodicity of the machine, which is the greatest common divisor between the number of pole pairs, p and number of slots, Q:

$$t_p = G.C.D.(Q, p) \tag{3-8}$$

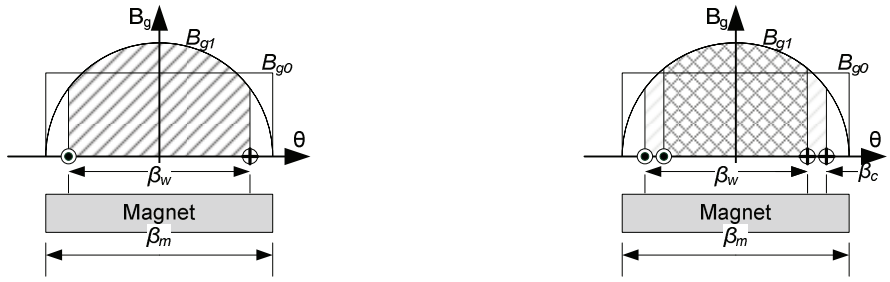

a) b)

Figure 3-3: Graphical explanation of the a) span factor and b) pitch factor

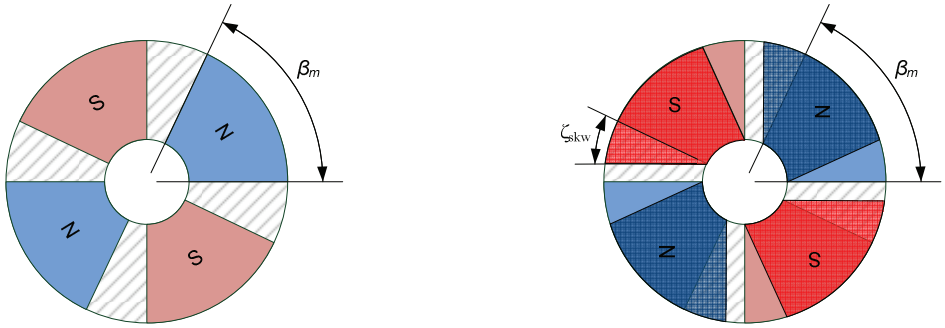

a) b)

Figure 3-4: Graphical explanation of the skew: a) Not skewed magnets y b) Skewed magnets

- Pitch factor

The pitch factor, ξ_p, reflects the relation between the flux linkage in a group of conductors placed with a pitch angle β_c and flux linkage with those conductors placed in the same angle:

$$\xi_{p_k} = \frac{\sin\left(k\, t_p \frac{\beta_c(r)}{2}\right)}{k\, t_p \frac{\beta_c(r)}{2}} \tag{3-9}$$

Figure 3-3 shows a graphical illustration of the concepts of span and pitch angle.

- Skew factor

The skew factor, ξ_{skw}, depends on the relative inclination angle between the radial orientation of the slots or conductors and the poles in the rotor. The use of the skew is quite common when the elimination or at least the reduction of the cogging torque is desired:

$$\xi_{skw_k} = \frac{\sin\left(k\, t_p \frac{\zeta_{skw}}{2}\right)}{k\, t_p \frac{\zeta_{skw}}{2}} \tag{3-10}$$

where ζ_{skw} is the skew angle or the inclination angle between the slot and rotor poles. Figure 3-4 shows a graphic illustration of this relationship.

Finally, the winding factor is the sum of the effect caused by the above-mentioned three factors:

$$\xi_k = \xi_{s_k}\, \xi_{p_k}\, \xi_{skw_k} \tag{3-11}$$

The induced voltage in each phase of electromotive force *EMF* is defined as:

$$EMF = \frac{B_{g1}^m}{\sqrt{2}}\, \xi_1 N_{ph} \frac{1}{8}(1 - k_r^2) D_o^2 \omega_{\mathrm{m}} \tag{3-12}$$

where ω_m is the rotational speed of the machine in radians per second. From the rotational speed and number of pole pairs, it is possible to obtain the electrical frequency, f_e:

$$f_e = p \frac{\omega_m}{2\pi} \tag{3-13}$$

Another expression with which it is possible to obtain the electromagnetic torque, knowing the *EMF* and the current in each phase, and having an equilibrated system is:

$$T_{em} = \frac{m\, EMF\, I_{ef}}{\omega_m} cos(\alpha) \tag{3-14}$$

where α is the load angle, which is the angle between the induced voltage and the current as it is shown in the phasor diagram in Figure 3-5. When this angle is 0º, commonly called quadrature load (the magnet field and the current are in quadrature), the torque is maximum.

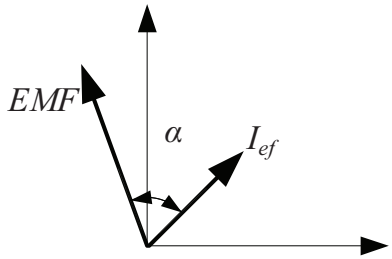

Figure 3-5: Phasor diagram

3.2.2 Sizing of the Machine

Once the electromagnetic equations have been solved, it is possible to proceed with the machine optimization. This optimization can be done in different terms, although one of the most common optimizations is torque density, in other words, the torque capability per volume unit.

The optimization process for the axial flux machines proposed in this thesis is explained step-by-step below. It should be clarified that the process is defined for one-side machines, even if it is the same for other cases.

The configuration of the stator and rotor (winding and pole pairs) is selected to fulfill the requirements of the application. This configuration gives the winding factor and electrical frequency. The magnets and the air gap have to be selected, in order to obtain the air gap field. The linear load and shape factor are also fixed. Once these parameters are obtained (3-1), the outer diameter is calculated:

$$D_o = \sqrt[3]{\frac{T_{em}}{\pi \xi_1 \frac{B_{g1}^m}{\sqrt{2}} A \frac{1}{8} k_r (1 - k_r^2)}} \tag{3-15}$$

The inner diameter is immediately obtained from the outer diameter and the shape factor. Thus, by knowing the number of phases and the supply current, it is possible to obtain the number of turns per phase from (3-3). Consequently, the number of turns per each coil, N_b is obtained with the next expression:

$$N_b = \frac{N_{ph}}{(Q/2m)n_l} \tag{3-16}$$

where n_l is the number of layers in the winding. The number of layers is two if there are as many coils as slots, and it is one in the case of half coils.

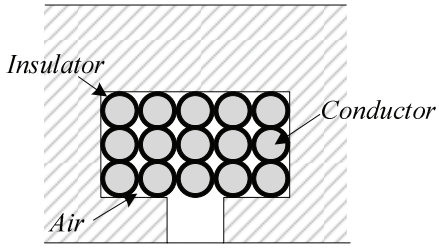

Figure 3-6: Filling of the slot with the conductors

The number of conductors in each slot, Z is:

$$Z = n_l N_b \tag{3-17}$$

The dimension of the conductors is given by their current density:

$$J_{cu} = \frac{I_{ef}}{A_{ce}} \tag{3-18}$$

where A_{ce} is the conductor section J_{cu} is the current density. This density usually does not exceed $7.5\ A/mm^2$ in continuous operation, although the characteristics given by the copper wire manufacturer must be observed.

From the number of conductors in a slot, the copper section and the fill factor K_f, the total section of the slot, A_s.is obtained:

$$A_s = \frac{Z A_{ce}}{K_f} \tag{3-19}$$

This fill factor is a reflection of the quality of the winding. The closer to unity, the better the use of the space in the slot is. Because of the insulation impregnation of the wires, its rounded shape, and the complexity of the winding process, the fill factor is usually around 0.3-0.6. Figure 3-6 shows a graphic illustration.

In the next step, the properties of the used material, in both the rotor and the stator core are taken into account. The geometries of the ferromagnetic cores are obtained with the values of the saturation fields of these materials. Figure 3-8 shows the dimensions obtained in this stage.

All the dimensions are calculated following the law of flux conservation:

$$\phi = B_a S_a = B_b S_b \tag{3-20}$$

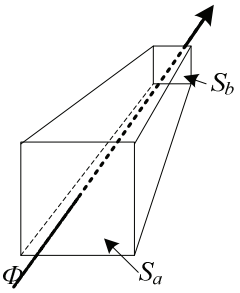

Figure 3-7: Flux conservation principle

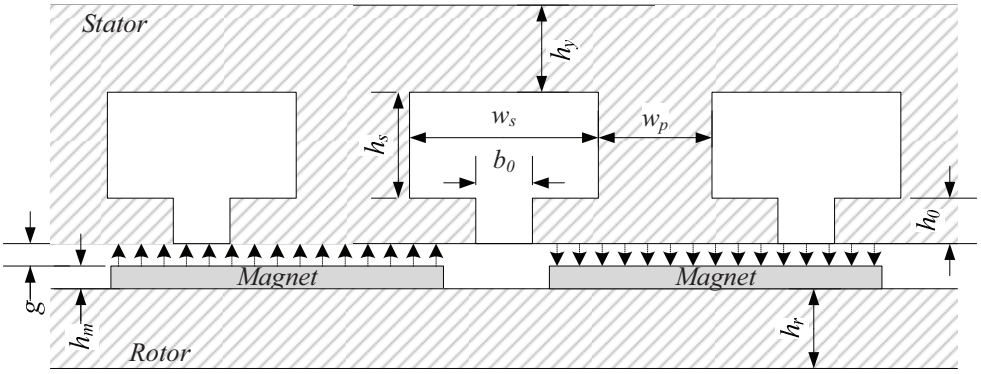

Figure 3-8: Detail of the slot and machine dimensions

where B_a y S_a are the field and section in the *a* face, while B_b y S_b are the field and section in the *b* face *b*. Φ is the magnetic flux. Figure 3-7 shows the flux conservation principle.

Following the flux conservation principle, the minimum rotor yoke height is calculated as:

$$h_r l B_{SATr} = \frac{w_m l}{2} \frac{B_{g1}}{\sqrt{2}} \tag{3-21}$$

where B_{SATr} is the saturation field of the rotor core. The most critic saturation point is when the width of the magnet, w_m is maximum. This happens in the outer radium when the magnets are trapezoidal. The flux induced by the magnets is divided in two equal paths along the stator and rotor yokes as shown in Figure 3-9-a.

The stator yoke height, h_y, is similarly obtained, with the difference that the saturation field B_{SATs} might vary depending on the material:

$$h_y l B_{SATs} = \frac{w_m l}{2} \frac{B_{g1}^m}{\sqrt{2}} \tag{3-22}$$

Finally, the width of the teeth or pillars in the stator is w_p. An approximated value can be obtained from the next equation:

$$\frac{p}{Q} w_p l B_{gSATs} = w_m l \frac{B_{g1}^m}{\sqrt{2}} \tag{3-23}$$

In this case, the flux induced by the magnets is dispersed along all the pillars as shown in Figure 3-9-b. The ratio p/Q is the amount of teeth per pole.

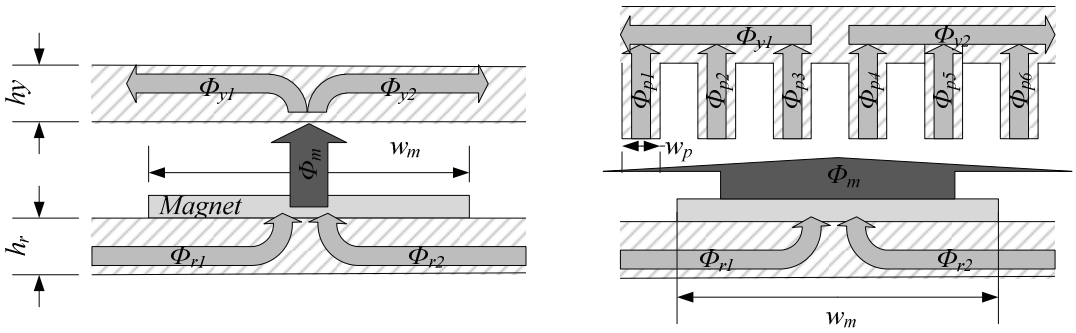

Figure 3-9: Flux conservation a) in rotor and stator yokes and b) in the stator teeth

The inner diameter of the core is the most critical point for the teeth width, w_p. At that point, the perimeter is the smallest, and the teeth have to allow space for the coils. Thus, the width of the slots is:

$$w_s = \frac{\pi D_i}{Q} - w_p(D_i) \tag{3-24}$$

Once the slot width and sections are known, the height, h_s can be easily obtained:

$$h_s = \frac{A_s}{w_s} \tag{3-25}$$

The total diameter of the machine, D_t is the sum of the outer diameter of the cores and the end winding:

$$D_t = D_o + 2l_{ew} \tag{3-26}$$

where l_{ew} is the end winding length (Figure 3-10). This length depends on the type of winding and its quality, but in general, the length is equal to the slot width with a single layer winding and half with a double layer winding.

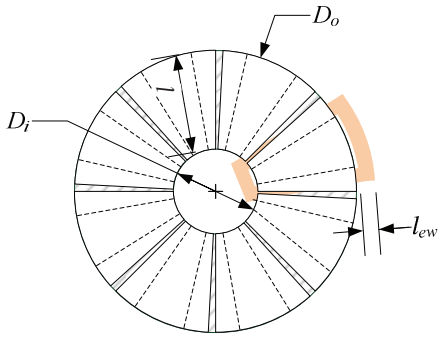

Figure 3-10: Detail of the end winding

The axial length of the machine, L_t, is the sum of all the heights: The rotor yoke height, h_r, magnet height, h_m, air gap, g, slot height, h_s and the stator yoke height h_y:

$$L_t = h_r + h_m + g + h_s + h_y \tag{3-27}$$

The total volume V_t is:

$$V_t = L_t \left(\frac{D_t}{2}\right)^2 \tag{3-28}$$

The torque density is:

$$Torque\ density = \frac{T_{em}}{V_t} \tag{3-29}$$

The torque density is the target parameter in this optimization process.

Two points should be clarified. On the one hand, in slotless machines the coils are placed in the air gap, so this has to be taken into account during the design process to ensure that there is enough space in the air gap to place the coils. On the other hand, it should be mentioned that more than one-side machines should be assumed. A valid method is to design a machine as a single side machine with corresponding torque because each side behaves as an independent machine. The total electrical load is the sum of the electrical load of each side.

3.2.3 Equivalent Electrical Circuit

Several works in which different methods were used to obtain the equivalent electrical circuit of a machine are reported in the literature [74–76]. In general, the equivalent electrical circuit is represented as shown in Figure 3-11. That circuit can be mathematically defined with a vector sum in terms of concentrated parameters:

$$\vec{v}_s = R_{cu}\vec{\imath} + \frac{d\psi}{dt} = R_{cu}\vec{\imath} + \omega_e L_s \vec{\imath}_0 + \omega_e \psi_{pm} \tag{3-30}$$

where R_{cu} is the phase copper resistance and L_s is the phase inductance, respectively. V_s and I_s are the supply voltage and current, respectively. The relation between the mechanical speed and electrical speed, ω_e, is:

$$\omega_e = p\omega_m \tag{3-31}$$

The relation between the totalized magnet flux, ψ_{pm} and the induced voltage, E_0 is:

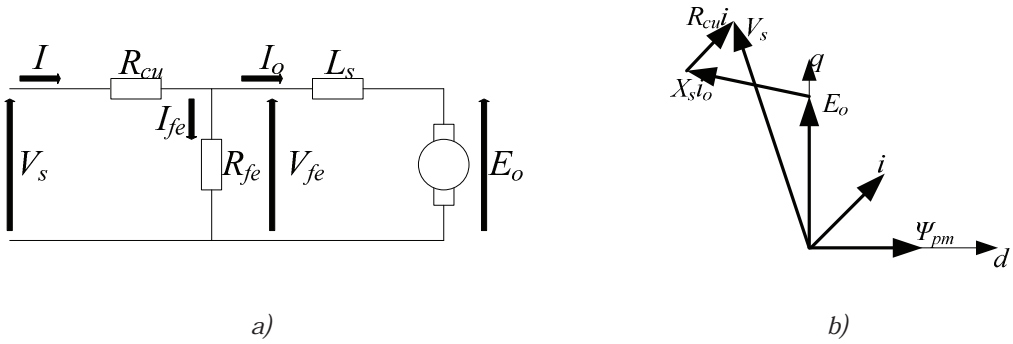

Figure 3-11: a) Equivalent lumped parameters electrical circuit and b) vector diagram

$$E_0 = \omega_e \psi_{pm} \tag{3-32}$$

If the vector equation is transformed to *dq* axis, the inductance is constant and not position-dependent, and the saturation effects are always neglected:

$$v_{ds} = R_{cu} i_{ds} - \omega_e L_{sq} i_{q0} \tag{3-33}$$
$$v_{qs} = R_{cu} i_{qs} + \omega_e L_{sd} i_{d0} + \omega_e \psi_{pm} \tag{3-34}$$

In the case of superficial permanent magnet machines, the synchronism inductance is equal along the *d* and *q* axes.

Figure 3-11-a shows a parallel resistance R_{fe} in the circuit. This resistance considers the magnetic losses of the machine.

The output mechanical power of the machine is obtained by:

$$P = 3 I_0 E_0 \cos(\alpha) \tag{3-35}$$

where I_o and E_o are the *rms* value of the current and voltage, respectively. Maximum power is obtained when the current is in phase with the *EMF*. However, in cases where, for example, flux weakening is used, it is possible to push the current in the *d* axis so that the rotation speed is increased.

Obtaining the lumped parameters is both important and interesting since these parameters define the voltage and current of the controller. The calculation of the lumped parameters is explained in the next section.

- **Copper resistance**

The resistance in the wire of each phase caused by the resistivity of the copper is calculated as follows:

$$R_{cu} = \rho(T)\frac{l_{cu}}{A_{cu}} \tag{3-36}$$

where l_{cu} is the length of the copper in each phase and ρ_{cu} is the copper resistivity dependent on the temperature T:

$$\rho(T) = \rho(T_0)[1 + \alpha_{cu}(T - T_0)] \tag{3-37}$$

Being α_{cu} is the copper temperature coefficient. T_0 is referred to the initial temperature (usually 20 ºC or 25 ºC) and T to the working temperature.

- **Resistance due to iron losses**

Typically, the iron losses produced in the magnetic core can be considered by adding an equivalent resistance in the electric circuit (R_{fe}). The value of this equivalent resistance can be computed by applying the next expression:

$$R_{fe} = \frac{3\left|V_{fe}^2\right|}{P_{fe}} \tag{3-38}$$

where V_{fe} is the voltage at the equivalent resistance terminals and P_{fe} is the iron losses. These losses depend on both the speed and the load state of the machine. The calculation of the magnetic losses in the iron is a quite arduous process, so numerical tools are used for this task, which is explained in Chapter Four.

- **Synchronous inductance: L_s**

The synchronous inductance of each phase is the sum of three components: the air gap inductance, the slot inductance, and the end-winding inductance [5] [8] [76] [77].

$$L_s = L_g + L_r + L_{ew} \tag{3-39}$$

- *Air gap inductance: L_g*

In the general definition of the air gap inductance in a coil, L_g is the division between the flux linkage in that coil, referred to as the flux induced by the armature, and the current through that coil:

$$L_g = \frac{\psi}{i} \tag{3-40}$$

In section 3.3.2.7, the air gap inductance is calculated using the Fourier series. This inductance embraces two components. On the one hand, it is the main inductance or the fundamental component inductance. On the other hand, there is a dispersion inductance linked to the harmonic content of the field in the air gap. This dispersion inductance is considered a leakage inductance.

- *Slot leakage inductance: L_r*

This component of the inductance is due to the flux leakage inside the slot. The value of the inductance is strongly linked to the shape of the slots, the position of the coils, and the number of winding layers. The slot leakage inductance for each slot can be computed by the following equation [73]:

$$L_r = \mu_0 N_s^2 (R_o - R_i) \lambda_s \tag{3-41}$$

where N_s is the number of conductors per slot, and λ_S is the slot shape factor. In the case of slots with the shape shown in Figure 3-12-a, the shape factor can be obtained by the following expression [8]:

$$\lambda_s = \frac{h_s}{3w_s} + \frac{h_a}{w_s} + \frac{2h_c}{w_s + b_o} + \frac{h_o}{w_s} \tag{3-42}$$

In the case of double layer windings, the last expression is not valid for all cases as it was developed for the particular cases of single layer windings. Furthermore, the model does not assume the differential leakage inductance, which is the effect that one coil in a slot generates the inductance of the other coil in the same slot. These two issues make the calculation of the leakage inductance less accurate. However, in many cases this approximation can give valid results.

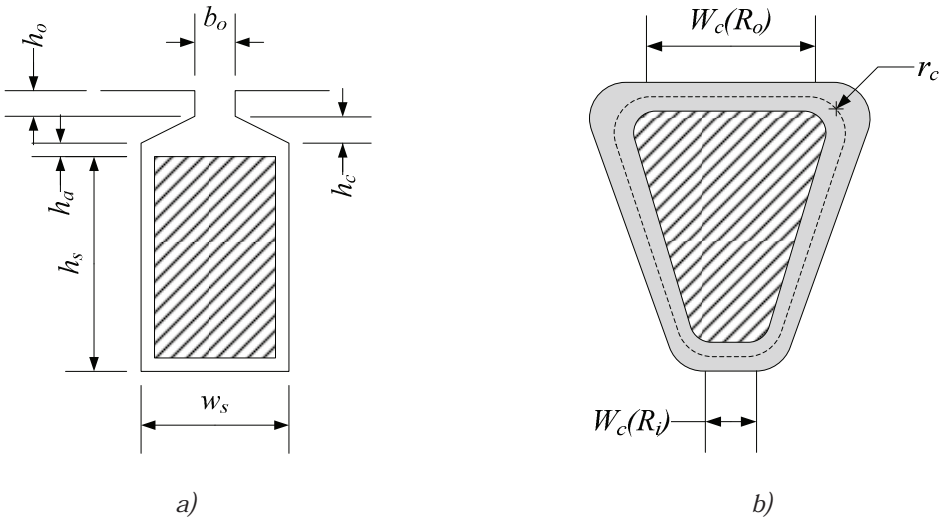

Figure 3-12: a) Detail of the dimensions of the slot and b)dimensions of the coils

- *End-winding leakage inductance: L_{ew}*

The parameter of end-winding inductance is a complicated calculation because of the difficulty of obtaining the real shape of these end-windings.

In the case of axial flux machines, the inner (L_{ew_o}) and the outer (L_{ew_o}) end-winding inductances are different, because the end-windings are different, as shown in Figure 3-12 -b. These inductances can be computed by the following equations, which were developed from the expressions proposed in [5] for radial machines:

$$L_{ew\_o} = \frac{1}{2}\frac{\mu_0}{\pi} N_{ph}^2 \left(2\pi r_c + w_c(R_o)\right) ln\left(K_e \frac{(w_c(R_o) + 2r_c)}{2r_c}\right) \quad (3\text{-}43)$$

$$L_{ew\_i} = \frac{1}{2}\frac{\mu_0}{\pi} N_{ph}^2 \left(2\pi r_c + w_c(R_i)\right) ln\left(K_e \frac{(w_c(R_i) + 2r_c)}{2r_c}\right) \quad (3\text{-}44)$$

where r_c is the curvature radius of the end-winding and K_e is the shape factor of the end-winding. The total end-winding inductance is the sum of both terms:

$$L_{ew} = L_{ew\_o} + L_{ew\_i} \quad (3\text{-}45)$$

In the case of a toroidal winding, the end-winding inductance is calculated similarly, but in this case, the inner and outer inductances are the same.

3.2.4 Analytical Sizing Equations for Comparison of Axial and Radial Machines

The performance comparison of radial flux machines and axial flux machines has been addressed by many authors [103], [110–116]. Indeed, a comparison between both types of machines is quite complex because of the many options for comparison, such as cost, volume, and loses.

However, in order to perform a comparison, the machine that best suits the application must be chosen. This should be done at the beginning of the design process by evaluating the advantages and drawbacks of both types of machine.

In both cases, the sizing process follows the same steps. First, the number of pairs of poles and slots, torque, electric load, and current density in the wires, the shape factor and properties of magnets are defined. Once these parameters are preset, sizing is done using the expressions set out in Chapter Three. These expressions are for axial machines but with simple modifications they can be extrapolated to radial flux machines. Figure 3-13 shows the dimensions of the axial and radial machines that are calculated. The steps for dimensioning and the equations used in them are summarized in Table 3-1.

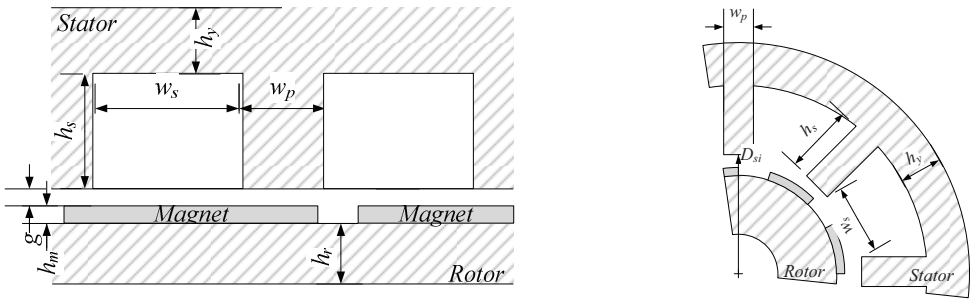

a) b)

Figure 3-13: Geometry of the machine: a) axial and b) radial

Step	Radial	Axial
1	$D_{si} = \sqrt[3]{\frac{T_{em}}{\pi\xi_1 \frac{B_{g1}^m}{\sqrt{2}} A \frac{k_{rad}}{2}}}$	$D_o = \sqrt[3]{\frac{T_{em}}{\pi\xi_1 \frac{B_{g1}^m}{\sqrt{2}} A k_r \frac{(1-k_r^2)}{8}}}$
2	$L_e = D_{si} K_{rad}$	$D_i = D_o K_r$
3	$N_{ph} = \frac{A\pi D_{si}}{2mI_{rms}}$	$N_{ph} = \frac{A\pi D_i}{2mI_{rms}}$
4	$B_{ph} = \frac{Q}{2mn_l}$	
5	$N_b = \frac{N_{ph}}{B_{ph}}$	
6	$Z = n_l N_b$	
7	$h_r = \frac{B_{g1}}{\sqrt[2]{2}B_{sr}} \beta_m \frac{D_{si}}{2}$	$h_r = \frac{B_{g1}}{\sqrt[2]{2}B_{sr}} \beta_m \frac{D_o}{2}$
8	$h_y = \frac{B_{g1}}{\sqrt[2]{2}B_{ss}} \beta_m \frac{D_{si}}{2}$	$h_y = \frac{B_{g1}}{\sqrt[2]{2}B_{ss}} \beta_m \frac{D_o}{2}$
9	$w_p = 2h_y \frac{2p}{Q}$	
10	$A_s = \frac{I_{rms}}{J} Z k_f$	
11	$w_s = \frac{\pi D_{si}}{Q} - w_p$	$w_s = \frac{\pi D_i}{Q} - w_p \frac{D_i}{D_o}$
12	$h_s = \frac{A_s}{w_s}$	
13	$D_{radial} = D_{si} + 2h_b + 2h_y$	$D_{axial} = D_o + w_s$
14	$L_{radial} = L_e + 2w_s$	$L_{axial} = h_r + h_m + g + h_s + h_y$
15	$V_{radial} = \pi \left(\frac{D_{radial}}{2}\right)^2 L_{radial}$	$V_{axial} = \pi \left(\frac{D_{axial}}{2}\right)^2 L_{axial}$

Table 3-1: Sizing equations for axial and radial machines

3.3 Model in Fourier Series

3.3.1 Methodology of the Model

This section describes the methodology of the model in terms of Fourier series. First, the hypotheses are enumerated and then the Fourier series are defined. Finally, based on Fourier series, the stages of the proposed model are described. This methodology is similar to the one presented in [5], [79], but adapted for axial flux machines.

3.3.1.1 Hypothesis of the model

The following hypotheses develop the model in Fourier series:

- The material in both the stator and in the rotor is a ferromagnetic material with infinite permeability.
- The field in the air gap is completely perpendicular to the surface without a tangential component.
- A linear system is assumed because the saturation of the ferromagnetic material is not considered.
- The magnet's working point is inside the linear part of its curve.

3.3.1.2 Definition and Properties of Fourier Series

According to Fourier series, any periodical signal, regardless of shape, can be defined as the sum of its sine and cosine components, as shown in the next general expression for those series:

$$f(\theta) = \frac{1}{2}A_0 + \sum_{n}^{\infty} \mathrm{A_n}\cos(n\theta) + \sum_{n}^{\infty} \mathrm{B_n}\sin(n\theta) \tag{3-46}$$

where n is an integer number referred to the harmonic, A_0 is the continuous component of the signal and A_n and B_n are the amplitudes of the sine and cosine components, respectively. It is also possible to define Fourier series as an exponential function, which is useful for the proposed methodology:

$$f(\theta) = \sum_{-\infty}^{\infty} C_n e^{jn\theta} \tag{3-47}$$

where C_n is the amplitude of the n order exponential component and j is the imaginary number.

3.3.1.3 Steps of the Model

The proposed model is divided into five stages. The first step is to calculate the magnetic flux density induced by the magnets in the air gap. Then in the second step, the distribution of

the conductors C is calculated. This distribution obtains the magneto motive force per current unit F, which is necessary to obtain the magneto motive force MMF. When the MMF is obtained, the flux field induced by the armature in the air gap can be calculated.

The third step is carried out in slotted machines. In this case, the slot effect is implemented. This is presented in a relative permeability form λ. The slot effect directly affects the expressions of the flux density in the air gap, induced by both the magnets and the armature, thus obtaining new expressions.

The fourth stage is the calculation of the electromagnetic coupling of the machine. Here the armature-flux linkage ψ, the electromagnetic force EMF, and finally the electromagnetic torque T_{em} are obtained. In cases where slots exist, a new component of the torque, known as the cogging torque appears.

Finally, the model is completed by the electrical parameters of the machine, in other words, by obtaining the equivalent electrical circuit.

Figure 3-14 shows the flow chart of the proposed model.

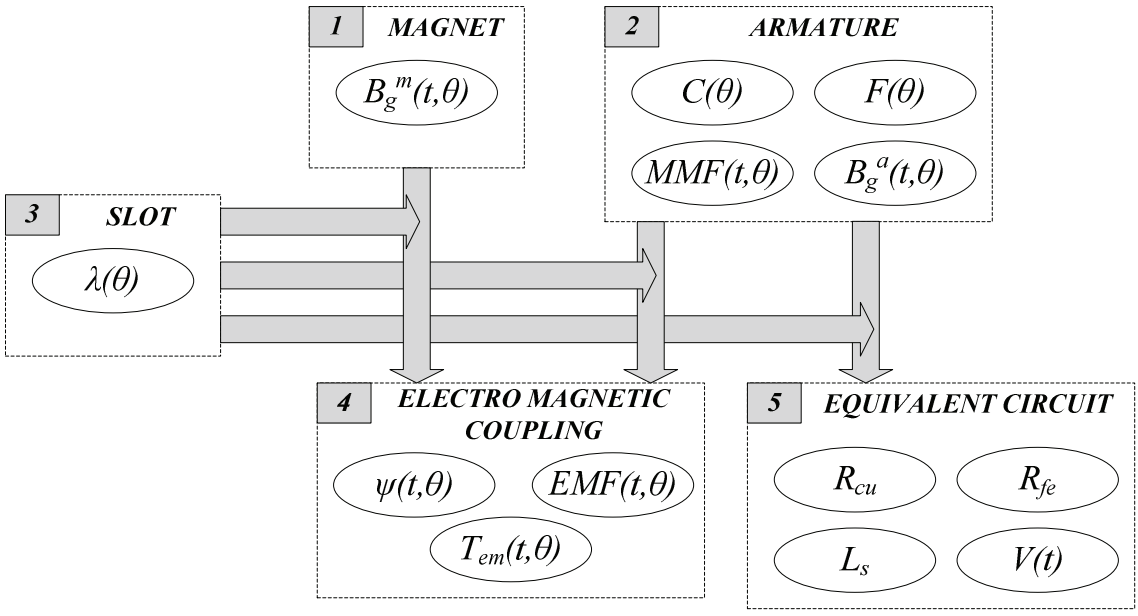

Figure 3-14: Flow chart of the proposed model

3.3.2 Model for Axial Flux Machines

3.3.2.1 Flux Field Induced by the Magnets in the Air-gap

The general expression of the space-time distribution of the flux density induced by the magnets in the air gap in terms of Fourier series is:

$$B_g^m(t,\theta) = \sum_{-\infty}^{\infty} \vec{B}_{gk}^m e^{-jpk\theta} \tag{3-48}$$

where k is the number of the harmonic, θ is the angular position and vector $\vec{B}_{gk}^m$ is:

$$\vec{B}_{g_k}^m = B_{g_k}^m e^{-jpk(\varphi_0 + \omega_m t)} \tag{3-49}$$

where φ_0 is the initial position of the rotor.

In this section, a quasi-rectangular distribution of the field is assumed, as shown in Figure 3-15. The real shape of the field distribution is not rectangular if the dispersion of the flux lines in the edges of the magnets is considered. Using a fringing function to assume this dispersion does not entail a great computational cost and the results are quite accurate.

The coefficients $B_{g_k}^m$ are obtained from the waveform shown in Figure 3-15:

$$B_{g_k}^m = \frac{\hat{B}_{g0}^m}{K\pi}(1-\cos(k\pi))\sin\left(kp\frac{\beta_m}{2}\right)\frac{1}{1+(akp)^2} \tag{3-50}$$

where a is the fringing function parameter. This function is not necessary; however, it is a very simple function that improves the results significantly and is represented as:

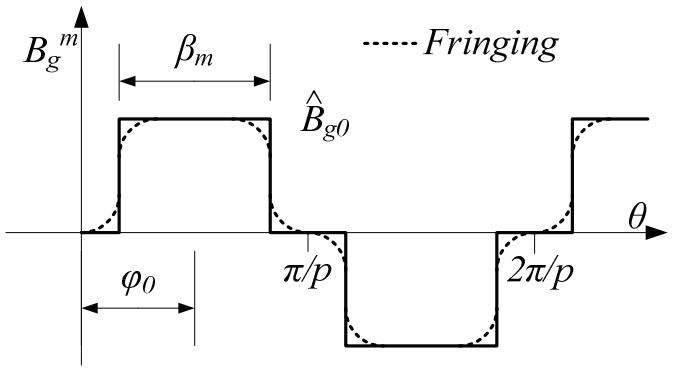

Figure 3-15: Magnetic field induced by the magnets in the air gap

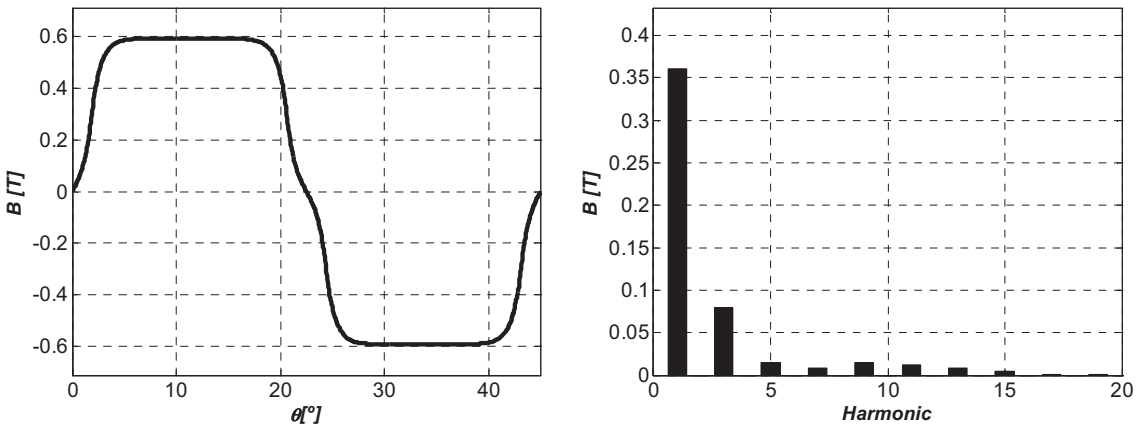

a) *b)*

Figure 3-16: Field in the air gap induced by the magnets: a) spatial waveform and b) spectrum

$$a = \sqrt{\frac{g(g')}{D_{av}}} \tag{3-51}$$

where D_{av} is the average diameter. This parameter is developed from [80]. The maximum value of the field is:

$$\hat{B}_{g0}^{m} = \frac{B_r}{1 + g'} \tag{3-52}$$

The space-time expression of the field induced by the magnets in the air gap developed in Fourier series takes the next shape:

$$B_g^m(t,\theta) = \sum_{K=-\infty}^{\infty} B_{g_k}^m e^{jpk(\varphi_0 + \omega_m t)} \tag{3-53}$$

Developing (3-53) to get an expression for positive harmonics, we use:

$$B_g^m(t,\theta) = \sum_{k=1}^{\infty} 2B_{g_k}^m \cos\left(pk(\varphi_0 - \theta + \omega_m t)\right) \tag{3-54}$$

The waveform of the field in the air gap rotates at mechanical speed as the magnets are placed in the rotor. Furthermore, from the term $(1 - cos(k\pi))$ of the equation (3-50) it is immediately concluded that the field induced by the magnets in the air gap has only even harmonics, as shown in Figure 3-16-b. This figure shows the spectrum of the field in the air gap

of a machine with eight pole pairs. The span angle of the magnets is 18.75º. Figure 3-16-a shows the waveform of the same field.

3.3.2.2 Armature MMF

The magneto motive force is defined as:

$$MMF(t,\theta) = F(\theta)\Re\{i(t)\} \tag{3-55}$$

where i is the supply current and F is the magneto motive current per current unit. The general expression of this last parameter in Fourier series is:

$$F(\theta) = \sum_{-\infty}^{\infty} \vec{F}_n e^{-jnt_p\theta} \tag{3-56}$$

The vector $\vec{F}_n$ depends on the angle of the winding factor:

$$\vec{F}_n = \sum_{-\infty}^{\infty} F_n e^{j\angle\xi_n} \tag{3-57}$$

The F_n coefficients are calculated with the next expression:

$$F_n = \frac{N_{ph}}{\pi n t_p} \frac{sin\left(nt_p \frac{\beta_c}{2}\right)}{nt_p \frac{\beta_c}{2}} \tag{3-58}$$

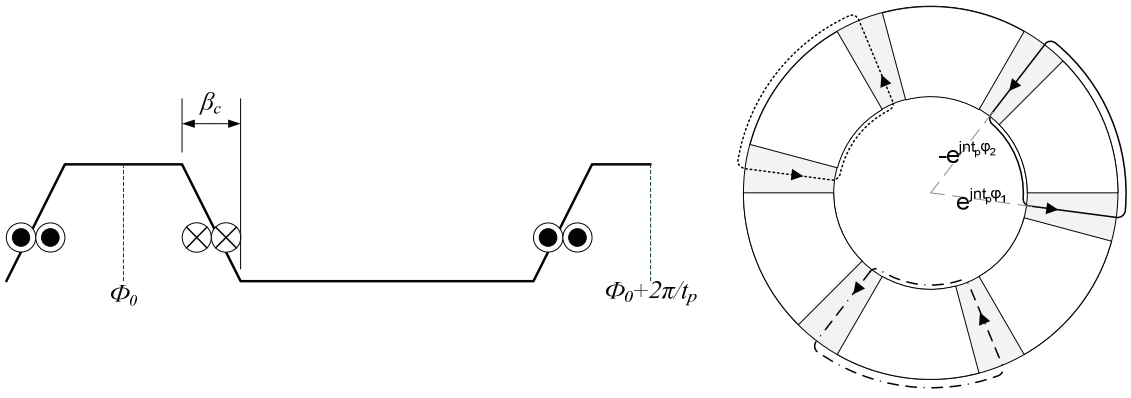

Figure 3-17: a) Magneto motive force per current unit and b) schema to calculate the winding factor

where β_c is the distribution angle of the conductors or the pitch angle (Figure 3-17-a). In the case of a very small distribution angle or a slotted stator, expression (3-58) can be simplified as

$$F_{n_{(a_c=0)}} = \lim_{a_c \to 0} F_n = \frac{N_{ph}}{\pi n t_p} \xi_n \tag{3-59}$$

Although the method described in section 3.2.1 to obtain the winding factor has already been explained, that method does not assume the angle. However, the phase of the winding factor is needed to calculate the magneto motive force that is proposed here. The simplest way to obtain the winding factor with module and phase is from the physical position of the coils in the slots. This is developed from the star of slots theory proposed by *Bianchi et al.* [81].

$$\vec{\xi}_n = \frac{\sum_x \pm e^{jnt_p\varphi_x}}{\left|\sum_x \pm e^{jnt_p\varphi_x}\right|} \tag{3-60}$$

where ξ_n is the winding factor vector for the 'n' order harmonic and φ_x is the position of the 'x' vector. A vector sum is obtained by adding all coils of the same phase in one direction and resting the ones in the other direction. Figure 3-17-b shows a schema of how the sum is obtained. It should be noted that this method to obtain the winding factor refers only to the armature configuration, so the effects of the skew are not contemplated.

Finally, the space distribution of F represented in terms of Fourier series is:

$$F(\theta) = \sum_{-\infty}^{\infty} F_n e^{j(\angle\xi_n - nt_p\theta)} \tag{3-61}$$

Developing this general expression, it is possible to obtain the magneto motive force per current unit in each phase for positive harmonics:

$$F_a(\theta) = \sum_{n=1}^{\infty} 2F_n \sin\left(\angle\xi_n - nt_p\theta\right) \tag{3-62}$$

$$F_b(\theta) = \sum_{n=1}^{\infty} 2F_n \sin\left(\angle\xi_n - nt_p\theta - \frac{2\pi}{3}\right) \tag{3-63}$$

$$F_c(\theta) = \sum_{n=1}^{\infty} 2F_n \sin\left(\angle\xi_n - nt_p\theta + \frac{2\pi}{3}\right) \tag{3-64}$$

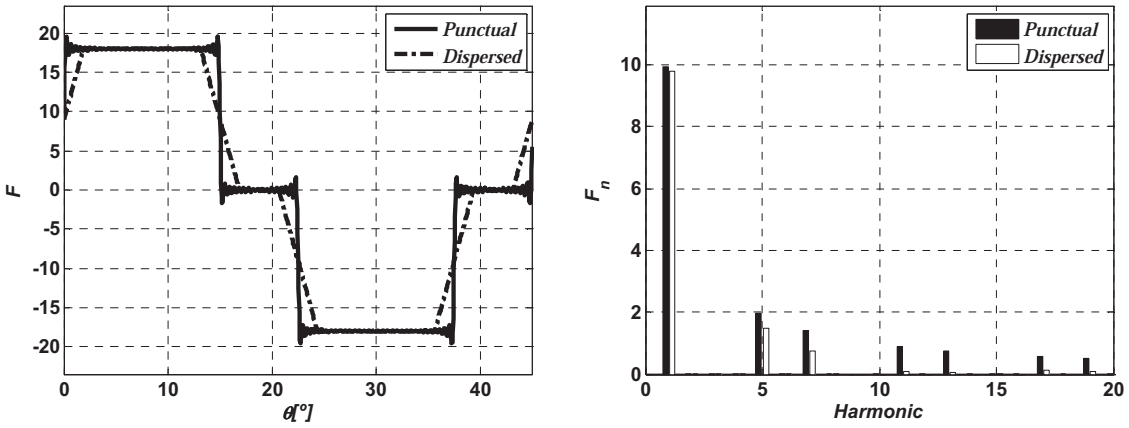

a)0 *b)*

Figure 3-18: F in a phase of the armature: a) spatial waveform and b) spectrum

In Figure 3-18, the F in a phase of the armature is shown. For the sake of comparison, the F assuming punctual conductor or conductor with a dispersion angle is shown. Similarly, the spectrum is shown, where it is very noticeable that the high order harmonics are attenuated with dispersed conductors.

The magneto motive force *MMF* per phase assuming a three-phase machine is calculated by multiplying the F and the current in each phase.

$$MMF_a(t,\theta) = \sum_{n=1}^{\propto} 2i_a(t)F_n \sin\left(\angle\xi_n - nt_p\theta\right) \tag{3-65}$$

$$MMF_b(t,\theta) = \sum_{n=1}^{\propto} 2i_b(t)F_n \sin\left(\angle\xi_n - nt_p\theta - \frac{2\pi}{3}\right) \tag{3-66}$$

$$MMF_c(t,\theta) = \sum_{n=1}^{\propto} 2i_c(t)F_n \sin\left(\angle\xi_n - nt_p\theta + \frac{2\pi}{3}\right) \tag{3-67}$$

In an ideal case, the currents in each phase are sinusoidal with only a real component that can be represented as a vector I rotating at w_e speed.

$$i_a(t) = \Re\left\{Ie^{jw_e t}\right\} \tag{3-68}$$

$$i_b(t) = \Re\left\{Ie^{jw_e t - \frac{2\pi}{3}}\right\} \tag{3-69}$$

$$i_c(t) = \Re\left\{Ie^{jw_e t + \frac{2\pi}{3}}\right\} \tag{3-70}$$

The total *MMF* is the sum of the *MMF* of each phase:

$$MMF(t,\theta) = F_a(\theta)i_a(t) + F_b(\theta)i_b(t) + F_c(\theta)i_c(t) \tag{3-71}$$

Developing the last expression:

$$MMF(t,\theta) = \Re\left\{\sum_{n=-\infty}^{\infty} F_n I e^{jw_e t} e^{-jt_p\theta} e^{j\angle\xi_n}\left(1 + 2\cos\left(\frac{2\pi}{3}(n-1)\right)\right)\right\} \tag{3-72}$$

The term in brackets, named d_n, for the harmonic analysis of the *MMF*:

$$d_n = 1 + 2\cos\left(\frac{2\pi}{3}(n-1)\right) \tag{3-73}$$

The harmonics of the magneto motive force in an equilibrated three-phase system are only those where d_n is not annulated, as shown in Table 3-2.

Figure 3-19-a and Figure 3-19-b show the spatial waveforms of the *MMF*. In Figure 3–18-a, the punctual conductors are assumed, while in Figure 3–18-b, the conductors are placed at a certain distribution angle. It should be noted that over time, the spatial waveform of the *MMF* changes, but the spectrum is always the same because if a harmonic of the *MMF* exists in the positive range, it does not appear in the negative range, as shown in Table 3-2. The positive harmonics rotate in one direction while the negative harmonics rotate in the other direction.

The flux density induced by the armature in the air gap is calculated immediately from the magneto motive force:

$$B_g^a(t,\theta) = \frac{\mu_0}{2g'} MMF(t,\theta) \tag{3-74}$$

n	-9	-8	-7	-6	-5	-4	-3	-2	-1	1	2	3	4	5	6	7	8	9
d_n	0	**3**	0	0	**3**	0	0	**3**	0	**3**	0	0	**3**	0	0	**3**	0	0

Table 3-2: Values of d_n as a function of the "n" harmonic

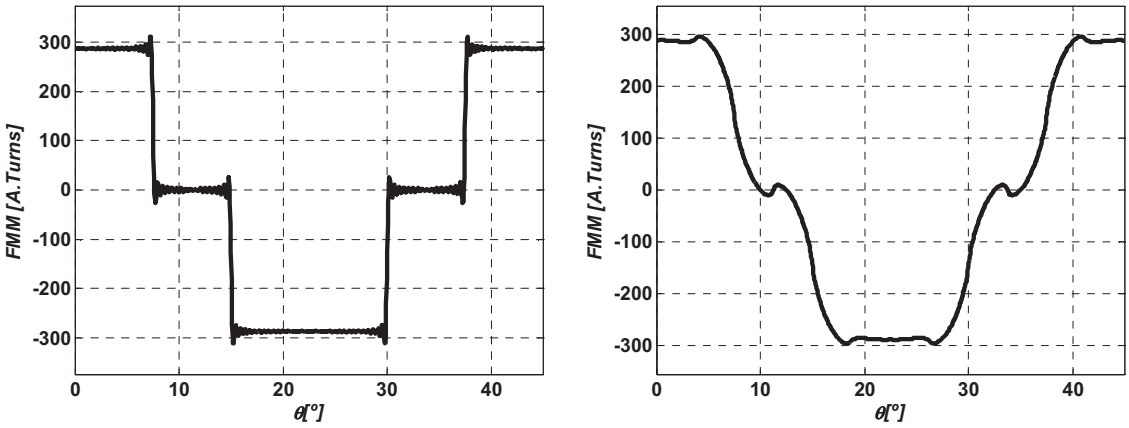

Figure 3-19: MMF. a) Punctual conductors and b) conductors with a dispersion angle

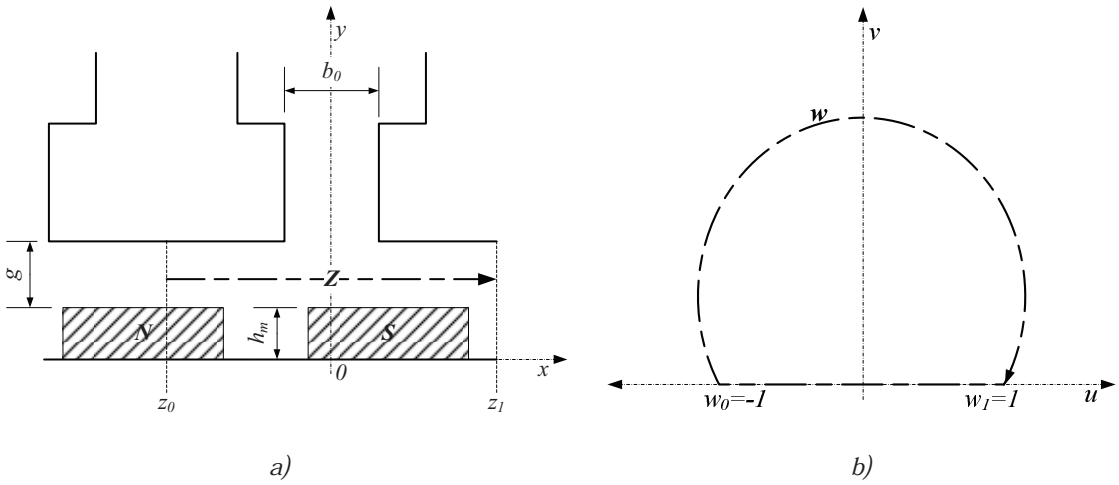

Figure 3-20: Conformal transformation. a) Z plane and b) W plane

3.3.2.3 Slot Effect

The slot effect is commonly represented as a relative permeability function λ. In slotless machines, this permeability is constant but in slotted machines, it is variable along the angle, because the effective air gap length varies. This relative permeability alters the field in the air gap:

$$B_{gs}(\theta) = B_g(\theta)\lambda(\theta) \tag{3-75}$$

This function can be obtained with different mathematical approximations. The simplest approximation assumes a curved flux path on the tooth edge, which does not include the effect of flux concentration on this edge [64] [80] [81]. In order to assume this concentration, some authors used experimental curves to obtain the permeability function [84]. Another option is the use of the scalar magnetic potential equation [83] [84]. In the present study, the conformal transformation is used to obtain the relative permeability function as presented in [62], [87–89].

This method is a complex iterative mathematical process that is easy to implement. The method used is developed for the case of axial flux machines from [62]. Zhu et al. proposed a method to implement the slot effect by the conformal transformation for radial flux machines. This thesis has modified their proposal to use with axial machines. First, the plane on the average radius is created on the Z plane, thereby changing the coordinates from polar to Cartesian (Figure 3-20-a). The z path is then transformed to the w path in the W plane (Figure 3-20-b). When the points in the Z plane are obtained, the relative permeability of one slot is calculated with the next expression:

$$\lambda_{S1}(w) = \frac{1}{\sqrt{1 + \left(\frac{b_0}{2g'}\right)^2 - \left(\frac{b_0}{2g'}w\right)^2}} \tag{3-76}$$

The points in Z and W plane are linked by the next expression:

$$z(w) = \frac{b_0}{\pi}\left\{\arcsin\left(\frac{w}{za}\right) + \frac{g'}{b_0} ln\left[\frac{\sqrt{za^2 - w^2} + \frac{2g'}{b_0}w}{\sqrt{za^2 - w^2} - \frac{2g'}{b_0}w}\right]\right\} \tag{3-77}$$

where za is:

$$za = \sqrt{1 + \left(\frac{2g'}{b_0}\right)^2} \tag{3-78}$$

The effect of the slots makes the relative permeability function a periodic function that is repeated as many times as the number of slots (Figure 3-21). Thus, by using the superposition principle, the relative permeability function can be easily obtained:

$$\lambda_{S1} = \sum_{x=1}^{Q} \lambda_{S1} e^{j\frac{2\pi}{Q}x} \tag{3-79}$$

Figure 3-22 shows how the relative permeability affects the flux density in the air gap.

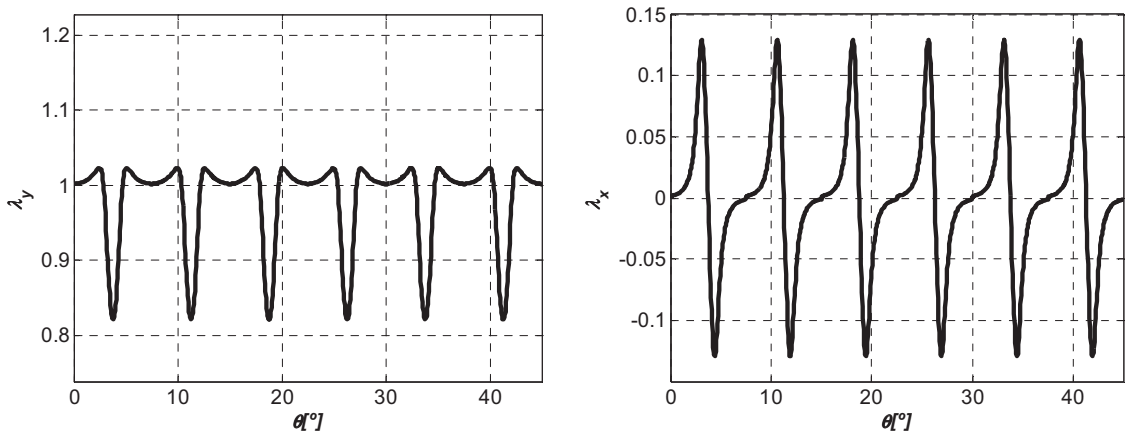

a) *b)*

Figure 3-21: Relative permeability of a 48 slot machine. a) axial direction and b) tangential direction

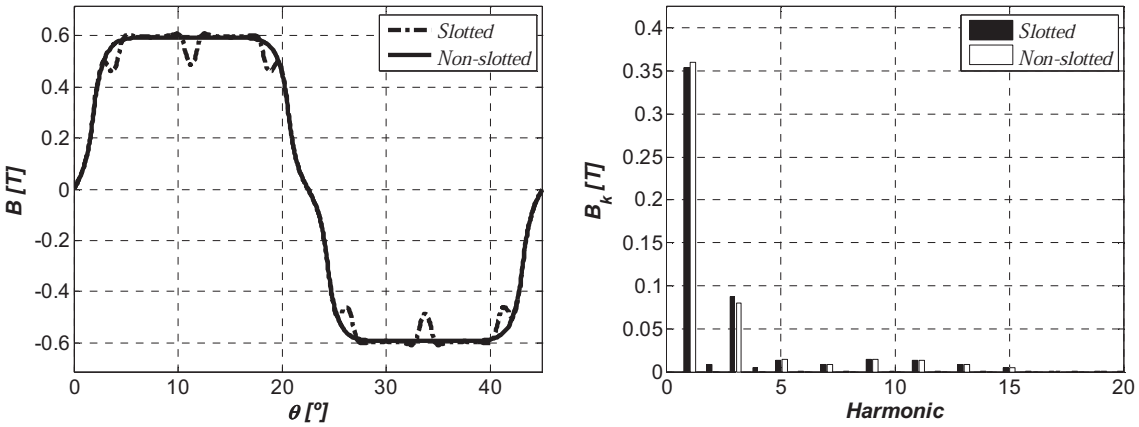

a) *b)*

Figure 3-22: Air-gap fields in a slotted and a slotless machine: a) Spatial waveform and b) the spectrum

3.3.2.4 Flux Linkage and Electro Motive Force in Open Circuit

The general expression of the magnet flux linkage can be expressed as:

$$\psi(t) = \int_A B_g^m(t,\theta)F(t,\theta)dA \tag{3-80}$$

In the case of axial machines, the integral of the area A corresponds with the double integral along the radius and the angle:

$$\psi(t) = t_p \int_0^{\frac{2\pi}{t_p}} \int_{R_i}^{R_o} rB_g^m(t,\theta)F(t,\theta)drd\theta \tag{3-81}$$

If expression (3-81) is developed in terms of Fourier series, the flux linkage in each phase is:

$$\psi_a(t) = t_p \int_0^{\frac{2\pi}{t_p}} \int_{R_i}^{R_o} r\left[\sum_{k=-\infty}^{\infty} 2B_{g_k}^m F_k \sin\left(pk(\varphi_0 + \Omega_m t) + \angle\xi_k\right)\right] drd\theta \tag{3-82}$$

$$\psi_b(t) = t_p \int_0^{\frac{2\pi}{t_p}} \int_{R_i}^{R_o} r\left[\sum_{k=1}^{\infty} 2B_{g_k}^m F_k \sin\left(pk(\varphi_0 + \Omega_m t) + \angle\xi_k - \frac{2\pi}{3}\right)\right] drd\theta \tag{3-83}$$

$$\psi_c(t) = t_p \int_0^{\frac{2\pi}{t_p}} \int_{R_i}^{R_o} r\left[\sum_{k=1}^{\infty} 2B_{g_k}^m F_k \sin\left(pk(\varphi_0 + \Omega_m t) + \angle\xi_k + \frac{2\pi}{3}\right)\right] drd\theta \tag{3-84}$$

From these expressions, it can be demonstrated that the flux linkage is zero unless the following condition is fulfilled:

$$n = -\frac{pk}{t_p} \tag{3-85}$$

Developing the integral of expressions (3-82), (3-83) and (3-84), the next ones are obtained for each phase of the machine:

$$\psi_a(t) = 2\pi\frac{(R_o^2 - R_i^2)}{2}\sum_{k=1}^{\infty} 2B_{g_k}^m F_k \sin\left(pk(\varphi_0 + \Omega_m t) + \angle\xi_k\right) \quad (3\text{-}86)$$

$$\psi_b(t) = 2\pi\frac{(R_o^2 - R_i^2)}{2}\sum_{k=1}^{\infty} 2B_{g_k}^m F_k \sin\left(pk(\varphi_0 + \Omega_m t) + \angle\xi_k - \frac{2\pi}{3}\right) \quad (3\text{-}87)$$

$$\psi_b(t) = 2\pi\frac{(R_o^2 - R_i^2)}{2}\sum_{k=1}^{\infty} 2B_{g_k}^m F_k \sin\left(pk(\varphi_0 + \Omega_m t) + \angle\xi_k + \frac{2\pi}{3}\right) \quad (3\text{-}88)$$

Figure 3-23 shows the temporal waveform of the flux linkage and its spectrum.

Once the flux linkage is obtained, the electro motive force *EMF* or the induced voltage is immediately obtained. According to Faraday`s Law, the induced voltage in a coil is equal to the time variation of the flux linkage in that coil. Thus, the induced voltage in each phase is:

$$EMF_a(t) = \frac{d\psi_a}{dt} = -2\pi\frac{(R_o^2 - R_i^2)}{2}\Omega_m\sum_{k=1}^{\infty} 2B_{g_k}^m F_k cos\left(pk(\varphi_0 + \Omega_m t) + \angle\xi_k\right) \quad (3\text{-}89)$$

$$EMF_b(t) = \frac{d\psi_b}{dt} = -2\pi\frac{(R_o^2 - R_i^2)}{2}\Omega_m\sum_{k=1}^{\infty} 2B_{g_k}^m F_k cos\left(pk(\varphi_0 + \Omega_m t) + \angle\xi_k - \frac{2\pi}{3}\right) \quad (3\text{-}90)$$

$$EMF_c(t) = \frac{d\psi_c}{dt} = -2\pi\frac{(R_o^2 - R_i^2)}{2}\Omega_m\sum_{k=1}^{\infty} 2B_{g_k}^m F_k cos\left(pk(\varphi_0 + \Omega_m t) + \angle\xi_k + \frac{2\pi}{3}\right) \quad (3\text{-}91)$$

Figure 3-24 shows the temporal waveform of the induced voltage and its spectrum.

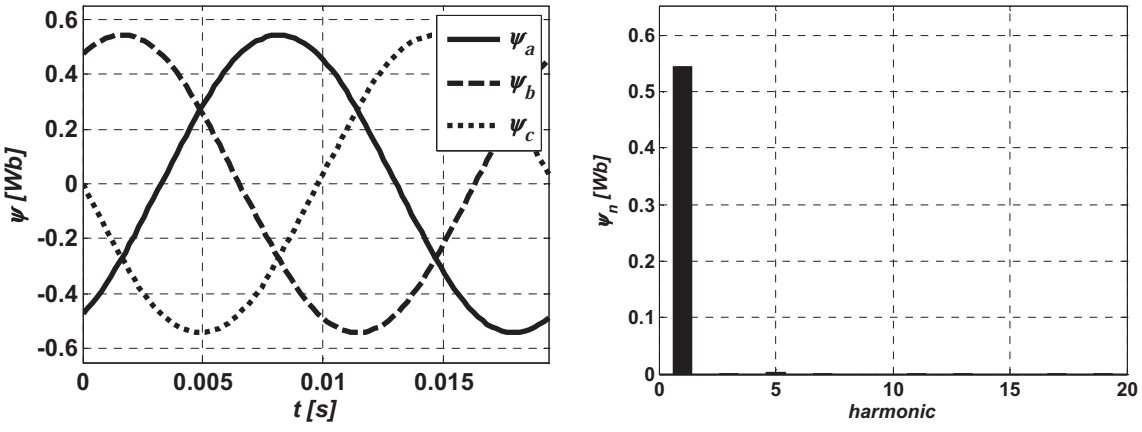

a) b)

Figure 3-23: a) Temporal waveform of the flux linkage in the three phases of the armature and b) the spectrum of the flux linkage

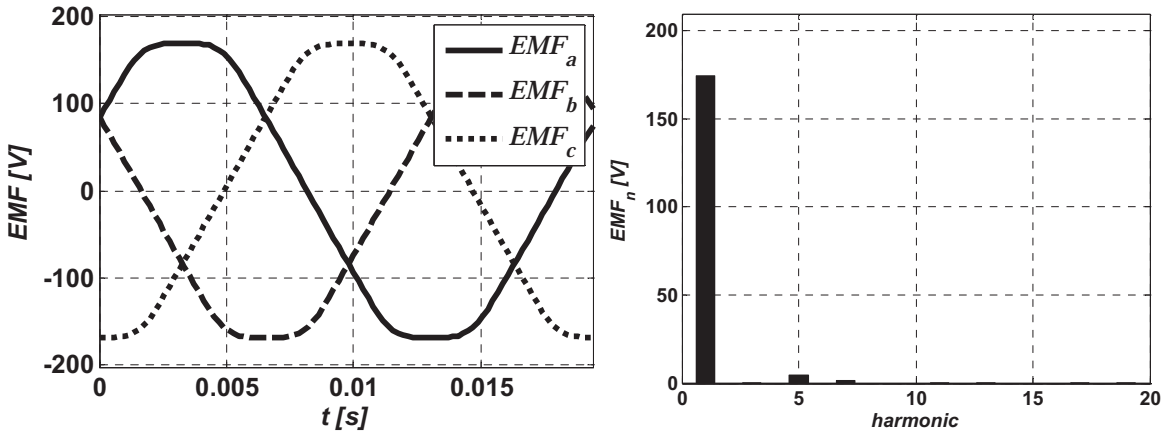

a) *b)*

Figure 3-24: a) Temporal waveform of the induced voltage in the three phases of the armature and b) the spectrum of the induced voltage

3.3.2.5 Electromagnetic Torque

Once the *EMF* and current waveforms of each phase are obtained, the electromagnetic torque is immediately obtained. The easiest way is to multiply point-to-point the *EMF* and current in each phase and then sum the torque in all phases to obtain the total value of the torque:

$$T_{em}(t) = \frac{EMF_a(t)i_a(t) + EMF_b(t)i_b(t) + EMF_c(t)i_c(t)}{\Omega_{\mathrm{m}}} \tag{3-92}$$

The expression of the torque is developed from the expressions of the *EMF* and current to obtain the Fourier series form:

$$T_{em}(t) = \Re\left\{2\pi\frac{(R_o^2 - R_i^2)}{2}\sum_{k=-\infty}^{\infty}\vec{B}_{g_k}^{m}\vec{F}_k I e^{j(k-1)w_e t}e^{-jnp(\theta+\varphi_0)}e^{j\angle\xi_k}\left(1 + 2cos\left(\frac{2\pi}{3}(k-1)\right)\right)\right\} \tag{3-93}$$

This expression is very useful for observing how the harmonics of the *EMF* affect the harmonic content of the torque. The components of the *EMF* spectrum are null, so they do not generate torque. Moreover, components of the *EMF* spectrum that are multiples of three do not generate torque. This is because in a symmetrical three-phase machine, multiples of three of the current spectrum are null. The average torque of the torque is generated by the fundamental

component of the *EMF*. High-order components of the torque are in multiples of six: the components -5 and 7 of the *EMF* generate the sixth component of the torque, -11 and 13 generate the 12th, and so on.

By knowing the magnetic field and *MMF* spectrums, it is possible to identify the components that cause the torque ripple. Hence, it would be interesting to design the machine such that those components are eliminated or at least attenuated. Thus, the torque ripple could be decreased.

3.3.2.6 Cogging Torque

The cogging torque is an effect caused by the tendency of the magnets to alienate the teeth in the stator. This occurs because the flux tries to flow along the easiest path, which happens because the reluctance is the minimum when the magnets and teeth are alienated. Depending on the number of slots, and rotor poles this cogging torque may be quite problematic. Hence usually this cogging torque is attenuated by using skew techniques [83], [90], [91].

The most frequently used methods for the calculation of cogging torque are the virtual work method [83], [90] and the Maxwell´s tensor method [91], [92]. In the latter method, the tangential force tensor over a ferromagnetic body is integrated along a circular contour inside the air gap:

$$dF = \frac{1}{2\mu_0} B^2 dA \tag{3-94}$$

The cogging torque is computed by considering the tangential component of the magnetic force over the stator. This tangential force depends on the flux penetrating through the side faces of the slots. In each slot, two opposing tangential forces appear, as shown in Figure 3-25 (*F1 and F2*). A superposition is then done to compute the total cogging torque by adding the cogging due to each slot:

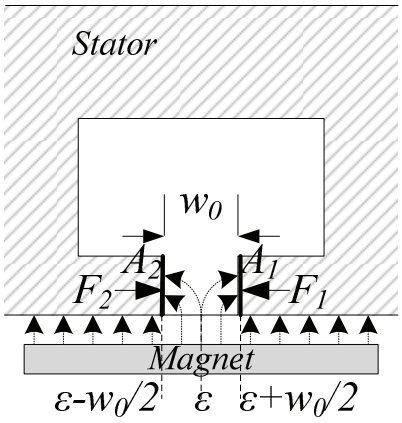

Figure 3-25: Maxwell's tensor in a slot

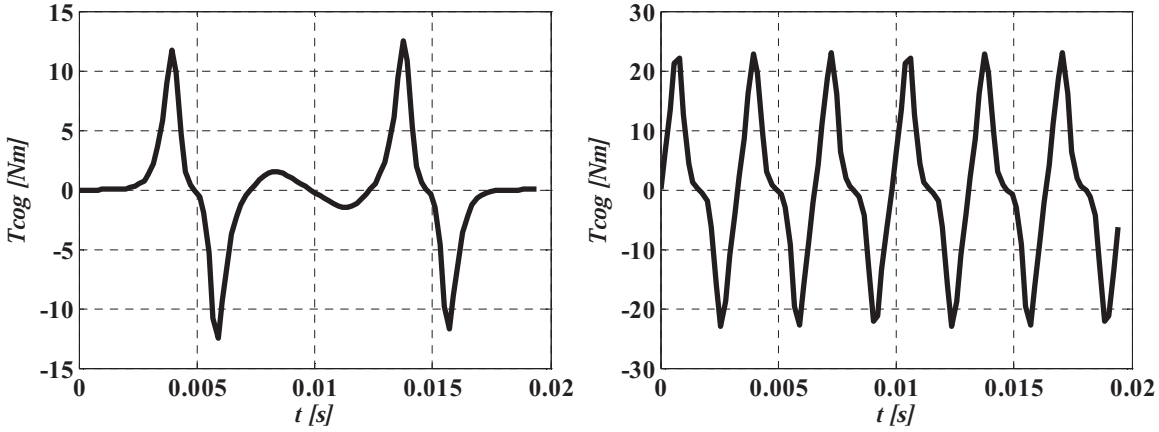

a) *b)*

Figure 3-26: Cogging torque: a) in a slot and b) superposition of all slots

$$T_c(t) = R_{av} \sum_{x=1}^{Q} \frac{1}{2\mu_0} \frac{R_o^2 - R_i^2}{2} \left[\int_{x\left(\epsilon - \frac{w_0}{2}\right)}^{x\epsilon} B_{gs}^2(t,\theta) d\theta - \int_{x\epsilon}^{x\left(\epsilon + \frac{w_0}{2}\right)} B_{gs}^2(t,\theta) d\theta \right] \quad (3\text{-}95)$$

This method is quite accurate, although it must be mentioned that due to phenomena, such as the saturations in the ferromagnetic cores, the method could lose accuracy. Furthermore, the Maxwell's tensor method gives a wide vision of the effect of the number of poles, as well as the number and dimensions of the slots

Figure 3-26-a shows the cogging torque caused by a slot. Figure 3-26-b shows the total cogging torque after the superposition of all the slots.

3.3.2.7 Synchronous Inductance

The armature flux linkage, in this case phase *A,* can be calculated as:

$$\psi_A^a(t) = \int_S B_g^a(t,\theta)\, F_a(\theta) dA \tag{3-96}$$

Developing expression (3-96) with (3-74) and knowing that the inductance is the division of the flux linkage in a phase and the current in the same phase, the components of self and mutual inductances can be obtained:

$$L_{AA} = \pi \frac{(R_o^2 - R_i^2)}{2} \frac{\mu_0}{g'} \sum_{n=-\infty}^{\infty} F_n^2 \tag{3-97}$$

$$L_{AB} = \pi \frac{(R_o^2 - R_i^2)}{2} \frac{\mu_0}{g'} \sum_{n=-\infty}^{\infty} F_n^2 cos\left(\frac{2\pi}{3}(n-1)\right) \tag{3-98}$$

$$L_{AC} = \pi \frac{(R_o^2 - R_i^2)}{2} \frac{\mu_0}{g'} \sum_{n=-\infty}^{\infty} F_n^2 cos\left(-\frac{2\pi}{3}(n-1)\right) \tag{3-99}$$

The total synchronous inductance is the sum of all the components:

$$L_A = L_{AA} + L_{AB} + L_{AC} \tag{3-100}$$

As described in section *3.2.3*, the synchronous inductance is composed by the main inductance because of the fundamental harmonic and the leakage inductance caused by the harmonic content.

3.3.3 Validation of the Model

In this section, a validation of the proposed model is performed. To this end, a machine of 48 slots and 8 pole pairs has been modeled. The validation was done comparing the results obtained from the analytical model with those obtained from finite element method. The results in Figure 3-27 show the validity of the proposed method. The analysis performed here is not very deep because a more exhaustive validation is performed in the paper entitled "*Analytical Model of Axial Flux Permanent Magnet Machines Considering Spatial Harmonics*" which is included in the Appendix.

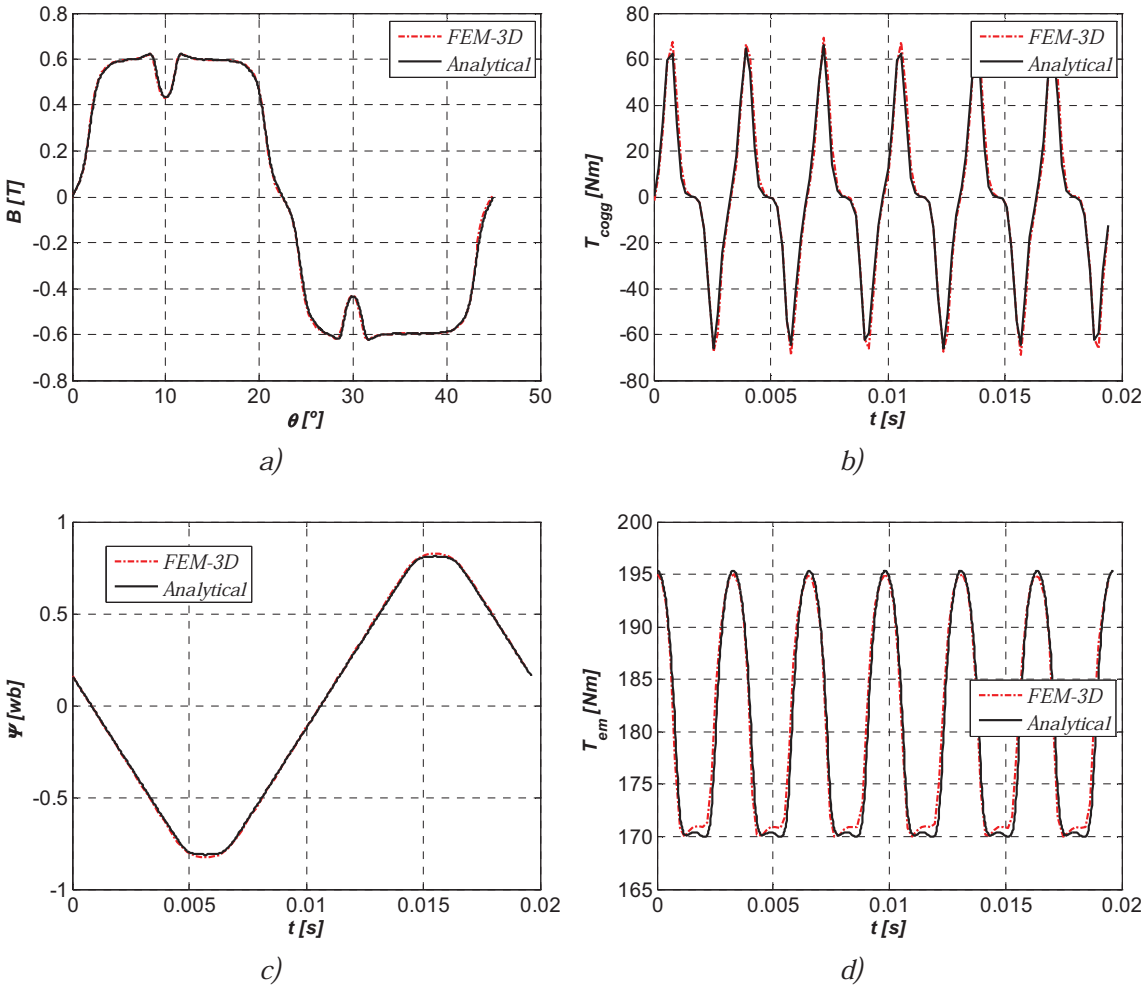

Figure 3-27: Analytical model vs. FEM: a) flux density in the air gap b) cogging torque c) flux linkage and d) electromagnetic torque

3.4 Conclusions

This chapter presented the analytical tools developed for the design of permanent magnet axial flux machines. These tools are very helpful for the design of the machines. The pre-design allowed a first sizing of the machine, while the Fourier series gave information about the machine that was more specific.

The main conclusions of this chapter are as follows:

- The accuracy of the tools is good compared with the finite element simulations. These simulations were launched assuming linear materials. It is quite complicated to define the accuracy, but in the validation carried out, an accuracy of 95% was reached.

- It has to be stated that modeling the slot effect with the conformal transformation, obtained almost the same results as the ones obtained with the finite element method, neglecting the non-linearity of the materials.

- The good results obtained show that the analytical tools are a good option for the design or analysis of a machine.

- The main limitation of these analytical tools is the impossibility of assuming the non-linearity of the materials.

Chapter 4.

NUMERICAL TOOLS FOR THE DESIGN OF AXIAL FLUX MACHINES

One of the most frequently used numerical tools in all kind of engineering problems is the finite element method (FEM). The design of electrical machines is not an exception as this method is appropriate to solve electromagnetic problems.

The present-day computing resources used with finite element method applications enable precise electrical machine designs. The use of only numerical tools could cause a great amount of computational work leading to a large consumption of time. Hence, using these tools with the analytical tools presented in the previous chapter emerges as the right option.

This chapter describes the numerical tools used for the design of axial flux machines. Furthermore, a new method, in which FEM-2D and analytical tools are combined to model axial flux machines, is presented.

4.1 Introduction to the Finite Element Method

The finite element method (*FEM*) is a general numerical method that approximates a continuous physical system by using differential equations. The finite element process is based on dividing the continuous system into triangular (Figure 4-2-a) or rectangular (Figure 4-2-b) elements, depending on the mesh. The behavior of each system depends on its physical variables. When solving a problem, the values of these variables are calculated by differential equations in all linking points between the aforementioned elements. These linking points are commonly known as nodes. It is possible to create additional nodes in the medium points of the edges by a second order mesh. The values of the variables in the nodes define the physical behavior of the finite elements by interpolation functions.

The quality and accuracy of the results are strongly linked to the quality of the mesh. Increasing the number of nodes, especially in regions with a complex geometry, the accuracy will be improved. However, the number of elements also directly affects the computation time. Hence, it is essential to find an agreement between accuracy and computation time when using *FEM* tools.

Nowadays a great deal of *FEM* software is available on the market. It focuses on different topics, such as mechanical or electrical engineering. The software *FLUX* by *CEDRAT®* was used in this thesis because it fulfilled the requirements.

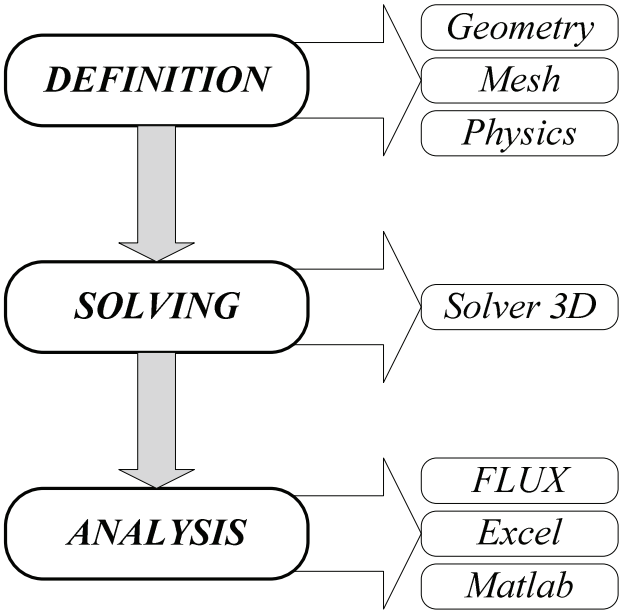

Figure 4-1: Flow chart of the finite element method

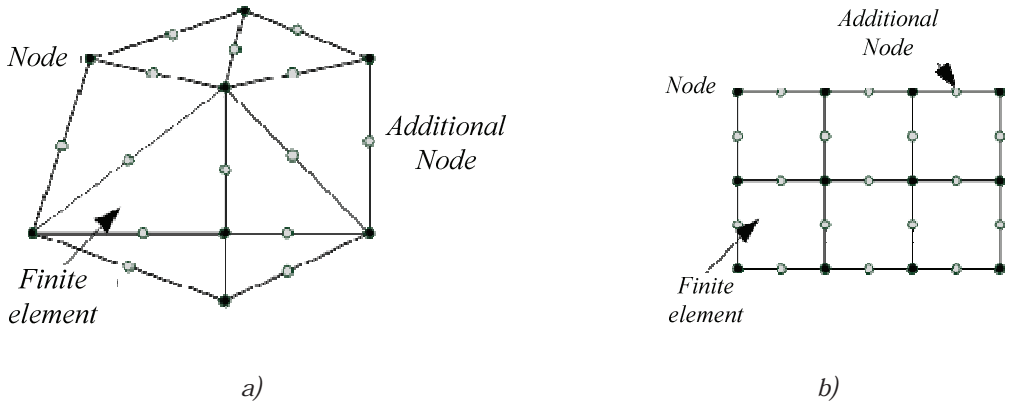

Figure 4-2: Finite elements a) triangular and b) rectangular

4.2 Finite Element Method for Axial Flux Machines

The process may be quite similar in all *FEM* software; however, this section focuses on *FLUX*. Figure 4-1 shows the steps in the process. These steps are almost the same for both 2D and 3D problems. The problem is first defined and then the solution can be executed to complete the analysis of the results.

4.2.1 Problem Definition

The first stage, which is the definition of the problem, consists of three steps. First, the geometry of the machine is defined or drawn. The mesh is then established to reach a good compromise between accuracy and computation time. Finally, the physical parameters of the system are defined. These parameters embrace the properties of the materials, the electrical coupling, and the movement. The following section explains these steps.

4.2.1.1 Definition of the Geometry

Defining the geometry is an important step. The drawing is done using points, lines, and arcs. In the case of *FEM-2D*, the faces of the regions are defined, while in *FEM-3D* the volume regions are defined. If possible, the properties of symmetries and periodicities of the machine should be used in order to make the problem computationally lighter. Because of periodicity, a t_p-th part of the machine can be drawn. Furthermore, in the case of double side axial machines, the symmetry properties can be used.

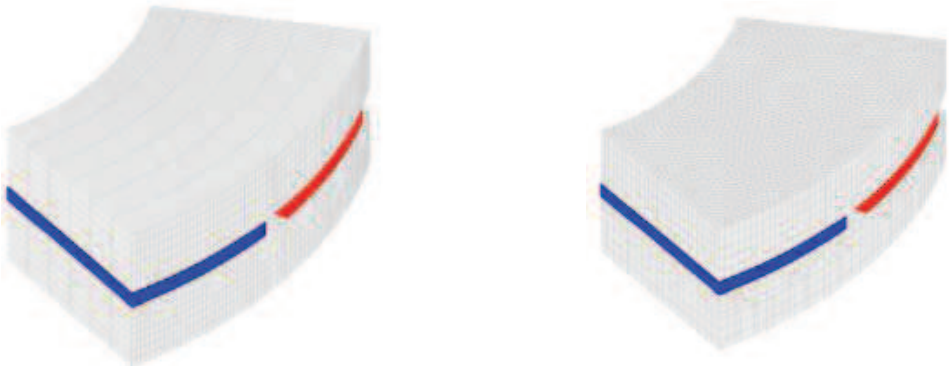

a) *b)*

Figure 4-3: Mesh in a Q48p8 machine:, a) rectangular mesh and b) triangular mesh

4.2.1.2 Definition of the Mesh

The definition of the mesh is one of the most important steps, as the mesh directly affects the results.

The finite elements defined by the mesh may be triangular or rectangular (Figure 4-3). In general, it can be stated that that a rectangular mesh is recommended in problems where the state variables follow a transversal or straight-line direction, as occurs in linear machines. Hence, triangular elements are the most commonly used in rotating electrical machines.

The mesh density directly affects the accuracy of the results as well as the computation time. A correct mesh is necessary, especially in complex geometrical shapes and regions where the state variables may suffer great variations. However, it is recommended to ease the density of the mesh in less critical regions in order to decrease the computation time (Figure 4-4).

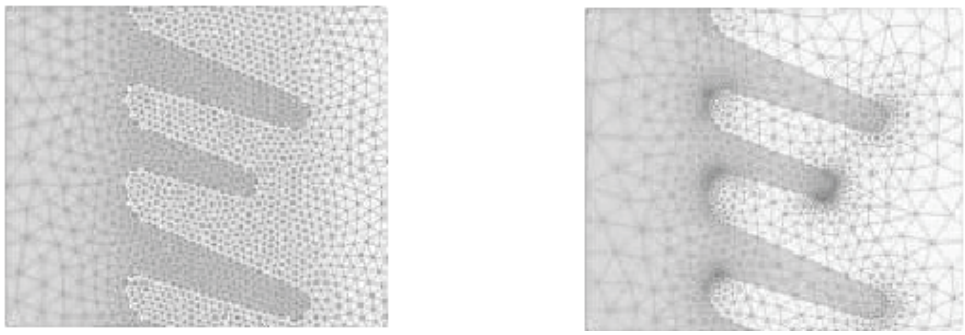

a) *b)*

Figure 4-4: Mesh example [93]*: a) Very dense mesh with 62000 nodes and b) optimized mesh with 34000 nodes*

4.2.1.3 Definition of the Physics

The definition of the physics is divided into three sections.

First, the physical properties of the different regions are defined. In an electrical machine four kinds of regions usually appear: magnetic cores, magnets, coils, and air. The magnetic cores are usually defined as non-conducting magnetic regions with a ferromagnetic material. The magnets have to be set as a magnetic region with a magnetization direction. The coils can be defined in two ways, in a 3D environment, this is done with non-meshed coils (Figure 4-5-b), while in a 2D environment, the coils are defined as a conducting region (Figure 4-5-a). Finally, the air is defined simply as air.

Second, the mechanical properties of the system have to be set. In a transient analysis, the rotor is defined as a region with a certain rotation speed while the stator is defined as static. Logically, in a magneto-static computation all regions are set as static.

Third, the electrical coupling is done. Once the electrical circuit has been defined, it is connected to the problem. Depending on the analysis to be carried out, the circuit may vary. Usually two analyses are performed: open circuit analysis and load analysis. In the first analysis, the circuit is completed with resistances of high values in series with the coils (Figure 4-6-a). In the second analysis, the easiest way is to set the current sources in series with the coils (Figure 4-6-b).

a) *b)*

Figure 4-5: Q6p2 one layer axial machine: a) 2D and 3D with non-meshed coils

a) *b)*

Figure 4-6: Coupled electrical circuits. a) open circuit and b) load circuit

4.2.2 Solving the Problem

While solving the problem, the processor computes the values of the state variables in all the nodes of the mesh. This process is carried out in three steps: First, the equations are integrated and assembled; second, the linear equations are solved; finally, in cases where the equations are not linear, these are solved with an iterative method. For example, in electromagnetic problems, the permeability of the ferromagnetic material depends on the magnetic field, so the equation is not linear.

The transient state magnetic models are governed by Maxwell´s formulas in quasi-static form where the displacement currents are not considered:

$$\begin{aligned} \vec{\nabla}\vec{B} &= 0 \\ \vec{\nabla} \times \vec{H} &= \vec{J} \\ \vec{\nabla} \times \vec{E} &= -\frac{\partial \vec{B}}{\partial t} \end{aligned} \tag{4-1}$$

where $\forall$ is the divergent operator, $\forall x$ is the rotational operator, B is the flux density, H is the intensity of the magnetic field, J is the current density, and E is the electrical field. In addition to these equations, the electromagnetic problem next considers constitutive laws:

$$\begin{aligned} \vec{B} &= [\mu]\vec{H} \\ \vec{J} &= [\sigma]\vec{E} \end{aligned} \tag{4-2}$$

where μ and σ are the permeability and the resistivity of the system, respectively.

The solving of a problem in finite elements consists in minimizing the residual value of a target function. As a result of this solution, a state variable is then obtained. In *FLUX* using the 3D solver in both 2D and 3D environments, the state variable is the scalar magnetic potential (ϕ). The target function is not unique, but it changes from one region to another. However, a general notation that can be used in any kind of region exists:

$$\nabla\left([\mu_r]\mu_0\left(-\mathrm{grad}(\phi) + \vec{T}\right) + \vec{B}_r\right) = 0 \tag{4-3}$$

where T depends on the current sources of the region. This general notation varies depending on whether there are current sources in the region, and whether these are in the meshed region. In each case, the term T and the scalar magnetic potential ϕ change [94].

4.2.3 Analysis of the Results

Once the problem is solved, the output is a state variable. In this case, it is the characteristic scalar magnetic potential of each region. The local and global results are then derived from this variable. The local results are calculated in each node of the mesh—the magnetic field, for example. However, the global results are obtained by integrating the local variables along a region.

The first local variable derived from the scalar magnetic potential is the intensity of the magnetic field *H*. There are three options for calculating this variable, depending on the characteristics of the region as previously mentioned.

The first case is when the region does not have current sources so *J* is null. Here $T = 0$, ϕ_t is total, and *H* is defined as:

$$\vec{H} = -\text{grad}(\phi) \tag{4-4}$$

When the regions are non-meshed coils, the scalar magnetic potential ϕ_{rHj} is a function of H_j, and $T = H_j$, H_j being the intensity of the field created by the non-meshed coils. In these regions, the total *H* is defined as:

$$\vec{H} = -\text{grad}(\phi) + \vec{H}_j \tag{4-5}$$

Finally, in a meshed and conducting region, the scalar magnetic potential ϕ_{rTo} is a function of T_o. *H* is defined as:

$$\vec{H} = -\text{grad}(\phi) + \vec{T}_0 \tag{4-6}$$

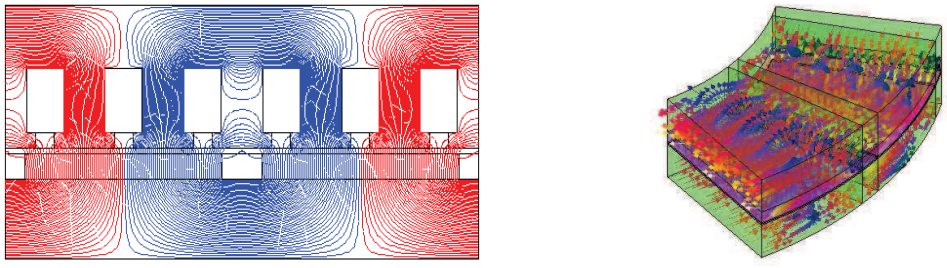

a) *b)*

Figure 4-7: Flux lines: a) 2D problem and b) 3D problem

Another important local variable is the magnetic field that can be obtained from H using the constitutive law defined in (4-2). Once B and H are obtained, global variables, such as magnetic energy, torque, or flux linkage can be obtained.

FLUX allows analysis of the results in the simulation environment, but as the manipulation of the information there is not that comfortable, it also provides the possibility to export data—to *Excel,* for example. These data can then be processed in mathematical software, such as *Matlab*.

Furthermore, it is possible to analyze the results graphically. For example, Figure 4-7 shows the flux lines in a 2D and 3D problem.

4.3 Combination of FEM-2D with analytical tools

As it previously mentioned, the study of axial flux machines involves a tri-dimensional electromagnetic problem, so using two dimensional finite element methods may not be possible. However, this might not be completely the case because by assuming certain conditions, this type of analysis may be useful. It is possible to find several proposals in which *FEM-2D* analysis is used.

One of these methods consists of carrying out simulations using *FEM-2D*. The *FEM-2D* approximation consists of taking a 2D plane of the geometry in a certain radius value, usually in the average radius [95]. This 2D plane is then treated similarly to a linear machine, with the exception that a cyclic boundary condition must be forced at the ends of the primary and secondary cores. This process is described in Figure 4-8. It is widely known that performing simulations in *FEM-2D* is much easier and faster than in the *FEM-3D* environment. Even the definition of the problem (geometry, mesh, and physical properties) is also easier and faster in *FEM-2D*. However, this solution may not be valid for two main reasons: the non-linearity of magnetic materials [96] and the geometrical shape of the magnetic cores [97].

Another possible solution that was reported in the literature, the quasi-*FEM-3D* method, consists of carrying out *FEM-2D* simulations in different planes of the machine. The accuracy of this method depends on the number of evaluated planes [98]. Thus, the more planes used, the more accurate the results are. Nevertheless, it must be considered that the time consumption of these simulations is directly proportional to the number of planes chosen.

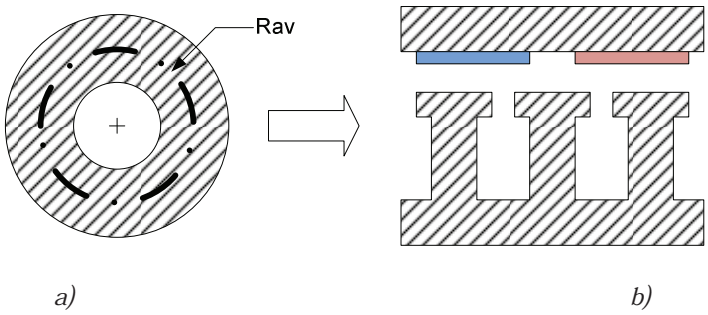

Figure 4-8: Process of picking a plane for the 2D approximation: a) Front view of axial machine and b) 2D plane of axial machine at average radius

In this work, a novel method for axial flux machine analysis is presented. This method consists of the combination of analytical tools with *FEM-2D* simulations. The main advantage of the proposed method is the saving of time compared with the *FEM-3D* method. Both computational time and problem definition time are shorter.

4.3.1 Geometrical Constraints in *FEM-2D* Simulations

One critical aspect related to the accuracy of *FEM-2D* results is the aforementioned geometrical shape of cores. This work focuses on this particular problem. In *FEM-2D* approximations, the geometry is supposed to be radially proportional as shown in Figure 4-9-a, Figure 4-10-a, and Figure 4-11-a, which means that the dimensions of any 2D plane obtained for a specific radius value are proportional to this radius value. In other words, the span angle of the magnets β_m, the pitch angle of the coils β_w, and the distribution angle of the conductors in a coil side β_c are constant for the entire machine.

The distribution angle of the conductors refers to the angle needed by the conductor in one side of the coil to be placed in a slotless stator (Figure 4-9). The pitch angle of the coils is the angle between both sides of a coil (Figure 4-10). The span angle of the magnets is the angle of the arc of the magnets (Figure 4-11).

In many cases, due to manufacturing requirements, the radially proportional structure may not be available. In other cases, a specific shape is chosen in order to reduce the torque ripple. The shape of the magnets or the way the coils are placed could cause a skew effect [99], [100]. Figure 4-10-b shows how the coils make a skew angle with respect to the pole pitch β_p. Figure 4-11-b shows how the magnets are skewed with respect to the pole pitch.

For example, this proportionality is not fulfilled when the shape of the distribution of the conductors in one side of the coil is rectangular instead of trapezoidal (see Figure 4-10-a and Figure 4-10-b). A constant distribution angle, β_c, is only possible with trapezoidal shape distribution as shown in Figure 4-9-a. However, this is quite difficult to accomplish and usually the conductors are placed in a rectangular shape with a constant width w_c, as shown in Figure 4-9-b. The effect caused by this disproportionality is noticeable only when the width w_c is relatively wide; otherwise, it could be neglected.

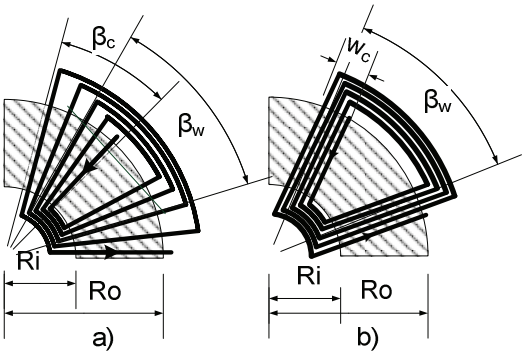

Figure 4-9: Placement of the conductors in a slotless stator a) trapezoidal shape (constant distribution angle) and b) rectangular shape (variable distribution angle)

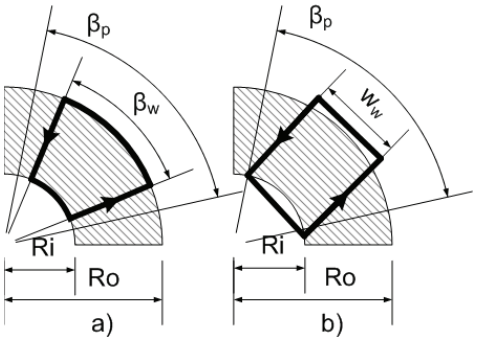

Figure 4-10: Placement of the coils a) radial (constant pitch angle) and b) parallel (variable pitch angle) (in both cases $\beta_c \rightarrow 0º$)

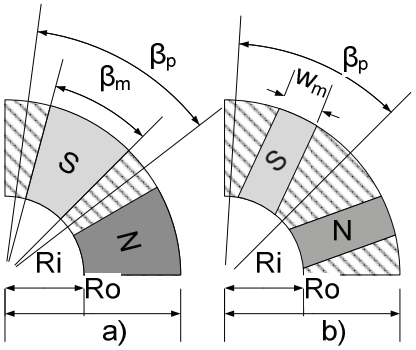

Figure 4-11: Shape of the magnets a) trapezoidal and b) rectangular

Another aspect to consider is the pitch angle β_w of the coils. This angle between both sides of a coil can be constant along the radius, as shown in Figure 4-10-a, or variable depending on the radius, as shown in Figure 4-10-b.

The third and last variable considered is the shape of the magnets. The magnets could be trapezoidal, as in Figure 4-11-a, which leads to a constant span angle along the radius, β_m. However, for manufacturing, performance, or price reasons, the shape of these magnets is not necessarily trapezoidal. For example, they could be rectangular with a constant width w_m, as shown in Figure 4-11-b.

When an axial flux machine is not radially proportional, the aforementioned angles vary along the radius, and consequently *FEM-2D* simulations on the average radius plane may not be as accurate as required. The shape of the time evolution curves of the electromagnetic variables, such as the flux linkage, would be wrong. A possible solution would be to launch *FEM-3D* simulations. These analyses could be quite laborious, so this paper proposes an alternative solution. The idea is to process the results obtained from the *FEM-2D* approximation with additional analytical tools. The details of the proposed method are given in the next section.

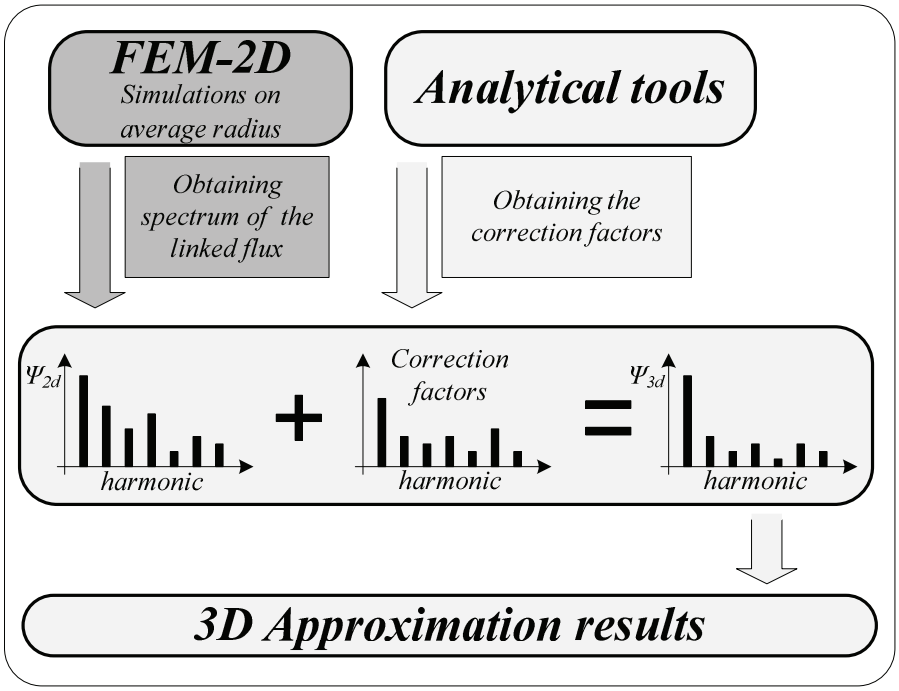

Figure 4-12: Block diagram of the proposed methodology for axial flux machine analysis

4.3.2 Proposed Method for the Analysis of Axial Flux Machines

The proposed method consists in the combination of *FEM-2D* simulations with analytical models based on the theory of Fourier series. The proposed methodology is described in Figure 4-12.

In the first stage, the machine is simulated in *FEM-2D* by considering the average radius plane. The harmonic content of the flux linkage is obtained from this simulation by a discrete *FFT*. The time step must be set according to the required number of harmonics. The correction factors that link the *FEM-2D* with the *FEM-3D* spectrum of the flux linkage are then obtained analytically. Hence, the harmonic content of the flux linkage obtained in *FEM-2D* is post-processed by the correction factors. The new harmonic content obtained in the post-process is an approximation of the one that would be obtained in *FEM-3D*.

- **Main electromagnetic equation, the flux linkage**

The most relevant performance results of the machine, such as the back electromotive force *EMF* or the electromagnetic torque T_{em}, can be calculated from the flux linkage in the armature windings Ψ. Although the expression of the flux linkage was presented in chapter 3, in that case a radially proportional machine was considered. However, for any type of machine the general expression of the flux linkage as a function of the time, angle, and radius is:

$$\Psi(t) = \int_S B_g^m(t,\theta,r)F(t,\theta,r)ds \tag{4-7}$$

In the case of radial machines, the radius is constant so that the resolution of (4-7) is much easier than in the case of axial flux machines where the radius is variable. Solving (4-7) for axial flux machines, the following expression can be obtained:

$$\Psi(t) = t_p \int_0^{\frac{2\pi}{t_p}} \int_{R_i}^{R_o} rB_g^m(t,\theta,r)F(t,\theta,r)drd\theta \tag{4-8}$$

This expression could also be defined in Fourier series as:

$$\Psi(t) = t_p \int_0^{\frac{2\pi}{t_p}} \int_{R_i}^{R_o} r \left[\sum_{k=-\infty}^{\infty} B_{gk}^m(r) \cos\left(kp(-\theta + \varphi_0)\right) \times \sum_{n=-\infty}^{\infty} F_n(\mathrm{r}) \sin\left(\mathrm{nt_p}(\theta + \lambda_0)\right) \right] dr d\theta \quad (4\text{-}9)$$

Both variables, the magnetic field in the air gap and the magneto-motive force per current unit, depend on the radius. Because there is no interaction between these two variables, their effects could be analyzed independently.

- **Analysis of the Magnetic Flux Density Induced by the Magnets in the Air Gap**

The harmonics of the magnetic flux density induced by the magnets in the air gap can be calculated by the following expression developed from (3-50):

$$B_{gk}^m(r) = \frac{\hat{B}_{g0}^m}{k\pi} \sin\left(kp \frac{\beta_m(r)}{2}\right) \frac{(1 - \cos(k\pi))}{1 + (a(r)kp)^2} \quad (4\text{-}10)$$

In this expression, the terms that depend on the radius are the magnet span and the fringing factor. This last factor takes the following shape when it is a function of the radius:

$$\mathrm{a(r)} = \sqrt{\frac{\mathrm{g(g')}}{2r}} \quad (4\text{-}11)$$

The part of the expression (4-8), which is a function of the radius, is related to the magnetic flux density induced by the magnets in the air gap:

$$\Phi_{\mathrm{g}}^{\mathrm{m}} = \int_{\mathrm{R_i}}^{\mathrm{R_o}} \mathrm{B_g^m(t, \theta, r)\, dr} \quad (4\text{-}12)$$

As previously mentioned, the variables in expression (4-10), which are functions of the radius, are the magnet span and the fringing function. Thus, the values of the coefficients are different when the magnets are trapezoidal or rectangular. In order to calculate the magnetic flux density caused by the magnets in the air gap, expression (4-10) must be integrated along the radius:

$$\Phi_{\mathrm{g\ k}}^{\mathrm{m}} \Big|_{\mathrm{a \neq cnt}}^{\beta_{\mathrm{m}} \neq \mathrm{cnt}} = \frac{\hat{B}_{g0}^m}{k\pi} (1 - \cos(k\pi)) \int_{\mathrm{R_i}}^{\mathrm{R_o}} \frac{sin\left(kp \frac{\beta_m(r)}{2}\right)}{1 + (a(r)kp)^2} \mathrm{dr} \quad (4\text{-}13)$$

The expression (4-13) is a general expression for any magnet shape, but in the case of trapezoidal magnets, this can be simplified, which leads to:

$$\Phi_{g\,k}^{m}\Big|_{a=cnt}^{\beta_m=cnt} = \frac{\hat{B}_{g0}^{m}}{k\pi}(1-\cos(k\pi))\frac{sin\left(kp\frac{\beta_m}{2}\right)}{1+(akp)^2}(R_o^2-R_i^2) \tag{4-14}$$

In this case, the magnetic flux density does not depend on the radius *r*. Hence, from (4-13) and (4-14) the correction factors related to the magnetic flux density XB_n for each spatial harmonic can be calculated as:

$$XB_k = \frac{\Phi_{g\,k}^{m}\Big|_{\alpha\neq cnt}^{\beta_m\neq cnt}}{\Phi_{g\,k}^{m}\Big|_{\alpha=cnt}^{\beta_m=cnt}} \tag{4-15}$$

These correction factors can then be applied to the spectrum of the flux linkage obtained from the *FEM-2D* simulations in order to calculate the flux linkage spectrum considering the entire geometry of the machine:

$$\psi_{k\_method} = \psi_{k\_2d} XB_k \tag{4-16}$$

where ψ_{k_method} and ψ_{k_2d} are the k order harmonics of the flux linkage of the proposed approximation and 2D simulation, respectively.

Next, the temporal flux linkage is calculated applying the inverse fast Fourier transformation (*IFFT*):

$$\psi(t) = \sum_{k=-\infty}^{\infty} \psi_{k\_method}\sin\left(kp(\Omega t-\lambda_0)\right) \tag{4-17}$$

- **Analysis of the Magneto-Motive Force per Current Unit**

The second effect is produced by the disposition of the conductors in the resultant magneto-motive force per current unit, *F*. The expression for each harmonic of *F* in function of the radius is:

$$F_n(r) = \frac{jN_{ph}}{\pi n\, t_p}\xi_n(r) \tag{4-18}$$

As shown in the previous expression, the winding factor ξ_k, is the part of the expression that is dependent on the radius. This factor is the combination of the winding distribution factor ξ_{s_k} and the winding pitch factor ξ_{p_k}, which also depend on the radius.

$$\xi_n(r) = \xi_{s\_n}(r)\xi_{p\_n}(r) \tag{4-19}$$

The distribution factor is defined as a function of the radius:

$$\xi_{p\_n}(r) = \frac{\sin\left(nt_p \frac{\beta_c(r)}{2}\right)}{nt_p \frac{\beta_c(r)}{2}} \tag{4-20}$$

The pitch factor is defined as a function of the radius:

$$\xi_{s\_n}(r) = \sin\left(nt_p \frac{\beta_w(r)}{2}\right) \tag{4-21}$$

It is interesting to note that the harmonics of the winding that link with those of the magnetic flux density induced by the magnets are used in the next expression.

$$n = -\frac{kp}{t_p}. \tag{4-22}$$

In this analysis, the part of the expression (4-8) that depends on the radius is related to the magneto-motive force per current unit:

$$\chi_g^a = \int_{R_i}^{R_o} F(t,\theta,r)dr \tag{4-23}$$

Developing the expression (4-23) with (4-18), the next general expression for any shape of the winding is obtained:

$$\chi_{g\,k}^{a}\Big|_{\beta_c \neq cnt}^{\beta_w \neq cnt} = \frac{\mathrm{jN_{ph}}}{\pi k\, t_p} \int_{R_i}^{R_o} \left[\sin\left(kt_p \frac{\beta_w(r)}{2}\right) \times \frac{\sin\left(kt_p \frac{\beta_c(r)}{2}\right)}{kt_p \frac{\beta_c(r)}{2}}\right] dr \tag{4-24}$$

Nevertheless, for a trapezoidal coil shape, the distribution and pitch angles are constant, so the expression (4-23) is simplified, which leads to:

$$\chi_{g\,k}^{a}\Big|_{\beta_c=cnt}^{\beta_w=cnt} = \frac{\mathrm{jN_{ph}}}{\pi k\ t_p}\left[\sin\left(kt_p\frac{\beta_w}{2}\right)\times\frac{\sin\left(kt_p\frac{\beta_c}{2}\right)}{kt_p\frac{\beta_c}{2}}\right](R_o^2-R_i^2) \tag{4-25}$$

From (4-24) and (4-25), the *XF* correction factors caused by the shape of the winding are computed:

$$\mathrm{XF_k} = \frac{\chi_{\mathrm{g_k}}^{\mathrm{a}}\Big|_{\beta_c\neq\mathrm{cnt}}^{\beta_w\neq\mathrm{cnt}}}{\chi_{\mathrm{g_k}}^{\mathrm{a}}\Big|_{\beta_c=\mathrm{cnt}}^{\beta_w=\mathrm{cnt}}} \tag{4-26}$$

When the XF correction factors are obtained, the flux linkage spectrum obtained with *FEM-2D* is post-processed. Thus, the flux linkage for the entire machine geometry is computed:

$$\psi_{\mathrm{k\_method}} = \psi_{\mathrm{k\_2d}}\mathrm{XF_k} \tag{4-27}$$

From the harmonic content of the flux linkage, it is possible to obtain the time waveform by applying the inverse Fourier transformation as in (4-24).

4.3.3 Validation of the Proposed Method

In order to validate the proposed method, a small configurable axial machine was built. This machine is not designed for a real application. Its purpose is to test different combinations to validate the method.

Two different conceptual prototypes were manufactured and tested. Figure 4-13 shows the laboratory test bench, which consists of a load motor, a torque sensor, and the test prototype.

The validation of the proposed method is done by comparing the results obtained with a simple *FEM-2D* simulation, the results obtained with the proposed method, the *FEM-3D* results, and the experimental results.

- **Description of the prototypes**

The two test prototypes are double rotor coreless stator axial flux machines (see Figure 4-14). Both machines have two pole pairs formed by rectangular magnets in their rotors, and a unique coil per phase in the stator, which leads to fractional machines with 0.25 coils per pole and per phase. The only difference between the two prototypes is the coil shape, which is rectangular in one and trapezoidal in the other. The stator coils are compacted in an epoxy resin

in order to obtain a coreless stator. As it is impossible to place a coil with infinitesimal width ($w_c = 0$), the real width of the conductor distribution, w_c, is about *6 mm* on both prototypes (Figure 4-15). Note that the coreless configuration of prototypes was chosen in order to make the manufacturing process inexpensive and simple.

The three coils are placed with a separation of 120^o from each other. The pitch angle of the coils is different in each prototype. In the stator with trapezoidal coils, the conductors are placed with a pitch angle (β_w) of 60^o, making a uniform distribution of the conductors, as shown in Figure 4-15-a. In this prototype, expression (4-23) is used to improve the results obtained from *FEM-2D*. The pitch angle with the rectangular coils is not constant along the radius. The distance between the positive and negative conductors, w_w , is *40 mm*, as shown in Figure 4-15-b. In this case, expression (4-34) is used to improve the results obtained from *FEM-2D*. The main characteristics of these prototypes are summarized in Table 4-1. Because the prototype machine is coreless, the total air gap is the distance between the magnets of both rotors. The stator is centered in this space, so there is a distance of one millimeter between each side of the stator and each rotor.

Parameter	***Value***
Number of pole pairs	*2*
Q	*6*
Number of winding layers	*1*
Number of phases	*3*
Number of coils	*3 (1 per phase)*
Number of turns per phase	*100*
Peak current	*1.5 A*
Rotational speed	*250 rpm*
Rotor outer diameter	*190 mm*
Rotor inner diameter	*55 mm*
Rotor disc thickness	*10 mm*
Stator outer diameter	*265 mm*
Stator inner diameter	*34 mm*
Stator disc thickness	*4 mm*
Total air gap	*6 mm*
Magnet thickness	*5 mm*
Magnet dimensions	*50 mm x 64 mm*
Magnet grade	*NEO 42 H*

Table 4-1: Main characteristics of the test prototypes

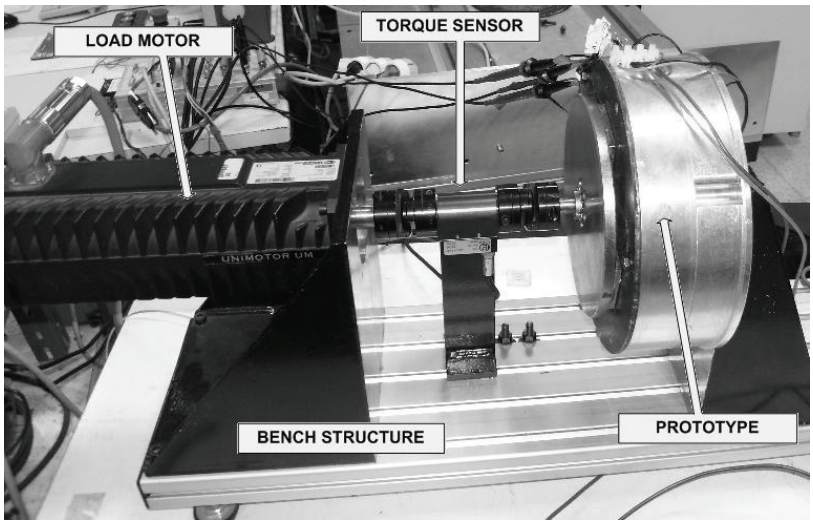

Figure 4-13: Picture of test bench

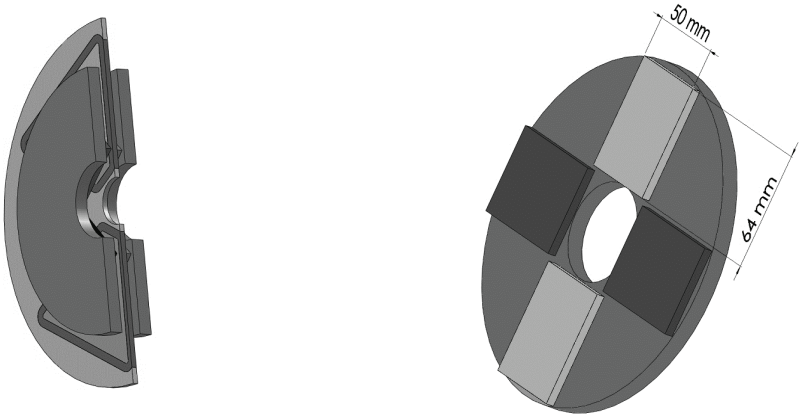

a) *b)*

Figure 4-14: a) Cut view of the complete machine and b) a view of the rotor

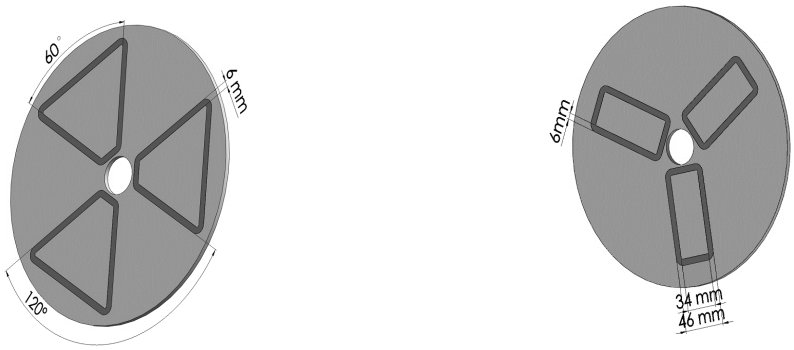

a) *b)*

Figure 4-15: Views of the stators of the prototypes, a) trapezoidal coils and b) rectangular coils

- **Results**

The experimental study consisted of two tests. The first one was the open circuit test. In this test, the prototypes were driven at rated speeds, and the back *EMF* was measured in the three phases. The second test was the so-called load test. In this test, the prototypes were controlled by a vector control to operate at a rated speed and load. In this situation, the torque was measured using a torque sensor characterized by a full scale of *15 Nm* and a resolution of *0.1 Nm.*

All experimental measurements were compared with the results obtained by *FEM-2D* approximation, the results obtained by *FEM-3D,* and the results obtained using the proposed method.

- **Prototype 1: Trapezoidal coils and Rectangular Magnets**

Figure 4-16-a shows a plot of the different back *EMF*. Figure 4-16-b shows the harmonic content of the four back *EMF* waveforms. Figure 4-17-a shows a plot of the time evolution of the electromagnetic torque, and Figure 4-17-b shows the harmonic content of the electromagnetic torque.

The results obtained with the proposed method showed good agreement with both the experimental measurements and the *FEM-3D* simulations.

The results obtained for the *EMF* waveforms and their spectrums are accurate, as shown in Table 4-2. The first harmonics were mostly the same for the *FEM-3D* simulation, experimental results and the proposed method (less than 1% of error between them). It is also noticeable that the correction was done in higher harmonics, as shown in Figure 4-16-b and Figure 4-17-b. It should be noted that the attenuation of these harmonics was caused by a skew effect produced by the shape of the magnets.

The results obtained for the torque are again quite good. The waveform is improved because it occurs with the harmonic content. Table 4-3 presents a summary of the results for the average torque and ripple torque. The torque ripple is the difference between average torque and peak torque. The skew effect originated by the magnet shape is quite noticeable when the *FEM-2D* torque ripple and the ripple obtained with the other methods are compared.

The effect of the distribution of the conductors of a coil side (w_c) is not important since this distribution is only 6 mm (Figure 4-15), so it could be neglected, and only the effect of the

shape of the magnets is assumed. The results obtained by either neglecting or assuming this effect are practically the same in this case.

	1^{st} Harmonic	5^{th} harmonic	7^{th} harmonic
Experimental	12.89 V	0.744 V	1.09 V
FEM-3D	12.82 V	0.874 V	1.03 V
FEM-2D	13.26 V	2.46 V	1.47 V
Proposed method	12.89 V	0.744 V	1.09 V

Table 4-2: EMF harmonics with trapezoidal coils and rectangular magnets

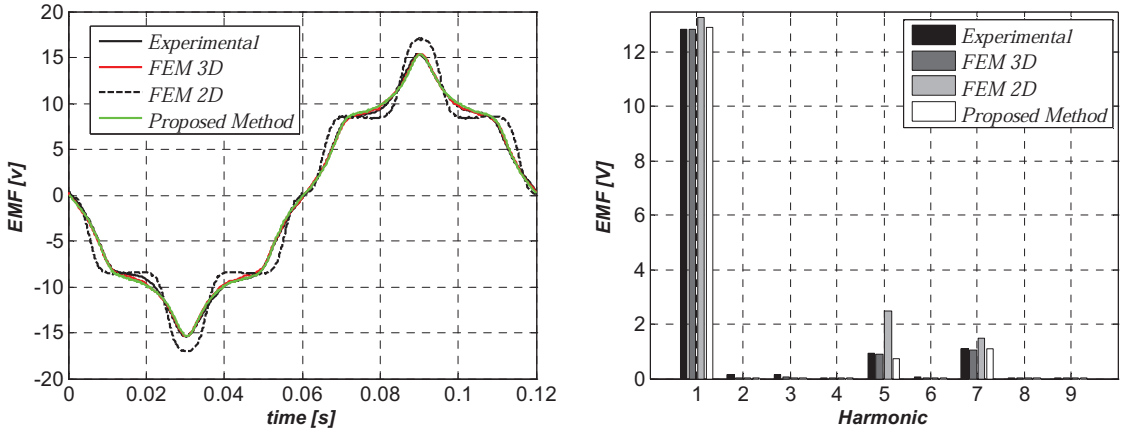

a) *b)*

Figure 4-16: a)Time evolution and b) harmonics of the of the EMF in the machine with trapezoidal coils

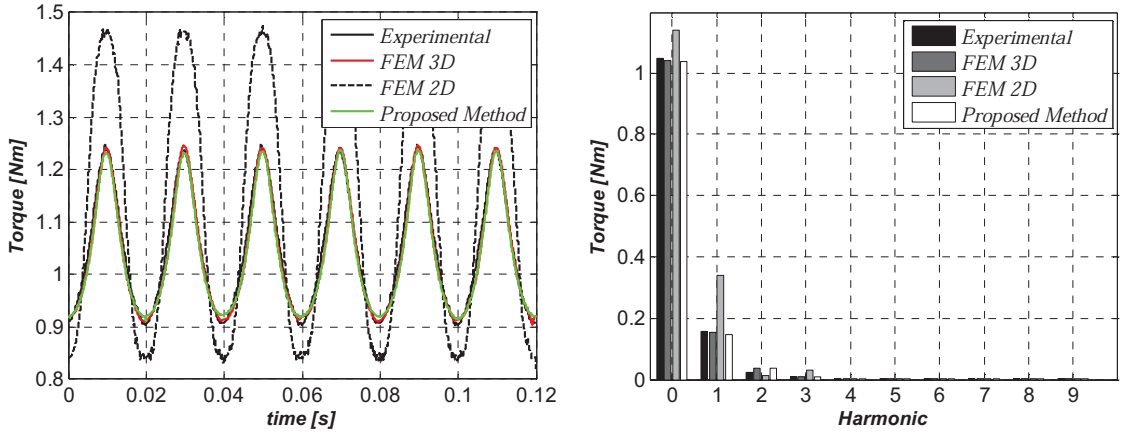

a) *b)*

Figure 4-17: a) Time evolution and b) harmonics of the of the T_{em} in the machine with trapezoidal coils

	Average Torque	*Torque Ripple*
Experimental	*1.037 Nm*	*0.1717 Nm*
FEM-3D	*1.04 Nm*	*0.1712 Nm*
FEM-2D	*1.14 Nm*	*0.328 Nm*
Proposed method	*1.047 Nm*	*0.1634 Nm*

Table 4-3: Torque with trapezoidal coils and rectangular magnets

- **Prototype 2: Rectangular coils and Rectangular Magnets**

Figure 4-18-a shows a plot of the back *EMF* curves. Figure 4-18-b shows the harmonic contents of these *EMF*s. Figure 4-19-a shows the time evolution of the electromagnetic torque, and Figure 4-19-b shows the harmonic content of the electromagnetic torque.

The results obtained with the second prototype were not as accurate as the ones obtained with the first prototype. The method tended to improve the results obtained with *FEM-2D,* by getting them closer to the experimental measurements. However, the error was slightly higher than in the previous prototype. The results obtained with *FEM-3D* and the proposed method are quite similar, so the difference in the experimental results may be due to a geometrical difference between the prototype and the *FEM* models. When the coils were placed in the epoxy, they could have moved and taken an unknown shape.

Table 4-4 shows the results obtained for different harmonics of the *EMF*. The first harmonics are quite similar in the experimental, *FEM-3D,* and method results, with less than 2% difference among them. However, the 3rd and 7th harmonics of the experimental results vary considerably from the other results.

Table 4-4 summarizes the torque results. The average torque is quite similar to the three methods, with an error of 1%, while compared with the *FEM-2D* results, the error is about 5%. The error committed in the torque ripple is higher but in comparison with the *FEM-2D* results, the approximation is quite good. In this prototype, the skew effect caused by the shape of the magnets and coils was more noticeable.

Although the results obtained with this second prototype were not as good as the ones obtained with the first prototype, it was demonstrated that the method is valid.

	1st Harmonic	3th Harmonic	7th Harmonic
Experimental	9.35 V	3.57 V	1.12 V
FEM-3D	9.24 V	4.04 V	0.49 V
FEM-2D	8.87 V	5.05 V	1.75 V
Proposed method	9.27 V	4.26 V	0.51 V

Table 4-4: EMF harmonics with rectangular coils and rectangular magnets

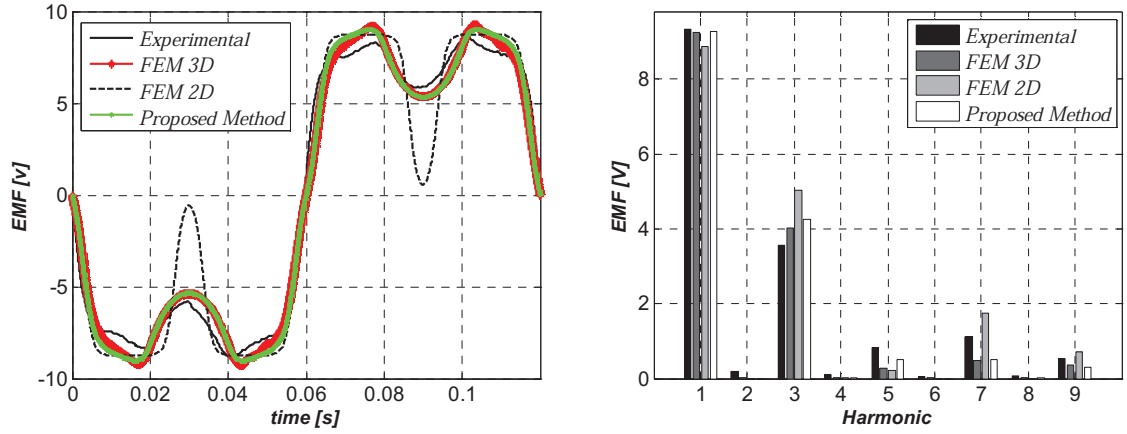

a) b)

Figure 4-18: a)Time evolution and b) harmonics of the EMF in the machine with rectangular

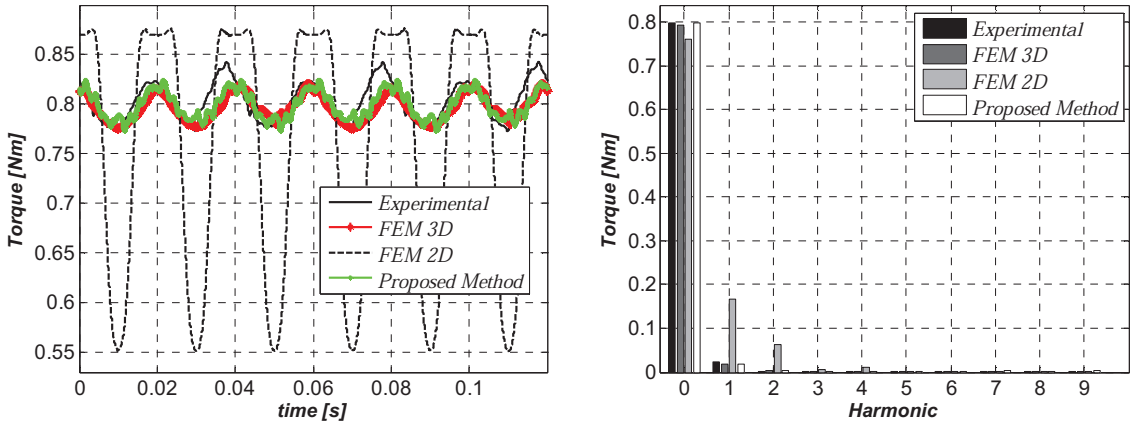

a) b)

Figure 4-19: a)Time evolution and b) harmonics the T_{em} in the machine with rectangular coils

	Average Torque	*Torque Ripple*
Experimental	*0.803 Nm*	*0.035 Nm*
FEM-3D	*0.7964 Nm*	*0.0226 Nm*
FEM-2D	*0.7620 Nm*	*0.162 Nm*
Proposed method	*0.799 Nm*	*0.0259 Nm*

Table 4-5: Torque with rectangular coils and rectangular magnets

4.3.4 Conclusions about the Proposed Method

In this work, a new methodology is presented as a new solution for modeling axial flux machines. This methodology consists of the combination of *FEM-2D* simulations and analytical models. This new solution enables the analysis of axial flux machines in a shorter time than when *FEM-3D* is used and with more precise results than with the original *FEM-2D* approximation.

In order to prove the validity of the proposed method, two conceptual prototypes were constructed and tested. The results were compared with those obtained using *FEM-3D* and the original *FEM-2D* approximation. The results obtained with these machines confirmed that this method significantly improved the *FEM-2D* simulations. Similar results were obtained with the *FEM-3D* approach and the proposed method.

In future research, it would be interesting to test the accuracy of this method in other conceptual prototypes and in industrial machines. It should be noted that although the method was tested for rectangular magnets and coils, it is valid for any shape.

The method has two main disadvantages. One the one hand, the value of the end-winding inductance cannot be obtained, although with an analytical approximation quite accurate values may be obtained. On the other hand, in machines where local saturations may occur, the method can lose precision.

4.4 Calculation of Magnetic Losses in FEM

The calculation of the magnetic losses in electrical machines is both important and difficult. These losses define the behavior of the machine because they affect its efficiency and thermal behavior. The latter is critical because the integrity of parts, such as magnets and coils, depend on it. The most common method used to calculate these magnetic losses was proposed by *Bertotti* [101]. He defined the losses as the sum of three components:

- Hysteresis losses P_h

Hysteresis losses are caused by the hysteresis cycle that the ferromagnetic material does when exposed to low frequency magnetic fields. These losses are approximated as:

$$P_h = K_h f B^2 \tag{4-28}$$

where K_h is the coefficient of hysteresis losses.

- Eddy current classical losses P_{Ed}

These losses are caused by the currents that are induced in a ferromagnetic material when it is exposed to an alternating magnetic field. They are calculated with next expression:

$$P_e = \frac{d^2\sigma}{10}\frac{1}{T}\int_T \left(\frac{dB}{dt}\right)^2 dt \tag{4-29}$$

where d is the width of the steel lamination and σ is the resistivity of the material.

- Excess losses P_{ex}

The computation of the classical eddy current losses considers that the homogeneous distribution of the field in the whole surface of the lamination. However, this is not the case because the induced currents distort the field, generating a local non-homogeneous field. Hence, the dynamic losses are higher than the classical eddy losses are. The difference is the excess losses. These take next shape as:

$$P_{ex} = 8.67 K_{ex} (fB)^{1.5} \tag{4-30}$$

where K_{ex} is the excess losses coefficient.

The analytic calculation of the magnetic losses is an arduous task with uncertain reliability. Some authors [102] proposed an analytical process in which the losses are calculated in each region and then summed to obtain the global losses. These regions are defined by parts of the machine where the field variation is quite similar. From this field variation, it may be possible to calculate the losses. However, even if an approximation is possible, the accuracy of the results is strongly linked to the number of regions and the quality of the estimated field wave in each region. Furthermore, this method does not include the component of the losses known as rotational losses. These losses occur when the direction of the field changes from the axial in the teeth to the tangential in the yoke. In [80] the implementation of these additional losses is

proposed. Taking into account all these difficulties, a very appealing option is to carry out numerical approximations with finite element software.

The software *FLUX* offers two possibilities for the computation of the losses in the magnetic cores:

- Method based on the separation of the losses (Bertotti)
- Method based on the *LS model* (Loss Surface)

In both methods, the calculation of losses is carried out after solving the problem. This is because *FLUX* only assumes the normal *B-H* curve of the material while neglecting the effects of hysteresis. In both methods, the losses are calculated from the flux density in each node and simulation step. In the case of the *LS model*, a family of hysteresis curves of the material is used to define the hysteresis and calculate the losses. The main inconvenience of this method is that it can be performed only with the materials in the *FLUX* data base.

The accuracy of *Bertotti´s model* depends strongly on the correct estimation of the coefficients of the material. The results may not be as accurate as with *LS model*, because minor cycles or skin effects are not considered. However, this method is valid for any material of which the *Bertotti´s* coefficients are known.

In the case of the rotor core and magnets, the losses are caused by eddy currents. These parts of the machine can be defined as solid conductors with a certain resistivity and the dissipated losses in them can be measured. In this case, the computation of the losses is done during the solving process and only in a *FEM-3D* simulation.

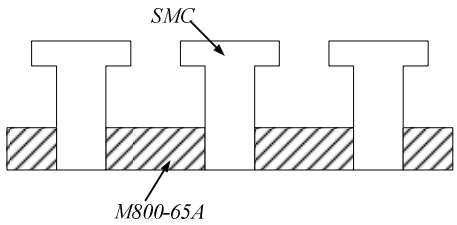

Figure 4-20: Stator core with SMC and M800-65A

Material	***LS model***	***Bertotti***
M800-65A	*33.74 W*	*36.92 W*
SMC	*Non-computable*	*34.43 W*
M800-65A+ SMC	*6.9 W (Steel)*	*7.03 W (Steel)+26.41 W (SMC)*

Table 4-6: Losses in a stator core with different materials

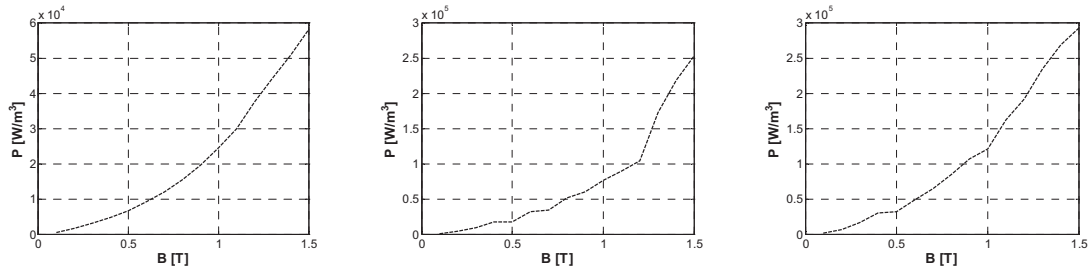

a) *b)* *c)*

Figure 4-21: Loss curve of M800-65A, a)50Hz, b) 100 Hz y c) 150 Hz

Coefficients	***M800-65A***	***SMC***
K_h *[w/(T²m³)]*	*123.99*	*536.0472*
σ *[s/m]*	*4000000*	*0*
K_{exc} *[w/(m³(T/s)^1.5)]*	*3.11*	*1.723*

Table 4-7: Berttoti coefficients for M800-65A and SMC (Somaloy Prototyping Material)

Table 4-6 shows the losses in the stator core of a Q18p8 machine. A machine with three different material configurations has been analyzed: *M800-65A* electrical steel, *SMC* and a combination of both teeth with *SMC*, and yoke with *M800-65A* (Figure 4-20).

The *SMC* material that was used here is the one that *Höganäs* manufactures for prototyping (*Somaloy Prototyping Material*). In the case of the *SMC,* the lamination length term does not exist, so two options are considered. The first option is to neglect the eddy current losses component and include these losses in the other components. The other option is to find an equivalent length. Both options must ensure that *Bertotti´s* equation follows the loss curve of the material.

In cases where *LS model* is used, this should be the first option, although the method of the separation of losses is very useful anyway. If several curves of losses for different flux densities and frequencies are available, it is possible to obtain accurate *Bertotti´s* coefficients by iterative mathematical methods. Figure 4-21 shows the curves of losses of the *M800-65A* material. These curves are used to obtain the coefficients shown in Table 4-7. These curves are offered by the manufacturer *Cogent.*

Knowing the values of these losses is essential for the later thermal analysis of the machine.

4.5 Conclusions

This chapter is divided in four sections. First, a brief introduction to the finite element method is done. The use of *FEM* tools for the analysis of axial flux machines is explained according to the differences between *FEM-2D* and *FEM-3D*. Because the *FEM-2D* may be not enough for the modeling of axial flux machines, and the *FEM-3D* may bring about a long computation time, a new method that combines *FEM-2D* and analytical tools is presented. Finally, after a short introduction to the magnetic losses, the possibilities that *FLUX* offers for the computation of this losses are presented.

The main conclusions of this chapter are as follows:

- The *FEM-2D* simulations may be not enough for certain problems, such as the disproportionality of the geometry or high saturation of the magnetic cores. Hence, *FEM-3D* is more credible and useful. In contrast, the computation time can be very high in 3D simulations.

- The proposed method in which *FEM-2D* and analytical tools are combined shows great accuracy (>95% in the validation). However, the problem of local saturations is not solved. Nonetheless, the proposed method is a good option to carry out a fast machine design.

- *FEM-3D* simulations are essential for a complete analysis of the machine. This kind of analysis allows obtaining all the parameters of the machine and avoiding uncertain situations, such as local saturations. The multi plane *FEM-2D* process could be an equivalent option, but eddy current losses and end-winding inductance cannot be calculated.

Chapter 5.

THERMAL MODELING OF AXIAL FLUX MACHINES

The thermal modeling of electrical machines is one of the most challenging tasks nowadays. Good thermal sizing may be accomplished in a smaller, cheaper, or safer machine. If the temperatures in different parts of the machine can be predicted, it is possible to optimize the size of the machine while assuring the integrity of critical parts, such as the magnets and coils.

This chapter introduces the thermal modeling of axial flux machine and proposes a simple model. Finally, a prototype is used to carry out several tests to study the thermal behavior of axial machines.

5.1 Introduction to Thermal Modeling

The thermal modeling of electrical machines is important, but it is also one of the most complicated issues. During the operation of the machines, heat is generated by the losses (e.g., copper losses, iron losses, and mechanical losses), and the influence of this heat in the critical parts of the machines, the magnets and the coils, must be controlled. Heat is removed from the machine by conduction, radiation, and convection. Conduction occurs when a temperature difference exists in a solid body, causing a heat flow from the hot region to the cold region. Radiation is the electromagnetic emission of heat from a body to the surrounding space. Convection is a phenomenon where the heat transfer is from a surface to a moving fluid. The thermal model can be approximated to a lumped parameter network that is similar to an electrical network, as shown in Table 5-1. The heat is transferred from a high temperature region T_h to a low temperature region T_c in the next expression, where P is the rate of heat transfer, and R_{oth} is the thermal equivalent resistance:

$$P = \frac{T_h - T_c}{R_{th}} \tag{5-1}$$

The knowledge of radial machines has led to an important number of works on the thermal analysis of these machines. However, recently several studies concerning the thermal analysis of axial machines have been carried out. In [8] *Gieras et al.* gave some basic notions of thermal issues in axial machines. Some other authors modeled their axial flux prototypes with equivalent thermal circuits developed from thermodynamic laws and the geometry of their machines. Examples are *Shin's* thesis [38], *Parviainen et al.* [37], [103], and the interesting work presented in [104]. Another option is the thermostatic modeling of the machine by finite element methods as in [105]. In [106] lumped parameter heat transfer model and an air-flow model is combined. Furthermore, in more advanced works the authors rely on *CFD* software to obtain more accurate thermal models, such as *Marignetti et al.* [107], [108] and *Airoldi et al.* [109].

Thermal	***Electrical***
Temperature difference (K)	*Voltage (V)*
Heat transfer (W)	*Current (A)*
Heat resistance (K/W)	*Electric resistance (V/A)*
Heat capacitance (Ws/K)	*Electric capacitance (As/v)*

Table 5-1: Comparison between thermal and electrical parameters

5.2 Simple Thermal Model for an Axial Flux Machine

The main aim of this thesis is not the thermal analysis of the axial machines. However, a global idea of the thermal behavior of these machines is essential for the design process. In this sense, a simple thermal model based on the model proposed by *Vilar et al.* [104] is developed. The idea is to simplify an equivalent lumped parameter model as much as possible. To achieve this, the heat conduction in the volumes is perfect because it is only considers the convection resistance from each volume into the air. Heat transfer between different volumes in contact is assumed with a single conduction resistance, and each volume is modeled with a single capacitance. Only copper losses are contemplated as a source of heat (P_{cu}), which is valid only when the other losses do not have great weight in the global value. Radiation is also neglected.

Figure 5-1 shows a general equivalent circuit, where R_{cu_st}, R_{st_str} and R_{st_rot} are the conduction thermal resistances, R_{cu_air}, R_{st_air}, R_{str_air} and R_{rot_air} are the thermal convection resistances, and C_{cu}, C_{st} C_{str} and C_{rot} are the thermal capacitances. The suffixes "*cu*", "*rot*", "*st*" and "*str*" refer to the copper, rotor, stator, and structure, respectively. Convection resistance is calculated as:

$$R_{th_{conv}} = \frac{1}{hA} \tag{5-2}$$

where h is the convection factor. This factor is a function of the surface finish, orientation, fluid properties, velocity, and temperature. A is the surface of the solid in contact with the fluid. The conduction thermal resistance is:

$$R_{th_{cond}} = \frac{l}{kA} \tag{5-3}$$

where k the thermal conductivity of the material. l and A are respectively the length and area of the body where the heat transfer occurs. Finally, the capacitance is calculated as:

$$C_{th} = c_p m \tag{5-4}$$

where c_p is the specific heat of the material and m is the mass of the solid.

In this thesis, the equivalent thermal circuit is simulated by *Portunus,* and the validation of the model is performed in section 5.4 and 6.6.2.3.

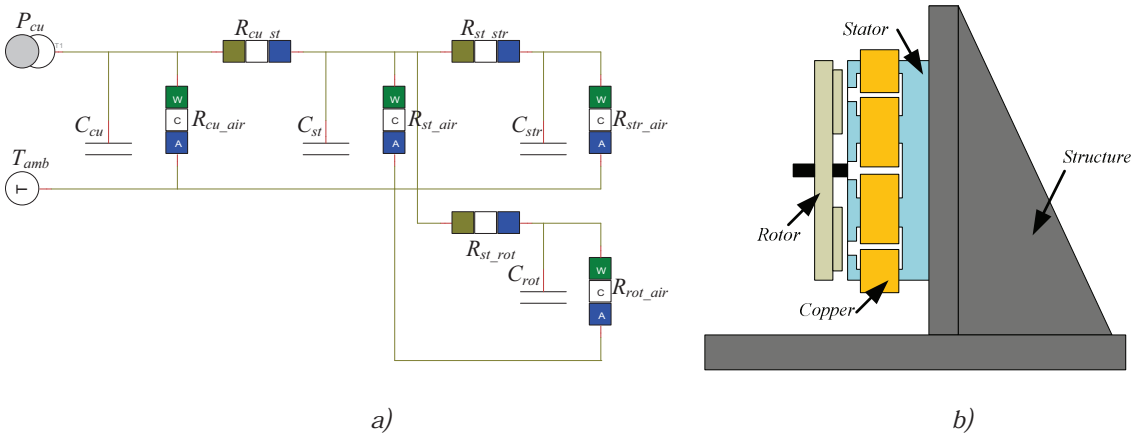

Figure 5-1: a) General equivalent thermal circuit for a simplified axial machine assembly as shown in b)

5.3 Thermal Behavior of Axial Flux Machines

This section describes impressions of the thermal behavior of axial machines. With that aim, a small axial machine is thermally tested at different conditions as presented below.

5.3.1 Machine for Thermal Tests

Parameter	*Nom.*	*Value*
Air-gap length	g	*1.85 mm*
Stator core length	L_s	*30 mm*
Rotor core length	L_r	*15 mm*
Number of stator slots	Q	*6*
Number of pole pairs	p	*2*
Outer diameter	D_o	*184.2 mm*
Inner diameter	D_i	*75.2 mm*
Magnet height	h_m	*5 mm*
Magnet		*64 mm x 54 mm*
Residual flux density	B_r	*1.34 T*
Relative permeability of the magnet	μ_r	*1.08*
Number of turns per phase	N_{ph}	*250*
Number of phases	m	*3*
Mechanical nominal speed	Ω_m	*250 rpm*
Phase resistance (T = 25 ºC)	R_{cu}	*6.15 Ω*

Table 5-2: Characteristics of the test machine

- **Characteristics of the test machine**

The modeled machine is an axial flux surface mounted PM synchronous machine. This machine has a single-side slotted stator configuration. The number of slots is $Q = 6$, and the number of pole pairs is $p = 2$. Double layer winding is implemented, which consists of six coils, that is, two coils per phase. Figure 5-2 shows the laminated stator with two-layer winding. Table 5-2 reports the main characteristics of the test prototype. The machine is quite similar to the test machine used in section 4.3, as the used rotor and main structure are the same. The test prototype also does not fulfill any application requirements, and it has been designed with the purpose of validating the analytical and numerical tools. It is also used for the thermal tests.

Different test bench configurations are used for the thermal experiments, as shown in Figure 5-3. In the first group of tests, the prototype is fed by a DC source. In the other two groups of tests, the prototype is driven by a traction motor that is controlled by a *Control Techniques®* drive. In both tests, the machine works as a generator, but in one case its terminals are connected to a load resistance while in the other case, the machine load is controlled in current. Regarding the measurements, a *15 Nm* torque transducer with a resolution of *0.1 Nm* is used to measure the mechanical torque in the shaft. Furthermore, a *PZ4000* power meter from *Yokogawa®* is used to measure the power and to acquire the voltage and current waveforms. The experiments take about six hours. At this time, the thermal stability of the machine is not reached, so results are extrapolated using the least squares method. These extrapolation functions allow the creation of approximate temperature curves.

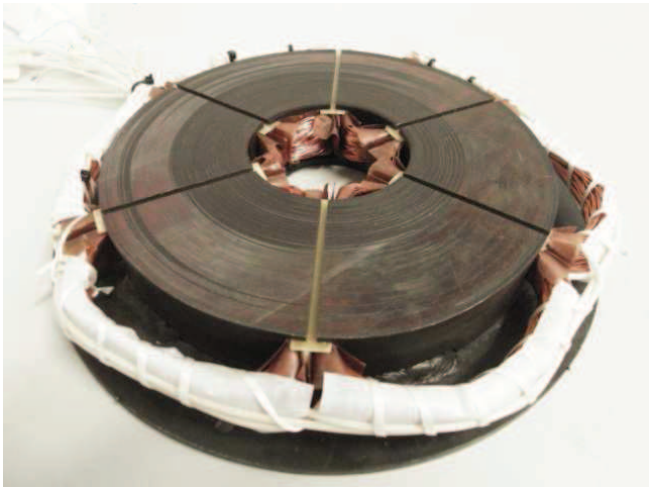

Figure 5-2: Finished stator, lamination, and winding

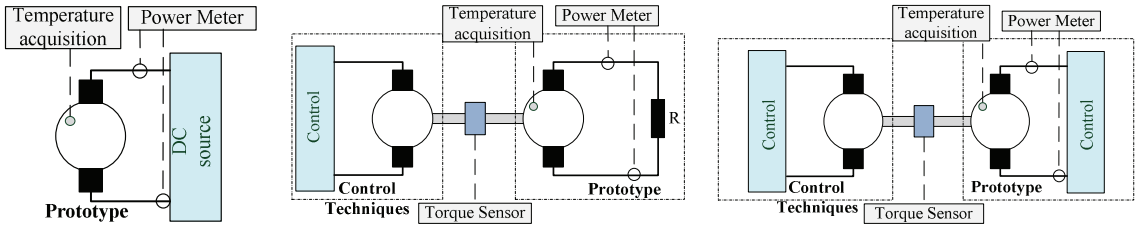

a) b) c)

Figure 5-3: Different test benches: a)DC tests, b)resistor load and c)controlled prototype

- **Position of the thermocouples**

A larger number of thermocouples are used to record the temperatures in different parts of the machine while the tests are being done. Eleven thermocouples are placed in the positions shown in Figure 5-4 and explained in Table 5-3. The measurements are processed by a *PXI* and *LABVIEW*. However, the data from the rotor is recorded with a wireless *USB* thermocouple reader that allows data acquisition while the rotor is moving.

Thermocouple	*Number*	*Position*
$T_{ambient}$	*1*	*At a half meter distance from the machine*
$T_{aluminium}$	*2*	*Aluminum frame where the stator is fixed*
$T_{stator\_backplate}$	*3*	*Back plate where the stator lamination is weld*
$T_{stator\_lamination}$	*4*	*Lamination of the stator*
$T_{end\text{-}winding\_in}$	*5*	*Inside the inner end winding*
$T_{winding}$	*6*	*Inside the coil at average radius*
$T_{end\text{-}winding\_out}$	*7*	*Inside the outer end winding*
$T_{coil\text{-}lamination}$	*8*	*Between a coil and the lamination at average radius*
$T_{coil\text{-}coil}$	*9*	*Between two coils of a slot at average radius*
$T_{structure}$	*10*	*Structure where the machine is fixed*
T_{rotor}	*11*	*Inside face of the rotor core*

Table 5-3: Placing of the thermocouples

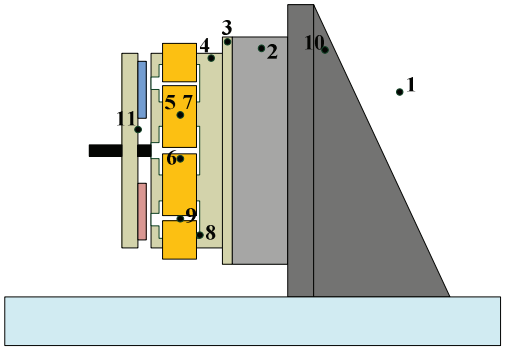

Figure 5-4: Sketch of the position of the thermocouples

5.3.2 Tests Results

A wide range of tests were performed. First, DC tests were carried out under different machine configurations. Second, tests under different load currents and nominal speed were performed. Finally, tests under different speeds were carried out.

5.3.2.1 Tests at different machine configurations

In this case, the tests were done with the machine in a static position (0 rpm). The three phases were fed in parallel with a DC source (Figure 5-3-a). The machine was tested with four different configurations:

- *Configuration 1*: The machine is screwed directly to the iron structure of the bench (Figure 5-5-a).
- *Configuration 2*: The machine is screwed directly to the iron structure of the bench, and it has a casing.
- *Configuration 3:* The machine is insulated from the iron structure of the bench (Figure 5-5-b).
- *Configuration 4*: The machine is insulated from the iron structure of the bench, and it has a casing (Figure 5-5-c).

The test conditions for all configurations are listed in Table 5-4. Table 5-5 lists the steady state temperatures in the magnet, winding, stator core, and structure. Figure 5-6 shows the evolution of these temperatures. The collected data showed that when a casing does not exist, the rotor is insulated from the stator but with the casing, the temperatures in both bodies were almost equal. It is also remarkable that in all cases, the temperature difference between the copper and magnets was quite marked. The worst situation happened in the fourth case, where the temperature difference was more than *19 ºC*. Another interesting point is that when the machine was fixed directly to the structure without an insulator the heat flowed through it.

Voltage [V]	***Phase current [I]***	***Current density [J]***	***Linear load [A]***	***Resistance [R_{cu}]***	***Power [P_{cu}]***
7.5 V	*1.23 A*	*$9.6x10^6$ A/m2*	*3905 A/m*	*6.35 Ω*	*28.8 W*

Table 5-4: Test conditions with different configurations

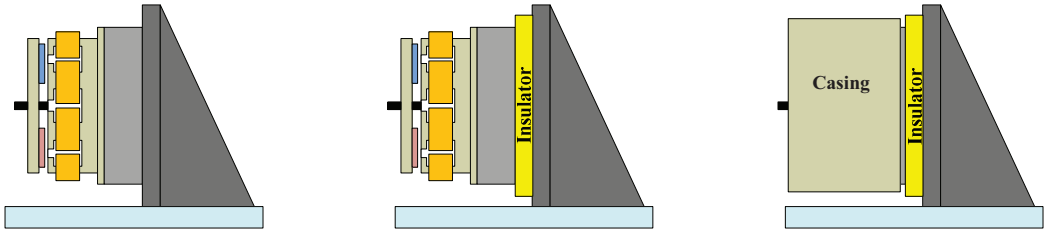

a) b) c)

Figure 5-5: Different configurations of testing machine: a)Placed directly in the structure b) insulated from the structure and c) insulated and with a casing

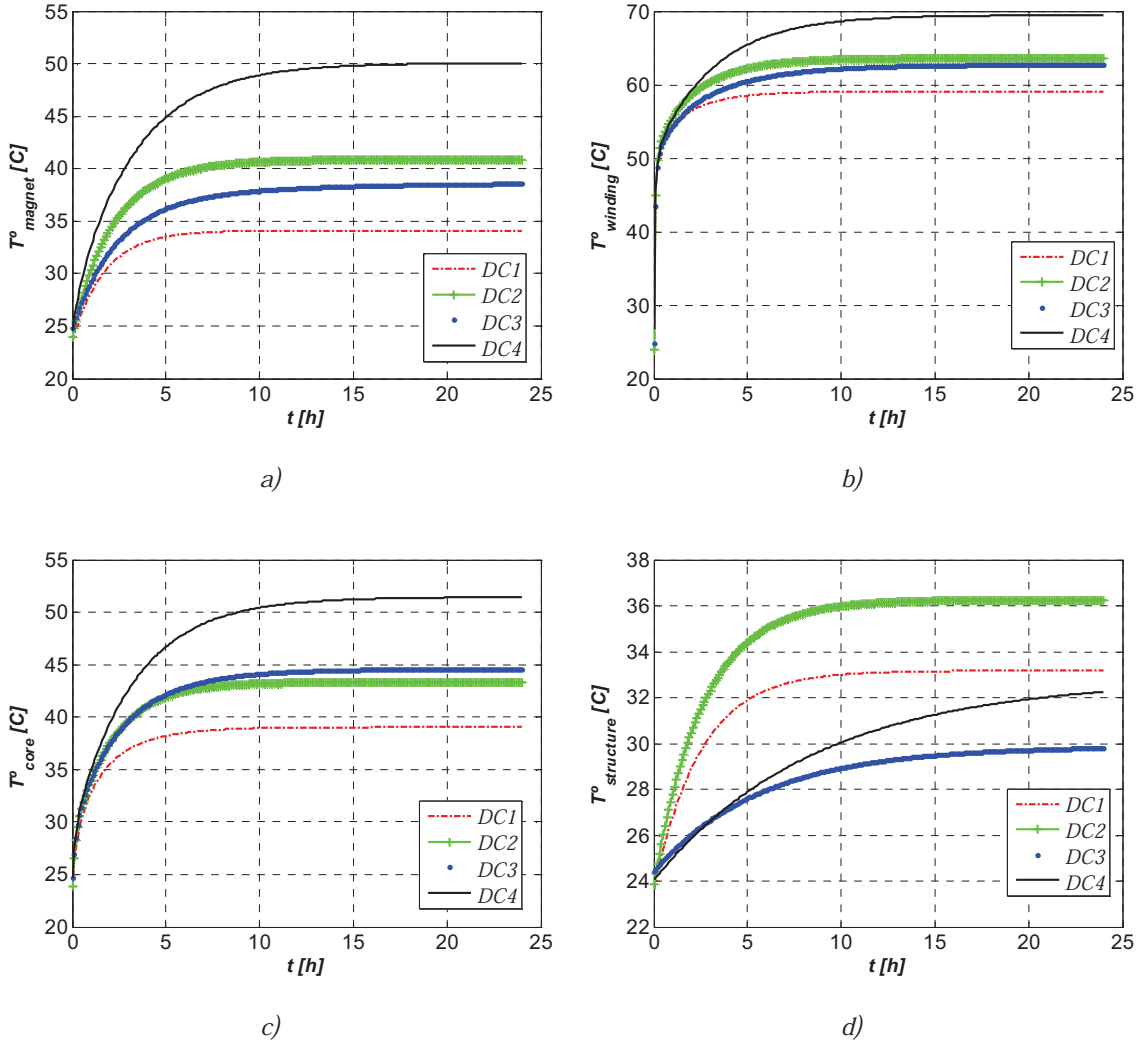

a) b) c) d)

Figure 5-6: Temperature time evolution with different configurations in: a) magnet, b) coil c) stator core and d)Structure

Configuration	DC1	DC2	DC3	DC4
T_{magnet} [ºC]	34.10	40.86	38.54	50.04
$T_{winding}$ [ºC]	59.07	63.56	62.71	69.47
T_{stator_core} [ºC]	39.05	43.34	44.57	51.43
$T_{structure}$ [ºC]	33.16	36.25	29.79	32.24

Table 5-5: Steady state temperatures (ºC) with different configurations

5.3.2.2 Tests at different load currents

These tests are carried out with the machine rotating at nominal speed (250 rpm) working as a generator to dissipate the energy in a load resistance (Figure 5-3-b). The value of the load resistance changes to obtain three different load conditions, as shown in Table 5-6.

Table 5-7 provides the steady state temperatures in the magnet, winding, stator core, and structure. Figure 5-7 shows the evolution of the same temperatures. The results show that heat transfer was mostly by convection from the end windings and conduction to the structure and the posterior convection. The main reasons for this claim are the non-proportionality between the temperature of the coil and the stator core on one side. However, on the other side the temperature difference between the stator core and the structure was almost constant. The higher the temperature, the greater the thermal difference between the stator and rotor, which denotes the isolation between both bodies. During this test, the rotor is exposed to the air without a covering.

Current [I]	Current density [J]	Linear load [A]	Phase Resistance [R_{cu}]	Power [P_{cu}]
0.48 A	$3.73x10^6$ A/m^2	1524 A/m	6.49 Ω	4.5 W
0.95 A	$7.4x10^6$ A/m^2	3016 A/m	7.15 Ω	19.35 W
1.76 A	$13.7x10^6$ A/m^2	5588 A/m	7.85 Ω	72.9 W

Table 5-6: Load conditions under different currents

Current [A]	0.48	0.95	1.76
T_{magnet} [ºC]	26.08	31.89	40.09
$T_{winding}$ [ºC]	31.37	49.03	112.16
T_{stator_core} [ºC]	28.31	34.66	53.72
$T_{structure}$ [ºC]	26.96	32.01	41.14

Table 5-7: Steady state temperatures (ºC) at different currents

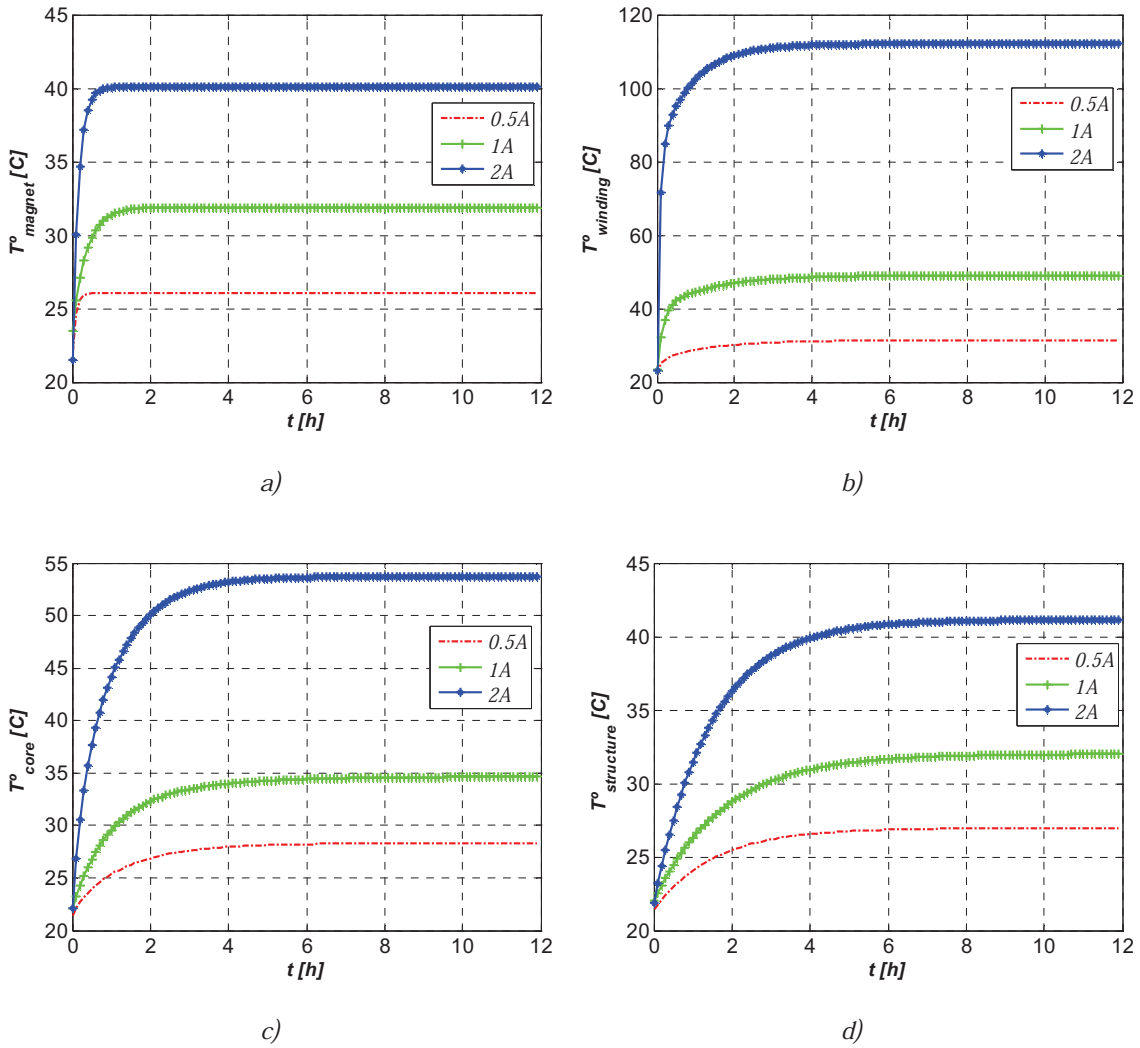

Figure 5-7: Temperature time evolution at different loads in: a) magnet, b) coil c) stator core and d)Structure

Speed [Ω_m]	***Current [I]***	***Current density [J]***	***Linear load [A]***	***Phase Resistance [R_{cu}]***	***Power [P_{cu}]***
0 rpm	*1.05 A*	*8.17x10^6 A/m^2*	*3353 A/m*	*6.34 Ω*	*20.96 W*
50 rpm	*1.046 A*	*8.14 x 10^6 A/m^2*	*3340 A/m*	*6.34 Ω*	*20.81 W*
200 rpm	*1.066 A*	*8.29 x 10^6 A/m^2*	*3404 A/m*	*6.33 Ω*	*21.58 W*

Table 5-8: Load conditions at different speeds

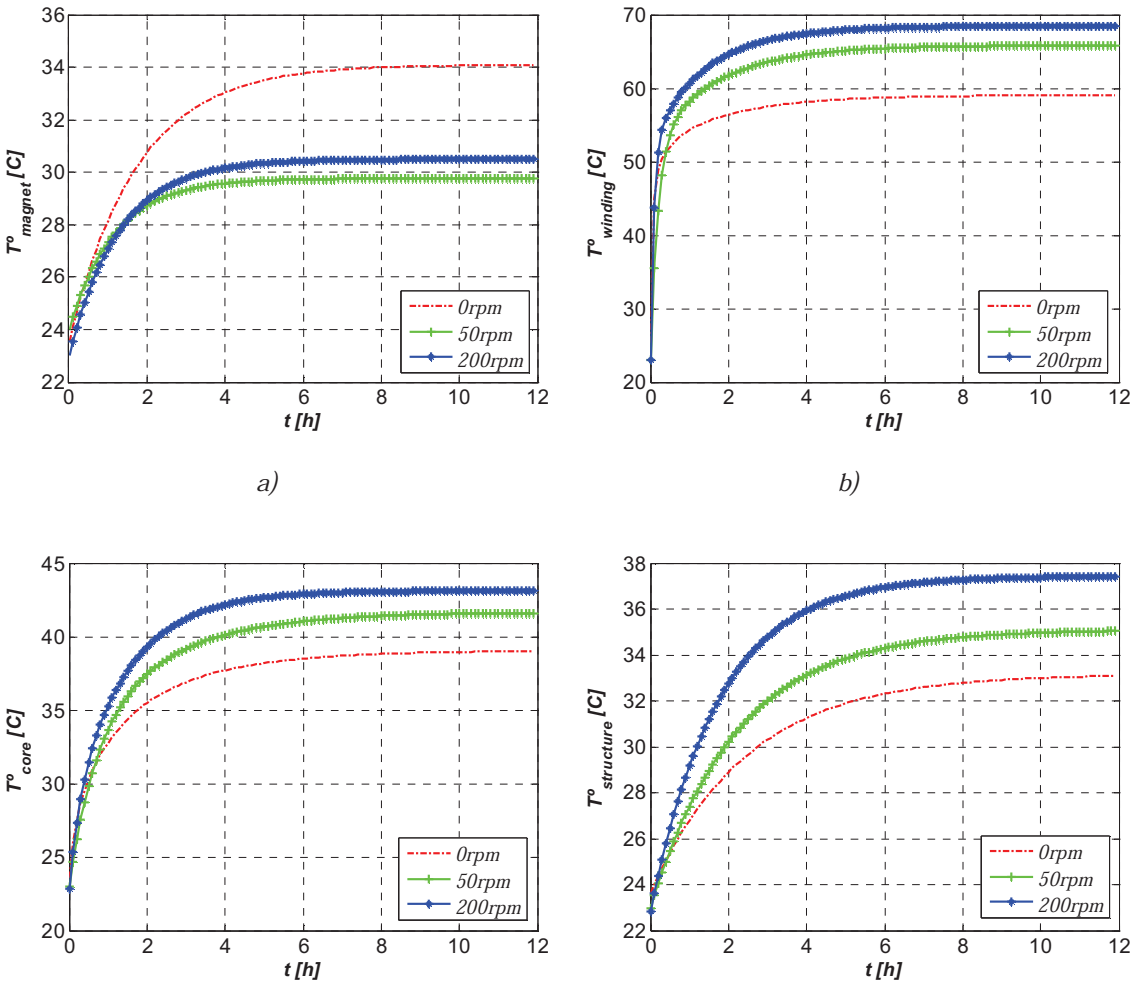

Figure 5-8: Temperature time evolution at different speeds in: a) magnet, b) coil c) stator core and d)Structure

Speed [Ω_m]	*0 rpm*	*50 rpm*	*200 rpm*
T_{magnet} [ºC]	37.17	29.75	30.49
$T_{winding}$ [ºC]	59.58	65.81	68.54
T_{stator_core} [ºC]	39.48	41.66	43.12
$T_{structure}$ [ºC]	33.16	35.09	37.43

Table 5-9: Steady state temperatures (ºC) at different currents

5.3.2.3 Tests at different speeds

The aim of these tests at different speed is to see if the rotor acts as a ventilator. As the iron losses are negligible (about *1.5 W* at *250 rpm*), and the load state of the machine is controlled in current, the conditions are practically the same in the three tests that were carried out. The speeds are *0 rpm*, *50 rpm*, and *200 rpm* while the current was *1.05* amps in all three tests.

Table 5-9 shows the steady state temperatures in the magnet, winding, stator core, and structure. Figure 5-8 shows the evolution of the same temperatures. The most remarkable results showed that the rotor cools as it moved. This in turn caused the temperature to rise in the stator. In this particular case, the value of rotational speed had little effect since the temperatures were very similar at *50 rpm* and *200 rpm*. In a machine with large eddy losses that would not be the case.

5.3.3 Conclusions about the Thermal Behavior of Axial Machines

A general conclusion for all axial machines is not possible for the tests performed here. However, the information collected may be valid for a conclusion about machines with the topology that was the tested, that is, single-side machines.

The first impression is that the rotation of the rotor has a cooling effect. However, when there is a casing, the temperature of the stator and rotor are equal. In all studied cases, the thermal jump between the winding and the rotor was considerable. This seems to be caused by the easy evacuation of heat by the end winding and the difficulty of heat flow from the coils to the stator core, as impregnation does not occur. A good heat flow through the structure was also noticed.

The results showed that a good bond between the machine and the mounting structure acts as a heat sink. On the other hand, as far as possible if the application allows, leaving the rotor open to the air could also help in maintaining cooler temperatures.

5.4 Validation of the Thermal Model

In this section a brief validation of the thermal model above presented is carried out. The machine that has been used for it, is the one tested at *200 rpm* speed in 5.3.2.3.

The performed test was six hour long so the temperature from this time on is predicted using functions created with minimum square methods. As it is shown in Figure 5-9 the results obtained experimentally and by simulation are quite accurate. The evolution of the temperature is very similar and as listed in Table 5-10 the final temperature error is less than *1 ºC* between both results.

It has to be mentioned that the thermal resistances and capacitances are calculated starting from the geometrical parameters of the machine. However as the model is simplified to the limit only a resistance and capacitance is used to model each part of the machine. This is actually a quite complicated to accomplish so, the resistances and capacitances values are then adjusted to match the results obtained experimentally.

	Experiment	***Simulation***	***Error***
T_{magnet}	*30.49 ºC*	*30.61 ºC*	*0.12 ºC*
$T_{winding}$	*68.54 ºC*	*67.88 ºC*	*0.66 ºC*
T_{stator_core}	*43.12 ºC*	*43.27 ºC*	*0.15 ºC*
$T_{structure}$	*37.43 ºC*	*37.21 ºC*	*0.22 ºC*

Table 5-10: Final temperatures in the open circuit test

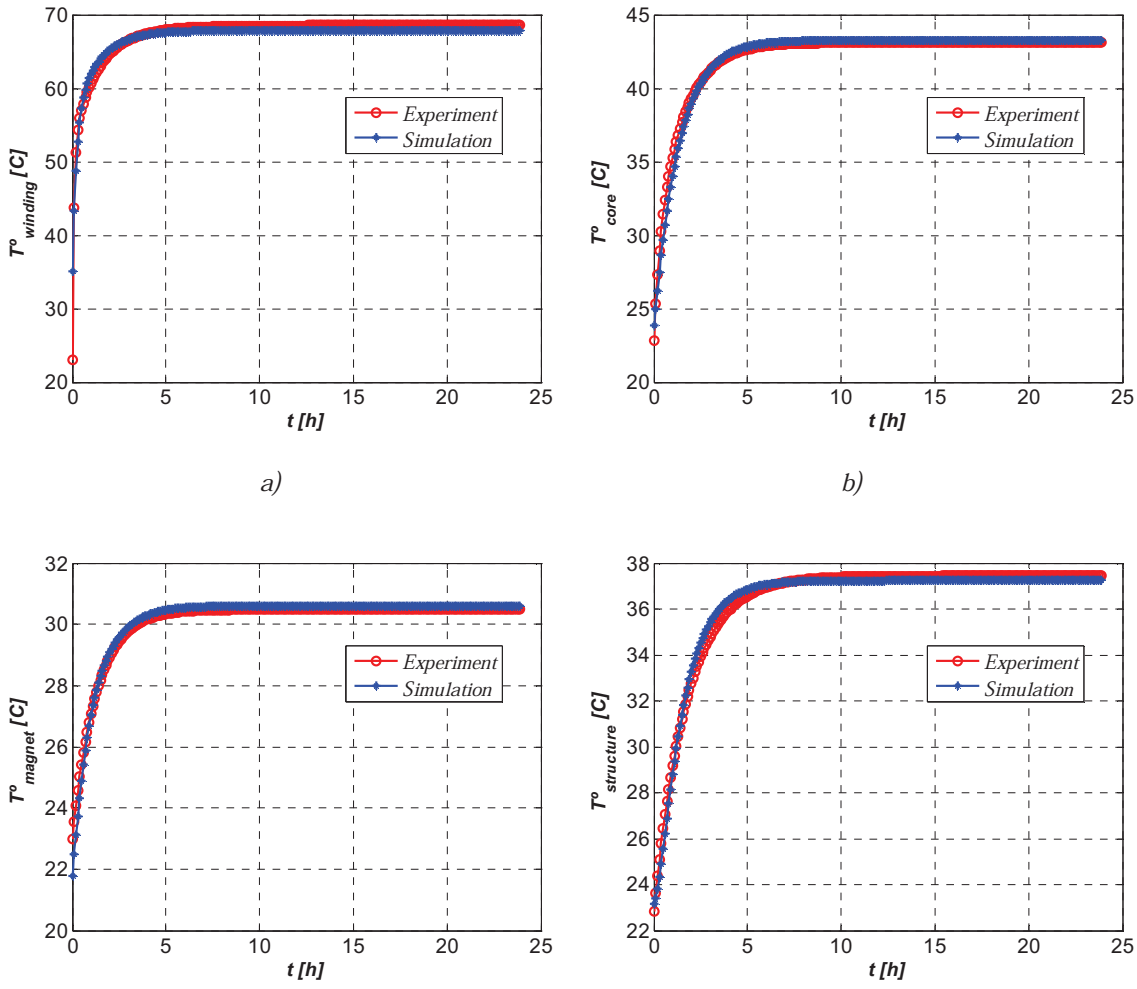

Figure 5-9: Temperature in: a) magnet, b) coil c) stator core and d) structure

Chapter 6.

DESIGN OF AN AXIAL FLUX MACHINE FOR AN ELEVATION APPLICATION

This chapter explains in detail the steps that are followed for the design and fabrication of a machine for an elevation application.

First, the application specifications are given in the form of features and geometric constraints. These define the specifications of the machine design.

The design process consists of several steps. First, the materials are selected. The topology is then selected. Next, the configuration is defined, in which the number of stator and poles as well as the characteristics of the magnets are selected. Finally, the sizing is performed with analytical tools.

The design obtained analytically is then checked by FEM. An optimization of the geometry may be also performed in this stage.

A real prototype is manufactured, the results of which are compared with the results from the previously proposed analytical and numerical tools. Finally, the prototype is thermally analyzed.

6.1 Specifications of the Design

The first step is to define the requirements of the elevation installation so that the characteristics of a machine that fulfills those requirements can be obtained. In this particular case, the characteristics of the elevation system where the machine is embedded are summarized in Table 6-1. Once these specifications are defined, the requirements of the machine are given in terms of torque and speed. Moreover, the limitations of the inverter are taken into account. These limitations are the maximum output current and voltage. The available inverter is limited to *230 V* phase voltage and *20 A* current.

The specifications of the target machine can be obtained by combining the requirements of the application and the limitations of the inverter. The rotating speed is defined by the vertical speed of the elevator cabin, the diameter of the pulley, and the configuration of the suspension. Both nominal and the maximum torque must fulfill the requirements of the installation and take into account the limitation of the maximum output current and voltage of the inverter. The electromagnetic characteristics of the machine are summarized in Table 6-2.

Parameter	***Nomenclature***	***Value***
Configuration		*Direct drive 2:1 suspension*
Diameter of Pulley	D_p	*160 mm*
Maximum Vertical Speed	v_{max}	*1 m/s*
Jerk	*Jerk*	*2 m/s^3*
Acceleration Time	t_a	*2.85 s*
Maximum Acceleration	a_{max}	*0.7 m/s^2*
Number of Passengers		*6*
Maximum Load	Q_{max}	*450 Kg*
Cabin Tare	M_{cb}	*1000 Kg*
Counterweight	M_{cp}	*1500 Kg*
Efficiency of the Installation	η	*83.3 %*
Torque at maximum load	T_r	*131 Nm*
Acceleration torque	T_{max}	*231 Nm (176%)*
RMS torque	T_{RMS}	*102 Nm (78%)*
Inertia of the system	J_{max}	*7.1 $K_g \cdot m^2$*

Table 6-1: Requirements of the elevation system

Parameter	*Nomenclature*	*Value*
Nominal Speed	Ω_m	*20.5rad/s (239.25 rpm)*
Nominal Torque	T_{nom}	*131 Nm (100%)*
Thermal Torque	T_{rms}	*102 Nm (78%)*
Maximum Torque		*231 Nm (176%)*
Torque Ripple	ΔT	$\leq \pm 3\%$
Supply Phase Voltage	V_s	$\leq 230\ V$
Number of Phases	m	*3*
Efficiency	η	$\geq 85\%$
Supply Current	I_s	$\leq 20\ A$
Power Factor	$Cos\phi$	≥ 0.80

Table 6-2: Characteristics of the target machine

6.2 Materials of the Machine

When selecting the material to be used in the fabrication of the machine, there is a tradeoff between performance and the cost. However, in this case the design is made using available materials.

For example, the rotors available from a previous prototype are exploited. These rotors have eight pairs of poles and with dimensions of *400 mm* outer diameter and *216 mm* inner diameter. The magnets placed in them are of degree *NEO33H*, with a height h_m of *4 mm* and an angle β_m of *18.75°* (Figure 6-1-b). The magnets are fabricated by *Calamit*. These rare earth magnets are comprised of neodymium, cadmium, and boron (*NeCdB*). The residual field is *1.14 T* and the coercivity is *812 kA/m*. The maximum working temperature of these magnets is around *120 °C*. A *BH* characteristic curve of *NEO33H* is shown in Figure 6-1-a.

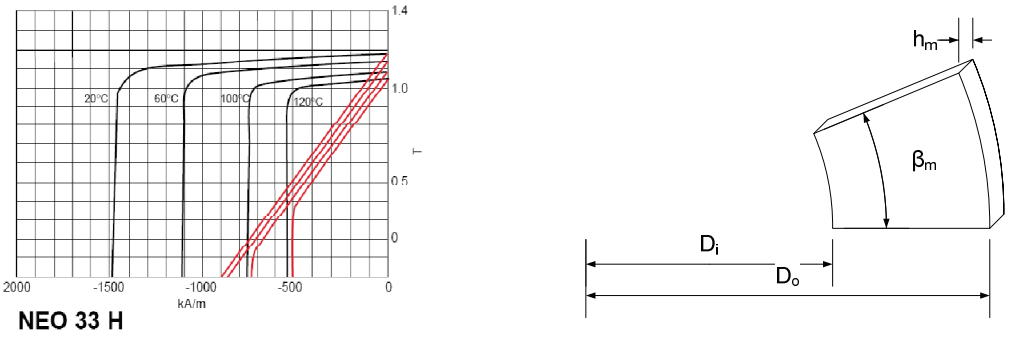

a) *b)*

Figure 6-1: a) characteristic BH curves of the NEO 33 H by Calamit and b) dimensions of the magnets

The back iron in the rotor was manufactured with *409 NI Stainless Steel* by *AK steels*. The typical composition of this material is summarized in Table 6-4. The low carbon stainless steel is the best option to limit eddy current losses and maintain good magnetic properties when the solid core is built.

M400-50A electrical sheets were used to build the ferromagnetic core of the stator core. The main reasons are provider availability and the availability of this material in the *FLUX* database, which allows for performing simulations verified by experimental tests. According to the European Standard *EN 10106*, *M400-50A* electrical sheets must meet the magnetic properties summarized Table 6-3.

Grade	***Width***	***Specific losses***		***Magnetic polarization***			***Density***
	mm	*J = 1,5T W/kg*	*1,0 T W/kg*	*H=2500 T*	*5000 T*	*10000 T*	*kg/dm³*
M400-50A	*0.50*	*4.0*	*1.7*	*1.53*	*1.63*	*1.73*	*7.70*

Table 6-3: Magnetic properties of M400-50A electrical sheets by Cogent

Component	*%*	***Component***	*%*
Carbon	*0.02*	*Chromo*	*11.00*
Manganese	*0.70*	*Nickel*	*0.85*
Phosphor	*0.020*	*Titanium*	*0.20*
Sulphur	*0.004*	*Nitrogen*	*0.015*
Silicon	*0.35*	*Iron*	*Balance*

Table 6-4: Typical composition of 409 NI Stainless Steel

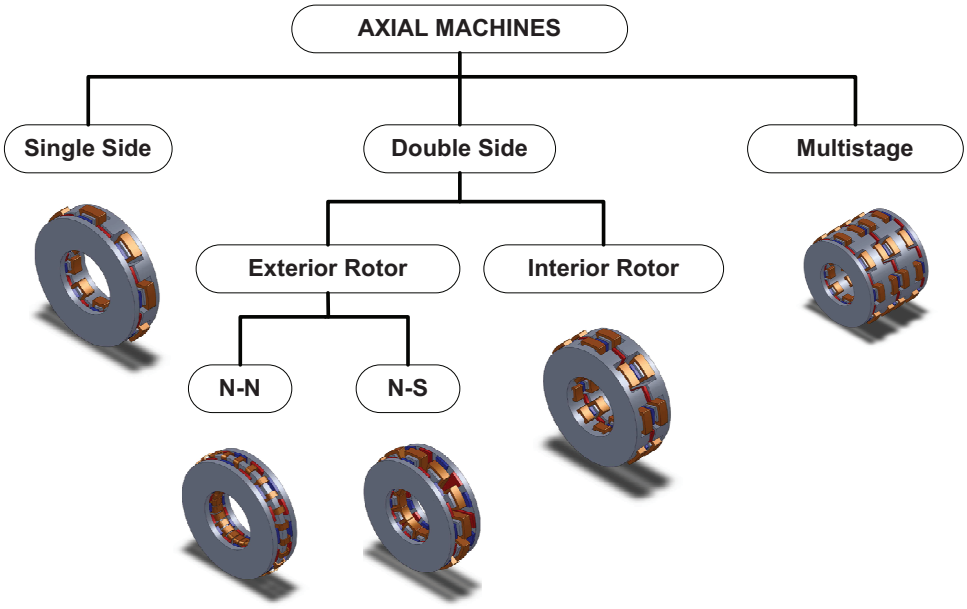

Figure 6-2: Axial machines topologies

6.3 Analytical Sizing

In the chapter of state of art in axial flux machines an analysis of the topologies that provide axial flux machines was made. In any case, Figure 6-2 shows a clear and concise outline of the possible topologies. Perhaps a further analysis of the advantages and disadvantages offered by each topology to select the most appropriate one according to the elevation application should be done. However, in this case, a single-side machine is selected because it is the simplest to manufacture.

The number of pole pairs and the rotational speed of the machine impose the frequency of the power source:

$$f_e = \frac{p\Omega_m}{2\pi} \qquad (6\text{-}1)$$

As the rotational speed is $\Omega_m = 25.054\ rad/s$ and the number of pole pairs is $p = 8$ (delimited by the available rotor), the electrical frequency is $f_e = 30.9\ Hz$. To select the number of slots the winding factors, resistance of the copper, torque ripple, and winding configuration were compared, which is shown in Table 6-5. The number of turns per phase refers to the machine with *48* slots. It shows how many turns per phase are needed in each setting to give the same torque. The torque ripple does not include the cogging torque or skew effects, although the shown values are sufficient for a first comparison.

All machines except the *48* slots machine are concentrated winding, making it easier to place the coils. It is noteworthy that in axial machines with distributed windings, the end windings can become considerably large compared to the effective length. This phenomenon should be analyzed further for different diameters and machine configurations, but it does seem that concentrate winding may be a better choice for axial flux machines.

When choosing the configuration, the winding factor should be close to unity, so there is better utilization of the energy of the magnet. Furthermore, the lower the winding factor, the greater will be the number of turns per phase in order to compensate the wastage of the magnet energy. This will increase the electrical charge of the machine and the space for the conductors or, alternatively, increase the current density through them. The *18* slot machine has the highest winding factor of the concentrated winding configurations. Furthermore, it offers a low torque ripple and the smallest copper resistance. Hence eight pole pairs and an *18* slot machine is chosen.

Q	q	ξ_1	N_{ph}[p.u]	T_{pp}[%]	R_{cu}[p.u.]
9	3/16	0.328	3.13	7.9	3.7
12	1/4	0.866	1.17	11.9	1.22
15	5/16	0.9375	1.08	1.04	1.04
18	3/8	0.945	1.08	1.9	0.969
21	7/16	0.8897	1.14	0.6	0.983
24	1/2	0.866	1.17	11.9	0.975
27	9/16	0.732	1.32	20.3	1.06
30	5/8	0.71094	1.41	1.5	1.11
48	1	1	1	11.9	1

Table 6-5: Comparison of different configurations

Once the topology and configuration are defined, the sizing is performed. The sizing of the machine is divided into two parts; different machines with different characteristics are analyzed to check which one fits the available rotor before the final sizing is done.

Several machines are analyzed for different air-gap distances. Some parameters are predefined: the nominal torque of *131 Nm*, the value of the supply current of *6.62 A* and the current density in conductors *J* is also limited to about *6.5 A/mm*^{2}. This last parameter is chosen to avoid thermal problems. Table 6-6 summarizes the parameters obtained by the analytical tools. A sweep for different values of the air gap is performed so the geometrical values and electrical variables as resistance and efficiency can be compared. The electrical load *A* must be about *25000 A/m* to meet the geometry rotor. Analyzing the three options precipitated the choice of the *2 mm* air gap as having the less resistance and better efficiency (magnetic losses are not covered). In addition, the voltage at the machine terminals is smaller, leaving more margin for the supply voltage.

g [mm]	D_i [mm]	D_o[mm]	L_t [mm]	V_t [dm^3]	N_{ph}	A [A/m]	R_{cu} [Ω]	η
2	212.1	400.29	43.7	6.25	420	25000	2.79	0.9
2	174.4	329	50.2	4.85	624	45000	3.41	0.88
2.5	218.2	411	42.4	6.4	432	25000	2.96	0.89
2.5	179.38	338.4	48.8	5	642	45000	3.62	0.87
3	223.9	422.5	41.5	6.6	444	25000	3.13	0.89
3	187.3	346.9	47.8	5.1	672	45000	3.87	0.869

Table 6-6: Comparison parameters for different air gaps and electric loads

The next step is to perform the final sizing. It should be mentioned that during the analytical design process, an attenuation coefficient of *0.95* was included in the equations with the intention of taking into account the attenuation caused by saturation of the materials. As mentioned, a previously build rotor is exploited so that the geometry and parameters are adjusted to match the characteristics of this rotor. The geometrical characteristics of the designed machine are shown in Table 6-7, and the electromagnetic characteristics are listed in Table 6-8. The torque is somewhat higher than that in the requirements—*135.5 Nm* instead of *131 Nm.* It is quite interesting to have a margin as the torque may decrease in the real case because of local saturations or manufacturing tolerances.

Parameter	***Nomenclature***	***Value***
Shape factor	k_r	*0.54*
Outer diameter	D_o	*400 mm*
Inner diameter	D_i	*216 mm*
Total diameter	D_t	*427 mm*
Total length	L_t	*44 mm*
Total volume	V_t	*6.3 dm*^{3}
Stator yoke height	h_y	*11 mm*
Tooth-tip height	h_o	*3 mm*
Slot opening	b_0	*3.4 mm*
Stator teeth height	h_s	*13.7 mm*
Slot width	w_s	*27 mm*
Rotor back height	h_r	*13.26 mm*

Table 6-7: Dimensions of the designed machine

Parameter	***Nomenclature***	***Value***
Number of turns per phase	*Nph*	*438*
Linear load	*A*	*25638 A/m*
Current density	*J*	*6.5 A/mm*^{2}
Current	*I*	*6.62 A*
Torque	*Tem*	*135.47 Nm*
Ripple Torque	*Tpp*	*6.07 Nm (4.5%)*
Induced Voltage	*EMF*	*171.2 V*
Inductance	*Ls*	*50.4 mH*
Resistance	*Rcu*	*2.97*

Table 6-8: Dimensions of the designed machine

6.4 Analytical Comparison of Axial and Radial Machines

This work is not intended to perform a deep comparison between axial and radial machines, but to obtain an objective comparison for a certain case. An analytical comparison between the volumes, lengths, and diameters of axial and radial machines is presented to ensure the fulfillment of the requirements of the application.

Different analyses are carried out to compare the resulting geometries of both axial and radial machines for application to an elevation with defined characteristics. It should be noted that the values of the air-gap length ($g = 2\ mm$) and magnet height ($h_m = 4\ mm$) are equal in both cases as well as the magnet grade. The linear load and the current are also equal. Hence, the variables that are calculated are the geometrics and the number of turns per phase.

A study of the evolution of the volumes is first done with respect to electric load (defined as the volume delimited by the axial length and the diameter, taking into account the end-windings), as shown in Figure 6-3-a. It can be seen that the axial machine is smaller than the radial at all linear loads. The radial machine has a disc shape only from *45000 A/m* onward, as shown in Figure 6-3-b, whereas the axial machine always maintains a disc shape.

A specific analysis of two different electric loads is then carried out. This analysis tries to show the dimensions of the machines at minimum volume for *25000 A/m* and *50000 A/m* electrical loads. The dimensions of the machines at both electric loads are listed in Table 6-9. At *25000 A/m* the axial machine is noticeably smaller than the radial machine. The volume of the axial machine is 75% of the volume of the radial machine. At *50000 A/m* the axial machine is still smaller than the radial machine, but now the volume of the axial machine is 76% of the volume of the radial machine. It should be added that even the volume of magnet and copper is lower in the axial machine. This demonstrates that at least at certain conditions, the axial machine could be smaller than the radial machine.

However, in this case because of the use of an available rotor, the optimal design was not possible, so the design was made to fit the rotor. This makes the size of designed machine bigger than the optimal size with a volume of *6.3* dm^3, which is still less than the optimal volume of the radial machine.

It should be noted that making a categorical statement about the advantage of axial machine could be risky. However, it can be said that under free geometry conditions, the axial machine might be smaller than the radial machine.

Parameter	Axial	Radial	Axial	Radial
Electric load	25000 A/m		50000 A/m	
Minimum Volume	6 dm^3	7.9 dm^3	4.4 dm^3	5.8 dm^3
Diameter at Minimum Volume	0.4197 m	0.1726 m	0.3331 m	0.1994 m
Length at Minimum Volume	0.0432 m	0.3387 m	0.0517 m	0.1867 m
Magnet Volume	140.76 cm^3	197.93 cm^3	90.23 cm^3	103.62 cm^3
Copper Volume	2.05 dm^3	2.63 dm^3	2.56 dm^3	2.94 dm^3

Table 6-9: Dimension of the machines with A = 25000 A/m and A = 50000 A/m

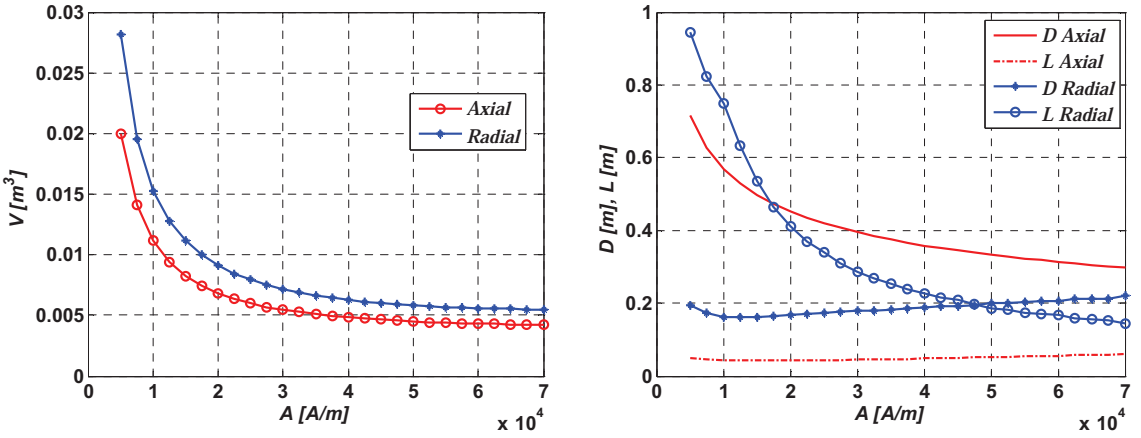

a) b)

Figure 6-3: Evolution of the geometric parameters versus the electric load a) volume and b) diameter and length

Parameter	Nomenclature	Nominal working point	Maximum working point.
Torque	T_{em}	135.51 Nm	229.7 Nm
Torque ripple	ΔT	5.5 Nm (≤4.3%)	13.24 Nm (≤5.7%)
Inductance	L_s	52.1 mH	49.8 mH
Supply power	Ps	3663 W	6828 W
Copper losses	P_{cu}	381 W	1166 W
Magnetic losses	P_{loss}	68 W	211 W
Efficiency	η	87.74 %	79.8 %
Current	I_s	6.62 A	11.585 A
Supply voltage	Vs	195.11 V	230.48 V
Power factor	$Cos\Phi$	0.945	0.852

Table 6-10: Electromagnetic values of the machine at nominal and maximum working point (FEM)

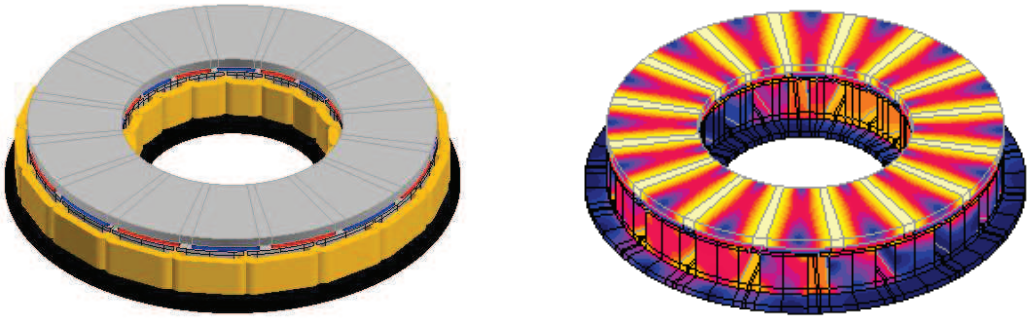

a) b)

Figure 6-4: FEM simulation: a) geometry and b) flux density map

6.5 Validation of the Design in FEM

After the analytical sizing, the validity of the machine is checked by *FEM*. If the *FEM* results show that the design does not meet the requirements, the machine can be resized in *FEM*. Furthermore, it is possible to polish the geometric details as the slot opening and adjust the dimensions to the minimum in the *FEM* environment. Figure 6-4-a shows the geometry of the *3D* model, and Figure 6-4-b shows the flux density map.

The results obtained in *FEM* simulations are summarized in Table 6-10. These simulations were performed at the nominal and the maximal working points to ensure the validity of the design in both cases. The torque at nominal working point was almost the same as that obtained analytically, which validates the design. The torque is still greater than the required one, giving some margin for fabrication tolerances. The theoretical value of the maximum torque is *237.5 Nm (181%)*, but because of local saturations, this value cannot be reached in *FEM* simulations. The simulation gives an overload limit of 175.5%. In this case a new sizing of the machine is not needed as the design fulfils the requeriments.

Thus, on one hand the realized design meets the requirements, and on the other hand the design methodology is validated.

6.6 Experimental Test Results

When the prototype was built, several tests were carried out to compare the real results with those obtained during the design by *FEM* tools. First, several electromagnetic tests were conducted and then the thermal analysis was performed. It should be mentioned that due to failures during the construction of the machine, a steel piece was included in the stator yoke.

This made the losses in this part of the machine very large; therefore, new *FEM* simulations were performed to assume these losses. This failure made the efficiency decrease, but it induced a warm up of the machine. The magnitude of the losses and its influence on both electromagnetic and thermal variables was analyzed throughout the tests.

6.6.1 Test Bench Description

The test bench actual assembly is shown in Figure 6-5-a, and Figure 6-5-b shows the block diagram of the test bench. The load machine is a *PM* radial machine with rated *18.8 kW, 383 rpm* and *468 Nm*. This machine is controlled with a *Control Technique Unidrive SP3402 18.4 kW* inverter. A similar device is used to control the prototype; in this case, it is the *SP2402 7.5kW* inverter. The torque was measured with a *500 Nm* torque sensor by *Lorenz Messtechnik*, with an accuracy of *0.5 Nm*. A *Yokogawa PZ400* power analyzer was used to measure the power in the prototype. In addition, a *National Instruments PXI* platform was used for the temperature acquisition in *Labview*.

6.6.2 Electromagnetic Tests

The electromagnetic tests are divided into two sections. The open circuit test is carried out. In this test, the machine is rotated at different speeds to measure the induced back electromotive force (*EMF*). The second test is the test under load. In this test, the machine is supplied with different currents and works as a machine at the rated speed at which the produced torque is measured.

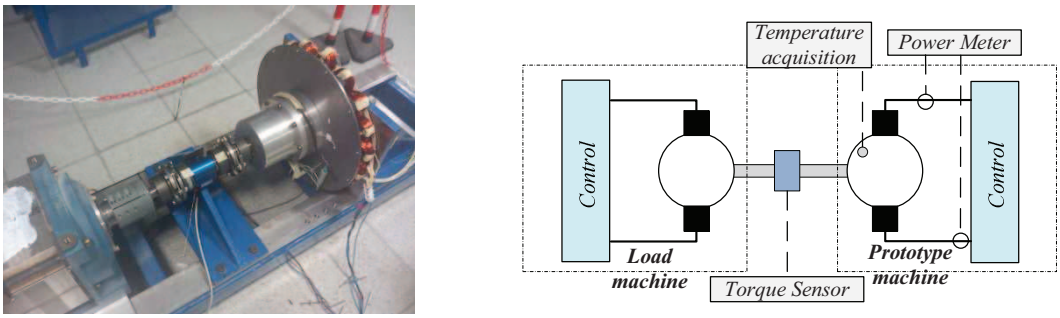

a) b)

Figure 6-5: Test bench: a) actual assembly and b) block diagram

6.6.2.1 Open Circuit Test

A force in opposition to the motion is measured in the open circuit test. This opposition torque is caused by eddy current losses in the steel plate in the stator yoke as the friction and bearing losses are negligible. The opposition torque in both the *FEM* simulations and the experimental tests at different speeds are shown in Figure 6-6-a. This torque is a result of the magnetic losses shown in Figure 6-6-b. Table 6-11 shows numerical information about the torque and magnetic losses shown in the above figures. The table shows a small difference between the *FEM* results and the experimental results. The purpose of this analysis is to quantify the heavy losses that occur because of the steel in the stator. Because these losses are unacceptable in a commercial machine, the separation of losses in *FEM* is done to quantify the losses in the steel plate. As shown in Table 6-12, at rated speed the total magnetic losses are *255 W*, including *1.75 W* and *8.3 W,* which were caused by eddy currents in the magnets and rotor core, respectively, and *26 W* in the stator core. Hence, the remaining *218.95 W* occurred in the steel piece in the stator yoke. Although these values were obtained in *FEM* simulations, they indicate the influence of this parasitic steel piece. The losses in this piece were 85% of the total losses. Without these losses, the opposition torque was about *1.65 Nm*, which is a much more reasonable value.

Speed	***Experimental***		***FEM***	
	Torque	P_{loss}	***Torque***	P_{loss}
0 rpm	*0 Nm*	*0 W*	*0 Nm*	*0 W*
50 rpm	*-1.505 Nm*	*37.7 W*	*-1.26 Nm*	*31.6 W*
100 rpm	*-3.592 Nm*	*90 W*	*-3.18 Nm*	*79.7 W*
150 rpm	*-5.987 Nm*	*150 W*	*-5.43 Nm*	*136 W*
200 rpm	*-8.781 Nm*	*220 W*	*-7.98 Nm*	*199.9 W*
239.25 rpm	*-10.98 Nm*	*275 W*	*-10.18 Nm*	*255 W*

Table 6-11: Opposition torque and magnetic losses at open circuit

Parameter	***Open circuit***	***Load (7.3 A-130 Nm)***
Total magnetic losses	*255 W (100%)*	*391.9 W (100%)*
Magnetic losses on magnets	*1.75 W (0.6%)*	*50.6 W (12.9%)*
Magnetic losses on rotor core	*8.3 W (3.25%)*	*69.6 W (17.75%)*
Magnetic losses on stator core	*26 W (10.2%)*	*29.8 W (7.6%)*
Magnetic losses on steel piece	*218.95 W (85.8%)*	*261.9 W (66.8%)*

Table 6-12: Separation of magnetic losses at open circuit and rated current obtained by FEM

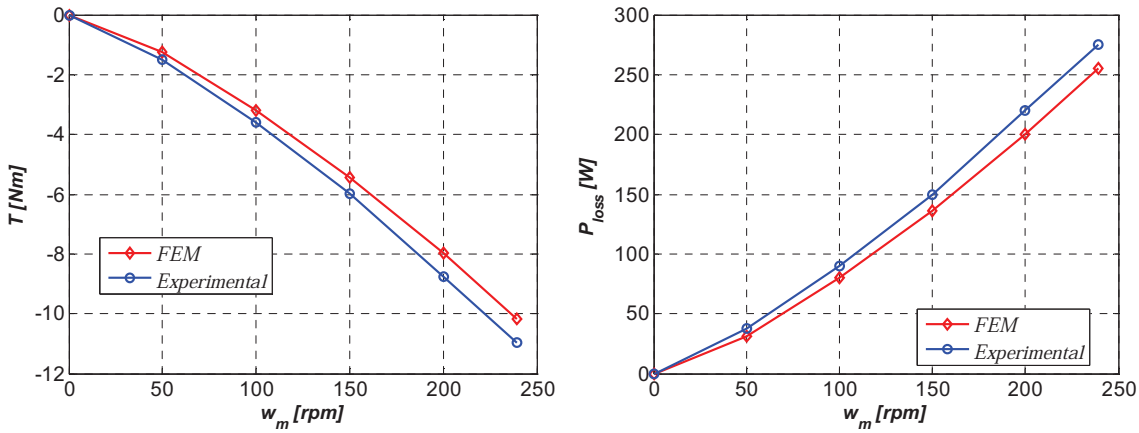

a) *b)*

Figure 6-6: Open circuit a)opposition torque and b) magnetic losses

Figure 6-7-a shows the evolution of the *rms* value of *EMF* with respect to the rotational speed. The speed range was from *0* to the rated speed of *239.25 rpm*. The values of the *EMF* at certain speeds are also listed in Table 6-13. The error was less than 1.2%. Figure 6-7-b shows the temporal evolution of the *EMF* of the results of both the *FEM* and the experiment. Both curves fit well, which demonstrates the validity of the tools.

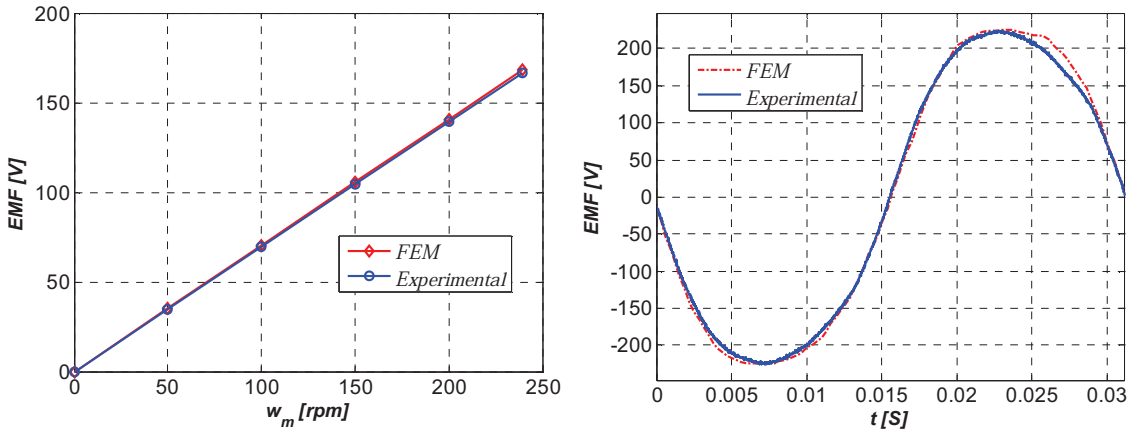

a) *b)*

Figure 6-7: a) EMF vs. speed and b)time evolution of EMF

Speed	Experimental	FEM	Error
0 rpm	0 V	0 V	0
50 rpm	34.8 V	35.2 V	0.4 V (1.14%)
100 rpm	69.6 V	70.4 V	0.8 V (1.13%)
150 rpm	104.4 V	105.6 V	1.2 V (1.14%)
200 rpm	139.2 V	140.8 V	1.6 V (1.14%)
239.25 rpm	166.5 V	168.5 V	2 V (1.19%)

Table 6-13: EMF vs. speed

6.6.2.2 Load Test

It is logical to assume that the opposition torque caused by magnetic losses will cause the electromagnetic torque decrease. To verify this phenomenon at the same time that the operation of the machine is tested, a load test for currents from *0 A* to the maximum allowed by the converter is performed. The maximum output phase voltage of the converter is *223 V,* which results in the maximum *11.05 A* supply current, as shown in Figure 6-8-b.

The opposition torque makes it necessary to feed the machine with a *7.38 A* current to reach *131 Nm* instead of the theoretical *6.62 A*. This involves a supply current that is *111%* of the theoretical value. If the machine is fed with the rated current, the torque is *117.17 Nm*, which means that a decrease of *13.78 Nm* with respect to the theoretical value. This value is similar to the opposition torque in the machine in the open circuit test in which the opposition torque is *10.98 Nm.* However, because the magnetic losses increase with the supply current, the opposition torque also increases. Table 6-14 shows the theoretical and measured torque for different currents. The percentages refer to the rated torque of *131 Nm* so that the torque decrease due to the magnetic losses is noticed. The theoretical value assumes magnetic losses in the stator, rotor, and magnets. However, the comparison gives a reliable picture of the great influence of magnetic losses in the steel piece in the prototype. Analysis of the data in Table 6-12 showed that the losses due to this steel piece in the stator with *7.3 A* current were *261.9 W*, which means *67%* of the total losses of *391 W*.

Table 6-15 shows the performance data of the real machine. Because of the losses in the stator steel piece, the efficiency is really low at small currents and not very good around nominal currents. In a machine without the steel piece, the efficiency might increase substantially, and its tendency would be to decrease with the current. Furthermore, the maximum torque might also improve although the maximum torque needed by the application cannot be reached because of the converter voltage limit. Figure 6-9 compares different

performance parameters obtained in the *FEM* and experimental tests. As the different graphs show, the results of the simulations and the experimental ones fit quite accurately.

Current	*Real*		*Theoretical*	
	Value	*Percentage*	*Value*	*Percentage*
0 A	*-12.5 Nm*	*-9.5%*	*-1.37 Nm*	*-1.04%*
1.097 A	*10.15 Nm*	*7.75%*	*21.7 Nm*	*16.6%*
3.3 A	*53.5 Nm*	*40.8%*	*68.71 Nm*	*49.8%*
4.41 A	*75.45 Nm*	*57.6%*	*87.26 Nm*	*66.6%*
6.62 A	*117.17 Nm*	*89.4%*	*135.1 Nm*	*103%*
7.38 A	*130.8 Nm*	*99.8%*	*146.03 Nm*	*111.5%*
11 A	*194.3 Nm*	*148.3%*	*219.2 Nm*	*167.3%*

Table 6-14: Measured torque and theoretical torque (without iron losses in the stator steel piece)

Speed	T_{em}	P_{loss}	P_s	η	V_s	*Cos (Φ)*
1,097 A	*10,15 Nm*	*282.5 W*	*546.2 W*	*0.465*	*166.89 V*	*0.994*
3.3 A	*53.5 Nm*	*290.3 W*	*1724.3 W*	*0.776*	*175.68 V*	*0.991*
4.41 A	*75.45 Nm*	*294 W*	*2338.9 W*	*0.807*	*180.01 V*	*0.981*
6.62 A	*117.17 Nm*	*359.2 W*	*3601.1 W*	*0.804*	*190.84 V*	*0.960*
7.38 A	*130.8 Nm*	*385 W*	*4056.3 W*	*0.799*	*194.74 V*	*0.9500*
11 A	*194.3 Nm*	*629 W*	*6467.1 W*	*0.751*	*222.95 V*	*0.877*

Table 6-15: Performance of the machine at different supply currents

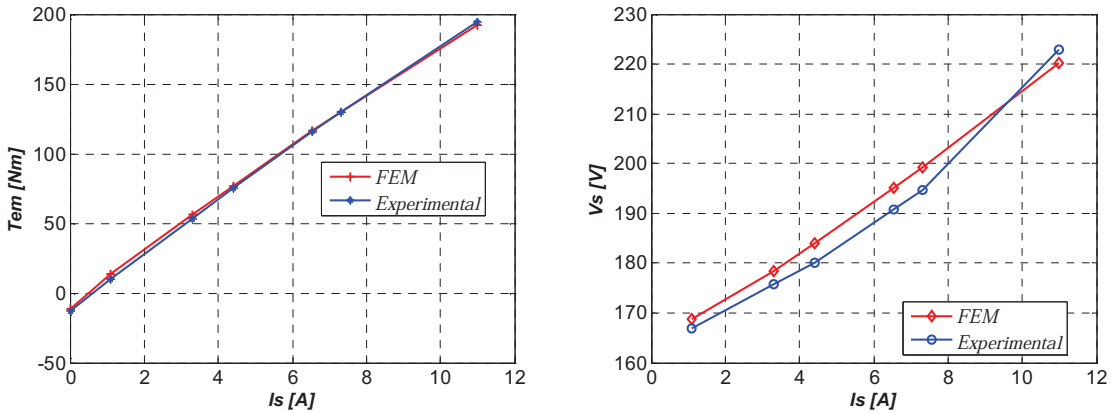

a) *b)*

Figure 6-8: a) electromagnetic torque vs. supply current and b) phase supply voltage vs. supply current

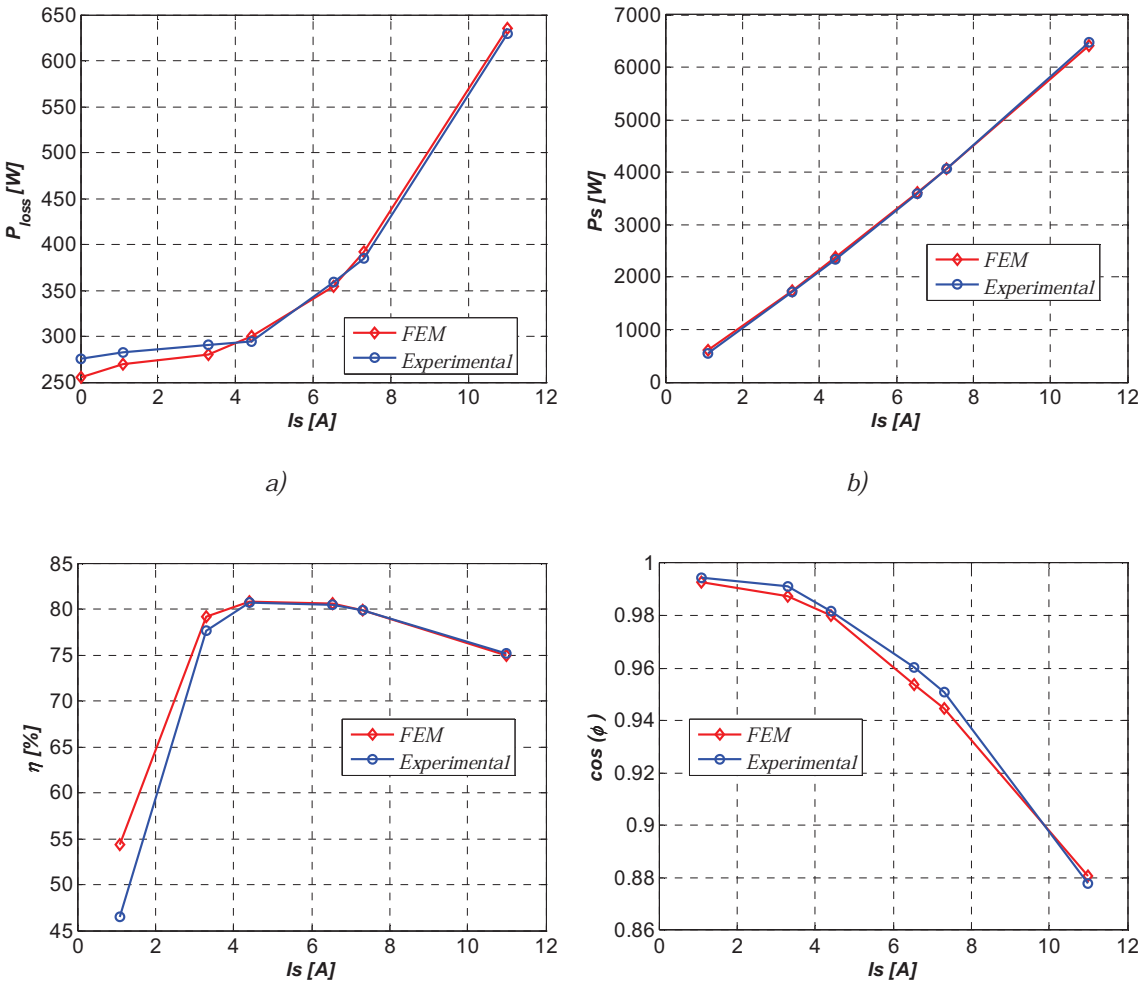

Figure 6-9: a) magnetic losses, b) supply power, c) efficiency and d) cos (Φ)

6.6.2.3 Characteristics of the Prototype Machine

After the experiential tests are performed, it is possible to obtain the parameters of the datasheet of the prototype machine. It should be remembered that unfortunately because of the back steel plate, the machine does not fulfill the application requirements. The datasheet is defined at the required nominal torque (*131 Nm*), which is reached with *7.38 A* instead of *6.62 A*. The most important parameters are listed in Table 6-16. The theoretical values obtained in *FEM* are also listed to show the torque that the machine would reach without the steel plate. As the data show, the machine would exceed the nominal torque. In addition, Figure 6-10 shows a detailed image of the machine while it was mounted.

Parameter	*Nomenclature*	*Experimental*	*Theoretical*
Torque	T_{em}	*130.8 Nm*	*135.1 Nm*
Torque ripple	ΔT	*6 Nm (≤4.6%)*	*7.5 Nm (≤5.5%))*
Inductance	L_s	*44.4 mH*	*50.5 mH*
Supply power	P_s	*4056.3 W*	*3836.3 W*
Copper resistance	R_{cu}	*2.42 (25 ºC)*	*2.42 (25 ºC)*
Efficiency	η	*79.9 %*	*97.4 %*
Current	I_s	*7.38 A*	*6.62 A*
Supply voltage	V_s	*195.11 V*	*193.2 V*
Power factor	*CosΦ*	*0.95*	*0.93*

Table 6-16: Prototype machine datasheet

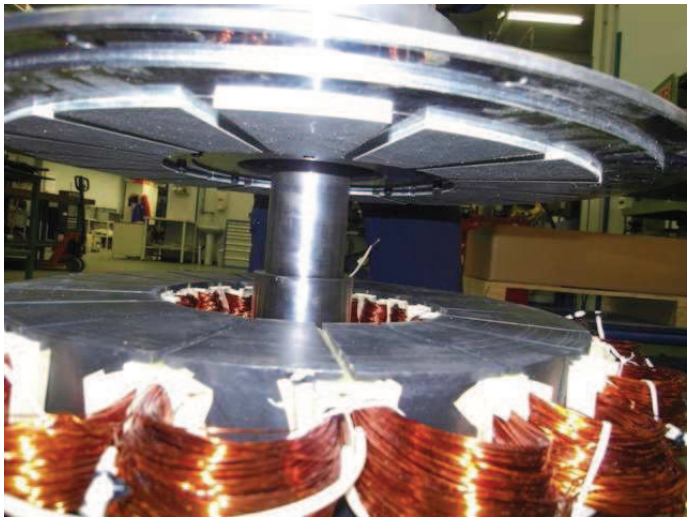

Figure 6-10: Detail of the machine while mounting

6.6.3 Thermal Tests

In addition to the electromagnetic test, thermal tests were also carried out with the prototype machine. Open circuit and load tests were again done. The results obtained during these tests are compared with those obtained by the simulation. This simulation is performed analytically using a thermal equivalent circuit using *Portunus*.

6.6.3.1 Thermal Model of the Test Machine

The thermal model used is a very simplified model, as presented in section 5.2. In this case, the heat sources are due to the copper, the eddy losses in the stator iron piece, the stator magnetic losses, and the losses in the rotor, which are the sum of the losses in the magnets and

the rotor core. To simplify the model further, other losses, such bearing and friction losses, were disregarded. The resulting thermal equivalent circuit is shown in Figure 6-11. The thermal conduction resistances in the air between different bodies of the machine are represented by R_{cu_st}, R_{st_ir}, R_{st_rot} and $R_{ir\_str.}$; the convection resistances are R_{cu_air}, R_{st_air}, R_{ir_air}, R_{str_air} and R_{rot_air}; and the capacitances are C_{cu}, C_{st}, C_{ir}, C_{str} and C_{rot}, where "*cu*" refers to the coil, "*st*" to the stator core, "*rot*" to the rotor "*ir*" to the iron plate in the stator, and "*str*" to the structure.

The values of the conduction and convection thermal resistors as well as the thermal capacitances are shown in Table 6-19. These values were initially approximated from the characteristics of the machine and then adjusted to fit the results obtained in the load test. Then the model is checked with other tests.

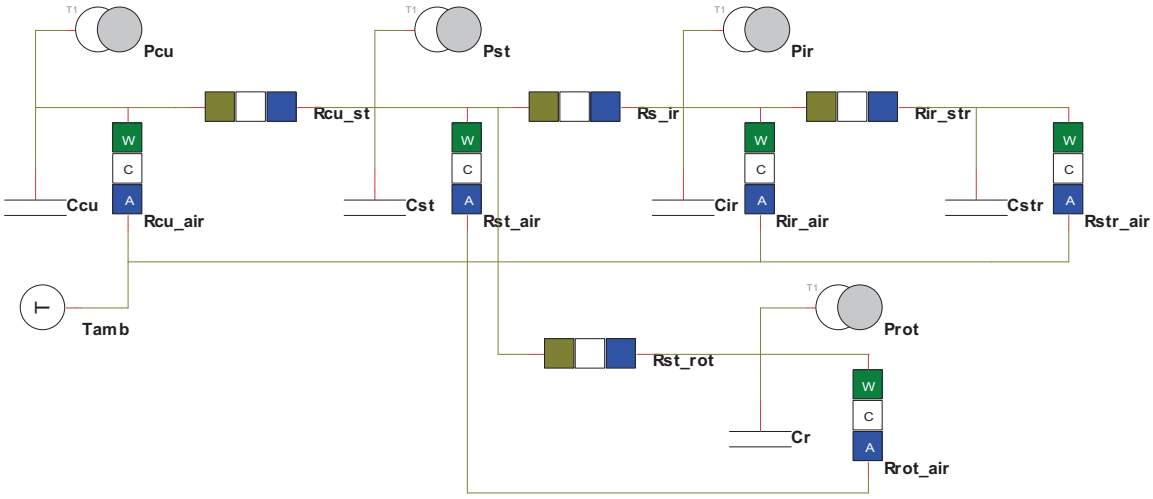

Figure 6-11: Equivalent thermal circuit of the test machine

Conduction		Convection		Capacitance	
R_{cu_st}	0.1904 ºC/W	R_{cu_air}	10.42 ºC/W	C_{cu}	770 Ws/ºC
R_{st_ir}	0.0432 ºC/W	R_{st_air}	14.38 ºC/W	C_{st}	8400 Ws/ºC
R_{st_rot}	0.7776 ºC/W	R_{ir_air}	49.311 ºC/W	C_{ir}	8330 Ws/ºC
R_{ir_str}	0.0204 ºC/W	R_{str_air}	16.4 ºC/W	C_{str}	41620 Ws/ºC
		R_{rot_air}	2.51 ºC/W	C_{rot}	4600 Ws/ºC

Table 6-17: Calculated values of the conduction and convection thermal resistances and thermal capacitances of the test machine

6.6.3.2 Open Circuit Thermal Test

The open circuit test is carried out by moving the machine at a rated speed (*239.25 rpm*). The influence on the temperature of the machine due to eddy losses in the stator iron plate is thus observed. During the six-hour test, the information obtained is treated with least squares functions to generate temperature curves for the desired time. The final temperatures obtained both experimentally and in the simulation are shown in Table 6-18. The errors between the two temperatures are also reflected in the table. The largest error occurred in the stator core temperature, at *4.88 °C*. A considerable error of *2.4 °C* in the magnet temperature is also evident. However, the simulation results shown in Figure 6-12 are considered valid for temporal evolution because the values of the temperature are similar to those obtained experimentally.

It should be noted that the temperature rise was caused by the losses in the back plate of the stator. In a properly fabricated machine rotating at low speed where the friction and bearing losses are negligible, the temperature will stay around ambient temperature. A small rise may occur if the losses in the stator are considerable, but there is never an increase of more than *20 ºC* in the magnet and *30 ºC* in the stator core, as in this case. The theoretical temperatures obtained by the model in the case where the back plate does not exist are listed in the fourth column in Table 6-18. The simulation gave a temperature rise of only about *3.5 ºC* in the worst case, as the ambient temperature is *24 ºC.*

	Experiment	***Simulation***	***Error***	***Theoretical***
T_{magnet}	*43.99 ºC*	*41.59 ºC*	*2.4 ºC*	*27.4 ºC*
$T_{winding}$	*47.66 ºC*	*47.65 ºC*	*0.01 ºC*	*26.9 ºC*
T_{stator_core}	*53.86 ºC*	*48.98 ºC*	*4.88 ºC*	*27.1 ºC*
$T_{structure}$	*45.29 ºC*	*44.52 ºC*	*0.77 ºC*	*26.51 ºC*

Table 6-18: Final temperatures in the open circuit test

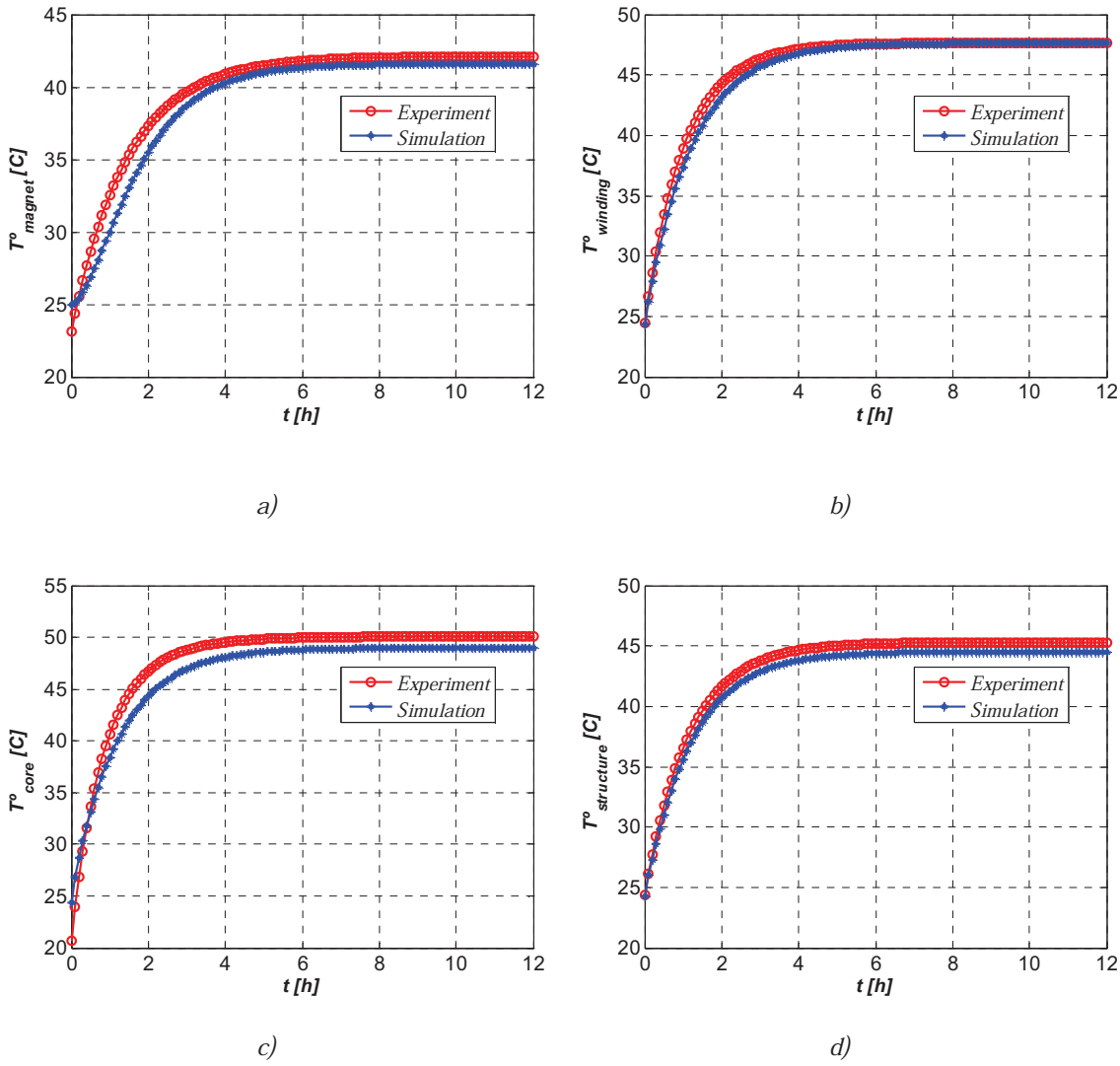

Figure 6-12: Temperature in: a) magnet, b) coil c) stator core and d) structure

6.6.3.3 Load Thermal Test

The load test is carried out over six hours by rotating the machine at a rated speed (*239.25 rpm*) and at 70% of the rated load, that is, *5.2 A,* also taking into account that the rated torque is reached at *7.38 A.* This gave a linear load of *19600 A/m* and a current density of *5.1 A/mm*^{2}. The information was treated with least squares functions to generate temperature curves for the desired time. The final temperatures were obtained both experimentally and in the simulation. The error between the two temperatures is shown in Table 6-19. In this case, the largest error occurred again in the stator core temperature, at *3.15 °C.* However, the temperature of the magnet was almost equal in both methods, with a visible error in the temperature of the copper

at *3.02 °C*. However, these minor errors served to validate the analytical model, as the values of the temperatures were similar in both temporal evolutions shown in Figure 6-13.

Here the negative influence of the losses in the back plate in the temperature of the machine must again be noted. Without this back plate, the model gave the temperatures listed in the fourth column in Table 6-19. As the table shows, the temperature decreased *4 ºC* in the magnets, *15 ºC* in the winding, *21 ºC* in the stator core, and *14 ºC* in the structure, which are significant drops in temperature.

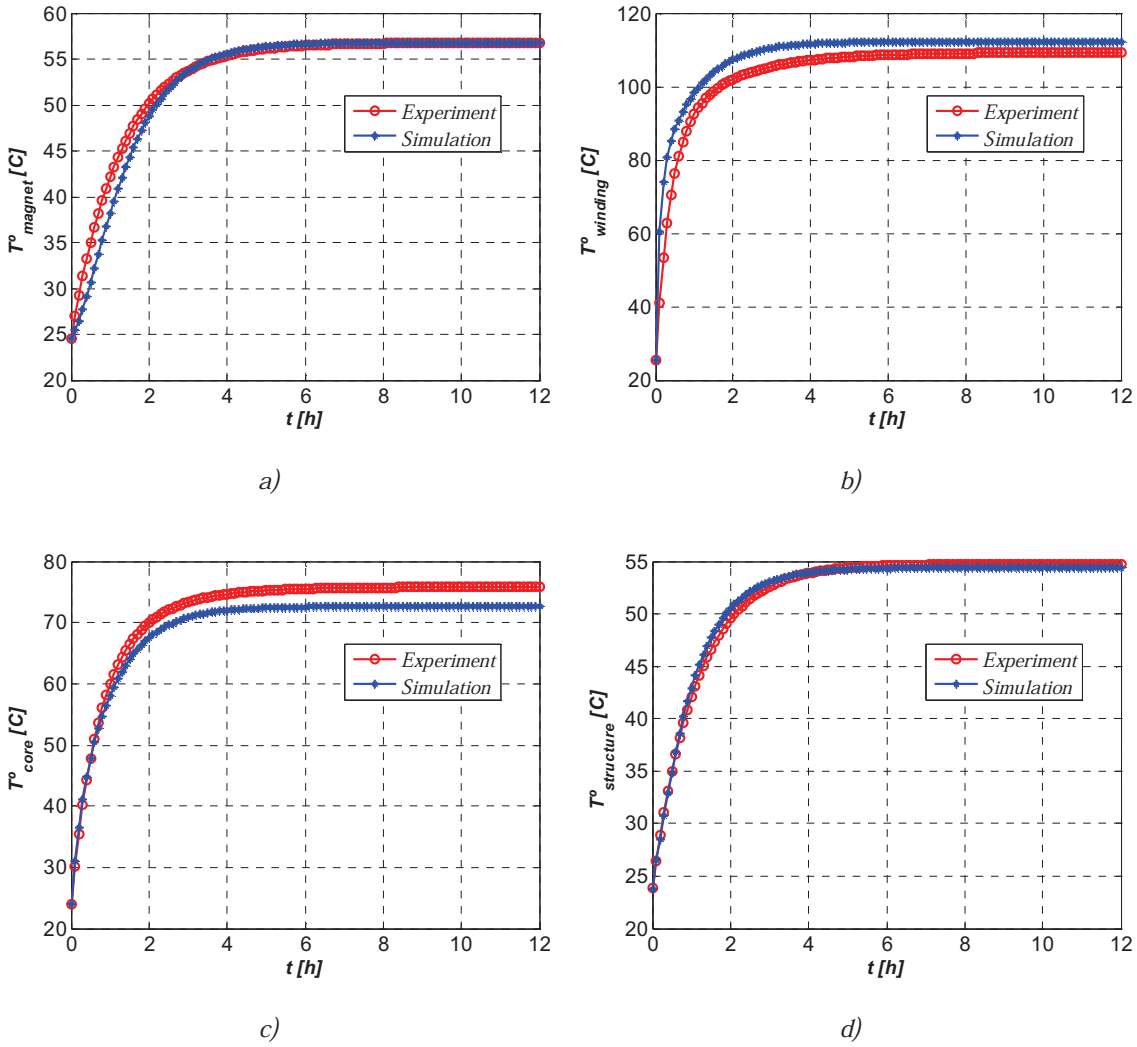

Figure 6-13: Temperature in: a) magnet, b) coil c) stator core and d) structure

	Experiment	Simulation	error	Theoretical
T_{magnet}	56.75 ºC	56.8 ºC	0.05 ºC	52.9 ºC
$T_{winding}$	109.25 ºC	112.27 ºC	3.02 ºC	95.8 ºC
T_{stator_core}	75.81 ºC	72.66 ºC	3.15 ºC	54.7 ºC
$T_{structure}$	54.75 ºC	54.43 ºC	0.32 ºC	40.6 ºC

Table 6-19: Final temperatures at load test

6.7 Conclusions

The main conclusion of this chapter is that the proposed methodology is valid, which is demonstrated by the accuracy shown in the analytical and numerical tools and the experimental results.

On the one hand, the electromagnetic test results of the prototype agreed with the ones obtained in simulation. Furthermore, it was demonstrated that both analytical and numerical tools gave almost the same results.

On the other hand, the prototype could be modeled thermally. Although the model is quite simple, the results are good enough. It has to be remembered that even if the analytic calculation of the parameters of the equivalent thermal circuit gives an approximation of the problem, these parameters have to be adjusted with thermal analyses. The model was checked in two different working conditions (open circuit and load), giving good results, which demonstrates its validity.

The failure occurring during the construction of the stator when the back plate was placed prevented the prototype from meeting the requirements. However, this fault allowed the study of certain phenomena, which otherwise would not have been possible.

Chapter 7.

CONCLUSIONS AND FUTURE RESEARCH

This chapter concludes the thesis document. First, the main conclusions are enumerated. These conclusions are separated into the main blocks that are described in the thesis. Suggestions for future research are then proposed.

7.1 Conclusions

The performed work is divided into three main blocks. First a state of the art in axial machines is performed, second the design tools are developed, and finally the proposed design methodology is applied in a real case study. Next the main conclusions are summarized:

Regarding to the main characteristics of axial flux machines:

- One of the most interesting characteristics of axial machines is their flexibility. They can have a wide range of topologies, which makes the axial machine a solution that can be highly integrated into applications. The axial machine can be adapted to any application, but depending on the specific application, either the axial machine or the radial machine should be selected. The axial machine could be a good option for applications in which disc-shaped machines are required.

- It can be stated that generally axial flux machines can be more compact than radial flux machines.

- Two main ideas must be mentioned regarding the materials and manufacturing techniques for axial machines. The materials are the same as those used in radial machines, but the manufacturing process is quite different. At first glance it seems more complicated and expensive. Further research should be done to simplify the manufacture process of axial machines and to standardize the different process and manufacturing tools.

- The possibilities of configurations that offer the axial machines are also quite interesting. In some of these configurations it is possible to avoid ferromagnetic material decreasing the weight and cost of the machine.

- Non-compensated attraction forces between stator and rotor in single side configurations can be one of the main drawbacks of axial flux machines. Due to this fact the mechanical design seems to be slightly more complicated than in radial flux machines although it has not been studied in this work.

Regarding to the proposed methodology and developed design tools:

- A detailed design methodology has been presented. This methodology makes possible to develop accurate motor designs in very short time consumption. It is possible thanks to the developed advanced design tools and the defined structure for the methodology. In every stage the most suitable tools are used in order to minimize the time consumption. For instance, initial steps in which a lot of iterations are faced, flexible and accurate analytical tools are used. On the other hand, posterior optimization task are developed using very accurate Finite Element simulations.

- The accuracy of the developed tools and the feasibility of the proposed methodology have been validated in a real case, in which an axial motor for elevators has been designed. The results obtained by design tools shown a very good agreement with the experimental results so that the number of prototypes could be reduced achieving this way accurate designs in a very short time consumption.

- Analytical tools are shown to be feasible and accurate. The accuracy of these tools has been checked, obtaining errors smaller than 5% in comparison with the results obtained by numerical tools. Furthermore, it can be stated that results obtained analytically give a good approximation of the final machine, which makes them very useful in the design process. These analytical tools are essential in the initial steps of the design. A broad analysis of different machine configurations and characteristics should be done so that the best option could be chosen to ensure credibility. However, this selection process could take too much in case it was performed by *FEM*.

- Regarding the numerical tools, it must emphasized that a new method was developed whereby *FEM-2D* can be used to model any kind of axial machine, obtaining accurate results and decreasing notably the simulation times with respect to *FEM-3D*. With the proposed new tool, the simulation time is about half an hour to achieve accuracy above 95, while in *FEM-3D* it takes about six hours.

- A very rough thermal analysis has been also developed. This analysis obtained an interesting, general observation about thermal behavior in axial machines.

Furthermore, a very simple thermal model based on equivalent lumped parameter circuit has been developed and then tested in a prototype, obtaining good results.

According to the designed motor for elevators:

- Finally, even if the prototype does not fulfill the requirements of the application, it is due mostly to the steel plate in the stator. However, the design methodology is validated as the analytical, numerical, and real results are in agreement. Furthermore, the design process is demonstrated to be agile, adaptable, and easy to follow

- It has been demonstrated that the designed axial machine is smaller than a radial machine with the same characteristics. The volume may be 25% smaller and even the quantity of magnet is 29% lower.

- It must be also marked the great temperature difference between the magnets and coils in the prototype. In the experiments this difference is of *53 ºC*. This difference is quite high although it must be mentioned the lack of impregnation in the stator core-coils. However this temperature difference does not usually happen in radial machines.

7.2 Future Prospects

Future contributions could explore several topics among which the following would be the most important:

- An outstanding topic could be to develop analytical tools for calculating the magnetic losses. One option could be to develop precise tools, but it also may be possible to obtain tools that give an approximation of the losses. The findings could be used to avoid using *FEM* or at least to have a realistic idea about the losses before using it.

- Much work could be done on the topic of the thermal modeling of axial flux machines. An interesting would be to use a simplified thermal model (as the presented in his thesis) with parameters that could be calculated previously in function of the geometry of the machine.

- From the point of view of fabrication, it could be interesting to carry out a deeper research to define an economical and straightforward fabrication process for axial flux machines.

- Finally, radial and axial flux machines could be compared. The advantages and drawbacks of each other may be defined more clearly. This comparison would not be an easy task as the comparison may depend on many different variables. However, it could be interesting to define guidelines for choosing the best option for each application.

LIST OF SYMBOLS

LIST OF FIGURES

LIST OF TABLES

BIBLIOGRAPHY

[1] C. Anyuan, R. Nilssen, and A. Nysveen, "Performance Comparisons Among Radial-Flux, Multistage Axial-Flux, and Three-Phase Transverse-Flux PM Machines for Downhole Applications," *IEEE Transactions on Industry Applications*, vol. 46, no. 2, pp. 779–789, Mar. 2010.

[2] Z. Makni, M. Besbes, and C. Marchand, "Multiphysics Design Methodology of Permanent-Magnet Synchronous Motors," *IEEE Transactions on Vehicular Technology*, vol. 56, no. 4, pp. 1524–1530, 2007.

[3] L. C. L. Gasc, S. Astier, M. Fadell, "Design to modeling of permanent magnet motors," in *International Conference on Electrical Machines, ICEM*, 2002.

[4] F. Leonardi and B. Ionescu, "Advancements in Tools and Methods for the Design of Permanent Magnet Integrated Starter Alternators," *IEEE International Conference on Electric Machines and Drives 2005*, pp. 212–218, 2005.

[5] G. Almandoz, "Metodología avanzada de diseño de máquinas multipolares de imanes permanentes, orientada a la aplicación," Mondragon Goi Eskola Politeknikoa, 2008.

[6] S. A. Semidey, Y. Duan, J. R. Mayor, R. G. Harley, and T. G. Habetler, "Optimal Electromagnetic-Thermo-Mechanical Integrated Design Candidate Search and Selection for Surface-Mount Permanent-Magnet Machines Considering Load Profiles," *IEEE Transactions on Industry Applications*, vol. 47, no. 6, pp. 2460–2468, 2011.

[7] T. D. Nguyen, K.-J. Tseng, S. Zhang, and H. T. Nguyen, "A Novel Axial Flux Permanent-Magnet Machine for Flywheel Energy Storage System: Design and Analysis," *IEEE Transactions on Industrial Electronics*, vol. 58, no. 9, pp. 3784–3794, 2011.

[8] J. F. Gieras, R. J. Wang, and M. J. Kamper, *Axial Flux Permanent Magnet Brushless Machines*. Kluwer Academic Publishers, 2004.

[9] M. Aydin, S. Huang, and T. A. Lipo, "Axial Flux Permanent Magnet Disc Machines: A Review," Univ. of Wisconsin - Madison, Oct. 2004.

[10] L. Del Ferraro, F. Caricchi, F. G. Capponi, and G. De Donato, "Axial-flux PM starter/alternator machine with a novel mechanical device for extended flux weakening capabilities," *Conference Record of the 2004 IEEE Industry Applications Conference, 2004. 39th IAS Annual Meeting*, vol. 3, pp. 1413–1419, 2004.

[11] F. Caricchi, F. Crescimbini, and O. Honorati, "Modular, axial-flux, permanent-magnet motor for ship propulsion drives," *IEEE Transactions on Energy Conversion*, vol. 14, no. 3, pp. 673– 679, May 1999.

[12] R. R. Wallace, J. A. Tapia, and L. A. Diaz, "Design of a 75 kW - 167 rpm axial-flux permanent magnet synchronous motor for copper mining applications," *International Symposium on Power Electronics, Electrical Drives, Automation and Motion, 2006. SPEEDAM 2006*, pp. 304–310, May 2006.

[13] P. J. Masson, M. Breschi, P. Tixador, and C. A. Luongo, "Design of HTS Axial Flux Motor for Aircraft Propulsion," *IEEE Transactions on Applied.Superconductivity*, vol. 17, no. 2, pp. 1533–1536, Jun. 2007.

[14] C. Yi, C. Pollock, and H. Pollock, "A permanent magnet flux switching motor for low energy axial fans," *Conference Record of the 2005 Industry Applications Conference. Fourtieth IAS Annual Meeting*, vol. 3, pp. 2168–2175, Oct. 2005.

[15] The European Wind Energy Association (EWEA), "Wind in power 2011 European statistics," 2012.

[16] Y. Duan and R. G. Harley, "Present and future trends in wind turbine generator designs," *IEEE Power Electronics and Machines in Wind Applications, 2009. PEMWA 2009*, pp. 1–6, 2009.

[17] C. Boccaletti, P. Di Felice, L. Petrucci, and E. Santini, "Parametric Analysis of Axial Flux Wind Generators Focused on Total Harmonic Distortion Evaluation," *Renewable Power Generation, IET*, vol. 5, no. 2, pp. 148–159, Mar. 2011.

[18] H. Don-Ha, L. Ki-Chang, K. Do-Hyun, K. Yong-Joo, C. Kyeong-Ho, and P. Doh-Young, "An modular-type axial-flux permanent magnet synchronous generator for gearless wind power systems," *30th Annual Conference of IEEE Industrial Electronics Society, 2004. IECON'2004*, vol. 2, pp. 1396–1399, Nov. 2004.

[19] Y. Chen and P. Pillay, "Axial-flux PM wind generator with a soft magnetic composite core," *Conference Record of the 2005 Fourtieth IAS Annual Meeting, Industry Applications Conference, 2005*, vol. 1, pp. 231–237, Oct. 2005.

[20] F. Chimento and A. Raciti, "A low-speed axial-flux PM generator for wind power systems," *IEEE International Symposium on Industrial Electronics, 2004.*, vol. 2, pp. 1479–1484, May 2004.

[21] B. J. Chalmers, W. Wu, and E. Spooner, "An axial-flux permanent-magnet generator for a gearless wind energy system," *Proceedings of the 1996 International Conference on Power Electronics, Drives and Energy Systems for Industrial Growth*, vol. 1, pp. 610–616, Jan. 1996.

[22] D. Patterson and R. Spee, “The design and development of an axial flux permanent magnet brushless DC motor for wheel drive in a solar powered vehicle,” *IEEE Transactions on Industry Applications*, vol. 31, no. 5, pp. 1054–1061, Sep. 1995.

[23] C. O. Sung and A. Emadi, “Test and simulation of axial flux-motor characteristics for hybrid electric vehicles,” *IEEE Transactions on Vehicular.Technology*, vol. 53, no. 3, pp. 912–919, May 2004.

[24] C. Versele, Z. De Greve, F. Vallee, R. Hanuise, O. Deblecker, M. Delhaye, and J. Lobry, “Analytical design of an axial flux permanent magnet in-wheel synchronous motor for electric vehicle,” *13th European Conference on Power Electronics and Applications, 2009. EPE.’09.*, pp. 1–9, Sep. 2009.

[25] R. Madhavan and B. G. Fernandes, “A novel axial flux segmented SRM for electric vehicle application,” *XIX. International Conference on Electrical Machines (ICEM), 2010*, pp. 1–6, Sep. 2010.

[26] W. N. Fu and S. L. Ho, “A novel axial-flux electric machine for in-wheel gearless drive in plug-in hybrid electric vehicles,” *14th Biennial IEEE Conference on Electromagnetic Field Computation (CEFC.), 2010.*, p. 1, May 2010.

[27] J. W. K. K. Jayasundara and D. A. I. Munindradasa, “Design of Multi Phase In-Wheel Axial Flux Permanent Magnet Motor for Electric Vehicles,” *First International Conference on Industrial and Information Systems*, pp. 510–512, Aug. 2006.

[28] K. M. Rahman, N. R. Patel, T. G. Ward, J. M. Nagashima, F. Caricchi, and F. Crescimbini, “Application of Direct-Drive Wheel Motor for Fuel Cell Electric and Hybrid Electric Vehicle Propulsion System,” *IEEE Transactions on Industry Applications*, vol. 42, no. 5, pp. 1185–1192, 2006.

[29] T. A. Lipo and M. Aydin, “Field Weakening of Permanent Magnet Machines – Design Approaches,” in *EPE Power Electronics and Motion Control Conference, EPE-PEMC’04, Sept*, 2004.

[30] F. G. Capponi, R. Terrigi, F. Caricchi, and L. Del Ferraro, “Active Output Voltage Regulation for an Ironless Axial-Flux PM Automotive Alternator With Electromechanical Flux Weakening,” *IEEE Transactions on Industry Applications*, vol. 45, no. 5, pp. 1785–1793, 2009.

[31] R. L. Ficheux, F. Caricchi, F. Crescimbini, and O. Honorati, “Axial-flux permanent-magnet motor for direct-drive elevator systems without machine room,” *IEEE Transactions on Industry Applications*, vol. 37, no. 6, pp. 1693–1701, 2001.

[32] P. Beckley, *Electrical Steels for Rotating Machines*. The Institution of Electrical Engineers, 2002.

[33] D. Kowal, P. Sergeant, L. Dupre, and A. Van den Bossche, "Comparison of Nonoriented and Grain-Oriented Material in an Axial Flux Permanent-Magnet Machine," *IEEE Transactions on Magnetics*, vol. 46, no. 2, pp. 279–285, Feb. 2010.

[34] S. Javadi, M. Mirsalim, and J. Sabzivand, "3-D FEM analysis of a novel structure for axial-flux homopolar generators using a grain-oriented silicon steel stator core," *International Conference on Electrical Machines and Systems, 2008. ICEMS 2008*, pp. 3640–3643, Oct. 2008.

[35] Höganas, "http://www.hoganas.com/en/Segments/Somaloy-Technology/Home/," 2011. .

[36] J. Kinnunen, "Direct-On-Line Axial Flux Permanent Magnet Synchronous Generator Static And Dynamic Performance," Lappeenranta University of Technology, 2007.

[37] A. Parviainen, "Design of AAxial-Flux Permanent-Magnet Low-Speed Machines and Performance Comparison Between Radial-Flux and Axial-Flux Machines," Lappeenranta University of Technology, 2005.

[38] F. Sahin, *Design and development of a high-speed axial-flux permanent-magnet machine*. Eindhoven, 2001.

[39] A. Parviainen, M. Niemela, and J. Pyrhonen, "A Novel Axial Flux Permanent Magnet Machine to Laboratory Use," in *Computer Engineering in Applied Electromagnetism*, S. Wiak, A. Krawczyk, and M. Trlep, Eds. Springer Netherlands, 2005, pp. 333–336.

[40] W. Fei, P. Luk, and K. Jinupun, "A new axial flux permanent magnet Segmented-Armature-Torus machine for in-wheel direct drive applications," *IEEE Power Electronics Specialists Conference, 2008. PESC.*, pp. 2197–2202, Jun. 2008.

[41] F. Marignetti, G. Tomassi, P. Cancelliere, and V. Delli Colli, "Electromagnetic and Mechanical design of a Fractional-slot-windings Axial-flux PM synchronous machine with Soft Magnetic Compound Stator," *IConference Record of the 2006 IEEE Industry Applications Conference, 2006. 41st IAS Annual Meeting.*, vol. 1, pp. 62– 69, 2006.

[42] G. Cvetkovski, L. Petkovska, M. Cundev, and S. Gair, "Improved Design of a Novel PM Disk Motor by Using Soft Magnetic Composite Material," *IEEE Transacions on Magnetics*, vol. 38(5), pp. 3165–3167, 2002.

[43] G. S. Liew, N. Ertugrul, W. L. Soong, and D. B. Gehlert, "Analysis and Performance Evaluation of an Axial-Field Brushless PM Machine Utilising Soft Magnetic Composites," *IEEE International Electric Machines & Drives Conference, 2007. IEMDC'07*, vol. 1, pp. 153–158, May 2007.

[44] D. Qiu-ling, P. Xiao, and X. Weicai, "Design of Axial Flux Permanent Magnet Synchronous Generators with Soft Magnetic Compound (SMC) Stator Core," *International Conference on Energy and Environment Technology, 2009. ICEET'09.*, vol. 2, pp. 119–122, Oct. 2009.

[45] M. A. Khan, P. Pillay, N. R. Batane, and D. J. Morrison, "Prototyping a Composite SMC/Steel Axial-flux PM Wind Generator," *41st IEEE Conference Record of the 2006 IAS Annual Meeting , Industry Applications Conference, 2006*, vol. 5, pp. 2374–2381, Oct. 2006.

[46] S. Javadi and M. Mirsalim, "A Coreless Axial-Flux Permanent-Magnet Generator for Automotive Applications," *IEEE Transactions on Magnetics*, vol. 44, no. 12, pp. 4591–4598, Dec. 2008.

[47] W. Fei, P. C. K. Luk, and K. Jinupun, "Design and analysis of high-speed coreless axial flux permanent magnet generator with circular magnets and coils," *Electric Power Applications, IET*, vol. 4, no. 9, pp. 739–747, Nov. 2010.

[48] M. Sadeghierad, H. Lesani, H. Monsef, and A. Darabi, "High-speed axial-flux permanent-magnet generator with coreless stator," *Canadian.Journal of Electrical and Computer Engineering*, vol. 34, no. 1, pp. 63–67, 2009.

[49] S. M. Hosseini, M. Agha-Mirsalim, and M. Mirzaei, "Design, Prototyping, and Analysis of a Low Cost Axial-Flux Coreless Permanent-Magnet Generator," *IEEE Transactions on Magnetics*, vol. 44, no. 1, pp. 75–80, Jan. 2008.

[50] W. Rong-Jie, M. J. Kamper, K. Van der Westhuizen, and J. F. Gieras, "Optimal design of a coreless stator axial flux permanent-magnet generator," *IEEE Transactions on Magnetics*, vol. 41, no. 1, pp. 55–64, Jan. 2005.

[51] T. Mi-Ching and H. Liang-Yi, "Design of a Miniature Axial-Flux Spindle Motor With Rhomboidal PCB Winding," *IEEE Transactions on Magnetics*, vol. 42, no. 10, pp. 3488–3490, Oct. 2006.

[52] S. Moury and M. T. Iqbal, "A permanent magnet generator with PCB stator for low speed marine current applications," *1st International.Conference on theDevelopments in Renewable Energy Technology (ICDRET), 2009*, pp. 1–4, Dec. 2009.

[53] Y. Guo-Jhih, H. Liang-Yi, W. Jing-Hui, T. Mi-Ching, and W. Xin-Yi, "Axial-Flux Permanent Magnet Brushless Motor for Slim Vortex Pumps," *IEEE Transactions on Magnetics*, vol. 45, no. 10, pp. 4732–4735, Oct. 2009.

[54] A. Cavagnino, M. Cristino, M. Lazzari, F. Profumo, and A. Tenconi, "A simple method to predict the induced EMF waveform and the d-axis and q-axis inductances of an axial flux interior PM synchronous motor," *IIEEE Conference Record of the 2000 Industry Applications Conference, 2000*, vol. 1, pp. 208–214, 2000.

[55] F. Profumo, A. Tenconi, Z. Zhang, and A. Cavagnino, "Novel axial flux interior PM synchronous motor realized with powdered soft magnetic materials," *The 1998 IEEE Industry Applications Conference, 1998.Thirty-Third IAS Annual Meeting.*, vol. 1, pp. 152–158, Oct. 1998.

[56] H. Polinder, J. G. Slootweg, J. C. Compter, and M. J. Hoeijmakers, "Modelling a linear PM motor including magnetic saturation," *International Conference on Power Electronics, Machines and Drives, 2002*, pp. 632–637, Jun. 2002.

[57] A. Sari, C. Espanet, D. Chamagne, F. Lanzetta, D. Marquet, and P. Nika, "Reluctance network modeling tubular linear alternator considering iron nonlinearities," *International Conference on Electrical Machines and Systems, 2009. ICEMS,2009.*, pp. 1–6, Nov. 2009.

[58] C. B. Rasmussen and E. Ritchie, "A magnetic equivalent circuit approach for predicting PM motor performance," *Conference Record of the 1997 IEEE Industry Applications Conference, 1997. Thirty-Second IAS Annual Meeting, IAS '97*, vol. 1, pp. 10–17, Oct. 1997.

[59] S. A. Saied, K. Abbaszadeh, and M. Fadaie, "Reduced Order Model of Developed Magnetic Equivalent Circuit in Electrical Machine Modeling," *IEEE Transactions on Magnetics*, vol. 46, no. 7, pp. 2649–2655, Jul. 2010.

[60] Z. Q. Zhu, D. Howe, E. Bolte, and B. Ackermann, "Instantaneous magnetic field distribution in brushless permanent magnet DC motors. I. Open-circuit field," *IEEE Transactions on Magnetics*, vol. 29, no. 1, pp. 124–135, Jan. 1993.

[61] Z. Q. Zhu and D. Howe, "Instantaneous magnetic field distribution in brushless permanent magnet DC motors. II. Armature-reaction field," *IEEE Transactions on Magnetics*, vol. 29, no. 1, pp. 136–142, Jan. 1993.

[62] Z. Q. Zhu and D. Howe, "Instantaneous magnetic field distribution in brushless permanent magnet DC motors. III. Effect of stator slotting," *IEEE Transactions on Magnetics*, vol. 29, no. 1, pp. 143–151, Jan. 1993.

[63] Z. Q. Zhu and D. Howe, "Instantaneous magnetic field distribution in permanent magnet brushless DC motors. IV. Magnetic field on load," *IEEE Transactions on Magnetics*, vol. 29, no. 1, pp. 152–158, Jan. 1993.

[64] A. B. Proca, A. Keyhani, and A. El-Antably, "Analytical model for permanent magnet motors with surface mounted magnets," *Electric.Machines.and Drives., 1999.International.Conference IEMD.'99.*, pp. 767–769, May 1999.

[65] G. Almandoz, J. Poza, M. A. Rodriguez, and A. Gonzalez, "Analytic model of a PMSM considering spatial harmonics," *International Symposium on Power Electronics, Electrical Drives, Automation and Motion, 2008. SPEEDAM 2008*, pp. 603–608, Jun. 2008.

[66] S. Huang, J. Luo, F. Leonardi, and T. A. Lipo, "A General Aprroach to Sizing and Power Density Equations for Comparison of Electrical Machines," *IEEE Transactions on Industry Applications*, vol. 34, pp. 92– 97, 1998.

[67] H. Surong, L. Jian, F. Leonardi, T. A. Lipo, S. Huang, and J. Luo, "A comparison of Power Density for Axial Flux Machines Based on General Purpose Sizing Equations," *IEEE transactions on Energy Conversion*, vol. 14, no. 2, pp. 185–192, Jun. 1999.

[68] M. Aydin, S. Huang, and T. A. Lipo, "Optimum design and 3D finite element analysis of nonslotted and slotted internal rotor type axial flux PM disc machines," *Power Engineering Society Summer Meeting, 2001*, vol. 3. pp. 1409–1416 vol.3, 2001.

[69] S. Huang, M. Aydin, and T. A. Lipo, "A Direct Approach to Electrical Machine Performance Evaluation: Torque Density Assessment and Sizing Optimization," *15th International Conference on Electrical Machines, ICEM 2002*, 2002.

[70] S. Huang, M. Aydin, and T. A. Lipo, "TORUS Concept Machines: Pre-Prototyping Design Assessment for Two Major Topologies," *IConference Record of the 2001 IEEE Industry Applications Conference, 2001, Thirty-Sixth IAS Annual Meeting*, vol. 3, pp. 1619– 1625, 2001.

[71] F. Sahin, A. M. Tuckey, and A. J. A. Vandenput, "Design Considerations of the Flywheel-Mounted Axial-Flux Permanent-Magnet Machine for a Hybrid Electric Vehicle," *Design, development and testing of a high-speed axial-flux permanent-magnet machine*, vol. 3, pp. 1640 – 1647, 2001.

[72] M. Aydin, *Axial flux surface mounted permanent magnet disc motors for smooth torque traction drive applications*. University of Wisconsin--Madison, 2004.

[73] D. C. Hanselman, *Brushless Permanent Magnet Motor Design*. The Writer's Collective, 1997.

[74] A. H. Wijenayake and P. B. Schmidt, "A more accurate permanent magnet synchronous motor model by taking parameter variations and loss components into account for sensorless control applications," *IEEE International Electric Machines and Drives Conference Record, 1997*, pp. TD1/1–TD1/1, May 1997.

[75] A. Consoli and A. Raciti, "Analysis of permanent magnet synchronous motors," *IEEE Transactions on Industry Applications*, vol. 27, no. 2, pp. 350–354, Mar. 1991.

[76] N. Urasaki, T. Senjyu, and K. Uezato, "Relationship of parallel model and series model for permanent magnet synchronous motors taking iron loss into account," *IEEE Transactions on Energy Conversion*, vol. 19, no. 2, pp. 265–270, Jun. 2004.

[77] A. M. El-Refaie, Z. Q. Zhu, T. M. Jahns, and D. Howe, "Winding Inductances of Fractional Slot Surface-Mounted Permanent Magnet Brushless Machines," *IEEE Industry Applications Society Annual Meeting, 2008. IAS '08*, pp. 1–8, Oct. 2008.

[78] Z. Q. Zhu, D. Howe, and J. K. Mitchell, "Magnetic field analysis and inductances of brushless DC machines with surface-mounted magnets and non-overlapping stator windings," *IEEE Transactions on Magnetics*, vol. 31, no. 3, pp. 2115–2118, May 1995.

[79] G. Ugalde, "New topologies in Permanent Magnet Machines for direct drive applications," Mondragon Unibertsitatea, 2009.

[80] J. R. Hendershot and T. J. E. Miller, *Design of brushless permanent-magnet motors*. Magna Pysics Pub., 1994.

[81] N. Bianchi and M. Dai Pre, "Use of the star of slots in designing fractional-slot single-layer synchronous motors," *IEE Proceedings -Electric Power Applications,*, vol. 153, no. 3, pp. 459–466, May 2006.

[82] A. B. Proca, A. Keyhani, A. El-Antably, L. Wenzhe, and D. Min, "Analytical model for permanent magnet motors with surface mounted magnets," *IEEE Transactions on Energy Conversion*, vol. 18, no. 3, pp. 386–391, Sep. 2003.

[83] B. Ackermann, J. H. H. Janssen, R. Sottek, and R. I. van Steen, "New technique for reducing cogging torque in a class of brushless DC motors," *Electric Power Applications, IEE Proceedings B*, vol. 139, no. 4, pp. 315–320, Jul. 1992.

[84] M. J. Chung and D. G. Gweon, "Modeling of the armature slotting effect in the magnetic field distribution of a linear permanent magnet motor," *Electrical Engineering (Archiv fur Elektrotechnik)*, vol. 84, no. 2, pp. 101–108, May 2002.

[85] Z. J. Liu and J. T. Li, "Analytical Solution of Air-Gap Field in Permanent-Magnet Motors Taking Into Account the Effect of Pole Transition Over Slots," *IEEE Transactions on Magnetics*, vol. 43, no. 10, pp. 3872–3883, Oct. 2007.

[86] F. Dubas and C. Espanet, "Analytical Solution of the Magnetic Field in Permanent-Magnet Motors Taking Into Account Slotting Effect: No-Load Vector Potential and Flux Density Calculation," *IEEE Transactions on Magnetics*, vol. 45, no. 5, pp. 2097–2109, May 2009.

[87] B. L. J. Gysen, E. A. Lomonova, J. J. H. Paulides, and A. J. A. Vandenput, "Analytical and Numerical Techniques for Solving Laplace and Poisson

Equations in a Tubular Permanent-Magnet Actuator: Part I. Semi-Analytical Framework," *IEEE Transactions on Magnetics*, vol. 44, no. 7, pp. 1751–1760, Jul. 2008.

[88] B. L. J. Gysen, E. A. Lomonova, J. J. H. Paulides, and A. J. A. Vandenput, "Analytical and Numerical Techniques for Solving Laplace and Poisson Equations in a Tubular Permanent Magnet Actuator: Part II. Schwarz&Christoffel Mapping," *IEEE Transactions on Magnetics*, vol. 44, no. 7, pp. 1761–1767, Jul. 2008.

[89] D. Zarko, D. Ban, and T. A. Lipo, "Analytical calculation of magnetic field distribution in the slotted air gap of a surface permanent-magnet motor using complex relative air-gap permeance," *IEEE Transactions on Magnetics*, vol. 42, no. 7, pp. 1828–1837, Jul. 2006.

[90] J. F. Gieras, "Analytical approach to cogging torque calculation of PM brushless motors," *IEEE Transactions on Industry Applications*, vol. 40, no. 5, pp. 1310–1316, Sep. 2004.

[91] Z. Q. Zhu and D. Howe, "Analytical prediction of the cogging torque in radial-field permanent magnet brushless motors," *IEEE Transactions on Magnetics*, vol. 28, no. 2, pp. 1371–1374, Mar. 1992.

[92] D. Zarko, D. Ban, and T. A. Lipo, "Analytical Solution for Cogging Torque in Surface Permanent-Magnet Motors Using Conformal Mapping," *IEEE Transactions on Magnetics*, vol. 44, no. 1, pp. 52–65, Jan. 2008.

[93] CEDRAT, "http://www.cedrat.com/en/software-solutions/flux.html," 2011. .

[94] CEDRAT, "Flux 10 User´s guide. Volume 3. Phusical Applications: Magnetic, Electric, Thermal.," 2007.

[95] P. Van Tichelen and E. Peeters, "Design of a new axial flux permanent magnet generator for hybrid electric vehicles," *IEEE 58th Vehicular Technology Conference, 2003. VTC 2003*, vol. 5, pp. 3192–3196, Oct. 2003.

[96] K. Kyoung-Ho, C. Yun-Hyun, K. Do-Hyun, J. Yen-Ho, and K. Jong-Mu, "Characteristics analysis of axial flux type reluctance motor using 2 and 3-dimensional finite element method," *IEEE International Symposium on Industrial Electronics , 2001. ISIE 2001*, vol. 2, pp. 1169–1174, 2001.

[97] S. Gair, A. Canova, J. F. Eastham, and T. Betzer, "A new 2D FEM analysis of a disc machine with offset rotor," *Proceedings of the International Conference onPower Electronics, Drives and Energy Systems for Industrial Growth, 1996.*, vol. 1, pp. 617–621, Jan. 1996.

[98] A. Parviainen, J. Pyrhonen, and M. Niemela, "Axial flux interior permanent magnet synchronous motor with sinusoidally shaped magnets," *Electromagnetic Fields in Electrical Engineering. ISEF'01*, pp. 271–276, 2001.

[99] D. A. Gonzalez, J. A. Tapia, and A. L. Bettancourt, "Design Consideration to Reduce Cogging Torque in Axial Flux Permanent-Magnet Machines," *IEEE Transactions on Magnetics*, vol. 43, no. 8, pp. 3435–3440, Aug. 2007.

[100] F. Caricchi, F. G. Capponi, F. Crescimbini, and L. Solero, "Experimental study on reducing cogging torque and no-load power loss in axial-flux permanent-magnet machines with slotted winding," *IIEEE Transactions on Industry Applications*, vol. 40, no. 4, pp. 1066–1075, Jul. 2004.

[101] G. Bertotti, A. Boglietti, M. Chiampi, D. Chiarabaglio, F. Fiorillo, and M. Lazzari, "An improved estimation of iron losses in rotating electrical machines," *IEEE Transactions on Magnetics*, vol. 27, no. 6, pp. 5007–5009, Nov. 1991.

[102] F. Magnussen, Y. K. Chin, J. Soulard, A. Broddefalk, S. Eriksson, and C. Sadarangani, "Iron losses in salient permanent magnet machines at field-weakening operation," *39th Conference Record of the 2004 IEEE IIAS Annual Meeting Industry Applications Conference, 2004*, vol. 1, p. 47, Oct. 2004.

[103] A. Parviainen, M. Niemela, J. Pyrhonen, and J. Mantere, "Performance comparison between low-speed axial-flux and radial-flux permanent-magnet machines including mechanical constraints," *IEEE International Conference on Electric Machines and Drives, 2005*, pp. 1695–1702, May 2005.

[104] Z. W. Vilar, D. Patterson, and R. A. Dougal, "Thermal analysis of a single sided axial flux permanent magnet motor," *31st Annual Conference of IEEE Industrial Electronics Society, 2005. IECON 2005*, p. 5 pp., 2005.

[105] O. Maloberti, C. Marchand, Y. Choua, D. Condamin, L. Kobilansky, and E. Bomme, "Multi-Physical QuasiStatic Modelling of an Axial Flux Permanent Magnet Machine," *Flux*, no. 3, pp. 1–6, 2010.

[106] R. J. Wang, M. J. Kamper, and R. T. Dobson, "Development of a Thermofluid Model for Axial Field Permanent-Magnet Machines," *IEEE Transactions on Energy Conversion*, vol. 20, no. 1, pp. 80–87, 2005.

[107] F. Marignetti, V. D. Colli, and Y. Coia, "Design of Axial Flux PM Synchronous Machines Through 3-D Coupled Electromagnetic Thermal and Fluid-Dynamical Finite-Element Analysis," *IEEE Transactions on Industrial Electronics*, vol. 55, no. 10, pp. 3591–3601, 2008.

[108] F. Marignetti, "Thermal and fluid dynamical aspects in the design of an Axial Flux Permanent Magnet Synchronous Machine with Soft Magnetic Compound Stator," *32nd Annual Conference on IEEE Industrial Electronics, IECON 2006*, pp. 4847–4852, 2006.

[109] G. Airoldi, G. L. Ingram, K. Mahkamov, J. R. Bumby, R. G. Dominy, N. L. Brown, A. Mebarki, and M. Shanel, "Computations on heat transfer in axial flux permanent magnet machines," *18th International Conference on Electrical Machines, 2008. ICEM 2008*, pp. 1–6, 2008.

[110] A. Chen, R. Nilssen, and A. Nysveen, "Performance comparisons among radial flux, multi-stage axial flux and three-phase transverse flux PM machines for downhole applications," *IEEE International Electric Machines and Drives Conference, 2009. IEMDC'09*, pp. 1010–1017, May 2009.

[111] A. Cavagnino, M. Lazzari, F. Profumo, and A. Tenconi, "A comparison between the axial flux and the radial flux structures for PM synchronous motors," *IIEEE Transactions on ndustry Applications*, vol. 38, no. 6, pp. 1517–1524, Nov. 2002.

[112] D. J. Patterson, J. L. Colton, B. Mularcik, B. J. Kennedy, S. Camilleri, and R. Rohoza, "A comparison of radial and axial flux structures in electrical machines," *IEEE International Electric Machines and Drives Conference, 2009. IEMDC.'09*, pp. 1029–1035, May 2009.

[113] Z. Rahman, "Evaluating radial, axial and transverse flux topologies for 'in-wheel' motor," in *Power Electronics.in Transportation., 2004.*, 2004, pp. 75–81.

[114] N. Balkan Simsir and H. Bulent Ertan, "A comparison of torque capabilities of axial flux and radial flux type of brushless DC (BLDC) drives for wide speed range applications," *Proceedings of the IEEE 1999 International Conference onPower Electronics and Drive Systems, 1999. PEDS'99*, vol. 2, pp. 719–724, 1999.

[115] R. Bojoi, A. Cavagnino, A. Miotto, A. Tenconi, and S. Vaschetto, "Radial flux and axial flux PM machines analysis for More Electric Engine aircraft applications," *IEEE Energy Conversion Congress.and Exposition (ECCE.), 2010*, pp. 1672–1679, Sep. 2010.

[116] Q. Ronghai, M. Aydin, and T. A. Lipo, "Performance comparison of dual-rotor radial-flux and axial-flux permanent-magnet BLDC machines," *IEEE International Electric Machines and Drives Conference, 2003. IEMDC'03*, vol. 3, pp. 1948–1954, Jun. 2003.

Appendix A

PUBLICATIONS

In this appendix A the complete version of the papers published during the development of the PhD Thesis are enclosed.

Analytic Model of Axial Flux Permanent Magnet Machines Considering Spatial Harmonics

A.Egea*[1], G.Almandoz[1], J.Poza[1] and A.Gonzalez[2]
1 University of Mondragon/Faculty of Engineering, Arrasate, (Spain)
2 ORONA Elevator Innovation Centre, Hernani, (Spain)

Abstract— **This work deals with the development of a complete analytic model for axial flux surface mounted permanent magnet synchronous machines. The magnetic field in the air-gap, the induced electromotive force *EMF*, the linked flux ψ and the electromagnetic torque are represented as sum of spatial-temporal components. Then, the accuracy of the model is evaluated comparing the results with those obtained in numerical analysis by 3D simulations.**

Keywords—Axial Flux Permanent Magnet Synchronous Machine, Fourier series, Analytic Model, 2D and 3D FEM simulations

Topic—Design and Optimization of Electrical Machines*

I. INTRODUCTION

Nowadays, electric drives technology tends to compact, low maintenance cost, comfortable and eco-friendly solutions. In this framework, direct drive applications based on permanent magnet (PM) machines show to be the best option to fulfil these requirements.

Among PM machine topologies, axial flux machines are considered as a very interesting option for several applications such as elevators or electrical vehicles. The inherent characteristics of axial flux machines fit properly in situations where flatness is a request. In addition the power density in axial flux machines is normally higher than in radial flux machines which may lead to considerable reduction of the total volume.

In direct drive applications a high grade of optimization of the electrical machine design may be required. Therefore, the design process may take an important number of iterations. The performance of many iterations using exclusively finite element method (FEM) analysis could lead to large computation times. An initial design, previous to the FEM analysis, based on analytical models could enable to reduce the time consumption of the design process.

Analysis of electrical machines using analytic models is not supposed to be as accurate as analysis based on numerical methods. However it gives an insight into the functioning of the machine and makes possible to identify correlations between different design variables and the performance of the machine.

As radial flux machines are the most popular, almost the majority of analytical models found in the literature are related to this type of machine. However these models could be perfectly valid also for axial flux machines if some changes in terms of geometrical parameters are made.

One quite extended modelling method is based on Fourier series [1-6]. This technique considers the time-space distribution of electromagnetic variables so that it enables to identify the cross-coupling between different spatial and temporal components. Therefore, this modelling method provides a very interesting insight into the correlation between different design variables and the machine performances.

In the literature is possible to find some references related to analytical models based on Fourier series, mainly for radial flux machines. For example, *Zhu et al.* carry out in four publications a complete representation of the magnetic field in the air-gap of a PMSM [1-4]. In [1] they represent the magnetic field induced by the magnets in the air-gap as a sum of spatial components for a slot-less machine. The shape of the spatial waveform is defined by solving in polar coordinates the magnetic potential distribution equations in the air-gap. In [2] the armature field in the air-gap is represented in the same way. In [3] the effect of stator slots on the magnetic field is considered. And finally in [4] the magnetic field in load condition is represented. Moreover, in [5] the same authors predict the cogging torque based on the magnetic field representation carried out in previous works.

This approximation proposed by *Zhu et al.* for the definition of the magnetic field in the air-gap has been used for other authors as well. For example, in [7] models for PM synchronous machines inspired in the same method are proposed. In this works complete models representing the electromagnetic torque and the back electro-motive force induced in the armature winding are developed for radial flux machines.

Regarding to axial flux machines, several authors [8-11] proposed sizing and optimization equations for them. Nevertheless these equations consider only the fundamental components, so they are not suitable to represent the time-space variation of electromagnetic variables.

The aim of this work is to carry out a complete analytical model for axial flux machines by using Fourier series. The field induced in the air-gap by the magnets, the magneto-motive force, the inductance value, the linked flux by the windings, the back electro-motive force and the electromagnetic torque will be carried out for surface mounted permanent magnet machines.

* *Ph. D student holding a grant from the Government of the Basque Country*

II. Modelling Methodology and Assumptions

This model is performed in very clear stages. Initially the magnetic field induced by the magnets in the air-gap is represented by means of Fourier series. In a second stage the winding conductor distribution is defined in the same way. Once magnet and winding configuration are defined, in a third stage the electromagnetic coupling is analyzed, calculating the linked flux on the winding (ψ), the electromotive force (*EMF*) and the electromagnetic torque (T_{em}). Finally, the inductances for the single phase steady state equivalent circuit could be calculated from the linked flux obtained in the third stage.

The following assumptions are made to carry out the model:

- The stator and rotor cores are considered ideal: ferromagnetic material with infinite permeability
- Only the normal component of the field in the air-gap is taken into account.
- Magnet leakage flux is not taken into consideration and magnets are considered to work in the linear zone
- The model is linear so that saturations are neglected

The different variables are represented in the following way,

$$X_b^a(Y,Z) \tag{1}$$

X is the name of the variable. The superscript *a* defines the cause of the variable and the subscript *b* means where the variable is located. *Y* and *Z* are the variables on which the main variable depends.

The analytical model is based in two general equations. These equations depend on two dimensions, one along the angle θ and the other along the radium *r* as shown in Fig 2.

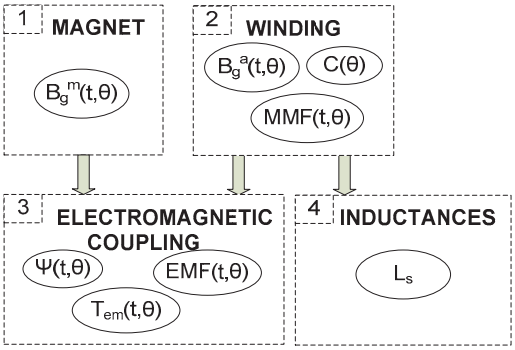

Fig 1: Proposed modeling methodology

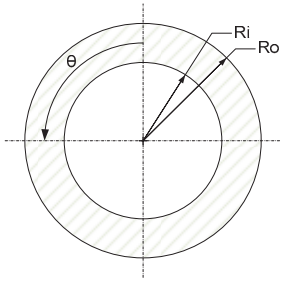

Fig 2: Two dimensions of the integration

On the one hand the magnetic field induced by the magnets in the air-gap is represented in the following form:

$$B_g^m(t,\theta,r) = \sum_{n=-\infty}^{\infty} B_n(r)\cdot e^{jpn\varphi_0}\cdot e^{-jpn\theta}\cdot e^{-jpn\Omega_m t} \tag{2}$$

Where R_o and R_i are the outer and inner radius respectively, *p* is the number of pole pairs, B_n is the *n*-th harmonic component and φ_0 is the initial angle.

On the other hand appears the expression for the spatial distribution of the winding conductors (see Fig5):

$$C(\theta,r) = \sum_{k=-\infty}^{\infty} \vec{C}_k(r)\cdot e^{-jt_p k\theta} \tag{3}$$

Where C_k is the *k*-th harmonic component and t_p is the periodicity of the machine.

$$t_p = G.C.D(Q,p) \tag{4}$$

Once having these two equations all other parameters such as linked flux, electromagnetic force or electromagnetic torque can be developed easily.

The magneto-motive force per current unit is defined as:

$$F(\theta,r) = \int C(\theta,r)d\theta \tag{5}$$

Then the linked flux is calculated applying the following expression:

$$\psi_x(t) = t_p \int_{Ri}^{Ro}\int_0^{2\pi/t_p} rB_g^m(t,\theta,r)F(\theta,r)d\theta dr \tag{6}$$

Where *x* is referred to the phase number. The electromagnetic force can be calculated by:

$$EMF_x(t) = \frac{d\psi_x(t)}{dt} \tag{7}$$

And finally the electromagnetic torque is calculated as:

$$T_{em}(t) = \sum_{x=1}^{m} \frac{EMF_x(t)\cdot i_x(t)}{\Omega_m} \tag{8}$$

Where i_x is the current of the *x* phase, *m* is the number of phases and Ω_m is the mechanical speed of the machine.

III. Model Description

In this section a brief description of the developed model for surface mounted PM axial flux synchronous machines is given. It is important to remark that the proposed model assumes only the average radium of the machine. This assumption is valid in cases where the magnets are radially proportional so that their span angle is constant along the radium.

A. Magnetic Field in the Airgap

The magnetic field induced by the magnets in the air-gap can be expressed by developing (2) for the average radium in the following way:

$$B_g^m(t,\theta) = \sum_{n=1}^{\infty} 2B_n\cdot\cos\left(np\left(-\theta-\Omega_m t+\varphi_0\right)\right) \tag{9}$$

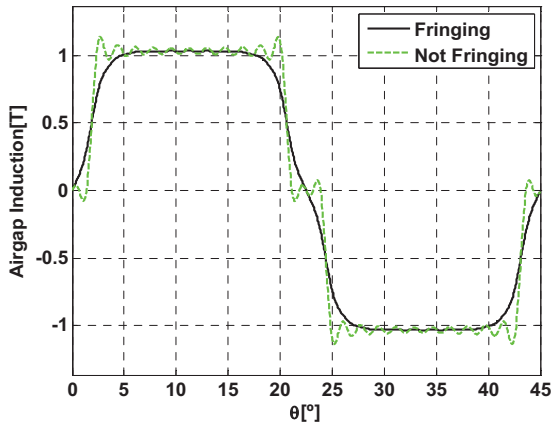

Fig 3: Magnetic field induced by the magnets in the air-gap with and without fringing function

As positive and negative components are symmetrical, only positive harmonics are considered in the sum. The coefficient B_n is calculated as:

$$B_n = \frac{B_{g\max}}{n\pi}\sin\left(np\frac{\beta_m}{2}\right)\frac{(1-\cos(n\pi))}{\left(1+(anp)^2\right)} \tag{10}$$

β_m is the magnets span angle in electrical degrees and a is the fringing function coefficient. The geometry of magnets is shown in Fig 8. The B_{gmax} value is referred to the maximum value of the field and it is calculated as following:

$$B_{g\max} = \frac{B_r}{1+\mu_r\frac{g}{h_m}} \tag{11}$$

Where B_r and μ_r are the residual value of the magnetic field value and the relative permeability of the magnets, g is the air-gap length and h_m is the height of the magnets.

It has been demonstrated that the expression (12) of the fringing coefficient leads to a quite accurate approximation of the shape of the magnetic field on the air-gap. This expression is developed from [12]. Fig 3 shows the difference on the waveform of the magnetic field induced by the magnets in the air-gap with and without the fringing coefficient.

$$a = \frac{\sqrt{g\left(g+h_m/\mu_r\right)}}{D_{av}} \tag{12}$$

B. Winding Factor

Obtaining the winding factor is the next step that should be made. With the expression (13) it is possible to obtain the harmonic content of the winding factor.

$$\vec{\xi}_k = \frac{\sum_{x=1}^{Q/t_p m} \pm e^{jkt_p\varphi_x}}{Q/\left(t_p m\right)} \tag{13}$$

Where Q is the number of stator slots. A vector sum is made adding all the coils with a positive direction of current and resting the negative ones of the same phase. Fig 4 shows a schema of how the sum is made.

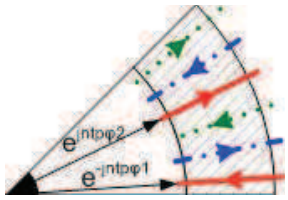

Fig 4: Schema of how the winding factor is calculated

Once the winding factor is obtained it is possible to continue with the development of the model for the electro-magnetic parameters.

C. Winding Distribution

The winding conductor distribution leads to the expression (14) when no variation in the radial dimension is assumed:

$$C(\theta) = \sum_{k=-\infty}^{\infty}\vec{C}_k\cdot e^{-jt_pk\theta} \tag{14}$$

In case of current sheets (in case the conductors are concentrated in a single point) C_k coefficients are calculated as:

$$\vec{C}_k = \frac{N_{ph}}{\pi}\xi_k e^{j\angle\xi_k} \tag{15}$$

N_{ph} is the number of turns per phase and ξ_k and $\angle\xi_k$ are the winding factor amplitude and its angle respectively. The magneto-motive force MMF is defined as:

$$MMF(t,\theta) = F(\theta)\cdot\Re\{i(t)\} \tag{16}$$

Where F and i are the magneto-motive force per current unit and the supply current. F is defined as:

$$F(\theta) = \int C(\theta)\cdot d\theta \tag{17}$$

From (14), (15) and (17) the definition of F in Fourier series is the following:

$$F(\theta) = \sum_{k=1}^{\infty}2\cdot F_k\cdot\sin\left(-kt_p\theta+\angle\xi_k\right) \tag{18}$$

The expression of the Fourier coefficient F_k is:

$$F_k = \frac{N_{ph}}{\pi\cdot k\cdot t_p}\xi_k \tag{19}$$

In cases the conductors of the coils are not placed just in a point but they are distributed with certain span angle, an attenuation effect due to this dispersion appears. This attenuation effect can be modelled considering an additional coefficient:

$$K_k = \frac{\sin\left(k\cdot t_p\cdot\alpha_w/2\right)}{k\cdot t_p\cdot\alpha_w/2} \tag{20}$$

Where α_w is the span angle of the coil in the average radium R_{av} of the stator as shown in Fig 6. This factor affects directly in the coil winding conductor distribution C. So with (20) the expression (19) changes to (21).

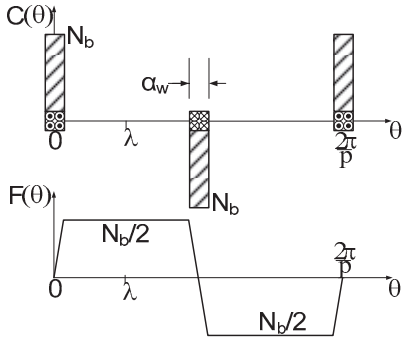

Fig 5. Spatial conductor distribution and resulting F

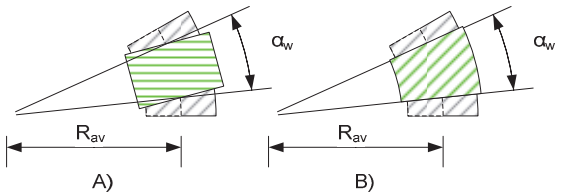

Fig 6: Placing of a coil in the stator. A) Rectangular coil and B) radially proportional coil.

$$F_k = \frac{N_{ph}}{\pi \cdot k \cdot t_p} \xi_k \frac{\sin\left(k \cdot t_p \cdot \alpha_w / 2\right)}{k \cdot t_p \cdot \alpha_w / 2} \tag{21}$$

The effect of this coil dispersion is shown in Fig 5. Where N_b is the number of conductors in each coil and is calculated as:

$$N_b = \frac{N_{ph}}{\left(\frac{Q \cdot h}{m} / 2\right) \cdot n_l} \tag{22}$$

n_l is the number of layer of the winding and h is the number of sides of the machine.

The coils could be placed in several ways, but when a rectangular form of the coil Fig 6 *A)* instead of a radial proportional coil Fig 6 *B)* is used, the obtained effect is practically the same if the angle of the distribution is taken in the average radium of the stator.

The model represents the behaviour of the machine in steady state. So the armature currents are defined as following in case of three symmetric phases:

$$i_1(t) = \mathrm{Re}\left\{Ie^{jw_s t}\right\} \quad i_2(t) = \mathrm{Re}\left\{Ie^{jw_s t - \frac{2\pi}{3}}\right\} \quad i_3(t) = \mathrm{Re}\left\{Ie^{jw_s t + \frac{2\pi}{3}}\right\} \tag{23}$$

After defining the *MMF* the armature field in the air-gap can be calculated as:

$$B_g^a(t,\theta) = \mu_o \frac{MMF(t,\theta)}{g} \tag{24}$$

D. Electromagnetic Coupling

The electromagnetic coupling consists in the calculation of the magnet flux linkage, the *EMF* and the electromagnetic torque. The flux linkage per phase is defined as:

$$\Psi_x^m(t) = t_p \int_0^{\frac{2\pi}{t_p}} \frac{R_o^2 - R_i^2}{2} \cdot B_g^m(t,\theta) \cdot F(\theta) \cdot d\theta \tag{25}$$

Where D_o and D_i are the outer diameter and the inner diameter of the rotor ring. Developing the expression (25) with (10) and (18):

$$\Psi_x^m(t) = t_p \int_0^{\frac{2\pi}{t_p}} \left(\frac{R_o^2 - R_i^2}{2} \cdot \sum_{n=1}^{\infty} 2B_n \cos\left(np\left(-\theta + \Omega_m t + \varphi_0\right)\right) \cdot \sum_{k=1}^{\infty} 2F_k \sin\left(-kt_p\theta + \angle\xi_k\right) \right) \cdot d\theta \tag{26}$$

The flux linkage is zero unless

$$k = -\frac{n \cdot p}{t_p} \tag{27}$$

So developing (26):

$$\Psi_x^m(t) = \pi\left(R_o^2 - R_i^2\right) \sum_{n=1}^{\infty} 2F_{\left(\frac{np}{tp}\right)} B_n \sin\left(np\left(-\Omega_m t + \varphi_0\right) + \angle\xi_{\left(\frac{np}{tp}\right)}\right) \tag{28}$$

After calculating the flux linkage, the *EMF* can be computed from (7). Considering (28) it is possible to obtain the following expression for the induced electromotive forces in a phase when the machine operates in open-circuit mode.

$$EMF_x^m(t) = \left[-\pi\left(R_o^2 - R_i^2\right) np\Omega_m \times \sum_{n=1}^{\infty} 2F_{\left(\frac{np}{tp}\right)} B_n \cos\left(np\left(-\Omega t + \varphi_0\right) + \angle\xi_{\left(\frac{np}{tp}\right)}\right) \right] \tag{29}$$

In a surface mounted permanent magnet machine the electromagnetic torque is divided in two components: the mutual torque and the cogging torque. In case of a slot-less machine only mutual torque exists. If the supply currents are equilibrated the expression of the mean value of the mutual torque is:

$$T_{em} = \frac{3}{\Omega_m} \frac{EMF_x I_x}{2} \tag{30}$$

For the temporal expression of the torque all the phases are taken into account.

$$T_{em}(t) = \frac{EMF_1(t)I_1(t) + EMF_2(t)I_2(t) + EMF_3(t)I_3(t)}{\Omega_m} \tag{31}$$

E. Inductance

The calculus of the inductance is also very valuable for the correct characterisation of the machine. In the case of slot-less toroidal machines de inductance could be divided in two components: the air-gap inductance L_g and the end-winding leakage inductance L_{ew}. The air gap inductance for each phase is the sum of the self inductance and the mutual inductances, as shown in the next expression.

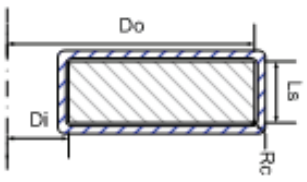

Fig 7: Detail of the dimensions of the coil

$$L_{g1} = L_{11} + L_{12} + L_{13} \tag{32}$$

Where L_{g1} is the air-gap inductance of phase 1, L_{11} is the self inductance of phase 1, and L_{12} and L_{12} are the mutual inductances. The expressions for different inductance components are the following;

$$L_{11} = \pi\left(R_o{}^2 - R_i{}^2\right)\frac{\mu_0}{\delta}\sum_{k=-\infty}^{\infty} F_k{}^2 \tag{33}$$

$$L_{12} = \pi\left(R_o{}^2 - R_i{}^2\right)\frac{\mu_0}{\delta}\sum_{k=-\infty}^{\infty} F_k{}^2 e^{j\frac{2\pi}{3}(k-1)} \tag{34}$$

$$L_{13} = \pi\left(R_o{}^2 - R_i{}^2\right)\frac{\mu_0}{\delta}\sum_{k=-\infty}^{\infty} F_k{}^2 e^{j\frac{2\pi}{3}(-k+1)} \tag{35}$$

The end-winding inductance can be computed by the following equation, [13].

$$L_{ew} = \frac{1}{2}\frac{\mu_0}{\pi} N_{ph}{}^2\left(\pi R_c + L_s\right) \tag{36}$$

Fig 7 shows the dimensions of the coil in detail.

IV. Model Validation

In this section some results obtained with the proposed model are shown. In order to validate the developed model these results have been compared with those obtained in 3D FEM analysis.

A. Specifications of the Modeled Machine

The modelled machine is an axial flux surface mounted PM synchronous machine. The machine is a double-sided interior stator which means that it has two rotor discs. The slot-less stator is wounded by the so called toroidal winding. Details of the machine configuration are shown in Fig 8. In TABLE I. the main characteristics of the machine are reported.

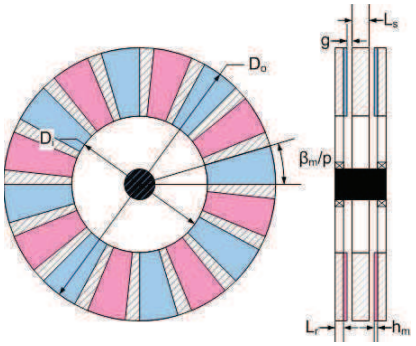

Fig 8: Geometry of the modeled machine

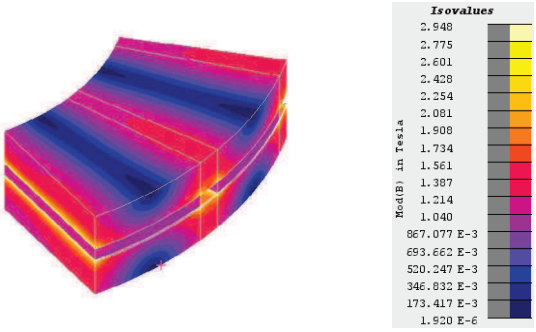

Fig 9: Spatial distribution of the magnetic field induced by the magnets

TABLE I.
Modelled Machine Characteristics

g	Air-gap length	4 mm
L_s	Stator Core length	30 mm
L_r	Rotor Core length	15 mm
Q_s	Number of stator slots	48
D_o	Outer Diameter	323.7 mm
D_i	Inner Diameter	194.2 mm
h_m	Magnet height	5 mm
β_m	Pole Arc	150º
B_r	Remanent Value of Magnet Flux Density	1.26T
μ_r	Relative permeability of the magnet	1.08
p	Number of pairs of pole	8
N_{ph}	Number of turns per phase	288
h	Number of sides	2
m	Number of phases	3
I_{ef}	Current RMS value	14 A
α_w	Coil dispersion angle	4.45º(10mm)
Ω_m	Mechanical speed	382.5 rpm

B. Results

In this section the results obtained with the proposed analytical model are compared with FEM3D results. For example in Fig 10 the spatial distribution of the magnetic field induced by the magnets in the air-gap is shown. On the other hand in Fig 11 is represented the temporal evolution of the flux linked by the winding. In Fig 12 the torque is shown. Finally in Table II the inductance values are summarized.

Summarizing the results show that the accuracy of the model in comparison with FEM3D is really good. It can be state that the accuracy is around 99%. Thus it can be concluded that the proposed analytical model is rather accurate and it has a good agreement with the FEM3D results.

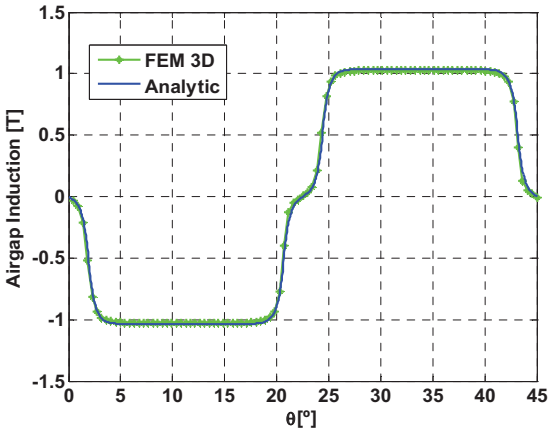

Fig 10: Magnetic field induced by the magnets in the air-gap

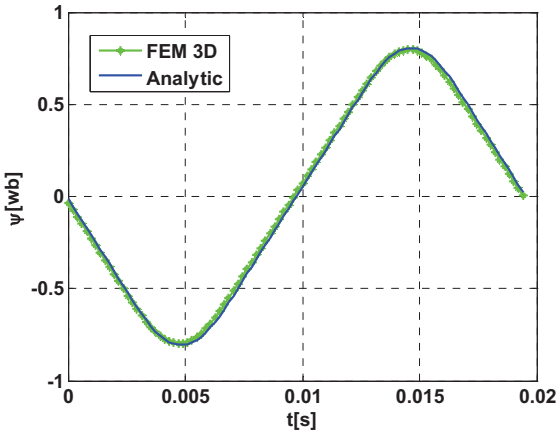

Fig 11: Flux linked by the winding

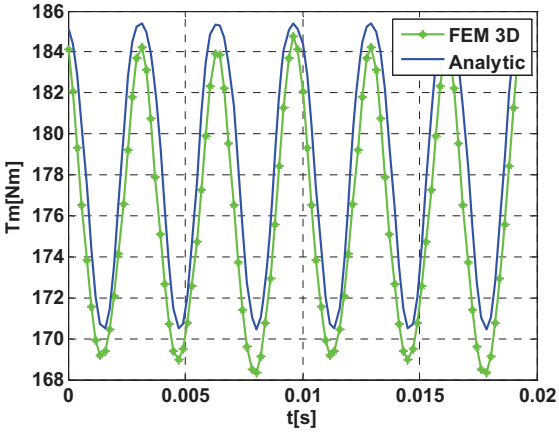

Fig 12: Mutual component of the electromagnetic torque

TABLE II.
CALCULATED INDUCTANCES

	L_g[mH]	L_{ew} [mH]	L [mH]
FEM 3D	2.97	0.5082	3.4782
Analytic	2.9249	0.5237	3.4486

V. CONCLUSIONS

In this work the complete mathematical representation of axial flux PM synchronous machines based on Fourier series is proposed. Electromagnetic variables are defined as the sum of space-time harmonics and the couplings between different components are well identified. Amplitudes of these components are directly related to design variables such as magnetic and mechanical properties of magnets, winding conductor distribution or dimensions of the machine geometry. By this way a parametric model is developed. So using the proposed model, an iterative optimization of the machine design may be performed in a relatively easy and quick way.

The accuracy of the model has been evaluated comparing the results with that obtained by numerical analysis in FEM3D. In case the magnets are radially proportional, it has been demonstrated that the proposed analytical model is valid.

VI. REFEENCES

[1] Z.Q. Zhu, D. Howe, E. Bolte and B. Ackermann, "Instantaneous Magnetic Fiel Distribution in Brushless Permanent Magnet DC Motors I: Open-circuit Field", *IEEE Transactions on Magnetics, vol. 29, no. 1, pp. 124-135, 1993*

[2] Z.Q. Zhu, D. Howe, E. Bolte and B. Ackermann, "Instantaneous Magnetic Fiel Distribution in Brushless Permanent Magnet DC Motors II: Armature Reaction Field", I*EEE Transactions on Magnetics, vol. 29, no. 1, pp. 136-142, 1993*

[3] Z.Q. Zhu, D. Howe, E. Bolte and B. Ackermann, "Instantaneous Magnetic Fiel Distribution in Brushless Permanent Magnet DC Motors III: Effect of Stator Slotting", *IEEE Transactions on Magnetics, vol. 29, no. 1, pp. 143-151, 1993*

[4] Z.Q. Zhu, D. Howe, E. Bolte and B. Ackermann, "Instantaneous Magnetic Fiel Distribution in Brushless Permanent Magnet DC Motors IV: Magnetic Field on Load", *IEEE Transactions on Magnetics, vol. 29, no. 1, pp. 152-158, 1993*

[5] Z. Q. Zhu and D. Howe, "Analytical prediction of the cogging torque in radial-field permanent magnet brushless motors", *IEEE Transactions on Magnetics, vol. 28, no. 2, pp. 1371-1374, 1992*

[6] A.B. Proca, A. Keyhani, A. El-Antably, W. Lu and M. Dai, "Analytical Model for Permanent Magnet Motors with Surface Mounted Magnets",*2003*

[7] G. Almandoz, J. Poza, M.A. Rodríguez and A. González, "Analytic Model of a PMSM Considering Spatial Harmonics", *Speedam, 2008.*

[8] S. Huang, J. Lou, F. Leonardi and T.A. Lipo, "A Comparison of Power Density for Axial Flux Machines Based on General Purpose Sizing Equations", *IEEE Transactions on Energy Conversion, vol. 14 no. 2, June 1999.*

[9] M. Aydin, S. Huang and T.A. Lipo, "Design and 3D Electromagnetic Field Analysis of Non-slotted and Slotted TORUS Type Axial Flux Surface Mounted Permanent Magnet Disc Machines", *IEEE International Electric Machines and Drives Conference, IEMDC 2001.*

[10] A. Parviainen, "Design of Axial-flux Permanent Magnet Low-speed Machines and Performance Comparison between Radial-flux and Axial-flux Machines", *Lappeenranta University of technology, April 2005*

[11] F. Sahin. "Design and Development of High-Speed Axial-flux Permanent Magnet Machines." *Technische Universiteit Eindhoven, 2001*

[12] J.R. Hendershot and T. Miller, "Design of Brushless Permanent-Magnet Motors" *Magna Physics Publishing and Claredon press, Oxford 1994*

[13] D. Hanselman, "Brushless Permanent Magnet Motor Design" *The Writers´ Collective, 2003*

Modelado FEM 3D de Máquinas Síncronas de Imanes Permanentes y Flujo Axial

A.Egea*[1], G.Almandoz[1], J.Poza[1] and A.Gonzalez[2]
1 Mondragon unibertsitatea/Escuela Politécnica Superior, Arrasate
2 ORONA Elevator Innovation Centre, Hernani

***Abstract*—En los últimos años debido en gran medida a las mejoras en la calidad de los materiales y en las técnicas de fabricación, las máquinas síncronas de imanes permanentes en general y en concreto la topología de flujo axial está adquiriendo un protagonismo cada vez mayor. Las herramientas numéricas basadas en métodos de elementos finitos (FEM) resultan de gran ayuda a la hora de diseñar este tipo de máquinas. Sin embargo debido a la estructura constructiva de las mismas, para poder hacer un análisis más profundo es necesario llevar a cabo estudios tridimensionales. Cabe destacar la complejidad de este tipo de simulaciones en comparación con las bidimensionales. En este artículo se expone la metodología utilizada para la simulación tridimensional de las máquinas axiales y se hace especial hincapié en detalles o consideraciones inherentes a estas simulaciones.**

***Keywords*— FEM 3D, Flujo axial, Máquinas síncronas de imanes permanentes.**

I. Introducción

Hoy en día los accionamientos eléctricos tienden hacia soluciones cada vez más compactas, con reducidos costes de mantenimiento, confortables y respetuosos con el medio ambiente. En este marco de trabajo las máquinas síncronas de imanes permanentes (PMSM) se presentan cono una de las topologías que mejor se ajusta a estos requisitos.

Entre las topologías de PMSM, las máquinas de flujo axial están consideradas realmente interesantes para cierto tipo de aplicaciones como es el caso de vehículos eléctricos o ascensores. Las características intrínsecas de las máquinas axiales las hacen muy adecuadas en situaciones en las que la estrechez es importante. Además la densidad de potencia de las máquinas axiales puede ser mayor que la de las máquinas de flujo radial, traduciéndose en una considerable reducción del volumen total [1].

En aplicaciones *direct-drive* o de accionamiento directo un ajuste óptimo del diseño de la máquina eléctrica es fundamental. En consecuencia, el proceso de diseño puede necesitar de un alto número de iteraciones. La utilización de tan solo herramientas de elementos finitos (FEM) a la hora de realizar el diseño podría conducir a tiempos de computación muy extensos. Sin embargo, tras un primer diseño basado en modelos analíticos el estudio mediante FEM se hace fundamental.

*Beca para formación y perfeccionamiento de personal investigador del departamento de educación del Gobierno Vasco.

La resolución de problemas electromagnéticos mediante FEM en dos dimensiones (FEM-2D) es un ámbito bastante conocido y la cantidad de información existente es muy extensa. Sin embargo, debido a las características constructivas de la máquina axial el problema que se presenta es de naturaleza tridimensional, con lo que normalmente es necesario llevar a cabo simulaciones tridimensionales en elementos finitos (FEM-3D). De todas maneras ciertos autores plantean la opción de extrapolar el problema FEM-3D de la máquina axial a una aproximación FEM-2D en el radio medio de la máquina como se muestra en la Fig 1 [2-4]. Sin embargo, esta aproximación sólo puede ser válida para aquellos casos en los que las dimensiones de la máquina sean proporcionales al radio. Para superar esta limitación algunos autores proponen un análisis denominado *quasi-3D* , el cual consiste en analizar diferentes planos 2D de la máquina obtenidos para diferentes valores de radio [5]. De esta forma se obtienen unos resultados más precisos cuanto mayor sea el número de planos analizados. De todos modos, obviamente los resultados que mejor se ajustan a la realidad se obtienen en FEM-3D, sobre todo en cuanto a saturaciones y pérdidas magnéticas se refiere. Además ésta es la forma más correcta de computar la inductancia de dispersión asociada a las cabezas de bobina.

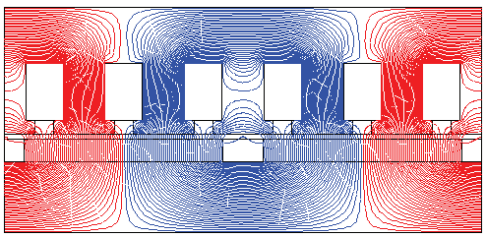

Fig 1: Líneas de flujo sobre un problema simplificado FEM-2D en el radio medio de una máquina axial

Uno de los mayores problemas de las simulaciones de las máquinas axiales en FEM-3D es que aunque se pueda encontrar cierta información en la literatura [6-10], esta no es muy detallada por lo que puede resultar un proceso bastante tedioso. Además el tiempo computacional y la carga de cálculo de las simulaciones FEM-3D son por lo general mucho más extensos que en las simulaciones FEM-2D.

El objetivo de este artículo es presentar una metodología simple para la simulación de una máquina axial en el software FLUX3D de la compañía Cedrat®. Además se pretenden enumerar las principales características de las simulaciones FEM-3D y también las consideraciones a tener en cuenta a la

hora de ejecutar una simulación de este tipo. Para ello se expondrán los pasos seguidos a la hora de definir y resolver el problema, y se mostrarán los resultados más relevantes.

II. MÁQUINA MODELO

La máquina modelada es una máquina síncrona de imanes permanentes y flujo axial. En este caso se ha optado por una máquina denominada como de doble cara, el cual consta de dos rotores de imanes superficiales y un estator interior con un devanado toroidal. Los detalles de la máquina se muestran en la Fig 2.

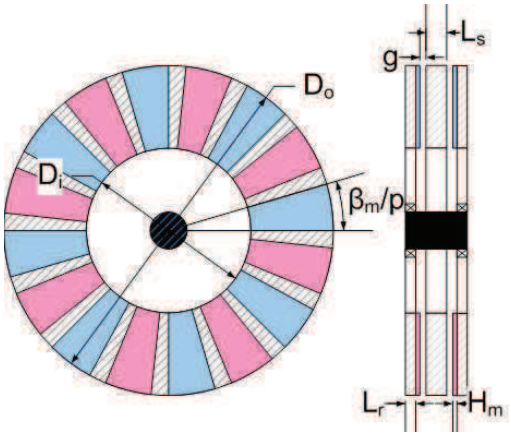

Fig 2: Plano de la máquina analizada

Cada rotor está compuesto por 8 pares de polos, siendo estos imanes de neodimio. El estator dispone de $Q_s=18$ ranuras. El termino ranuras en este caso se refiere al número de bobinas, ya que el estator no dispone de ranuras físicas. El diámetro interior tanto del rotor como del estator es de $D_i=216mm$ mientras que el diámetro exterior es de $D_o=400mm$.

El entrehierro es de $g=4mm$ de forma que los conductores quepan en ese espacio. Los conductores se distribuyen en el espacio disponible entre el núcleo magnético de estator y del entrehierro. Estos conductores se colocan en dos capas, una por cada bobina, siendo el diámetro de cada uno de ellos de 1.45mm (AWG#15). El entrehierro efectivo es de entorno a 1.1mm. La densidad de corriente es de $J=8.48\ A/mm^2$. Todo esto se muestra gráficamente en la Fig 3.

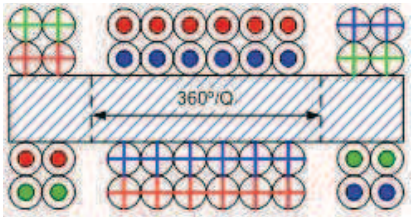

Fig 3: Colocación de los conductores

Lo imanes seleccionados son de grado N30H. Su remanencia es $Br=1.08T$ y el valor coercitivo $Hc=780KA/m$. Todos los imanes están magnetizados en dirección normal y su altura es de $hm=4mm$.

Con las dimensiones mencionadas la carga eléctrica de la maquina en el diámetro interior es de $A=3400\ A/m$ y el volumen de la máquina es de entorno a $6.8\ cm^3$.

Todos estos parámetros se muestran más detalladamente en la TABLA I.

TABLA I
Características de la máquina modelada

g	Entrehierro	4 mm
L_s	Longitud del núcleo del estator	18 mm
L_r	Longitud del núcleo del rotor	9.5 mm
Q_s	Número de ranuras del estator	18
D_o	Diámetro exterior	400 mm
D_i	Diámetro interior	216 mm
h_m	Altura del imán	4 mm
β_m	Arco del polo	150º
B_r	Densidad de flujo remanente de los imanes	1.08T
μ_r	Permeabilidad relativa de los imanes	1.08
p	Número de pares de polos	8
N_{ph}	Número de vueltas por fase	276
h	Número de caras	2
Ief	Corriente eficaz	14 A
J	Densidad de corriente	8.48 A/mm^2
A	Carga eléctrica	34000A/m
V	Volumen total	6.8 cm^3

III. MÉTODO DE SIMULACIÓN

En este apartado se procede a explicar detalladamente los pasos que se han seguido para una correcta simulación en FLUX3D. Básicamente el proceso que se sigue es el que se muestra en el diagrama de la Fig 4.

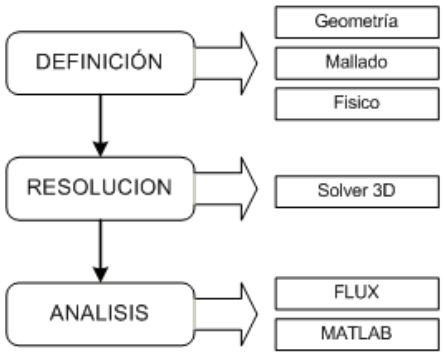

Fig 4: Diagrama del método de simulación

A. Definición del problema

El problema a tratar es el análisis de una máquina de flujo axial, por lo que se utiliza FLUX3D, definiendo el problema como magneto transitorio. Aquí se definen la geometría, el mallado y el apartado físico del problema.

1) Definición de la geometría

Al tratarse de una máquina de 18 ranuras y 8 pares de polos la periodicidad de la máquina es T_p=2, por lo que con definir la mitad de la máquina y aplicar una periodicidad es suficiente.

Además al ser la máquina simétrica solo es necesario definir un lado. En la Fig 5 se muestran los volúmenes definidos con sus respectivas regiones.

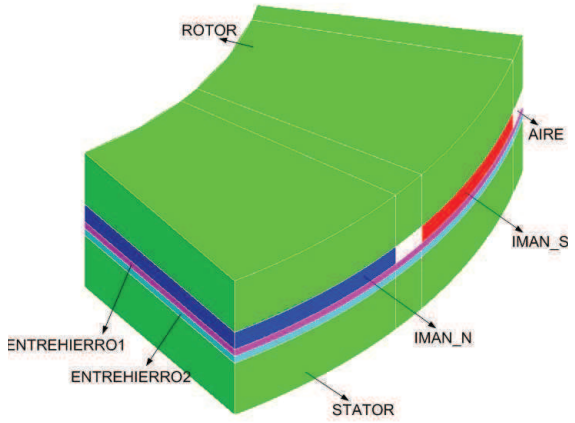

Fig 5: Volúmenes y regiones definidos

Las regiones *Rotor*, *Imán*, *Aire* y *Entrehierro1* completan la parte del rotor de la máquina. Estas regiones forman parte de la definición mecánica móvil, mientras que el estator es fijo. En el caso del entrehierro este se divide en dos regiones diferentes, ya que se recomienda que el movimiento se produzca entre dos superficies que corresponden al mismo medio. Con esto, la región *Entrehierro1* se define como móvil mientras que la región *Entrehierro2* se define como fija, perteneciendo ambos dos a un medio vacío.

2) Definición del mallado

La densidad del mallado es una de las variables que más influye al tiempo de computación como tal, pero también al tiempo de definición del problema. Por ello es recomendable definir un mallado mapeado, es decir dividido en sectores rectangulares como se muestra en la Fig 6, con tal de reducir tiempos. Esto permite la obtención de un mallado con el que el tiempo de computación no es demasiado extenso, sin comprometer por ello la calidad de los resultados obtenidos.

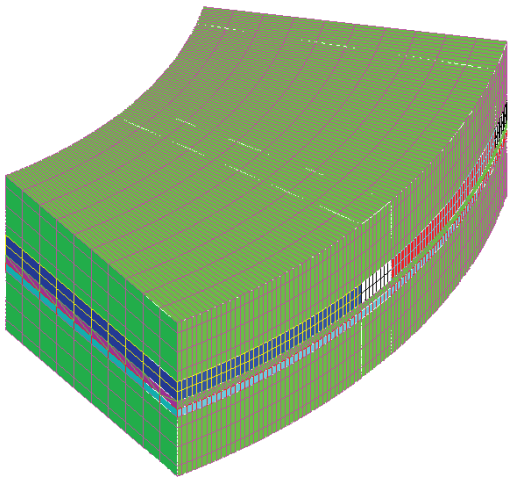

Fig 6: Mallado de los volúmenes

Por un lado las líneas de la geometría del estator y del rotor no tienen por qué coincidir, sobre todo si resulta ser un estator ranurado. Por otro lado si se realizara un mallado mapeado en ambos volúmenes del entrehierro habría que hacer coincidir el paso de giro para que el mallado quedase alineado en cada paso. Debido a estas dos razones se opta por mallar uno de los volúmenes del entrehierro con sectores triangulares. El detalle del mallado en las regiones del entrehierro se muestra en la siguiente figura.

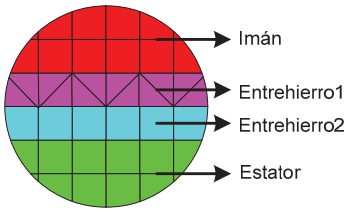

Fig 7: Detalle del mallado en las regiones del entrehierro

El número de sectores del mallado tanto en el sentido de giro como en la dirección radial es crítico desde el punto de vista del tiempo de computación. Sin embargo, es recomendable que en el sentido radial el número de sectores sea par para que así se dispongan de nodos del mallado en el radio medio del entrehierro. Esto es importante en caso de que se pretenda comparar la inducción obtenida en el entrehierro con los resultados obtenidos con las herramientas analíticas o incluso en FEM-2D donde la máquina se analiza justo en el radio medio.

3) Definición física

Flux ofrece dos opciones para la inclusión de componentes eléctricos. Por un lado cabe la posibilidad de determinar corrientes en ciertas regiones .La segunda opción es la de acoplar un circuito eléctrico al problema electromagnético. Esta última resulta la más intuitiva.

Con dos ensayos, uno en circuito abierto y otro en carga se obtiene suficiente información para caracterizar la máquina. En ambos casos la máquina se conecta en estrella y la colocación de una tierra es indispensable. Sin embargo, en el caso del ensayo en circuito abierto han de colocarse unas resistencias *R* de alto valor resistivo en serie con las bobinas de cada fase, Fig 8a). En el caso de circuito en carga, dos de las fases son alimentadas con sendas fuentes de corriente *I*, siendo la corriente de la tercera fase la resultante de una alimentación equilibrada, Fig 8 b).

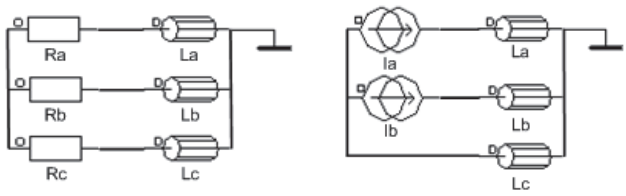

a) b)

Fig 8: Circuito eléctrico de la máquina, a) en circuito abierto y b) en carga.

En cuanto a la colocación de las bobinas, *non-meshed coil,* Fig 9, la mayor restricción es que éstas no pueden estar en contacto con el núcleo magnético del estator si se quieren obtener unos resultados adecuados. La forma de estas

dependerá del análisis a realizar, pero cuanto más se parezcan a la disposición final el resultado será más acorde a la realidad.

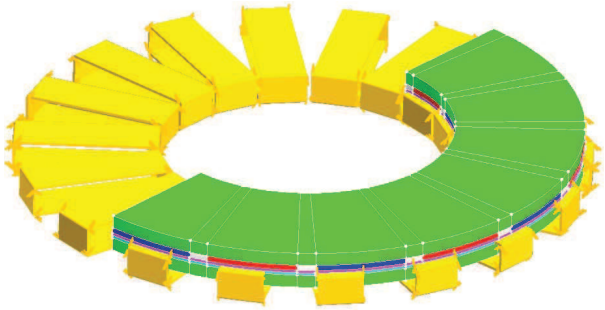

Fig 9: Colocación de las bobinas

Por último han de definirse diferentes materiales así como sus propiedades. En el entorno 3D dos son las propiedades mecánicas a definir, por un lado el movimiento y por otro el fijo.

B. Resolución del problema. Solver

Los modelos magnéticos en régimen transitorio se rigen por medio de las ecuaciones de Maxwell formuladas de forma quasi-estática, en las cuales no se consideran las corrientes de desplazamiento.

$$\vec{\nabla}\cdot\vec{B}=0$$
$$\vec{\nabla}\times\vec{H}=\vec{J} \qquad (1)$$
$$\vec{\nabla}\times\vec{E}=-\frac{\partial\vec{B}}{\partial t}$$

Siendo $\nabla\cdot$ el operador divergente, ∇x el operador rotacional, B el campo magnético, H la intensidad del campo magnético, J la densidad de corriente y E el campo eléctrico. Además de estas ecuaciones el problema electromagnético considera las siguientes leyes constitutivas.

$$\vec{B}=[\mu]\cdot\vec{H}$$
$$\vec{J}=[\sigma]\cdot\vec{E} \qquad (2)$$

Donde μ es la permeabilidad magnética del medio y σ es la conductividad eléctrica del medio.

La resolución de un problema en elementos finitos consiste en minimizar el valor residual de una función objetivo. Luego como resultado de esta resolución se obtiene una variable de salida denominada variable de estado. En cuanto al software FLUX hace referencia, la resolución de problemas FEM2D y FEM3D se diferencian por una parte en la función objetivo a minimizar, y por otra parte en la variable de estado. En el caso de FEM2D la variable de estado es el vector potencial magnético A, mientras que en el caso de FEM3D es el potencial escalar magnético ϕ. Por otra parte, en problemas FEM2D, la función objetivo es única en todas las regiones del problema y es la que se especifica a continuación,

$$\vec{\nabla}\times\left(v_o\cdot[v_r]\cdot\left(\vec{\nabla}\times\vec{A}\right)-\vec{H}_c\right)=J \qquad (3)$$

Siendo v_o la reluctividad magnética del medio vacío, v_r la reluctividad relativa del medio magnético, H_c la fuerza coercitiva del campo magnético y A el potencial vector magnético.

En problemas FEM3D la función objetivo no es única sino que cambia de una región a otra. De todas formas existe una notación general que sirve para todo tipo de región, el cual se detalla a continuación.

$$\nabla\cdot\left([\mu_r]\cdot\mu_o\cdot\left(-grad(\phi)+\vec{T}\right)+\vec{B}_r\right)=0 \qquad (4)$$

Donde μ_o es la permeabilidad magnética del medio vacío, μ_r es la permeabilidad relativa del medio magnético, ϕ es el potencial escalar magnético, T es un término que depende de las fuentes de corriente de la región y Br es la remanencia del campo magnético de los imanes permanentes. Esta denotación general varía de una región a otra dependiendo de si hay o no fuentes de corriente en la región, y dependiendo de si las fuentes de corriente corresponden a un medio mallado o sin mallar. Lo que cambia en cada caso es el término T y el potencial escalar magnético ϕ [11].

Por ejemplo, cuando se trata de una región sin fuentes de corriente la densidad de corriente J es nula. En este caso $T=0$, el potencial escalar magnético ϕ_t es total y la intensidad de campo se define como,

$$\vec{H}=-grad\phi_t \qquad (5)$$

Cuando se trata de regiones con fuentes de corriente y no malladas, el potencial escalar magnético ϕ_{rHj} está relativizado con respecto a H_j, y $T=H_j$, siendo H_j la intensidad del campo magnético creado por las bobinas no malladas. Este campo se computa analíticamente mediante la ley de *Biot-Savart*. En estas regiones la intensidad de campo total se define como,

$$\vec{H}=-grad\phi_{rHj}+\vec{H}_j \qquad (6)$$

La tercera de las opciones es cuando se trata de una región conductora y mallada. En este caso el potencial escalar magnético ϕ_{rTo} está también relativizado pero con respecto a T_o. La intensidad de campo se define por lo tanto como,

$$\vec{H}=-grad\phi_{rToj}+\vec{T}_o \qquad (7)$$

C. Post-Proceso. Análisis de Resultados

Una vez resuelto el problema magnético se obtiene como salida la variable de estado, que en este caso es un potencial escalar magnético característico a cada región. Luego todos los resultados se derivan a partir de esta variable. Los resultados se pueden diferenciar como locales o globales. Los locales son aquellos que se calculan en cada nodo del mallado, como por ejemplo el campo magnético. Mientras que los globales son los que se obtienen de integrar las variables locales a lo largo de una región, como por ejemplo el flujo magnético que atraviesa una superficie.

La primera variable local que se deriva del potencial escalar magnético es la intensidad del campo magnético. Hay tres formas diferentes de calcular esta variable dependiendo de la naturaleza de la región tal y como se ha señalado anteriormente.

$$\vec{H} = -gr\vec{a}d\phi$$
$$\vec{H} = -gr\vec{a}d\phi_{rHj} + \vec{H}_j \quad (8)$$
$$\vec{H} = -gr\vec{a}d\phi_{rTo} + \vec{T}_o$$

Otra variable muy típica es el campo magnético, el cual se calcula a partir de la intensidad de campo aplicando la ley constitutiva definida en (2). Entre las variables globales más comunes en el análisis de máquinas se encuentra la energía magnética W_m almacenada en un volumen.

$$W_m = \int_V \int_0^B \vec{H} \cdot d\vec{B} \quad (9)$$

V es volumen de la región. Otro parámetro interesante es el par electromagnético T_{em} el cuál se determina mediante el método del trabajo virtual.

$$T_{em} = \frac{\partial W_m}{\partial \theta} \quad (10)$$

θ es la posición del rotor. Otro resultado muy típico es el flujo magnético total Ψ enlazado por una bobina de N espiras,

$$\Psi = N \int_S \vec{B} \cdot d\vec{s} \quad (11)$$

Siendo S la superficie delimitada por una espira. A partir de este flujo se pueden derivar la fuerza electromotriz inducida FEM en los conductores y el valor L de la inductancia.

$$FEM = \frac{d\Psi}{dt} \quad (12)$$

$$L = \frac{\Psi}{i} \quad (13)$$

Siendo i la corriente que atraviesa el conductor.

IV. Análisis y Caracterización de la Máquina Axial en Simulación FEM3D

En este apartado se analizan los resultados de simulación en FEM3D de la máquina axial que se ha descrito previamente. El análisis se centra por un lado en las prestaciones electromagnéticos de la maquina como pueden ser los niveles de inducción, el flujo enlazado por fase o el par electromagnético. Por otra parte se procede también con la obtención de los parámetros del circuito eléctrico equivalente haciendo especial hincapié en el cálculo de la inductancia de fase.

En cuanto al nivel de inducción este se puede analizar en todo el volumen tanto en carga como en circuito abierto, Fig 10, siendo muy útil para la identificación de saturaciones locales.

Por otro lado, otro dato relevante es el campo en el entrehierro ya que las prestaciones del motor están condicionadas en gran medida a este parámetro. En la Fig 11 se muestra la distribución espacial de este campo medido a la altura del radio medio.

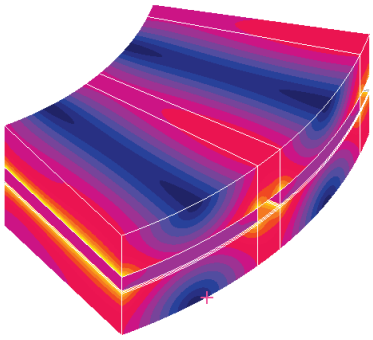

Fig 10: Nivel de inducción de la máquina en circuito abierto

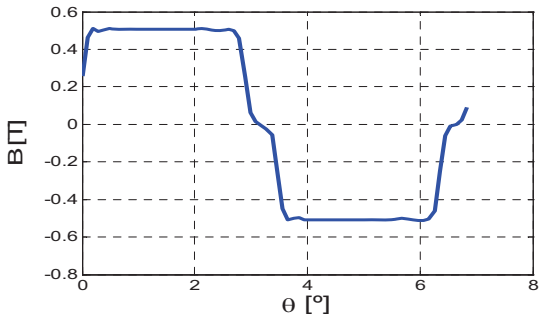

Fig 11: Campo en el entrehierro

El análisis del flujo enlazado por fase en circuito abierto y el de la tensión inducida se podría tomar como uno, ya que el segundo término se deriva del primero (12). En este caso el flujo enlazado por fase es el que se muestran en la Fig 12.

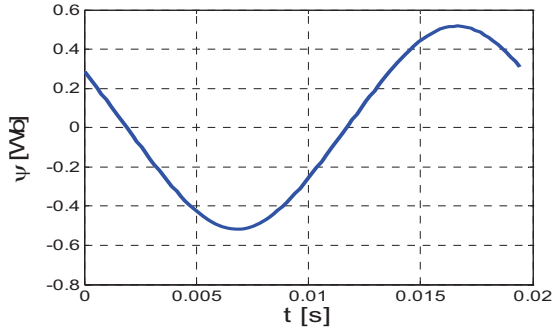

Fig 12: Flujo enlazado

Finalmente el último parámetro analizado es el par electromagnético. En la Fig 13 se muestra la evolución temporal del par cuando se simula el circuito en carga nominal.

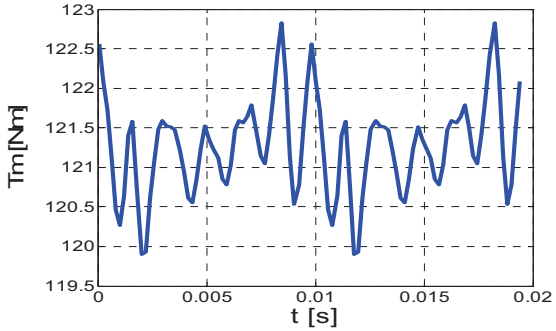

Fig 13: Par electromagnético

Si el objetivo fuese analizar el rizado con una mayor precisión habría que aumentar la resolución disminuyendo el paso de cálculo definido en la resolución del problema. Sin embargo para determinar el par medio y tener una referencia aproximada del rizado de par la resolución adoptada es suficiente.

En cuanto al circuito eléctrico equivalente, el análisis en 3D resulta muy útil para la obtención de la inductancia de fase. La inductancia obtenida contemplara tanto la inductancia asociada a los conductores activos como la correspondiente a cabezas de bobina. El método que se aplica consiste en transformar tantos los flujos trifásicos Ψ_{abc} y las corrientes I_{abc} a un sistema de ejes de referencia *dq* giratorio y asociado al campo de los imanes. Una vez obtenidas las componentes I_{dq} y Ψ_{dq} el cálculo de la inductancia es inmediato a partir de las ecuación (14).

$$\begin{aligned} \psi_d\left(i_d, i_q\right) &= \psi_{pm} + L_d \cdot I_d \\ \psi_q\left(i_d, i_q\right) &= L_q \cdot I_q \end{aligned} \qquad (14)$$

Esta notación es general y válida tanto para el caso de máquinas de imanes superficiales como para las de imanes incrustados. En el caso de máquinas de imanes superficiales la inductancia de fase L_s es igual a la del eje q y d (15).

$$L_s = L_d = L_q \qquad (15)$$

El valor de la inductancia depende del nivel de saturación de la máquina. Esta dependencia es más acentuada en máquinas con estator ranurado y de imanes incrustados. En este caso al tratarse de una máquina sin ranuras y de imanes superficiales la inductancia se mantiene prácticamente constante a diferentes niveles de carga tal y como se muestran en la Fig 14.

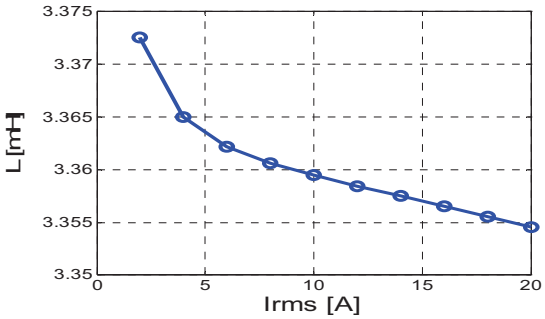

Fig 14: Inductancia de fase según la carga eléctrica

V. Conclusión

En este artículo por una parte se han descrito las simulaciones FEM-3D en general, haciendo especial hincapié en detalles diferenciadores con respecto a las simulaciones FEM-2D. Se han proporcionado unas nociones básicas para poder definir y resolver problemas, y analizar los resultados a posteriori. Por otra parte se ha abordado la simulación FEM-3D de una máquina axial de imanes permanentes y se ha descrito la caracterización de la misma.

Por lo general las simulaciones FEM-3D son más complicadas de ejecutar que las de FEM-2D. La definición del problema es más ardua, en gran medida debido al mallado, y el tiempo de cálculo así como la carga computacional son mucho mayores.
Aunque este articulo se centra exclusivamente en el análisis FEM-3D, hay que subrayar que la metodología de diseño óptima en cuanto a tiempos de desarrollo se refiere, es aquella que combina las simulaciones FEM-3D con simulaciones FEM-2D y con las herramientas analíticas. Las herramientas analíticas son muy útiles para acotar el diseño y perfilar un esbozo inicial de la máquina. Las simulaciones FEM-2D permiten evaluar las prestaciones de la máquina axial con una precisión más que aceptable, pero no lo suficientemente preciso. Para obtener una mejor precisión y afinar el diseño en la mejor medida posible se recurre a las simulaciones FEM-3D.
Por último resaltar que en este articulo no se describe la caracterización completa de la máquina. Aunque se han calculado gran parte de las prestaciones, faltaría el cálculo de la eficiencia, para lo cual es necesario abordar el tema de las pérdidas. El cálculo de las pérdidas por sí ya es lo bastante complicado en FEM-2D, y en FEM-3D lo es todavía un poco más. Esta tarea se perfila como posible línea futura para completar la metodología de análisis propuesta.

VI. Referencias bibliográficas

[1] J. K. Gieras, R. J. Wang, and M. J. Kamper, *Axial Flux Permanent Magnet Brushless Machines* Springer, 2005.

[2] F. Caricchi, F. Crescimbini, and E. Santini, "Basic Principle and Design Criteria of Axial-Flux PM Machines Having Counterrotating Rotors," *IEEE TRANSACTIONS ON INDUSTRY APPLICATIONS,* vol. 31 No.5 1995.

[3] M. Hörz, H. G. Herzog, and A. Haas, "Axial flux machine with single tooth fractional slot winding - Comparison of different winding design approaches,", SPEEDAM ed 2006.

[4] T. F. Chan, L. L. Lai, and S. Xie, "Field Computation for an Axial Flux Permanent-Magnet Synchronous Generator," *IEEE TRANSACTIONS ON ENERGY CONVERSION*, vol. 24 No.1 2009.

[5] A. Parviainen, M. Niemelä, and J. Pyrhönen, "Modeling of Axial Flux Permanent-Magnet Machines," *IEEE TRANSACTIONS ON INDUSTRY APPLICATIONS,* vol. 40 No.5 2004.

[6] D. González, J. A. Tapia, R. Wallace, and A. Valenzuela, "Magnetic Design Considerations for an Axial Flux PM Machine with Field Control Capability.,", N. 51 CEDRAT - CEDRAT TECHNOLOGIES - MAGSOFT Corp. ed 2006.

[7] A. Parviainen and P. Kontkanen, "Axial Flux Permanent Magnet Generator for Wind Power Applications.,", N.48 CEDRAT - CEDRAT TECHNOLOGIES - MAGSOFT Corp. ed 2005.

[8] C. Boccaletti, C. Bruzzese, E. Santini, and P. Sordi, "ACCURATE DESIGN OF AXIAL FLUX PM SYNCHRONOUS MACHINES BY MEANS OF 3D FINITE ELEMENT ANALYSIS," 2009.

[9] S. Huang, M. Aydin, and T. A. Lipo, "TORUS Concept Machines:Pre-Prototyping Design Assessment for Two Major Topologies," 2009.

[10] W. Fei, P. C. K. Luk, and K. Jinupun, "A New Axial Flux Permanent Magnet Segmented-Armature-Torus Machine for In-Wheel Direct Drive Applications," 2008.

[11] FLUX 10. User's guide. Volume 3. Physical Applications: Magnetic, Electric, Thermal. 2007

Axial Flux machines modelling with the combination of 2D FEM and analytic tools

A. Egea*[1], G. Almandoz[1], J. Poza[1], A. Gonzalez[2]
1 University of Mondragon/Faculty of Engineering, Mondragon, (Spain)
2 ORONA Elevator Innovation Centre, Hernani, (Spain)

***Abstract* – This paper deals with the development of performance analysis tools for axial flux permanent magnet machines. Modeling with 3D Finite Element Method (FEM3D) software could take too much time, and both the definition and the problem solving may be very arduous.**

In this work an analysis method for axial flux machines is proposed. This method consists in the combination of FEM2D simulations in the average radius plane with analytical models. The obtained results prove that the proposed method could be a very interesting option in terms of time and accuracy.

***Index Terms*— Axial flux machines, FEM, analytic models.**

I. Introduction

In the last few years the importance of the axial flux machines has been increasing in sectors like the elevation or the electric transport [1;2]. One of the most common types of these machines is the permanent magnet synchronous machine PMSM, which is the case of the analysis in this paper.

The analysis of axial flux machines involves a tri-dimensional electromagnetic problem. So the most accurate mode for modeling the machine is by three dimensional finite element method FEM3D [3;4]. Anyway, this method is high time consuming and both, the definition of the problem and the solving process are quite tedious. As alternative solution different analysis methods can be performed. One of these methods consists in carrying out simulations using two dimensional finite element method FEM2D. The 2D geometry is obtained in a plane which is normally situated at the average radius of the machine[5] . Performing simulations in FEM2D is much easier and faster than FEM3D. However this solution may not be valid in non-linear problems with saturation effects, or in case the geometry of the machine is not radially proportional. Another possible solution appearing in the literature which is known as quasi-FEM3D method consists in carrying out FEM2D simulations in different planes of the machine. The precision of this method depends on the number of evaluated planes [6]. Thus the more planes are used the more accurate the results are. Nevertheless it must be considered that the time consumption of the simulations is directly proportional to the number of planes. On the other hand it is also possible to find analytical solutions in the literature, such as reluctance networks or Fourier series. For example, in [7;8] a quasi 3D analytical solution is proposed.

In this paper a novel method for axial flux machine analysis which consists in the combination of analytical tools with FEM2D simulations is presented. First the different constraints related to FEM2D simulations are mentioned, then the proposed method is explained in detail and finally it is validated comparing the results with that obtained by FEM3D simulations and by FEM2D simulations performed in the average radius plane. It is remarkable that using the proposed method the end winding inductances cannot be calculated. Hence, an analytic approximation or FEM3D simulations should be done for that purpose.

II. FEM2D Simulations in the Average Radius Plane

The FEM2D approximation consists basically on taking a plane of the axial machine in a certain radius, usually the average radius. This process is shown in Fig 1.

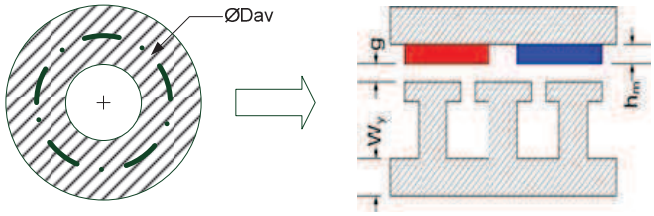

Fig 1: Process of picking a plane for the 2D approximation.

As mentioned before, FEM2D approximation is faster and it requires less calculation load in comparison with FEM3D analysis. However the results may not be so accurate due to two main reasons.

The first reason consists on the non linearity of the magnetic materials. This non linearity could cause a different saturation level in the different radius of the magnetic cores. This phenomenon is not possible to consider in the FEM2D approximation.

The second reason is the geometrical shape of the machine. This work is focused in this particular problem. In the FEM2D approximation the geometry is supposed to be radially proportional as shown in Fig 2 a), Fig 3 a) and Fig 4 a). It means that the dimensions of any 2D plane obtained for a specific radius value are proportional to this radius value. Nevertheless this condition may not be always fulfilled. For example when the distribution of the conductors in a slotless machine is rectangular instead of trapezoidal (see Fig 2), when the magnets are rectangular instead of trapezoidal (see Fig 4b), or when the slots are parallel instead of radial (see Fig 3b). In the following part these three issues are deeply explained.

This Ph.D. student holds a grant from the Basque government*

This work has been partially supported by the CDTI CENIT project NET0LIFT from the Spanish Government

A. Spatial distribution of the conductors in a slotless stator

The first analyzed option is the spatial distribution of the conductors in non slotted machines. A constant span of the conductors is only possible with trapezoidal shape placing, Fig 2 a). Actually this is quite difficult to accomplish and usually the conductor are placed in a rectangular shape, Fig 2 b).

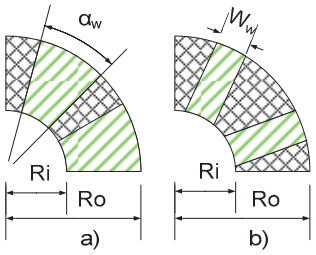

Fig 2: Placing of the coils in a slotless stator a) trapezoidal and b) rectangular

B. Radial distribution of the slots

Another aspect to consider is the radial distribution and the slot opening. In this paper the slot opening effect is not considered and the conductor distribution is taken into account as an equivalent current sheet. This way the span of the current sheet can be radially constant as shown is Fig3-b, or proportional to the radius as shown in Fig 3-a.

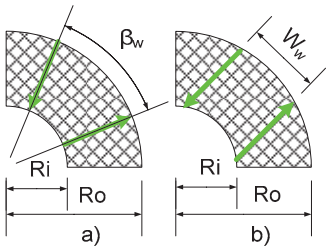

Fig 3: Placing of the slots or punctual conductors a) radial and b) parallel

C. The shape of the magnets

The third and last considered variable is the shape of the magnets. The magnets could be trapezoidal shaped as in Fig 4 a) which would be radial proportional. But due to manufacturing, performance or price reasons the shape of these magnets could be any. For example they could be rectangular as shown in Fig 4 b).

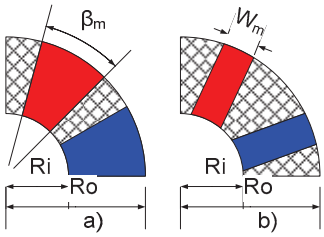

Fig 4: Shape of the magnets a) trapezoidal and b) rectangular

When an axial flux machine is not radially proportional, FEM2D simulations on the average radius plane become not enough. The obtained results would be wrong, being the accuracy of these results not easy to quantify. So the possible options are on the one hand to launch FEM3D simulations or on the other hand the use of analytical tools. Using analytical tools it is possible to post-process the results obtained by FEM2D and reach good results.

How these variables could be taken into account with the help of analytical tool is explained in the next section, then, the obtained results for the mentioned options are presented in the forth section.

III. Proposed Method for the Analysis of Axial Flux Machines: Combination of Analytical Models and FEM2D Simulations

The proposed method is based on the combination of FEM2D simulations with analytical models based on the theory of Fourier series. The proposed methodology is described in the Fig5. In the first stage the machine is simulated by FEM2D considering the average radius plane. Simultaneously some *X* factors which link the FEM2D with the FEM3D results are obtained analytically. Then the FEM2D results are post-processed by the obtained coefficients in order to get the final results. These results are an approximation of the ones would be obtained in FEM 3D.

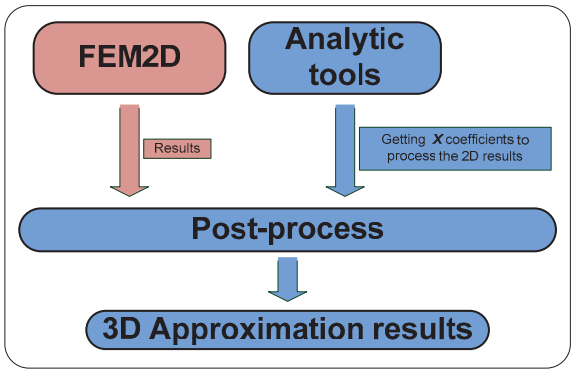

Fig 5: Block diagram of the proposed methodology for axial flux machine analysis

The most relevant performance results of the machine such as the back electromotive force EMF or the electromagnetic torque T_{em}, can be calculated from the magnet flux linked by the armature windings. This way the back electromotive force of each phase is defined as the derivative of the flux linkage of each phase:

$$EMF_x(t) = \frac{d\psi_x}{dt} \tag{1}$$

Once the *EMF* is obtained, the electromagnetic torque can be calculated as:

$$T_{em}(t) = \frac{EMF_a(t)\cdot i_a(t) + EMF_b(t)\cdot i_b(t) + EMF_c(t)\cdot i_c(t)}{\Omega_m} \tag{2}$$

So post-processing the flux linkage calculated in FEM2D it is possible to obtain the *EMF* and the electromagnetic torque for the whole machine geometry.

The magnet flux linked by each phase can be defined in the following way.

$$\psi(t) = \int_S^o B_g^m(t,\theta,r)\cdot F(t,\theta,r)\cdot ds \tag{3}$$

Where B_g^m is the magnetic field induced by the magnets in the air-gap, F is the magneto-motive force per current unit and S is the surface concerning one pole. In case of radial

machines the radius is constant so that the resolution of (3) is much easier than in case of axial flux machines in which the radius is variable. Solving (3) for axial flux machines the following expression can be obtained:

$$\psi(t) = t_p \int_0^{2\pi/t_p} \int_{R_i}^{R_o} r \cdot B_g^m(t,\theta,r) \cdot F(t,\theta,r) \cdot dr \cdot d\theta \quad (4)$$

Where t_p is the periodicity of the machine:

$$t_p = G.C.D.(Q,p) \quad (5)$$

The expression (4) could also be expressed in Fourier series:

$$\psi(t) = t_p \int_0^{2\pi/t_p} \int_{R_i}^{R_{oo}} r \cdot \left[\begin{array}{l} \sum_{n=-\infty}^{\infty} B_{g\_n}^m(r) \cdot \cos(np(-\theta+\varphi_0)) \\ \times \sum_{k=-\infty}^{\infty} F_k(r) \sin(\theta+\lambda_o) \end{array} \right] \cdot dr \cdot d\theta \quad (6)$$

Where $B_{g\_n}^m$ are the coefficients of the spatial components of the magnetic field, φ_o is the initial position of the magnets, F_k are the coefficients of the spatial components of the magneto-motive force per current unit and λ_o is the position of the magnetic potential created by the windings. Both variables, the magnetic field in the air-gap and the magneto-motive force per current unit depend on the radius. The effect of each variable does not depend on the other so each effect could be analyzed independently

A. Analysis of the Magnetic Field Induced by the Magnets in the Air-gap

Ideally the spatial distribution of the magnetic field induced by the magnets in the air gap can be considered as rectangular. Nevertheless, actually there are some fringing flux around the edge of the magnets which change slightly the shape of this distribution as shown in Fig 6.

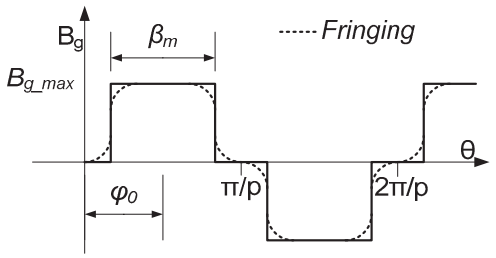

Fig 6: Spatial distribution of B_g

The coefficients of the magnetic field induced by the magnets in the air-gap can be calculated by the following expression:

$$B_{g\_n}^m = \frac{B_{g\max}}{n\pi} \sin\left(np\frac{\beta_m(r)}{2}\right) \frac{1-\cos(n\pi)}{1+(a(r)np)^2} \quad (7)$$

Where p is the number of pole pairs, β_m is the span of the magnets, a the fringing function coefficient and B_{gmax} is the maximum value of the spatial distribution of B_g which is defined as:

$$B_{g\max} = \frac{B_r}{1+\mu_r \frac{g}{h_m}} \quad (8)$$

μ_r is the relative permeability, h_m is the height of the magnets, B_r is the residual value of the magnetic field of the permanent magnets and g is the air-gap length. The fringing function which depends also on the radius can be expressed as:

$$a(r) = \sqrt{\frac{g\left(g + h_m/\mu_r\right)}{2 \cdot r}} \quad (9)$$

Some variables of the expression (6) such as the magnet span and the fringing function depend on the radius. So the values of the coefficients are different in case the magnets are trapezoidal or rectangular. In order to calculate the magnetic flux due to the magnets in the air gap, the following integral must be solved:

$$\Phi_{g\ n}^m \Big|_{\alpha\neq cnt}^{\beta_m\neq cnt} = \frac{B_{g\max}}{n\pi}(1-\cos(n\pi)) \int_{Ri}^{Ro} 2 \cdot r \cdot \frac{\sin\left(n \cdot p \cdot \frac{\beta_m(r)}{2}\right)}{1+(a(r) \cdot n \cdot p)^2} dr \quad (10)$$

It can be noticed that the radial density of the magnetic flux depends on the radius r. In case of trapezoidal magnets the expression (9) can be simplified and it leads to:

$$\Phi_{g\ n}^m \Big|_{\alpha=cnt}^{\beta_m=cnt} = \frac{B_{g\max}}{n\pi}(1-\cos(n\pi)) \frac{\sin\left(n \cdot p \cdot \frac{\beta_m}{2}\right)}{1+(a \cdot n \cdot p)^2} \left(R_o^2 - R_i^2\right) \quad (11)$$

In this case the radial density of the magnetic flux does not depend on the radius r. So from (9) and (10) a correction factor XB_n for each spatial component can be defined as:

$$XB_n = \Phi_{g\ n}^m \Big|_{\alpha\neq cnt}^{\beta_m\neq cnt} \Big/ \Phi_{g\ n}^m \Big|_{\alpha=cnt}^{\beta_m=cnt} \quad (12)$$

Then the correction factor can be applied to the spectrum of the flux linkage obtained from FEM2D simulations in order to calculate the results in 3D:

$$\psi_{n\_3d} = \psi_{n\_2d} \cdot XB_n \quad (13)$$

After that, the temporal flux linkage is calculated applying the Inverse Fast Fourier Transformation (IFFT):

$$\psi_{3d}(t) = \sum_{n=-\infty}^{\infty} \psi_{n\_3d} \sin(np\Omega t - \lambda_o) \quad (14)$$

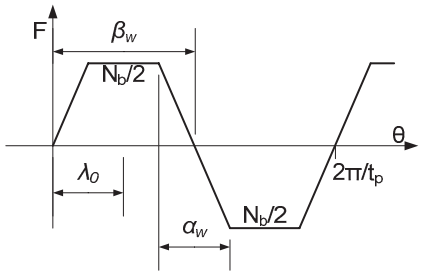

Fig 7: Spatial distribution of the F created by the winding of each phase

B. Analysis of the Magneto Motive Force per Current Unit

The second effect is the one produced by F. In Fig 7 is shown the spatial distribution of this parameter. The expression for each harmonic of F is the following:

$$F_k = \frac{j \cdot N_{ph}}{\pi \cdot k \cdot t_p} \xi_k \tag{15}$$

N_{ph} is the number of turns per phase. ξ is the winding factor, which is the combination of the span factor ξ_{s_k} and pitch factor ξ_{p_k}:

$$\xi_k = \xi_{s\_k} \cdot \xi_{p\_k} \tag{16}$$

The span factor is defined as:

$$\xi_{s\_k} = \sin\left(k \cdot t_p \cdot \frac{\beta_w(r)}{2} \right) \tag{17}$$

And the pitch factor is defined as:

$$\xi_{p\_k} = \frac{\sin\left(k \cdot t_p \cdot \frac{\alpha_w(r)}{2} \right)}{k \cdot t_p \cdot \frac{\alpha_w(r)}{2}} \tag{18}$$

β_w and α_w are the winding span angle and winding pitch angle respectively.

Not all the harmonics of the winding link with the ones of the flux density created by the magnets. The linked harmonics are the ones in the next expression.

$$F_n = F_k \left\{ k = \frac{-n \cdot p}{t_p} \right\} \tag{19}$$

The part of the expression (15) which depends on the radius is:

$$\chi_{g\,n}^{m} \Big|_{\alpha_w \neq cnt}^{\beta_w \neq cnt} = \int_{Ri}^{Ro} 2 \cdot r \cdot \left[\begin{array}{l} \sin\left(n \cdot p \cdot \frac{\beta_w(r)}{2} \right) \\ \times \frac{\sin\left(n \cdot p \cdot \frac{\alpha_w(r)}{2} \right)}{n \cdot p \cdot \frac{\alpha_w(r)}{2}} \end{array} \right] \cdot dr \tag{20}$$

Nevertheless, for a trapezoidal shape of the coils dispersion (β_w and α_w are constant) the expression (20) is simplified and it leads to:

$$\chi_{g\,n}^{m} \Big|_{\alpha_w = cnt}^{\beta_w = cnt} = \left[\begin{array}{l} \sin\left(n \cdot p \cdot \frac{\beta_w}{2} \right) \\ \times \frac{\sin\left(n \cdot p \cdot \frac{\alpha_w}{2} \right)}{n \cdot p \cdot \frac{\alpha_w}{2}} \end{array} \right] \cdot \left(R_o^2 - R_i^2 \right) \tag{21}$$

From (20) and (21) the XF correction factor for each spatial harmonic is:

$$XF_n = \chi_{g\,n}^{m} \Big|_{\alpha_w \neq cnt}^{\beta_w \neq cnt} \Big/ \chi_{g\,n}^{m} \Big|_{\alpha_w = cnt}^{\beta_w = cnt} \tag{22}$$

As in (13) once the XF factor is obtained the calculation of the flux linkage of the 3D machine from the 2D simulations results is immediate:

$$\psi_{n\_3d} = \psi_{n\_2d} \cdot XF_n \tag{23}$$

From this harmonic content of the linked flux is possible to obtain the temporal evolution with the Fourier series as in (14).

IV. Validation of the Proposed Method

Several simulations with three different machines have been made in order to validate the proposed method. The evaluated machines are the toroidal machine with dispersed coils (see Fig 2b), the machine with conductors placed in parallel (see Fig 3 b) and the machine with rectangular magnets (see Fig 4 b) and punctual conductors. All the machines have 48 slots (or coils) and 8 pole pairs.

A. Rectangular shape dispersion coils

In this paper the first analyzed machine is a toroidal non-slotted one. The placing of the coils is in a rectangular shape so that obtained distribution is not radially proportional as shown in Fig 2 b). In the analyzed case the width of each coil is W_w=11mm. In this case the pitch angle α_w depends on the radius and it is defined as:

$$\alpha_w(r) = 2 \arcsin\left(\frac{w_x / 2}{r} \right) \tag{24}$$

In Fig 8 the *EMF* obtained from FEM3D and FEM2D simulations as well as the result obtained with the proposed method are shown. The Fig 9 shows the harmonic content of the EMF. The same is done for the time evolution of the electromagnetic torque in Fig 10

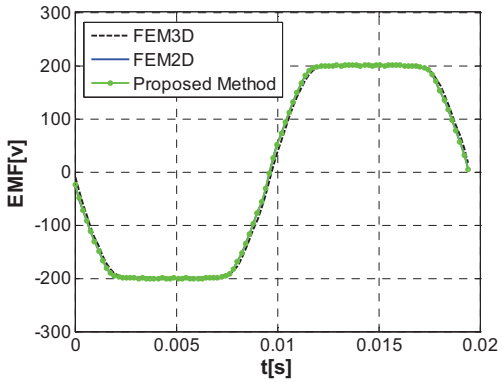

Fig 8: Time evolution of the EMF in the toroidal machine

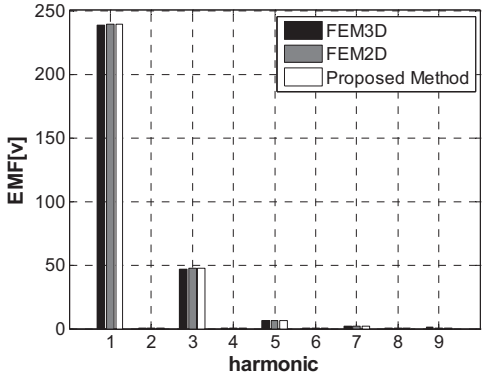

Fig 9: Harmonic components of the EMF in the toroidal machine

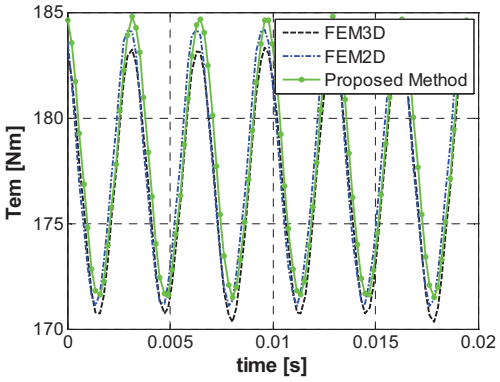

Fig 10: Time evolution of the T_{em} in the toroidal machine

In these figures could be seen that the harmonics are quite similar in the three options. Moreover the main harmonic is almost the same while the weight of higher order harmonics is quite low in comparison with the main one. When the width W_W of the dispersion is narrow the attenuation in the harmonic is not too high while when the coils are wide the *EMF* is more equal to a sinusoidal signal. In this last option the weight of the main harmonic is much more important than higher order harmonics.

Although the *EMF* is practically similar, there is a slight difference in the electromagnetic torque. It can be notice that the proposed method is more accurate than the FEM2D approximation.

B. Straight slots or conductors

The second analyzed situation is when the punctual conductors or the slots are not placed in a radial direction. This is not very common, but in certain circumstances, as manufacturing reason, it could happen. In this paper a case where the punctual conductors are placed in parallel way is analyzed as shown in Fig 3 b).

In Fig 8, the *EMF* obtained from FEM3D and FEM2D simulations as well as the result obtained with the proposed method are shown. The Fig 12 shows the harmonic content of the *EMF*. The same is done for the time evolution of the electromagnetic torque in Fig 13

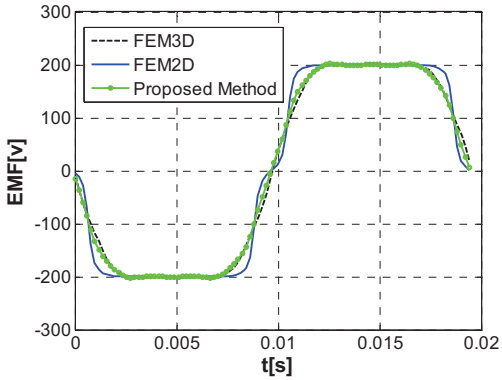

Fig 11: Time evolution of the EMF in the machine with parallel conductors

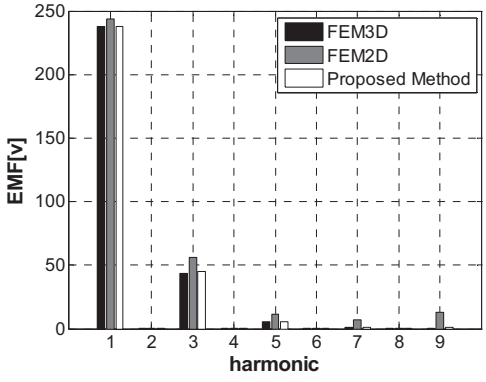

Fig 12: Harmonics of the EMF in the machine with parallel conductors

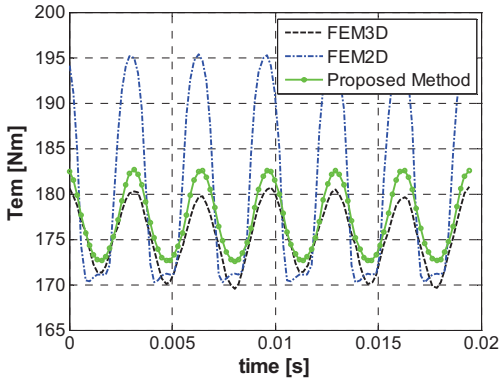

Fig 13: Time evolution of the T_{em} in the machine with parallel conductors

In this case the error of FEM2D approximation is appreciable in the waveform of the back *EMF* and in consequence in the electromagnetic torque ripple. Regarding to the results of the proposed method, they are very similar to that obtained by FEM3D.

C. Rectangular magnets

In the last machine the magnets are rectangular with a width of W_m=*30mm*. The expression of the magnet span is:

$$\beta_m(r) = 2\arcsin\left(\frac{w_m/2}{r}\right) \tag{25}$$

In Fig 14 the *EMF* obtained from FEM3D and FEM2D simulations as well as the result obtained with the proposed method are shown. The Fig 15 shows the harmonic content of the *EMF*. The same is done for the time evolution of the electromagnetic torque in Fig 16.

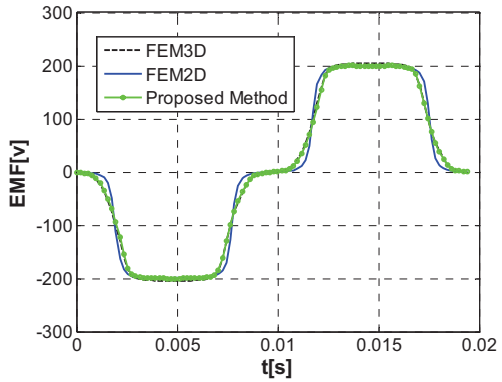

Fig 14: Time evolution of the EMF in the machine with rectangular magnets

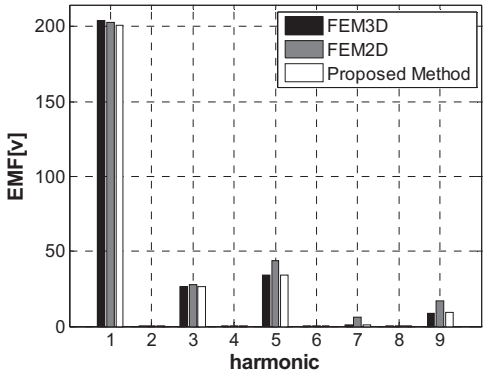

Fig 15: Harmonics of the EMF in the machine with rectangular magnets

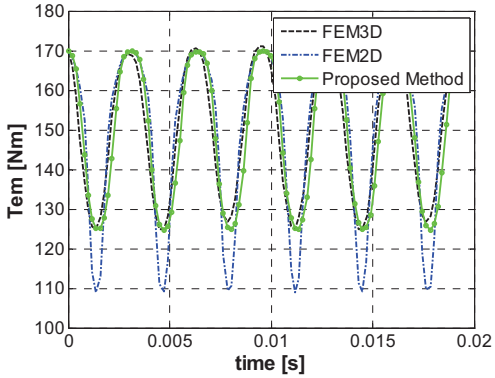

Fig 16: Time evolution of the T_{em} in the machine with rectangular magnets

Regarding to the results it can be noticed that the proposed method is more accurate than the FEM2D approximation.

V. Conclusions

The analysis of axial flux machines normally requires FEM3D simulations which are time consuming and difficult to carry out. In the literature it is possible to find different solutions that enable to obtain rather good results with less time consumption. The FEM2D approximation is one of these alternative solutions. This approximation consists in taking a plane of the axial flux machine in a certain radius, and simulating it in FEM2D. Although this method is rather accurate, there are some cases in which the results may not be accurate enough.

As solution in this work a new methodology is presented which consists in the combination of FEM2D simulations and analytical models. This methodology enables to analysis axial flux machines in a short time and with more precise results than with the original FEM2D approximation.

In order to prove the validity of the proposed method, three different machines have been analyzed and the results have been compared with that obtained using FEM3D and using the original FEM2D approximation. The results show a good agreement with that obtained using FEM3D.

VI. References

[1] F. Profumo, Z. Zhang, and A. Tenconi, "Axial Flux Machines Drives: A New Viable Solution for Electric Cars," *IEEE TRANSACTIONS ON INDUSTRY ELECTRONICS*, vol. Vol.44 1997.

[2] R. L. Ficheux, F. Caricchi, F. Crescimbini, and O. Honorati, "Axial-Flux Permanent-Magnet Motor for Direct-Drive Elevator Systems Without Machine Room," *IEEE TRANSACTIONS ON INDUSTRY APPLICATIONS,* vol. Vol.37 2001.

[3] A. Parviainen and P. Kontkanen, "Axial Flux Permanent Magnet Generator for Wind Power Applications.,", N.48 CEDRAT - CEDRAT TECHNOLOGIES - MAGSOFT Corp. ed 2005.

[4] D. González, J. A. Tapia, R. Wallace, and A. Valenzuela, "Magnetic Design Considerations for an Axial Flux PM Machine with Field Control Capability.,", N. 51 CEDRAT - CEDRAT TECHNOLOGIES - MAGSOFT Corp. ed 2006.

[5] P. Van Tichelen and P. Peeters, "Design of a New Axial Flux Permanent Magnet Generator for Hybrid Electric Vehicles," 2009.

[6] A. Parviainen, J. Pyrhönen, and M. Niemelä, "AXIAL FLUX INTERIOR PERMANENT MAGNET SYNCHRONOUS MOTOR WITH SINUSOIDALLY SHAPED MAGNETS," 2001.

[7] J. Azzouzi, G. Barakat, and B. Dakyo, "Quasi-3-D Analytical Modeling of the Magnetic Field of an Axial Flux Permanent-Magnet Synchronous Machine," *IEEE TRANSACTIONS ON ENERGY CONVERSION*, vol. Vol.20 2005.

[8] A. Parviainen, M. Niemelä, and J. Pyrhönen, "Modeling of Axial Flux Permanent-Magnet Machines," *IEEE TRANSACTIONS ON INDUSTRY APPLICATIONS,* vol. 40 No.5 2004.

VII. Biographies

A. Egea received the degree in electrical engineering from the University of Mondragon, Mondragon, Spain, in 2009. Currently he is developing his PhD at the Department of Electronics, Faculty of Engineering, University of Mondragon

His current research interests include permanent magnet machine design.

G. Almandoz received the degree in electrical engineering from the University of Mondragon, Mondragon, Spain, in 2003, and the Ph.D. degree in electrical engineering the University of Mondragon, Mondragon, Spain, in 2008

In 2003 he joined the Department of Electronics, Faculty of Engineering, University of Mondragon, where he is currently an Associate Professor.

His current research interests include the electrical machine design, modeling and control. He has participated in different research projects in the field of wind energy systems, lift drives, and railway traction.

J. Poza was born in Bergara, Spain,in June, 1975. He received the degree in electrical engineering from the University of Mondragon, Mondragon, Spain, in 1999, and the Ph.D. degree in electrical engineering from the Institut National Polytechniquede Grenoble, Grenoble, France.

In 2002 he joined the Department of Electronics, Faculty of Engineering, University of Mondragon, where he is currently an Associate Professor.

His current research interests include the electrical machines design, modeling and control. He has participated in different research projects in the field of wind energy systems, lift drives, and railway traction.

A. Gonzalez was born in Madrid, Spain, in August 1967. He received his B. Sc. Degree in electrical engineering from the Swiss Federal Institute of Technology Lausanne (Switzerland) in 1993.

In 1994, he joined ABB Generación. In 1995, he joined ORONA S. Coop. In 2002 he joined ORONA EIC where he is currently Drives Team responsible.

His research interests are oriented to development of drives and electrical machines for lifts.

Axial Flux machines modeling with the combination of FEM-2D and analytic tools

Aritz Egea
University of Mondragon
Loramendi 4
20500 Arrasate-Mondragón, Spain
aegea@eps.mondragon.edu

Gaizka Almandoz
University of Mondragon
Loramendi 4
20500 Arrasate-Mondragón, Spain
galmandoz@eps.mondragon.edu

Javier Poza
University of Mondragon
Loramendi 4
20500 Arrasate-Mondragón, Spain
jpoza@eps.mondragon.edu

Gaizka Ugalde
University of Mondragon
Loramendi 4
20500 Arrasate-Mondragón, Spain
gugalde@eps.mondragon.edu

Ana Julia Escalada
ORONA Elevator Innovation Centre
Ereñotzu auzoa
20120 Hernani, Spain
ajescalada@orona.es

***Abstract* – This paper deals with the development of analysis tools for axial flux permanent magnet machines. Normally the study of this kind of machine involves three dimensional Finite Element Method (FEM-3D) due to the 3D nature of the magnetic problem. As it is widely known FEM-3D software could take too much time and both, definition and solving processes of the problem may be very arduous.**

In this work a novel analysis procedure for axial flux synchronous machines is proposed. This method consists in the combination of FEM-2D simulations with analytical models based on Fourier series theory. The obtained results prove that the proposed method could be a very interesting option in terms of time and accuracy.

***Index Terms*— Axial flux machines, FEM, analytic models, Fourier Series.**

I. Introduction

In the last few years axial flux machines are becoming very attractive technological solution for certain applications such as electric traction or elevation, which require to the electrical machine high torque, high efficiency, compactness and shape flexibility [1;2]. Among these machines, the most relevant topology is the permanent magnet synchronous machine (PMSM), which is the case study of this paper.

The study of axial flux machines involves a tri-dimensional electromagnetic problem. So the most accurate solution for modeling the machine is by three dimensional Finite Element Method, FEM-3D [3;4]. Nevertheless, this method is high time consuming and both, the definition of the problem and the solving process are quite tedious. As alternative solution different analysis methods can be performed. One of these methods consists in carrying out simulations using FEM-2D. Applying this method, the 2D geometry is obtained in a plane which is normally situated at the average radius of the machine [5]. It is widely known that performing simulations in FEM-2D is much easier and faster than FEM-3D environment. However, this solution may not be valid in non-linear problems with strong saturation effects [6], or in case the geometry of the machine is not radially proportional [7]. Another possible solution appearing in the literature which is known as quasi-FEM-3D method consists in carrying out FEM-2D simulations in different planes of the machine. The accuracy of this method depends on the number of evaluated planes [8]. Thus the more planes are used the more accurate the results are. Nevertheless it must be considered that the time consumption of these simulations is directly proportional to the number of chosen planes. On the other hand it is also possible to find analytical solutions in the literature, such as mathematical models based on reluctance networks or Fourier series. For instance, in [9;10] a quasi 3D analytical solution is proposed. Generally the drawback of analytical models in comparison with FEM simulations is the accuracy of the results.

In this paper a novel method for axial flux machine analysis is presented. This method consists in the combination of analytical tools with FEM-2D simulations. The main advantage of the proposed method is mainly the saving of time on comparison with the FEM-3D method. Both computational time and problem definition time are shorter.

First the different constraints related to FEM-2D simulations are mentioned. After that the proposed method is explained in detail. Finally the presented procedure is validated in two stages. In the first stage the validation is carried out by simulations comparing the results of the proposed method with that obtained by FEM-3D simulations. In the second stage an experimental validation has been carried out to enhance the solidness of the proposed method. In addition, it is remarkable that the performed test with two different prototypes has also been valid for the quantification of the accuracy of FEM-3D simulations.

II. FEM-2D Simulations in the Average Radius Plane

The FEM-2D approximation consists basically in taking a 2D plane of the geometry in a certain radius value, usually in the average radius. Then, this 2D plane is treated similarly to a linear machine with the exception that a cyclic boundary condition must be forced at the ends of the primary and secondary cores. This process is described in Fig 1.

This Ph.D. student holds a grant from the Basque government*

This work has been partially supported by the Universidad Empresa project MEDIMAX from the Basque Government

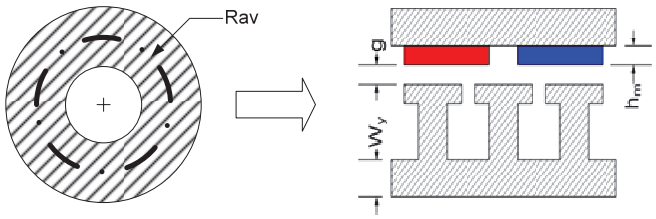

Fig 1: Process of picking a plane for the 2D approximation. a) Front view of Axial Machine and b) 2D Plane of Axial Machine at average radius

As mentioned before, it is well known that FEM-2D approximation is faster and it requires less computational load than FEM-3D simulations. Usually, even the definition of the problem (geometry, mesh and physics properties) is also easier and faster in FEM-2D. However the results obtained with this method may not be so accurate due to two main reasons: the non-linearity of magnetic materials and the geometrical shape of the magnetic cores.

Due to the non linearity of magnetic materials the saturation level may not be uniform along the different radius of magnetic cores. This phenomenon is not considered in FEM-2D approximation, unless multiple planes are taken into account.

Another critical aspect related to the accuracy of FEM-2D results is the aforementioned geometrical shape of core. This work is focused in this particular problem. In FEM-2D approximations the geometry is supposed to be radially proportional as shown in Fig 2-a, Fig 3-a and Fig 4-a. It means that the dimensions of any 2D plane obtained for a specific radius value are proportional to this radius value. In other words, the span angles of the magnets β_m, of the slots β_w and of the coils β_c are constant for the entire machine.

In many cases, due to manufacturing requirements the radially proportional structure may not be available. In other cases, a non trapezoidal shape can be chosen in order to reduce the torque ripple (using a skew effect).

For example, this proportionality is not fulfilled when the distribution of the conductors is rectangular instead of trapezoidal

A constant span angle β_c, of the conductors is only possible with trapezoidal shape placing as shown in Fig 2-a. Actually this is quite difficult to accomplish and usually the conductors are placed in a rectangular shape with a constant width w_c as shown Fig 2-b. The effect due to these unproportinality is only noticeable when the width w_c is relatively wide, otherwise it could be neglected.

Another aspect to consider is the spatial distribution of the slots. In this paper the conductor or slot distribution is taken into account as an equivalent current sheet. This way the span angle of the current sheet, β_w, can be constant along the radius as shown is Fig 3-a, or variable depending on the radius as shown in Fig 3-b.

The third and last considered variable is the shape of the magnets. The magnets could be trapezoidal shaped as in Fig 4-a, which leads to a constant span angle along the radius, β_m. But due to manufacturing, performance or price reasons the shape of these magnets could not be necessarily trapezoidal. For example they could be rectangular with a constant width w_m as shown in Fig 4-b.

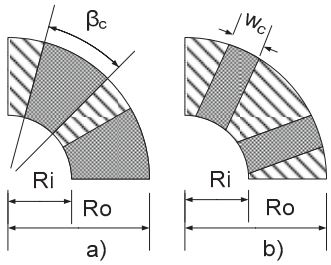

Fig 2: Placing of the armature coils in a slotless stator a) trapezoidal shape b) rectangular shape

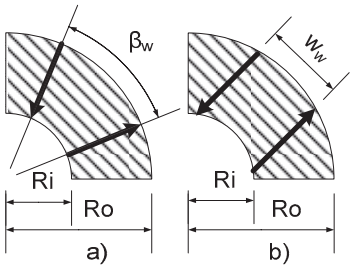

Fig 3: Placing of the stator slots or punctual conductors of the armature coils in slotless machines a) radial and b) parallel

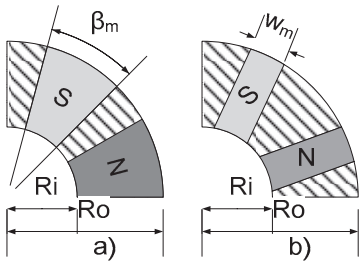

Fig 4: Shape of the magnets a) trapezoidal and b) rectangular

When an axial flux machine is not radially proportional, the aforementioned span angles vary along the radius, and in consequence FEM-2D simulations on the average radius plane may not be as accurate as required. The shape of the time evolution curves of the electromagnetic variables such as the linked flux would be wrong. As a solution, it would be possible to launch FEM-3D. FEM-3D analysis could be quite laborious so an alternative solution is proposed in this paper. The idea is to process the results obtained from the FEM-2D approximation with additional analytical tools.

The details of the proposed method are given in the next section. After that, the obtained results for the aforementioned options are presented in the forth section. Finally an experimental verification is developed in the fifth section.

III. Proposed Method for the Analysis of Axial Flux Machines: Combination of Analytical Models and FEM-2D Simulations

The proposed method consists in the combination of FEM2D simulations with analytical models based on the theory of Fourier series. The proposed methodology is described in Fig 5. In the first stage the machine is simulated by FEM-2D considering the average radius plane.

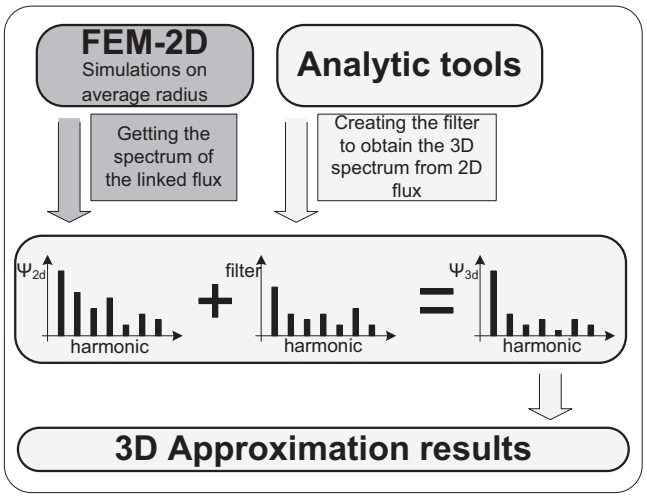

Fig 5: Block diagram of the proposed methodology for axial flux machine analysis.

The harmonic content of the linked flux is obtained from this simulation by a discrete FFT. The time step must be set according to the required number of harmonics. Simultaneously a filter which links the FEM-2D with the FEM-3D spectrum of the linked flux is obtained analytically. Then the harmonic content of the linked flux obtained in FEM-2D is post-processed by the filter. The new harmonic content obtained in the post-process is an approximation of the one would be obtained in FEM-3D.

In this section, first the main equations of the electromagnetic parameters are presented so afterwards the computation of the filter coefficients could be explained.

The Fourier Series approach used in this paper considers a constant air-gap with normally distributed magnetic field. The methodology is also applicable to more complicated Fourier Series models that take into account in detail magnetic field distribution around the air-gap and the slot.

A. *Main electromagnetic equations*

The most relevant performance results of the machine such as the back electromotive force *EMF* or the electromagnetic torque T_{em}, can be calculated from the magnet flux linked by the armature windings Ψ. This way the back electromotive force of each phase is defined as the derivative of the flux linkage of each phase:

$$EMF_x(t) = \frac{d\psi_x}{dt} \tag{1}$$

Once the *EMF* is obtained, the electromagnetic torque can be calculated as:

$$T_{em}(t) = \frac{EMF_a(t)\cdot i_a(t) + EMF_b(t)\cdot i_b(t) + EMF_c(t)\cdot i_c(t)}{\Omega_m} \tag{2}$$

So post-processing the flux linkage calculated in FEM-2D it is possible to obtain the *EMF* and the electromagnetic torque for the whole machine geometry.

The magnet flux linked by each phase can be defined in the following way.

$$\psi(t) = \int_S B_g^m(t,\theta,r)\cdot F(t,\theta,r)\cdot ds \tag{3}$$

Where B_g^m is the magnetic field induced by the magnets in the air-gap, *F* is the magneto-motive force per current unit and *S* is the surface area. In case of radial machines the radius is constant so that the resolution of (3) is much easier than in case of axial flux machines where the radius is variable. Solving (3) for axial flux machines the following expression can be obtained:

$$\psi(t) = t_p \int_0^{2\pi/t_p} \int_{R_i}^{R_o} r\cdot B_g^m(t,\theta,r)\cdot F(t,\theta,r)\cdot dr\cdot d\theta \tag{4}$$

Where t_p is the periodicity of the machine:

$$t_p = G.C.D.(Q,p) \tag{5}$$

The expression (4) could also be defined in Fourier series as:

$$\psi(t) = t_p \int_0^{2\pi/t_p} \int_{R_i}^{R_{o_g}} r\cdot \left[\begin{array}{l} \sum_{n=-\infty}^{\infty} B_{g\_n}^m(r)\cdot\cos\left(np(-\theta+\varphi_0)\right) \\ \times \sum_{k=-\infty}^{\infty} F_k(r)\sin(\theta+\lambda_o) \end{array}\right]\cdot dr\cdot d\theta \tag{6}$$

Where $B_{g\_n}^m$ are the spatial coefficients of the magnetic field, φ_o is the initial position of the magnets, F_k are the spatial coefficients of the magneto-motive force per current unit and λ_o is the position of the magnetic potential created by the windings. Both variables, the magnetic field in the air-gap and the magneto-motive force per current unit depend on the radius. As there is not any interaction between these two variables, their effects could be analyzed independently.

B. *Computation of the filter Coefficients*

1) Analysis of the Magnetic Field Induced by the Magnets in the Air-gap

Ideally the spatial distribution of the magnetic field induced by the magnets in the air-gap can be considered as a rectangular waveform. Nevertheless, actually there is some fringing flux around the edge of the magnets which change slightly the shape of this distribution as shown in Fig 6.

The coefficients of the magnetic field induced by the magnets in the air-gap can be calculated by the following expression:

$$B_{g\_n}^m(r) = \frac{B_{g\max}}{n\pi}\sin\left(np\frac{\beta_m(r)}{2}\right)\frac{1-\cos(n\pi)}{1+(a(r)np)^2} \tag{7}$$

Where *p* is the number of pole pairs, β_m is the span of the magnets, *a* is the fringing function coefficient and B_{gmax} is the maximum value of the spatial distribution of B_g which is defined as:

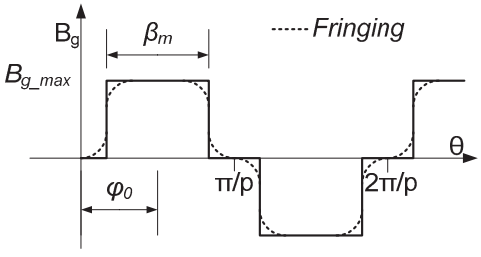

Fig 6: Spatial distribution of B_g

$$B_{g\max} = \frac{B_r}{1+\mu_r \frac{g}{h_m}} \tag{8}$$

μ_r is the relative permeability, h_m is the height of the magnets, B_r is the residual value of the magnetic field of the permanent magnets and g is the air-gap length. The fringing function which depends also on the radius can be expressed as:

$$a(r) = \sqrt{\frac{g\left(g + h_m / \mu_r\right)}{2 \cdot r}} \tag{9}$$

This analysis the part of the expression (4) dependant on the radius is the one related to the magnetic field induced by the magnets in the air-gap:

$$\Phi_g^m = \int_{R_i}^{R_o} B_g^m(t,\theta,r) \cdot dr \tag{10}$$

The variables of the expression (7) dependent on the radius are the magnet span and the fringing function. So the values of the coefficients are different in case the magnets are trapezoidal or rectangular. In order to calculate the magnetic flux due to the magnets in the air gap the expression (10) must be integrated:

$$\Phi_{g\,n}^{m}\Big|_{\substack{\beta_m \neq cnt \\ a \neq cnt}} = \frac{B_{g\max}}{n\pi}\left(1-\cos(n\pi)\right)\int_{Ri}^{Ro} \frac{\sin\left(n \cdot p \cdot \frac{\beta_m(r)}{2}\right)}{1+\left(a(r)\cdot n \cdot p\right)^2} dr \tag{11}$$

In case of trapezoidal magnets the expression (11) can be simplified and it leads to:

$$\Phi_{g\,n}^{m}\Big|_{\substack{\beta_m = cnt \\ a = cnt}} = \frac{B_{g\max}}{n\pi}\left(1-\cos(n\pi)\right)\frac{\sin\left(n \cdot p \cdot \frac{\beta_m}{2}\right)}{1+\left(a \cdot n \cdot p\right)^2}\left(R_o^2 - R_i^2\right) \tag{12}$$

In this case the radial density of the magnetic flux does not depend on the radius r. So from (11) and (12) a correction coefficient XB_n for each spatial component of the spectrum can be defined as:

$$XB_n = \Phi_{g\,n}^{m}\Big|_{\substack{\beta_m \neq cnt \\ a \neq cnt}} \Big/ \Phi_{g\,n}^{m}\Big|_{\substack{\beta_m = cnt \\ a = cnt}} \tag{13}$$

Then the correction filter can be applied to the spectrum of the flux linkage obtained from FEM-2D simulations in order to calculate the flux linkage spectrum considering the entire geometry of the machine:

$$\psi_{n\_3d} = \psi_{n\_2d} \cdot XB_n \tag{14}$$

Been ψ_{n_3d} and ψ_{n_2d} the components of n order of the linked flux of the 3D approximation and 2D simulation respectively.

After that, the temporal flux linkage is calculated applying the Inverse Fast Fourier Transformation (IFFT):

$$\psi_{3d}(t) = \sum_{n=-\infty}^{\infty} \psi_{n\_3d} \sin\left(np\Omega t - \lambda_o\right) \tag{15}$$

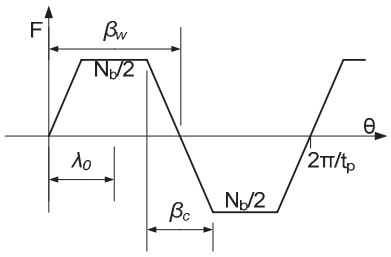

Fig 7: Spatial distribution of the F created by the winding of each phase

2) Analysis of the Magneto Motive Force per Current Unit

The second effect is the one produced by the disposition of the conductors. In Fig 7 is shown the spatial distribution of this parameter. The expression for each harmonic of F is the following:

$$F_k(r) = \frac{j \cdot N_{ph}}{\pi \cdot k \cdot t_p} \xi_k(r) \tag{16}$$

N_{ph} is the number of turns per phase. ξ_k is the winding factor, which is the combination of the span factor ξ_{s_k} and pitch factor ξ_{p_k}:

$$\xi_k(r) = \xi_{s\_k}(r) \cdot \xi_{p\_k}(r) \tag{17}$$

The span factor is defined as:

$$\xi_{s\_k}(r) = \sin\left(k \cdot t_p \cdot \frac{\beta_w(r)}{2}\right) \tag{18}$$

And the pitch factor is defined as:

$$\xi_{p\_k}(r) = \frac{\sin\left(k \cdot t_p \cdot \frac{\beta_c(r)}{2}\right)}{k \cdot t_p \cdot \frac{\beta_c(r)}{2}} \tag{19}$$

Not all the harmonics of the winding link with the ones of the flux density induced by the magnets. The linked harmonics are the ones in the next expression.

$$F_n = F_k\left\{k = \frac{-n \cdot p}{t_p}\right\} \tag{20}$$

In this analysis the part of the expression (4) dependant on the radius is the one related to the magneto-motive force per current unit:

$$\chi_g^a = \int_{R_i}^{R_o} F(t,\theta,r) \cdot dr \tag{21}$$

Developing the expression (21) with (16) the next expression dependent on the radius is obtained.

Developing the expression (21) with (16) the next expression dependent on the radius is obtained.

$$\chi_{g\,n}^{a}\Big|_{\substack{\beta_w \neq cnt \\ \beta_c \neq cnt}} = \frac{j \cdot N_{ph}}{\pi \cdot k \cdot t_p} \cdot \int_{Ri}^{Ro} \left[\frac{\sin\left(n \cdot p \cdot \frac{\beta_w(r)}{2}\right)}{n \cdot p \cdot \frac{\beta_c(r)}{2}} \times \frac{\sin\left(n \cdot p \cdot \frac{\beta_c(r)}{2}\right)}{n \cdot p \cdot \frac{\beta_c(r)}{2}} \right] \cdot dr \tag{22}$$

Nevertheless, for a trapezoidal shape of the coils dispersion (β_w and β_c are constant) the expression (22) is simplified and it leads to:

$$\chi_{g\,n}^{a}\Big|_{\beta_w=cnt}^{\beta_c=cnt} = \frac{j\cdot N_{ph}}{\pi\cdot k\cdot t_p}\cdot\left[\sin\left(n\cdot p\cdot\frac{\beta_w}{2}\right)\times\frac{\sin\left(n\cdot p\cdot\frac{\beta_c}{2}\right)}{n\cdot p\cdot\frac{\beta_c}{2}}\right] \tag{23}$$

From (22) and (23) the *XF* correction coefficient for each spatial harmonic of the spectrum is computed:

$$XF_n = \chi_{g\,n}^{m}\Big|_{\beta_w=cnt}^{\beta_c\neq cnt} \Big/ \chi_{g\,n}^{m}\Big|_{\beta_w=cnt}^{\beta_c=cnt} \tag{24}$$

Once the XF coefficients are obtained the flux linkage spectrum obtained by FEM-2D is filtered. This way, the flux linkage for the entire machine geometry is computed.

$$\psi_{n\_3d} = \psi_{n\_2d}\cdot XF_n \tag{25}$$

From this harmonic content of the flux linkage it is possible to obtain the time waveform applying the Inverse Fourier Transformation.

IV. FEM Validation of the Proposed Method

Several simulations with two different machines have been carried out in order to validate the proposed method. The two evaluated machines are slotless toroidal machines as the one shown in Fig 8. In the first one the conductors are punctual and they are placed in a parallel way as shown in Fig 3-b. while the magnets are trapezoidal. In the second machine the magnets are rectangular as shown in Fig 4-b, and the conductors are punctual and trapezoidal. The main characteristics of the simulated machines are summarized in TABLE I.

A. *Example 1: Punctual conductors in parallel with trapezoidal magnets*

This case may not be very common, but in certain circumstances, as manufacturing reason, it could happen.

In Fig 9 the *EMF* obtained from FEM-3D and FEM-2D simulations as well as the result obtained with the proposed method are shown. In Fig 10 the harmonic content of the *EMF* is shown and in Fig 11 the time evolution of the electromagnetic torque is shown.

In this case the error of FEM-2D approximation is appreciable in the waveform of the back *EMF* and in consequence in the electromagnetic torque ripple. The error in the torque ripple computed by FEM-2D is about 27%. Regarding to the results of the proposed method, it can be noticed that they are very similar to that obtained by FEM-3D.

As it could be deduced from the curves of the EMF and the torque, placing the conductors in parallel leads to a skew effect. The harmonic content of the EMF is reduced, so does the torque ripple.

TABLE I

Main Characteristics of the Simulated Machine

Number of pole pairs	*8*
Number of coils	*18*
Number of phases	*3*
RMS current	*14A*
Rotational speed	*382.5 rpm*

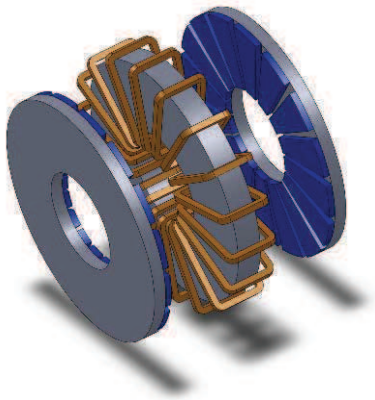

Fig 8: View of the simulated machine

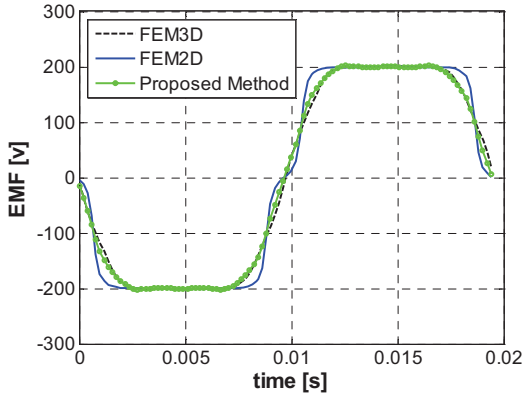

Fig 9: Time evolution of the EMF in the machine with parallel conductors

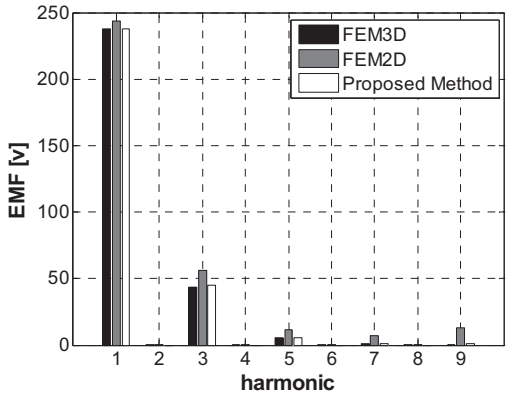

Fig 10: Harmonics of the EMF in the machine with parallel conductors

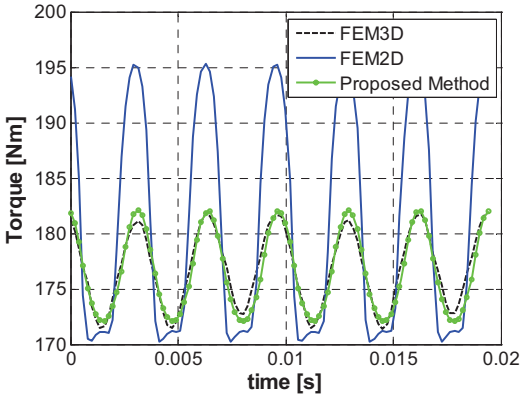

Fig 11: Time evolution of the T_{em} in the machine with parallel conductors

B. *Example 2: Rectangular magnets with trapezoidal punctual conductors*

In this machine the magnets are rectangular with a width of w_m=*30mm*. The expression of the magnet span depending on the radius is:

$$\beta_m(r) = 2\arcsin\left(\frac{w_m/2}{r}\right) \tag{26}$$

In Fig 12 the *EMF* obtained from FEM-3D and FEM-2D simulations as well as the result obtained with the proposed method are shown. In Fig 13 the harmonic content of the *EMF is shown*. While in Fig 14 the time evolution of the electromagnetic torque is shown.

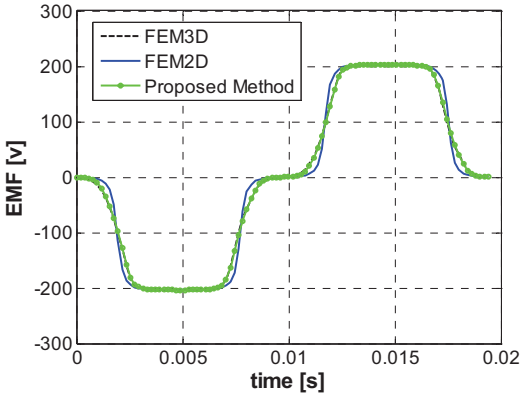

Fig 12: Time evolution of the EMF in the machine with rectangular magnets

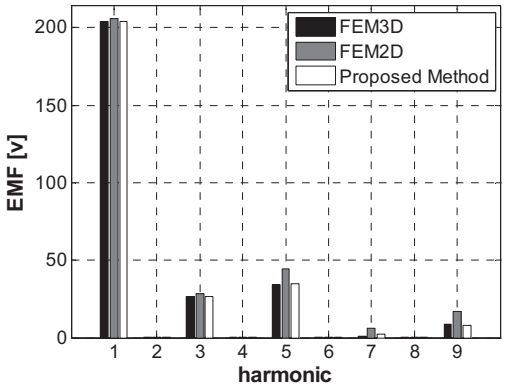

Fig 13: Harmonics of the EMF in the machine with rectangular magnets

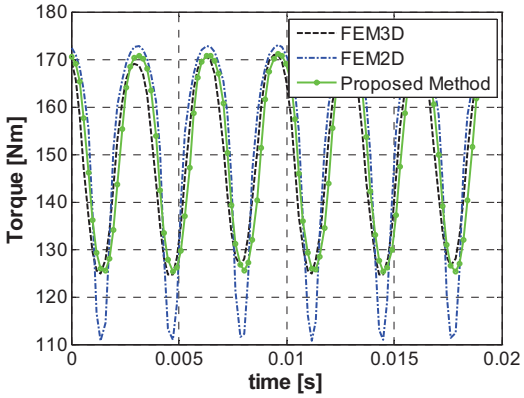

Fig 14: Time evolution of the T_{em} in the machine with rectangular magnets

Regarding to the results it can be noticed that the proposed method is more accurate than the FEM-2D approximation, and it is almost as accurate as FEM-3D simulations. The torque ripple computed by FEM-3D and the proposed method is ±22Nm, and value computed by FEM-2D is ±30Nm. So the error of FEM-2D in the torque computation is about 36%. In addition, the results show that using rectangular magnets a skew effect is achieved.

V. Experimental Validation of the Proposed Method

In order to validate the proposed method a small configurable axial machine is built. This machine has not a real purpose, but its purpose is to test easily different combinations.

Two different conceptual prototypes have been manufactured and tested. In Fig 15 the laboratory test bench is shown, which mainly consists of a load motor, a torque sensor and the test prototype

A. *Description of the prototypes*

The two test prototypes have the same configuration so that they are double side coreless axial flux machines (see Fig 16). Both have 2 pole pairs formed by rectangular magnets, and a unique coil per phase, which leads to fractional machines with 0.25 coils per pole and per phase. The only difference between the two prototypes is the coil shape that can be rectangular or trapezoidal. The stator coils are compacted in an epoxy resin in order to obtain a coreless stator. As it is impossible to place punctual conductors the real width of the conductor dispersion, w_w, is about 6 mm on both prototypes. Remark that the coreless configuration of prototypes has been chosen in order to make the manufacturing process low cost and simple.

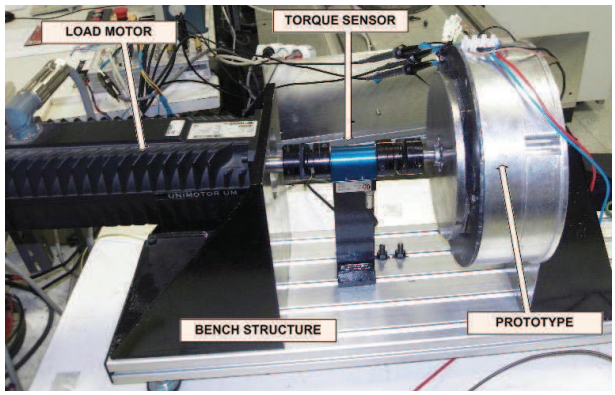

Fig 15: Picture of test bench

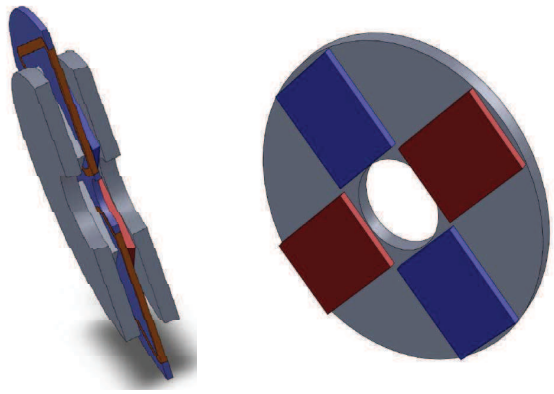

a) b)

Fig 16: a) Cutted view of the complete machine and b) a view of the rotor.

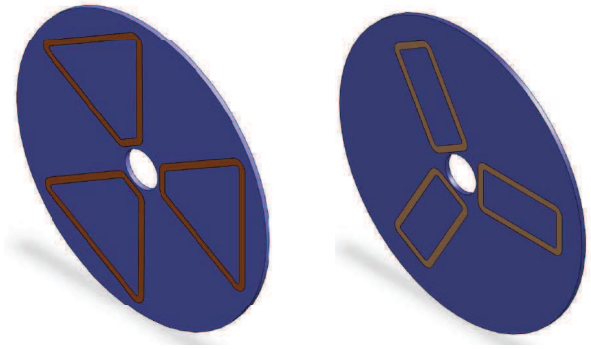

a) b)

Fig 17: Views of the stators of the prototypes, a) trapezoidal coils and b) rectangular coils.

TABLE II

MAIN CHARACTERISTICS OF THE TEST PROTOTYPES

Number of pole pairs	*2*
Number of slots	*6*
Number of winding layers	*1*
Number of phases	*3*
Number of coils	*3 (1 per phase)*
Number of turns per phase	*100*
Peak current	*1.5A*
Rotational speed	*250 rpm*
Rotor outer diameter	*190 mm*
Rotor inner diameter	*55 mm*
Rotor disc thickness	*10 mm*
Stator outer diameter	*265 mm*
Stator inner diameter	*34mm*
Stator disc thickness	*4 mm*
Total air-gap	*6 mm*
Magnet thickness	*5 mm*
Magnet dimensions	*50 mm x64 mm*
Magnet grade	*NEO 42 H*

The three coils are placed with a separation of 120º from each other. The layout of the positive and negative conductors is different in each prototype. In the stator with trapezoidal coils the conductors are placed with a span angle, β_w, of 60º, making a uniform distribution of the conductors as shown in Fig 17-a. The separation of the positive and negative conductors on the rectangular coils, w_w is 40 mm as the Fig 17-b shows. The main characteristics of these prototypes are summarized in TABLE II.

B. *Results*

The experimental study consists in two tests. The first one is the so called open circuit test, in the prototypes are driven at rated speed and the back EMF are measured on the three phases. The second test is the so called load test, in which the prototypes are controlled by a vector control to operate at rated speed and load. In this situation the torque is measured using a torque sensor characterized by a full scale of 15Nm and a resolution of 0,1Nm.

All experimental measurements are compared with the results obtained by FEM-2D approximation and with that obtained using the proposed method.

1) Prototype 1: Trapezoidal coils and Rectangular Magnets

In Fig 18 the different back *EMF* are plotted. In Fig 19 the harmonic content of the three back EMF waveforms are shown. The same is done for the time evolution of the electromagnetic torque in Fig 20 and the harmonic content of the electromagnetic torque in Fig 21.

It can be state that the results obtained with the proposed method have a good agreement with the experimental measurements. The torque ripple is ±0.2Nm in the case of experimental and proposed method results while in the FEM-2D is ±0.3Nm.

The effect of the dispersion of the conductors of a coil is not so remarkable since this dispersion is only of 6 mm so it could be neglected and assume only the effect of the shape of the magnets.

2) Prototype 2: Rectangular coils and Rectangular Magnets

In Fig 22 the different back *EMF* are plotted. In Fig 23 the harmonic contents of the three back-*EMFs* are shown. The same is done for the time evolution of the electromagnetic torque in Fig 24 and the harmonic content of the electromagnetic torque in Fig 25.

The results obtained with the second prototype are not as accurate as the ones obtained in the first one. The method tends to improve the results obtained with FEM-2D getting them closer to the experimental measurements. However the error is slightly higher than in the previous prototype. The torque ripple is ±0.25Nm in the prototype while ±0.5Nm with the proposed method. With the aim of identifying the reason for this, the results have been also compared with FEM-3D solution. The curves from FEM-3D and the ones obtained with the presented method are quite similar. Saying this, the problem of the failure of accuracy could come from the construction of the stator. The real disposition of the coils could vary from the theoretical ones leading to slight difference between simulations and experimental measurements.

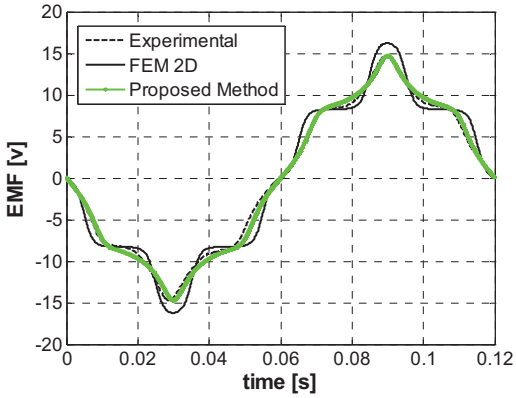

Fig 18: Time evolution of the EMF in the machine with trapezoidal coils

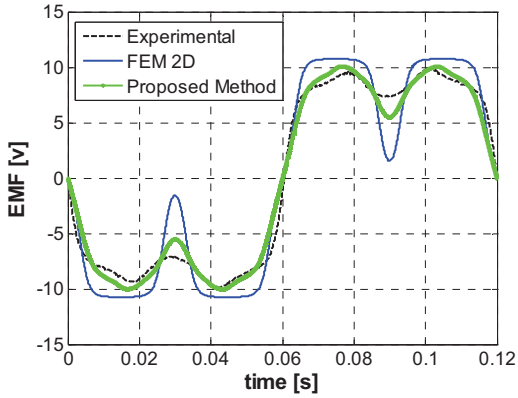

Fig 22: Time evolution of the EMF in the machine with rectangular coils

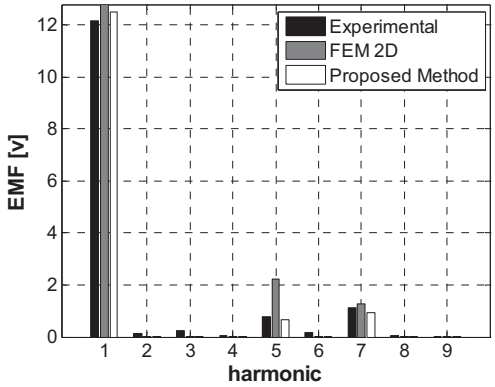

Fig 19: Harmonics of the EMF in the machine with trapezoidal coils

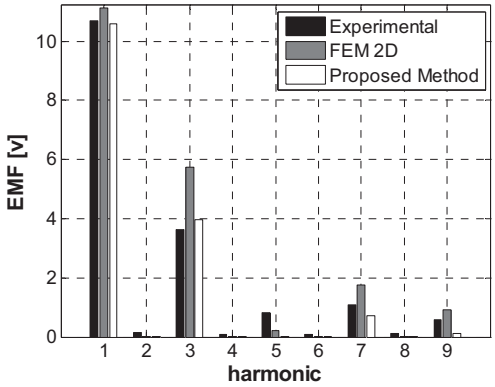

Fig 23: Harmonics of the EMF in the machine with rectangular coils

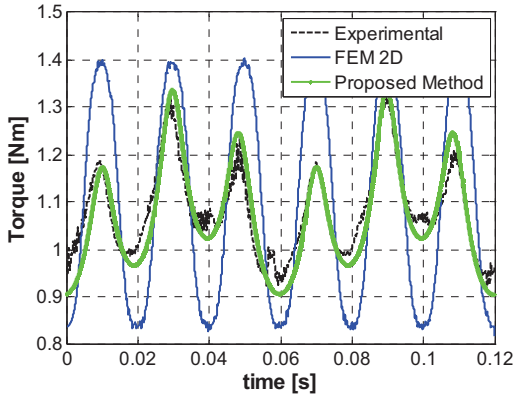

Fig 20: Time evolution of the T_{em} in the machine with trapezoidal coils

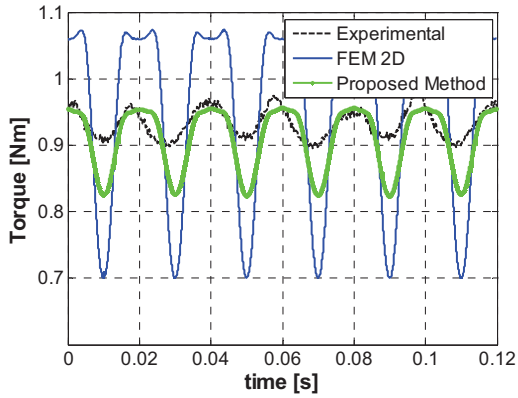

Fig 24: Time evolution of the T_{em} in the machine with rectangular coils

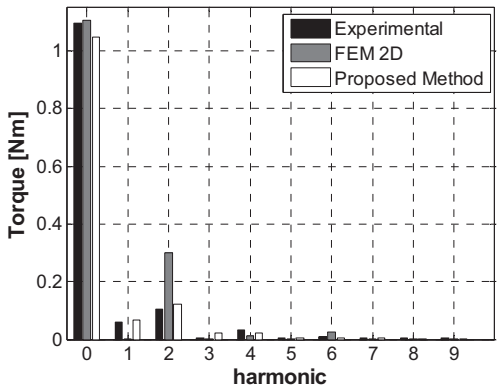

Fig 21: Harmonics of the T_{em} in the machine with trapezoidal coils

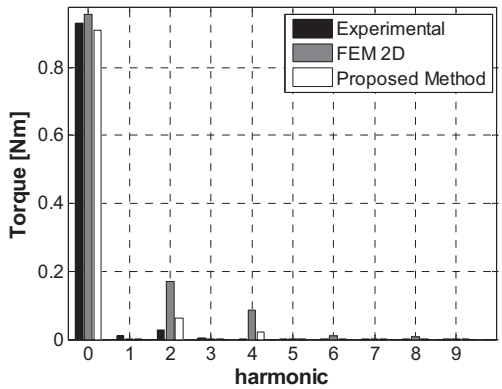

Fig 25: Harmonics of the T_{em} in the machine with rectangular coils

VI. Conclusion

As solution in this work a new methodology is presented which consists in the combination of FEM-2D simulations and analytical models. This methodology enables to analysis axial flux machines in a short time than FEM 3-D and with more precise results than with the original FEM-2D approximation.

In order to prove the validity of the proposed method, two different low speed and high torque machines have been analyzed and the results have been compared with that obtained using FEM-3D and using the original FEM-2D approximation. The results show a good agreement with that obtained using FEM-3D.

Furthermore two conceptual prototypes have been constructed and tested. The results obtained with these machines confirm that this method improves significantly the FEM-2D simulations. Similar results are obtained with FEM-3D approach.

As future prospect it would be interesting to test the accuracy of this method in other conceptual prototypes and in industrial machines.

References

[1] F. Profumo, Z. Zheng, and A. Tenconi, "Axial flux machines drives: a new viable solution for electric cars," *Industrial. Electronics. , IEEE Transactions on*, vol. 44, no. 1, pp. 39-45, Feb.1997.

[2] R. L. Ficheux, F. Caricchi, F. Crescimbini, and O. Honorati, "Axial-flux permanent-magnet motor for direct-drive elevator systems without machine room," *Industry Applications, IEEE Transactions on*, vol. 37, no. 6, pp. 1693-1701, Nov.2001.

[3] A. Parviainen, J. Pyrhonen, and P. Kontkanen, "Axial Flux Permanent Magnet Generator with Concentrated Winding for Small Wind Power Applications," 2005, pp. 1187-1191.

[4] J. A. Tapia, D. Gonzalez, R. R. Wallace, and M. A. Valenzuela, "AXIAL FLUX SURFACE MOUNTED PM MACHINE WITH FIELD WEAKENING CAPABILITY," in *Recent Developments of Electrical Drives*. S. Wiak, M. Dems, and K. Kom-Öza, Eds. Springer Netherlands, 2006, pp. 321-334.

[5] P. Van Tichelen and E. Peeters, "Design of a new axial flux permanent magnet generator for hybrid electric vehicles,", 5 ed 2003, pp. 3192-3196.

[6] K. Kyoung-Ho, C. Yun-Hyun, K. Do-Hyun, J. Yen-Ho, and K. Jong-Mu, "Characteristics analysis of axial flux type reluctance motor using 2 and 3-dimensional finite element method,", 2 ed 2001, pp. 1169-1174.

[7] S. Gair, A. Canova, J. F. Eastham, and T. Betzer, "A new 2D FEM analysis of a disc machine with offset rotor,", 1 ed 1996, pp. 617-621.

[8] A. Parviamen, J. Pyrhonen, and M. Niemela, "Axial flux interior permanent magnet synchronous motor with sinusoidally shaped magnets," in *Electromagnetic Fields in Electrical Engineering* Amsterdam, Netherlands: IOS Press, 2002, pp. 271-276.

[9] J. Azzouzi, "Quasi-3-D analytical modeling of the magnetic field of an axial flux permanent-magnet synchronous machine," Dec.2005.

[10] A. Parviainen, "Modeling of axial flux permanent-magnet machines," Sept.2004.

A. Egea received the degree in electrical engineering from the University of Mondragon, Mondragon, Spain, in 2009. Currently he is developing his PhD at the Department of Electronics, Faculty of Engineering, University of Mondragon

His current research interests include permanent magnet machine design.

G. Almandoz received the degree in electrical engineering from the University of Mondragon, Mondragon, Spain, in 2003, and the Ph.D. degree in electrical engineering the University of Mondragon, Mondragon, Spain, in 2008

In 2003 he joined the Department of Electronics, Faculty of Engineering, University of Mondragon, where he is currently an Associate Professor.

His current research interests include the electrical machine design, modeling and control. He has participated in different research projects in the field of wind energy systems, lift drives, and railway traction.

J. Poza was born in Bergara, Spain,in June, 1975. He received the degree in electrical engineering from the University of Mondragon, Mondragon, Spain, in 1999, and the Ph.D. degree in electrical engineering from the Institut National Polytechniquede Grenoble, Grenoble, France.

In 2002 he joined the Department of Electronics, Faculty of Engineering, University of Mondragon, where he is currently an Associate Professor.

His current research interests include the electrical machines design, modeling and control. He has participated in different research projects in the field of wind energy systems, lift drives, and railway traction.

G. Ugalde received the B.Eng. and Ph.D. degrees in electrical engineering from the University of Mondragon, Mondragon, Spain, in 2006and 2009, respectively.In 2009 he joined the Department of Electronics, Faculty of Engineering, University of Mondragon, where he is currently an Associate Professor.

His current research interests include permanent magnet machine design, modeling and control. He has participated in different research projects in the field of lift drives, and railway traction.

Ana Julia Escalada was born in Pamplona (Spain), in April 1977. She obtained the degree in Electronic Engineering from Basque Country University in 2001 and a B.Sc. in Physics from Cantabria University (Spain) in 2003. She joined the Power Electronics Department of the Technological Research Centre, Ikerlan, in 2001, where she received the Ph. D. degree in Automatic and Industrial Electronic Engineering in conjunction with Mondragon University (2007). She is currently working in the Electrical Drives Department of ORONA-EIC. Her interests are drives and electrical machines for lifts.

Analytical Model of Axial Flux Permanent Magnet Machines Considering Spatial Harmonics

A.Egea*[1], G.Almandoz[1], J.Poza[1] and A.Escalada[2]

1 University of Mondragon/Faculty of Engineering, Arrasate, (Spain)

2 ORONA Elevator Innovation Centre, Hernani, (Spain)

Abstract— **This work deals with the development of a complete analytic model for axial flux surface mounted permanent magnet synchronous machines. The magnetic flux density in the air-gap, the back electromotive force *EMF*, the linked flux ψ and the electromagnetic torque are represented as sum of spatial-temporal components, and they are defined as function of different design parameters such as mechanical dimensions, magnets properties and so on. Therefore, the proposed model gives a detailed inside view into the behaviour of axial flux machines.**

Finally the accuracy of the model is evaluated comparing the results with those obtained experimentally.

Keywords—Axial Flux Permanent Magnet Synchronous Machine, Fourier series, Analytic Model,

Topic—Design and Optimization of Electrical Machines*

I. INTRODUCTION

Nowadays, electric drives technology tends to compact, low maintenance cost, comfortable and eco-friendly solutions. In this framework, direct drive applications based on permanent magnet (PM) machines show to be the best option to fulfil these requirements.

Among PM machine topologies, axial flux machines are considered a very interesting option for several applications such as elevators or electrical vehicles. The inherent disc shape of axial flux machines fit properly in such applications where available space is cramped. In addition the power density in axial flux machines is normally higher than in radial flux machines which may lead to considerable reduction of the total volume.

In direct drive applications a high grade of optimization of the electrical machine design may be required. Therefore, the design process may take an important number of iterations. The performance of many iterations using exclusively finite element method (FEM) analysis could lead to large computation times. Probably an initial design previous to the FEM analysis and based on analytical models could enable to reduce the time consumption of the design process.

Analysis of electrical machines using analytic models is not supposed to be as accurate as analysis based on numerical methods. However it gives an insight into the functioning of the machine and makes possible to identify correlations between different design variables and the performance of the machine.

As radial flux machines are the most popular, almost the majority of analytical models found in the literature are related to this type of machine. However these models could be perfectly valid also for axial flux machines if some changes in terms of geometrical parameters are made.

One quite extended modelling method is based on Fourier series [1-6]. This technique considers the time-space distribution of electromagnetic variables so that it enables to identify the cross-coupling between different spatial and temporal components. Therefore, this modelling method provides a very interesting insight into the correlation between different design variables and the machine performances.

In the literature it is possible to find some references related to analytical models based on Fourier series, mainly for radial flux machines. For example, *Zhu et al.* carry out in four publications a complete representation of the magnetic flux density in the air-gap of a PMSM [1-4]. In [1] they represent the magnetic flux density induced by the magnets in the air-gap as a sum of spatial components for a slotless machine. The shape of the spatial waveform is defined by solving in polar coordinates the magnetic potential distribution equations in the air-gap. In [2]the armature flux density in the air-gap is represented in the same way. In [3] the effect of stator slots on the magnetic flux density is considered. And finally in [4] the magnetic flux density in load condition is represented. Moreover, in [5] the same authors predict the cogging torque based on the magnetic flux density representation carried out in previous works.

This approximation proposed by *Zhu et al.* for the definition of the magnetic flux density in the air-gap has been used by other authors too. For example, in [7] models for PM synchronous machines inspired in the same method are proposed. In this works complete

---

* *Ph. D student holding a grant from the Government of the Basque Country*

This work has been partially supported by the Universidad Empresa project MEDIMAX from the Basque Government.

models representing the electromagnetic torque and the back electro-motive force induced in the armature winding are developed for radial flux machines.

Regarding to axial flux machines, several authors [8-11] proposed sizing and optimization equations for them. Nevertheless these equations consider only the fundamental components, so they are not suitable to represent the time-space variation of electromagnetic variables.

The aim of this work is to carry out a complete analytical model for axial flux machines by using Fourier series. Spectrums of all variables and parameters such as air-gap flux density induced by the magnets, air-gap magneto-motive force created by the stator winding, inductance, flux linkage, back electro-motive force and electromagnetic torque are obtained by this model. It should be remarked that the proposed model is carried out considering surface mounted permanent magnet machines.

II. Modelling Methodology and Assumptions

The proposed model is performed in very clear four stages as shown in Fig 1. Initially the flux density induced by the magnets in the air-gap is represented by means of Fourier series. In a second stage the winding conductor distribution is defined in the same way and the magnetomotive force created by the winding is computed. Once magnet and winding configuration are defined, in a third stage the electromagnetic coupling is analyzed, computing the flux linkage (ψ), the electromotive force (*EMF*) and the electromagnetic torque (T_{em}). Finally, the inductances and copper resistance are calculated in order to obtain the parameters of the well known electric equivalent circuit.

The following assumptions are made to carry out the model:

- The stator and rotor cores are considered ideal: ferromagnetic material with infinite permeability
- Only the normal component of the flux density in the air-gap is taken into account.
- Magnet leakage flux is not taken into account and magnets are considered to work in the linear zone.
- The model is linear so that saturations are neglected.

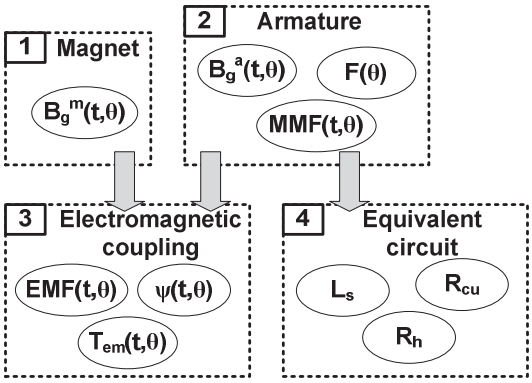

Fig 1: Proposed modeling methodology

The different variables are represented in the following way:

$$X_b^a(Y,Z) \tag{1}$$

X is the name of the variable. The superscript a defines the cause of the variable and the subscript b means where the variable is located. Y and Z are the variables on which the main variable depends.

The analytical model is based in two general equations: The equation of the air-gap flux density induced by the magnets and the equation of the magneto motive force per current unit. These equations depend on two dimensions, one along the angle θ and the other along the radius r as shown in Fig 2.

On the one hand the magnetic flux density induced by the magnets in the air-gap is represented in the following form:

$$B_g^m(t,\theta,r) = \sum_{n=-\infty}^{\infty} B_n(r)\cdot e^{jpn\varphi_0}\cdot e^{-jpn\theta}\cdot e^{-jpn\omega_m t} \tag{2}$$

Where R_o and R_i are the outer and inner radius respectively, p is the number of pole pairs, B_n is the n order harmonic, φ_0 is the initial angle and ω_m is the mechanical speed of the machine.

On the other hand the magneto-motive force per current unit is defined as:

$$F(\theta,r) = \sum_{k=-\infty}^{\infty} F_k(r)\cdot e^{-jt_p k\theta}\cdot e^{jt_p k\lambda_0} \tag{3}$$

Where F_k is the k order harmonic, λ_0 is the initial angle and t_p is the periodicity of the machine, calculated as following:

$$t_p = G.C.D.(Q,p) \tag{4}$$

G.C.D. stands for greatest common divisor while Q is the number of stator slots.

Once these two variables are defined, all other parameters such as flux linkage, EMF or electromagnetic torque can be developed.

The magnet flux linkage can be computed as shown next:

$$\psi(t) = \int_S B_g^m(t,\theta,r)F(\theta,r)ds \tag{5}$$

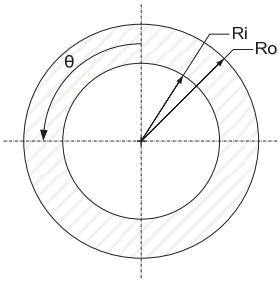

Fig 2: Two dimensions of the integration

In case of radial machines the radius is constant so that the resolution of (5) is much easier than in case of axial flux machines where the radius is variable. Setting out (5) for axial flux machines the following expression is obtained:

$$\psi(t) = t_p \int_{Ri}^{Ro} \int_0^{2\pi/t_p} r B_g^m(t,\theta,r) F(\theta,r) d\theta dr \tag{6}$$

Applying the well known Faraday's law the back electromotive force can be computed by derivating the flux linkage:

$$EMF(t) = \frac{d\psi(t)}{dt} \tag{7}$$

And finally the electromagnetic torque is calculated as:

$$T_{em}(t) = \sum_{x=1}^{m} \frac{EMF_x(t) \cdot i_x(t)}{\omega_m} \tag{8}$$

Being i_x the current of the x phase and m the number of phases.

III. MODEL DESCRIPTION

In this section a brief description of the developed model for surface mounted PM axial flux synchronous machines is given.

A. Flux density in the Airgap

The magnetic flux density induced by the magnets in the air-gap can be expressed by developing (2):

$$B_g^m(t,\theta) = \sum_{n=1}^{\infty} 2B_n(r) \cdot \cos(np(-\theta - \Omega_m t + \varphi_0)) \tag{9}$$

As positive and negative components are symmetrical, only positive harmonics are considered in the sum. The coefficient B_n is calculated as:

$$B_n(r) = \frac{B_{g\max}}{n\pi} \sin\left(np\frac{\beta_m(r)}{2}\right) \frac{(1-\cos(n\pi))}{(1+(a(r)np)^2)} \tag{10}$$

β_m is the magnets span angle in electrical degrees and a is the fringing function coefficient. The B_{gmax} value is referred to the maximum value of the flux density and it can be approximated as following:

$$B_{g\max} \approx \frac{B_r}{1+\mu_r \frac{g}{h_m}} \tag{11}$$

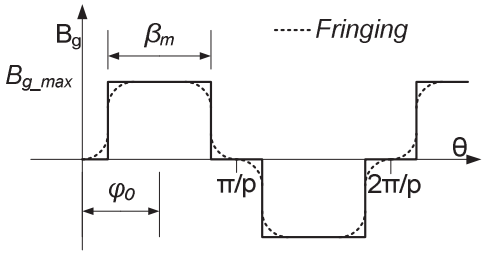

Fig 3: Spatial distribution of B_g

Where B_r and μ_r are the remanent magnetization and the relative permeability of the magnets, g is the air-gap length and h_m is the height of the magnets.

It has been demonstrated that the expression (12) of the fringing coefficient leads to a quite accurate approximation of the shape of the magnet flux density in the air-gap. This expression is developed from[12]. *Hendershot et al* proposed a fringing function for radial flux machines and this has been modified to use it in axial machines. Fig 3 shows the difference on the waveform of the flux density induced by the magnets in the air-gap with and without the fringing coefficient.

$$a(r) = \frac{\sqrt{g\left(g + h_m/\mu_r\right)}}{2r} \tag{12}$$

B. Winding Factor

Next step consist in computing the winding factor. Applying expression (13) it is possible to obtain the harmonic spectrum of the winding factor.

$$\vec{\xi}_k = \frac{\sum_x \pm e^{jkt_p\varphi_x}}{\left|\sum_x \pm e^{jkt_p\varphi_x}\right|} \tag{13}$$

ξ_k is the winding factor vector for the 'k' order harmonic and φ_x is the position of the 'x' vector. A vector sum is made adding all coils of the same phase in one direction and resting in the other direction. Fig 4 shows a schema of how the sum is made. This method of calculating the winding factor is a result of the star of slot theory presented by *Bianchi et al* [13].

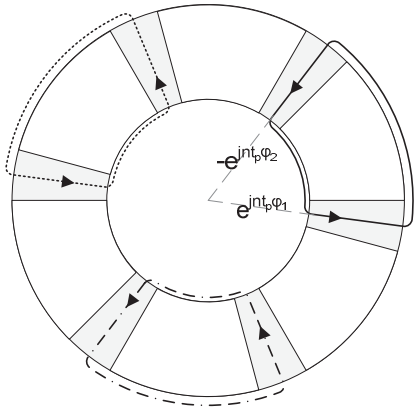

Fig 4: Schema of how the winding factor is calculated

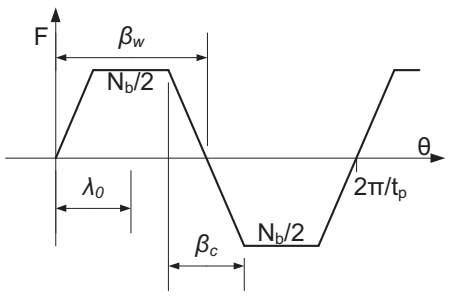

Fig 5: Spatial distribution of the F created by the winding of each phase

C. Winding Distribution

The magnetomotive force MMF is defined as:

$$MMF(t,\theta) = F(\theta)\cdot \Re\{i(t)\} \tag{14}$$

Where i is the supply current. Developing F from (3) the expression for positive harmonics is the following:

$$F(\theta,r) = \sum_{k=1}^{\infty} 2\cdot F_k(r)\cdot \sin\left(-kt_p(\theta+\lambda_0)\right) \tag{15}$$

The expression of the Fourier coefficient F_k is:

$$F_k(r) = \frac{N_{ph}}{\pi\cdot k\cdot t_p}\xi_k \frac{\sin\left(k\cdot t_p\cdot\frac{\beta_c(r)}{2}\right)}{k\cdot t_p\cdot\frac{\beta_c(r)}{2}} \tag{16}$$

N_{ph} is the number of turns per phase and ξ_k is the winding factor amplitude. In case of slotless stators where typically conductors are distributed with a given distribution angle, $\beta_{c,}$ an attenuation effect on the magneto-motive spectrum is added. The effect of this conductor distribution on the magnetomotive waveform is shown in Fig 5. N_b is the number of conductors in each coil and it is calculated as:

$$N_b = \frac{N_{ph}}{\left(\frac{Q}{m}\Big/2\right)\cdot n_l} \tag{17}$$

Being n_l the number of winding layers.

The model represents the behaviour of the machine in steady state. So the armature currents are defined as following in case of three symmetric phases:

$$i_A(t)=\mathrm{Re}\left\{Ie^{j\Omega t}\right\}\quad i_B(t)=\mathrm{Re}\left\{Ie^{j\Omega t-\frac{2\pi}{3}}\right\}\quad i_C(t)=\mathrm{Re}\left\{Ie^{j\Omega t+\frac{2\pi}{3}}\right\} \tag{18}$$

Where I is the supply current amplitude and Ω_e is the electrical frequency. After defining the *MMF* the armature flux density in the air-gap can be calculated as:

$$B_g^a(t,\theta) = \mu_o\frac{MMF(t,\theta)}{g'} \tag{19}$$

g' is the equivalent air-gap computed as following:

$$g' = g + \frac{h_m}{\mu_r} \tag{20}$$

D. Slot effect

The slot effect is commonly represented as a relative permeability function.

$$B_{g\_s}(t,\theta) = B_g(t,\theta)\lambda(\theta) \tag{21}$$

This function can be obtained with different mathematical approximations. The simplest approximation assumes a curved flux path on the tooth edge that does not include the effect of flux concentration on this edge [6;14]. In order to assume this concentration some authors use experimental curves to obtain the permeability function[15]. Another option is the use of the scalar magnetic potential equation [16;17]. In this paper the conformal transformation is used to obtain the relative permeability function as presented in [1;18-20].

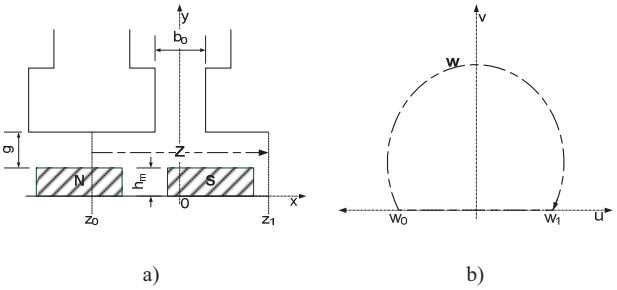

Fig 6: Conformal transformation. a) Z plane and b) W plane

This method is a quite complex iterative mathematical process that on the contrary is pretty easy to implement. The used method is developed for the case of axial flux machines from [1]. Zhu et al proposed a method to implement the slot effect by the conformal transformation for radial flux machine. In this paper their proposal has been modified to use with axial machines. First the plane on the average radius is created on the Z plane changing the coordinates from polar to Cartesian. Then the z path is transformed to the w path in the W plane. Once the points in the Z plane are obtained the relative permeability of one slot is calculated with the next expression:

$$\lambda_{S1}(w) = \frac{1}{\sqrt{1+\left(\frac{b_0}{2g'}\right)^2-\left(\frac{b_0}{2g'}w\right)^2}} \tag{22}$$

Where b_0 is the slot opening.

The points in Z and W plane are linked by the next expression:

$$z(w) = \frac{b_0}{\pi}\left\{\arcsin\left(\frac{w}{z_a}\right)+\frac{g'}{b_0}\ln\left[\frac{\sqrt{z_a^2-w^2}+\frac{2g'}{b_0}w}{\sqrt{z_a^2-w^2}-\frac{2g'}{b_0}w}\right]\right\} \tag{23}$$

Where Z_a is:

$$z_a = \sqrt{1+\left(\frac{2g'}{b_0}\right)^2} \tag{24}$$

The effect of the slots makes the relative permeability function a periodic function that is repeated as many times as slots number. So using the superposition principle the relative permeability function can be easily obtained:

$$\lambda_S = \sum_{x=1}^{Q}\lambda_{S1}e^{j\frac{2\pi}{Q}x} \tag{25}$$

E. Electromagnetic Coupling

The electromagnetic coupling consists in the calculation of the magnet flux linkage, the Electromotive

Force *EMF* and the electromagnetic torque. The flux linkage per phase is defined as:

$$\psi(t) = t_p \int_0^{2\pi/t_p} \int_{R_i}^{R_o} r \cdot B_g^m(\theta, r) \cdot F(\theta, r) \cdot dr \cdot d\theta \tag{26}$$

Where R_o and R_i are the outer radius and the inner radius of the rotor ring. Developing the expression (26) with (9) and (15):

$$\psi(t) = t_p \int_0^{2\pi/t_p} \int_{R_i}^{R_{oo}} r \cdot \left[\begin{array}{l} \sum_{n=-\infty}^{\infty} B_{g\_n}^m(r) \cdot \cos(np(-\theta + \varphi_0)) \\ \times \sum_{k=-\infty}^{\infty} F_k(r) \sin(kt_p(\theta + \lambda_o)) \end{array} \right] \cdot dr \cdot d\theta \tag{27}$$

From this expression it can be demonstrated that the flux linkage is zero unless the following condition is fulfilled:

$$k = -\frac{n \cdot p}{t_p} \tag{28}$$

Taking into account this condition the flux linkage expression leads to:

$$\psi(t) = t_p \int_0^{2\pi/t_p} \int_{R_i}^{R_{oo}} r \cdot \left(\sum_{n=1}^{\infty} B_{g\_n}^m(r) F_n(r) \cdot \sin(np(\theta + \varphi_0 + \lambda_o)) \right) \cdot dr \cdot d\theta \tag{29}$$

The spatial position can be represented as a function of time (t) and mechanical speed (Ω_m):

$$\theta = \Omega_m t \tag{30}$$

The time derivative of the flux linkage gives the EMF:

$$EMF(t) = \Omega_m t_p \int_0^{2\pi/t_p} \int_{R_i}^{R_{oo}} r \cdot \left(\sum_{n=1}^{\infty} B_{g\_n}^m(r) F_n(r) \cdot \cos(np(\theta + \varphi_0 + \lambda_o)) \right) \cdot dr \cdot d\theta \tag{31}$$

The EMF can be also represented in function of its harmonic content:

$$EMF(t) = \sum_{n=-\infty}^{\infty} E_n e^{-jn\Omega_e t} \tag{32}$$

The electromagnetic torque can be then easily calculated for a three phase equilibrated system with next expression:

$$T_{em}(t) = \frac{1}{\Omega_m} \Re\left\{ \sum_{n=-\infty}^{\infty} E_n I e^{-j(n-1)\Omega_e t} \left(1 + 2\cos\left((n-1)\frac{2\pi}{3} \right) \right) \right\} \tag{33}$$

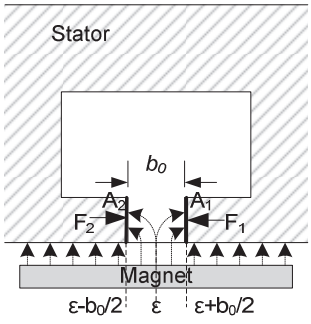

Fig 7: Maxwell's tensor in a slot

This last expression is very useful to see how the harmonics of the EMF affect in the harmonic content of the torque. Even components of the EMF spectrum are null so that they do not generate torque. Components of the EMF spectrum that are multiple of three do not generate torque do. This is because in a symmetric three phase machine the multiples of three of the current spectrum are null. The average torque of the torque is generated by the fundamental component of the EMF. High order components of the torque are multiple of six: the components -5 and 7 of the EMF generate the 6th component of the torque, -11 and 13 generate the 12th and so on.

F. Cogging torque

The stator slots cause a variation in the air-gap reluctance which leads to a parasitic torque component known as cogging torque. This is because the rotor tends to lock in certain positions in which the flux path length is minimum.

The most used methods for the calculation of the cogging torque are the virtual work method [14;21] and the Maxwell´s tensor method [5;22]. Applying this last method the tangential force tensor over a ferromagnetic body is integrated along a circular contour inside the air-gap:

$$dF = \frac{1}{2\mu_0} B^2 dA \tag{34}$$

The cogging torque is computed considering the tangential component of the magnetic force over the stator. This tangential force depends on the flux penetrating by the side faces of the slots. In each slot two tangential forces in opposition appear as it is shown in Fig 7 (F_1 and F_2). Then a superposition is done to compute the total cogging torque adding the cogging due to each slot:

$$T_{cogg} = R_{av} \sum_{x=1}^{Q} \frac{1}{2\mu_0} \frac{R_o^2 - R_i^2}{2} \left[\int_{x\left(\varepsilon - \frac{b_0}{2}\right)}^{x\varepsilon} B_{gs}^2(t,\theta) d\theta - \int_{x\varepsilon}^{x\left(\varepsilon + \frac{b_0}{2}\right)} B_{gs}^2(t,\theta) d\theta \right] \tag{35}$$

G. Equivalent Electric Circuit

Many times the behaviour of machines is simplified to a lumped electric parameter circuit. This circuit is very useful for the steady state analysis of motors but also for the control strategy. The way this equivalent circuit is obtained is presented in this section. In Fig 8-a the equivalent circuit for machine without saliency is shown.

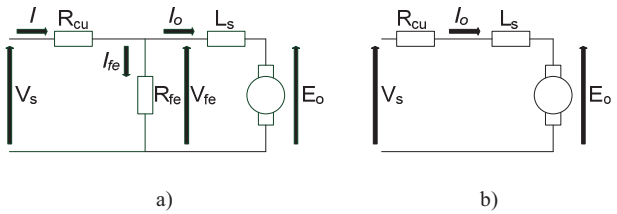

Fig 8: Equivalent circuit, a) complete and b) simplified

1) Coil Resistance

As it is well known the copper resistance depends on the length l_{cu} and cross-section A_{cu} of the wire, and also on the resistivity of the copper ρ_{cu}.

$$R_{cu} = \rho_{cu}(T)\frac{l_{cu}}{A_{cu}} \tag{36}$$

The resistivity of the copper depends on the temperature in such a way that:

$$\rho_{cu}(T) = \rho_{cu}(T_0)\left[1 + \alpha_{cu}\left(T - T_0\right)\right] \tag{37}$$

Where α_{cu} is the temperature coefficient.

2) Coil Inductance

The computation of the coil inductance is very valuable for the correct characterisation of the machine. In this section the computation of inductances is presented for rotor structures without saliency. That means, for rotors with surface mounted magnets, which is the most typical case in axial flux machines.

In the case of slotted machines the inductance could be divided in three components: the air-gap inductance L_g, the end-winding leakage inductance L_{ew} and the slot leakage inductance L_σ.

$$L_s = L_g + L_{ew} + L_\sigma \tag{38}$$

The air-gap inductance in each phase is the division between the armature reaction flux linkage in a phase ψ^a and the current in that phase:

$$L_{gA} = \frac{\psi_A^a(t,\theta)}{i_A(t)} \tag{39}$$

The armature reaction flux linkage of a phase is obtained with the surface integral of the magnetic flux density induced by that phase multiplied by the magneto motive force of the same phase:

$$\psi_A^a(t,\theta) = \int_S B_g^a(t,\theta)F_A(\theta)ds \tag{40}$$

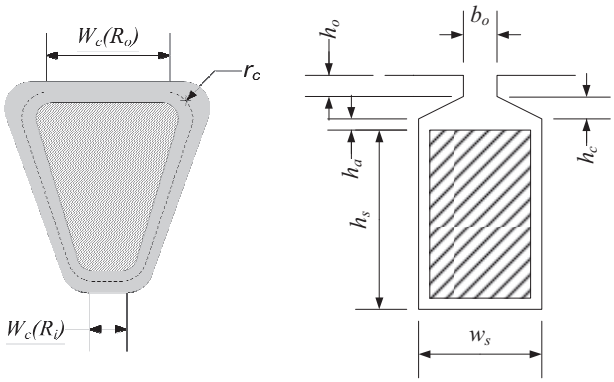

a) b)

Fig 9: a)Detail of the dimensions of the coil and b) Geometry of the slot

Where the magnetic flux density induced by a armature phase is:

$$B_g^a(t,\theta) = \frac{\mu_0}{2g'}MMF(t,\theta) \tag{41}$$

Developing (39) it appears that the air-gap inductance for each phase is the sum of the self-inductance and the mutual inductances, as shown in the next expression.

$$L_{gA} = L_{AA} + L_{AB} + L_{AC} \tag{42}$$

Where L_{gA} is the air-gap inductance of phase A, L_{AA} is the self-inductance, and L_{AB} and L_{AC} are the mutual inductances. The expressions for these components are the following:

$$L_{AA} = \pi\frac{\left(R_o^{\,2} - R_i^{\,2}\right)}{2}\frac{\mu_0}{g'}\sum_{k=-\infty}^{\infty}F_k^{\,2} \tag{43}$$

$$L_{AB} = \pi\frac{\left(R_o^{\,2} - R_i^{\,2}\right)}{2}\frac{\mu_0}{g'}\sum_{k=-\infty}^{\infty}F_k^{\,2}e^{j\frac{2\pi}{3}(k-1)} \tag{44}$$

$$L_{AC} = \pi\frac{\left(R_o^{\,2} - R_i^{\,2}\right)}{2}\frac{\mu_0}{g'}\sum_{k=-\infty}^{\infty}F_k^{\,2}e^{j\frac{2\pi}{3}(-k+1)} \tag{45}$$

In case of axial flux machines the inner (L_{ew_o}) and the outer (L_{ew_o}) end-winding inductances are different, because the end-windings itself are different as shown in Fig 9**¡Error! No se encuentra el origen de la referencia.**-a. These inductances can be computed by the following equations [23]:

$$L_{ew\_o} = \frac{1}{2}\frac{\mu_0}{\pi}N_{ph}^{\,2}\left(2\pi r_c + w_c(R_o)\right)\ln\left(K_e\frac{w_x(R_o)+2r_c}{2r_c}\right) \tag{46}$$

$$L_{ew\_i} = \frac{1}{2}\frac{\mu_0}{\pi}N_{ph}^{\,2}\left(2\pi r_c + w_c(R_i)\right)\ln\left(K_e\frac{w_x(R_i)+2r_c}{2r_c}\right) \tag{47}$$

Being the total end-winding inductance the sum of both terms.

$$L_{ew} = L_{ew\_i} + L_{ew\_o} \tag{48}$$

The slot leakage inductance for each slot can be computed by the following equation [23]:

$$L_\sigma = \mu_0 N_r^2\left(R_o - R_i\right)\lambda_S \tag{49}$$

Where N_r is the number of conductors per slot and λ_S is the slot shape factor. In case of slots with the shape shown in Fig 9**¡Error! No se encuentra el origen de la referencia.**-b, the shape factor can be obtained by the following expression [24]:

$$\lambda_S = \frac{h_s}{3w_s} + \frac{h_a}{w_s} + \frac{2h_c}{w_s + b_0} + \frac{h_0}{w_s} \tag{50}$$

In case of double layer windings the expression (50) is not totally valid as it is developed for the particular cases of single layer windings. Furthermore in the model the differential leakage inductance is not assumed. The differential leakage inductance is the effect that one coil in a slot generates in the inductance of the other coil in

the same slot. These two issues make the calculation of the leakage inductance less accurate. However in many cases this approximation can give valid results.

3) Equivalent Iron losses resistance

Typically the iron losses produced in the magnetic core can be considered adding an equivalent resistance in the electric circuit (R_{fe}). The value of this equivalent resistance can be computed applying the next expression:

$$R_{fe} = \frac{3\left|V_{fe}^2\right|}{P_{fe}} \tag{51}$$

Where V_{fe} is the voltage at the equivalent resistance terminals and P_{fe} is the iron losses.

In cases where the iron losses are not significant (f.e in low speed applications) this resistance can be neglected so the equivalent circuit is simplified as shown in Fig 8-b.

IV. Model Validation with FEM-3D Simulations and Experimental Results

In this section the proposed model is validated by numerical simulations and by experimental tests. Therefore, the results obtained with the analytical model have been compared with those obtained by FEM-3D simulations and also with experimental data.

A. Specifications of the Prototype

The modelled machine is an axial flux surface mounted PM synchronous machine. This machine has a single-side slotted stator configuration. Details of the prototype are shown in Fig 10. The number of slots is $Q=6$ and the number of pole pairs is $p=2$. Double layer winding is implemented which consists 6 coils, that means 2 coils per phase. In TABLE I. the main characteristics of the test prototype are reported.

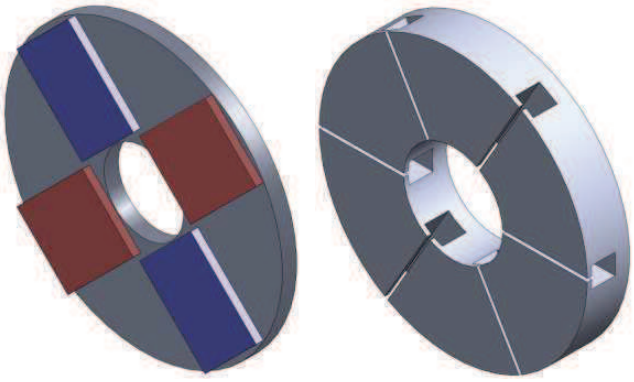

a) b)

Fig 10: Sketch of the machine, a) rotor and b) stator

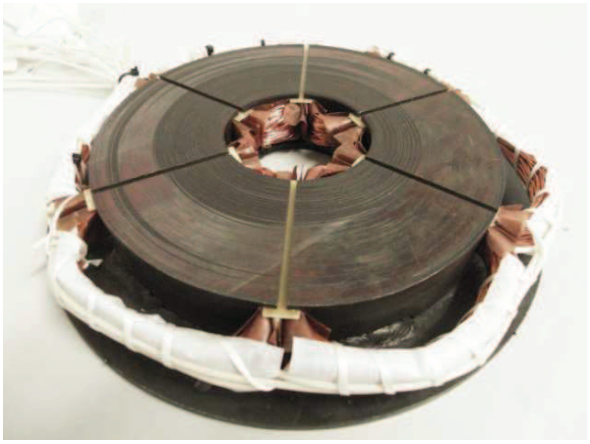

Fig 11: Finished stator, lamination and winding

TABLE I
MODELLED MACHINE CHARACTERISTICS

Air-gap length	g	1.85 mm
Stator Core length	L_s	30 mm
Rotor Core length	L_r	15 mm
Number of stator slots	Q	6
Number of pole pairs	p	2
Outer Diameter	D_o	323.7 mm
Inner Diameter	D_i	194.2 mm
Magnet height	h_m	5 mm
Magnet		64mmx54mm
Residual flux density	B_r	1.34T
Relative permeability of the magnet	μ_r	1.08
Number of turns per phase	N_{ph}	250
Number of sides	h	2
Number of phases	m	3
Mechanical speed	Ω_m	250 rpm

It must be mentioned that the test prototype does not fulfil any application requirements and it has been designed with the purpose of validating the proposed model. The structure of the machine and particularly the rectangular shape of the magnets have been chosen to obtain an electrical machine with not sinusoidal EMF and high torque ripple. This way the validation of the design tools can be more demonstrative. In Fig 11 the laminated stator with two layer winding is shown.

In Fig 12 the test bench configuration is shown. The prototype is driven by a traction motor which is controlled by a *Control Techniques®* drive. On the other hand, resistive loads are connected at prototype terminals so that it works as a generator. Regarding to the measurements, a 15Nm torque transducer with a resolution of 0.1Nm is used to measure the mechanical torque in the shaft. Furthermore the PZ4000 power meter of *Yokogawa®* is used to measure the power and also to acquire the voltage and current waveforms.

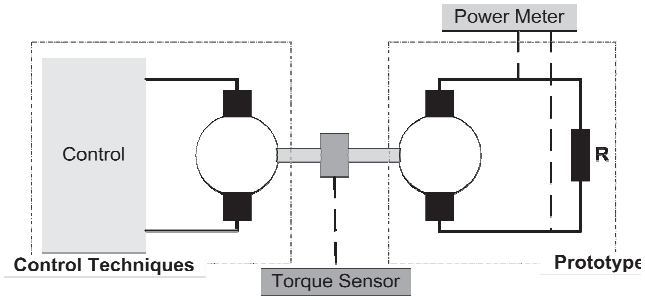

Fig 12: Sketch of the test bench

Two kind of test has been performed. First the so called open circuit test at nominal speed has been carried out. In this test back electromotive forces and the cogging torque have been measured. After that, the so called load test has been done. As aforementioned, in this test the prototype works as generator. Three star connected resistances (*R=10Ω per phase*) have been connected in order to test the prototype at rated power. This testing procedure has been chosen due to its simplicity.

B. Results

The results could be divided in two main groups. First the equivalent circuit is obtained. Then different measurements such as back EMF waveform, supply voltage waveform at rated conditions, cogging torque waveform and rated torque waveform are plotted.

In Table II iron losses estimated by experimental test and computed by FEM-3D simulations are shown. In case of FEM-3D simulations, these losses have been computed applying the well known Bertotti's formulation [25]. The experimental estimation has been done with a power balance neglecting the iron losses. Looking at the results shown in Table II, it can be stated that neglecting iron losses does not lead to a remarkable error. This happen in this particular case because the losses are practically insignificant.

TABLE II
LOSSES

	Pf_e [W]
FEM 3D	1.251
Experimental	1.45

TABLE III
RESISTANCE VALUE AT WORKING TEMPERATURE OF 60ºC

	$R_{ru}[\Omega]$
FEM 3D	7.1
Analytic	7.05
Experimental	7.13

TABLE IV
INDUCTANCES

	L_g+L_σ [mH]	L_{ew} [mH]	L [mH]
FEM 3D	28.9	6.5	35.4
Analytic	28.2	5.5	33.7
Experimental	-	-	31.6

The values of the copper resistances are shown in Table III. The real resistance has been measured by a micrometer, while the analytic value has been calculated by (37). The value of the resistance at 25ºC is about 6.15ohm, but the shown values are for a working temperature of about 60ºC in the copper.

Finally the values of the inductances are summarized in Table IV. In case of experimental measurement only the total phase inductance is shown. In the other two cases, FEM-3D simulations and analytical calculation, the inductance is split out in two components: the end-winding leakage inductance and the result of adding the air-gap inductance plus the slot leakage inductance. Results obtained by the analytical model are about 94% accurate. The results obtained by FEM-3D simulations confirm this accuracy.

Values of electric parameters such as resistances and inductances depend strongly on the shape of coils and their position in the slots. Assuming the actual shape of the end windings and coil position in the slot is not that easy what leads to some uncertain parameters. The difference between the experimental values and the ones obtained with FEM-3D and analytic could be explained due to these uncertain dimensional parameters. Nevertheless, looking at the results it can be stated that inductances and resistances computed by these two methods have rather good agreement with experimental data, but also between them.

After computing the electric parameters, the performance of the prototype is analyzed, and the model accuracy is evaluated comparing some temporal waveforms. Therefore, In Fig 13, Fig 15 and Fig 17 temporal waveforms of the back EMF, supply rated voltage and electromagnetic rated torque are shown respectively. In Fig 14, Fig 16 and Fig 18 the spectrum of these waveforms are plotted. In addition in Fig 20 the cogging torque waveform is shown.

Analyzing the temporal waveforms it can be stated that the accuracy of the analytic model comparing to experimental data is good. Where some differences between the analytic models and experimental data happen the FEM-3D simulations confirm the validity of the analytical model. Nevertheless a more precise analysis can be done comparing the different spectrums.

Regarding to the back EMF spectrum, the main harmonic is almost the same in the three cases. The most significant components among the high order harmonics are the 5^{th} and 7^{th}harmonics which lead to the 6^{th} harmonic in the electromagnetic torque. The accuracy in the 7^{th} harmonic is quite good (92% in comparison with experimental data). However the error in the 5^{th} harmonic is slightly higher (accuracy about 85% in comparison with experimental data). It can be also noticed that the 11^{th} and 13^{th} harmonics in the EMF generate the 12^{th} harmonic in the torque. The values of these harmonics are quite small which makes numerical errors possible and the experimental measuring quite difficult. This leads to not very accurate results, but

anyway the influence of the EMF harmonics in the torque can be appreciated.

Nevertheless it is important to enhance that the accuracy in 5th and 7th harmonics is good enough because the 6th harmonic of the electromagnetic torque is modelled with an acceptable precision (accuracy about 77.5% in comparison with experimental data and about 87% in comparison with FEM-3D). Furthermore, it can be seen that the average torque value is modelled with a very good accuracy. The value in case of analytical model is 3.17Nm while the experimental and FEM-3D data give 3.18Nm.

Finally in Fig 19 the cogging torque waveform is plotted. Measuring the cogging torque is not an easy task nor experimentally or with FEM-3D. A good measuring of the experimental cogging torque requires a quite sensible torque sensor and a constant speed rotating force. At the same time any external influence could make the measured data incorrect. In case of FEM-3D a very thin mesh is needed, which makes the simulation very slow and computationally heavy. Despite these inconvenient the obtained waveforms are quite similar and the cogging torque is about 0.375Nm in the maximum point in all the waveforms.

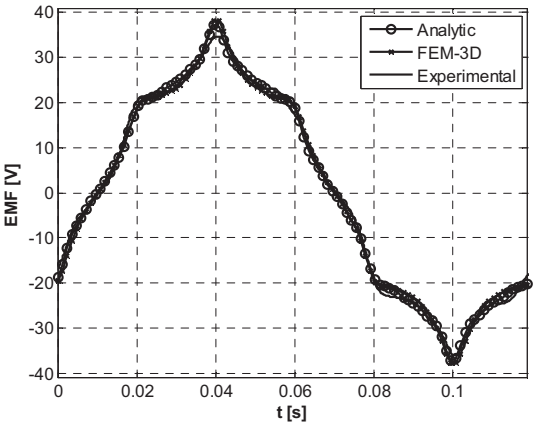

Fig 13: Temporal waveform of the back electro-motive force

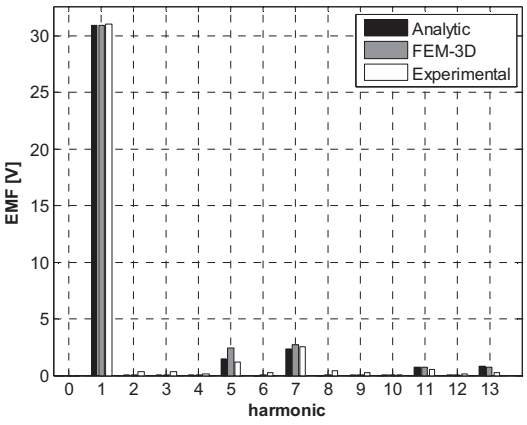

Fig 14: Spectrum of the back electro-motive force

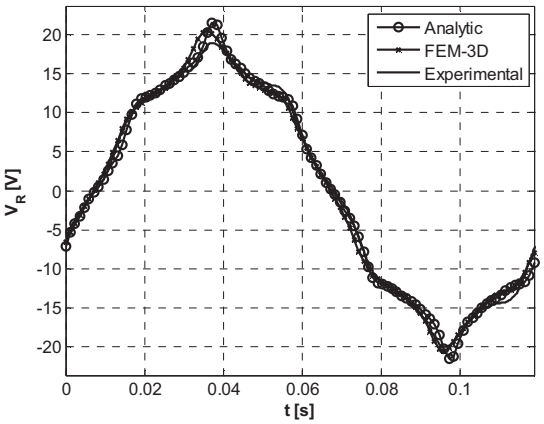

Fig 15: Temporal waveform of the supplying voltage at rated load

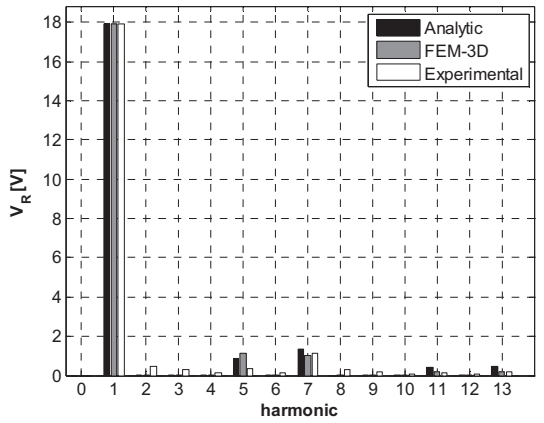

Fig 16: Spectrum of the supplying voltage at rated load

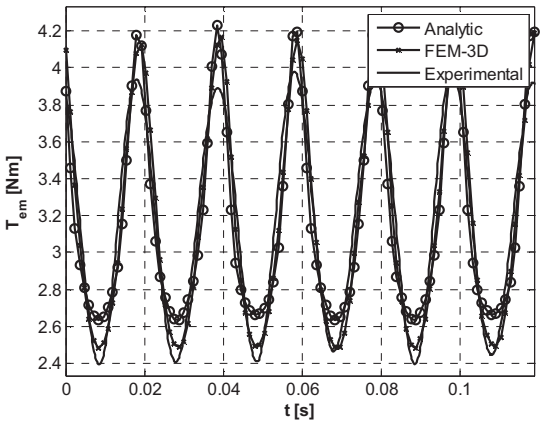

Fig 17: Temporal eaveform of electromagnetic torque at rated load

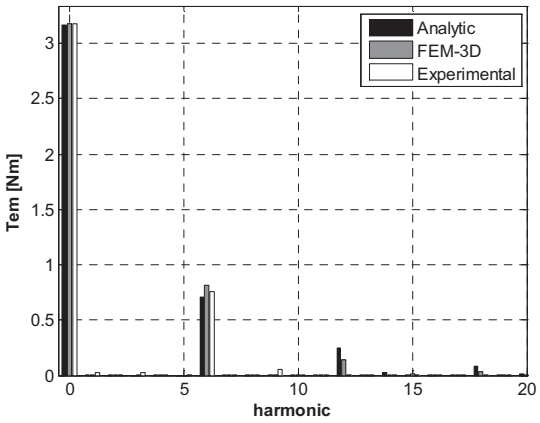

Fig 18: Spectrum of the electromagnetic torque at rated load

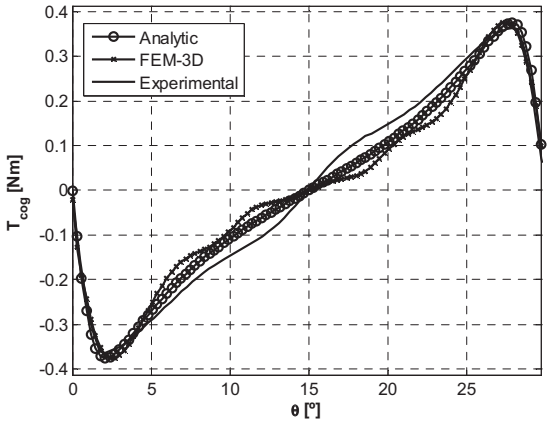

Fig 19: Cogging torque waveform

V. CONCLUSIONS

In this work the complete mathematical representation of axial flux PM synchronous machines based on Fourier series is proposed. Electromagnetic variables are defined as the sum of space-time harmonics and the couplings between different components are well identified. Amplitudes of these components are directly related to design variables such as magnetic and mechanical properties of magnets, winding conductor distribution or dimensions of the machine geometry. By this way a parametric model is developed.

Due to the feasibility of the proposed model it enables to perform design optimizations which normally consist of huge amount of iterations, in a relatively easy and quick way, obtaining accurate enough results In addition, the proposed model accounts for constructive details such as magnet and slot shapes, so that the influence of this constructive aspects on the final motor performances can be evaluated. For instance, it is possible to choose the optimum magnet shape in order to minimize the cogging torque and the overall torque ripple. Thus, the proposed model gives rather accurate inside view into the behaviour of axial flux machines, so that it is possible to identify directly the influence of different design parameters on the final performances of the machine.

The accuracy of the proposed model has been evaluated comparing the results with that obtained by numerical analysis in FEM3D and by experimental data. It can be stated that the accuracy of the proposed model is rather good as the results show a good agreement with that obtained by FEM-3D simulations and also with experimental data.

VI. REFEENCES

[1] Z. Q. Zhu and D. Howe, "Instantaneous magnetic field distribution in brushless permanent magnet DC motors. III. Effect of stator slotting," Magnetics. , IEEE Transactions. on, vol. 29, no. 1, pp. 143-151, Jan.1993.

[2] Z. Q. Zhu and D. Howe, "Instantaneous magnetic field distribution in brushless permanent magnet DC motors. II. Armature-reaction field," *Magnetics. , IEEE Transactions. on*, vol. 29, no. 1, pp. 136-142, Jan.1993.

[3] Z. Q. Zhu, D. Howe, E. Bolte, and B. Ackermann, "Instantaneous magnetic field distribution in brushless permanent magnet DC motors. I. Open-circuit field," *Magnetics. , IEEE Transactions. on*, vol. 29, no. 1, pp. 124-135, Jan.1993.

[4] Z. Q. Zhu and D. Howe, "Instantaneous magnetic field distribution in permanent magnet brushless DC motors. IV. Magnetic field on load," *Magnetics. , IEEE Transactions. on*, vol. 29, no. 1, pp. 152-158, Jan.1993.

[5] Z. Q. Zhu and D. Howe, "Analytical prediction of the cogging torque in radial-field permanent magnet brushless motors," *Magnetics. , IEEE Transactions. on*, vol. 28, no. 2, pp. 1371-1374, Mar.1992.

[6] A. B. Proca, A. Keyhani, A. El-Antably, L. Wenzhe, and D. Min, "Analytical model for permanent magnet motors with surface mounted magnets," *Energy Conversion. , IEEE Transactions. on*, vol. 18, no. 3, pp. 386-391, Sept.2003.

[7] G. Almandoz, J. Poza, M. A. Rodriguez, and A. Gonzalez, "Analytic model of a PMSM considering spatial harmonics," 2008, pp. 603-608.

[8] H. Surong, L. Jian, F. Leonardi, and T. A. Lipo, "A comparison of power density for axial flux machines based on general purpose sizing equations," *Energy Conversion. , IEEE Transactions. on*, vol. 14, no. 2, pp. 185-192, June1999.

[9] M. Aydin, H. Surong, and T. A. Lipo, "Design and 3D electromagnetic field analysis of non-slotted and slotted TORUS type axial flux surface mounted permanent magnet disc machines," 2001, pp. 645-651.

[10] A. Parviainen, "Design of an Axial-Flux Permanent-Magnet Low-Speed Machines and Performance Comparison Between Radial-Flux and Axial-Flux Machines." Lappeenranta University of Technology, 2005.

[11] F. Sahin, Design and development of a high-speed axial-flux permanent-magnet machine Eindhoven, 2001.

[12] J. R. Hendershot and T. J. E. Miller, *Design of brushless permanent-magnet motors* Magna Pysics Pub., 1994.

[13] N. Bianchi and M. Dai Pre, "Use of the star of slots in designing fractional-slot single-layer synchronous motors," *Electric. Power Applications. , IEE. Proceedings.* -, vol. 153, no. 3, pp. 459-466, May2006.

[14] B. Ackermann, J. H. H. Janssen, R. Sottek, and R. I. van Steen, "New technique for reducing cogging torque in a class of brushless DC motors," *Electric. Power Applications, IEE. Proceedings. B*, vol. 139, no. 4, pp. 315-320, July1992.

[15] M. J. Chung and D. G. Gweon, "Modeling of the armature slotting effect in the magnetic field distribution of a linear permanent magnet motor," *Electrical Engineering (Archiv fur Elektrotechnik)*, vol. 84, no. 2, pp. 101-108, May2002.

[16] Z. J. Liu and J. T. Li, "Analytical Solution of Air-Gap Field in Permanent-Magnet Motors Taking Into Account the Effect of Pole Transition Over Slots," *Magnetics. , IEEE Transactions on*, vol. 43, no. 10, pp. 3872-3883, Oct.2007.

[17] F. Dubas and C. Espanet, "Analytical Solution of the Magnetic Field in Permanent-Magnet Motors Taking Into Account Slotting Effect: No-Load Vector Potential and Flux Density Calculation," *Magnetics. , IEEE Transactions on*, vol. 45, no. 5, pp. 2097-2109, May2009.

[18] B. L. J. Gysen, E. A. Lomonova, J. J. H. Paulides, and A. J. A. Vandenput, "Analytical and Numerical Techniques for Solving Laplace and Poisson Equations in a Tubular Permanent-Magnet Actuator: Part I. Semi-Analytical Framework," *Magnetics. , IEEE Transactions on*, vol. 44, no. 7, pp. 1751-1760, July2008.

[19] B. L. J. Gysen, E. A. Lomonova, J. J. H. Paulides, and A. J. A. Vandenput, "Analytical and Numerical Techniques for Solving Laplace and Poisson Equations in a Tubular Permanent Magnet Actuator: Part II. Schwarz&Christoffel Mapping," *Magnetics. , IEEE Transactions on*, vol. 44, no. 7, pp. 1761-1767, July2008.

[20] D. Zarko, D. Ban, and T. A. Lipo, "Analytical calculation of magnetic field distribution in the slotted air gap of a surface permanent-magnet motor using complex relative air-gap permeance," *Magnetics. , IEEE Transactions on*, vol. 42, no. 7, pp. 1828-1837, July2006.

[21] J. F. Gieras, "Analytical approach to cogging torque calculation of PM brushless motors," *Industry Applications, IEEE Transactions on*, vol. 40, no. 5, pp. 1310-1316, Sept.2004.

[22] D. Zarko, D. Ban, and T. A. Lipo, "Analytical Solution for Cogging Torque in Surface Permanent-Magnet Motors Using Conformal Mapping," *Magnetics. , IEEE Transactions on*, vol. 44, no. 1, pp. 52-65, Jan.2008.

[23] D. C. Hanselman, *Brushless Permanent Magnet Motor Design* Magna Physics Publishing, 2006.

[24] J. F. Gieras, R. J. Wang, and M. J. Kamper, *Axial Flux Permanent Magnet Brushless Machines* Kluwer Academic Publishers, 2004.

[25] G. Bertotti, "General properties of power losses in soft ferromagnetic materials," *Magnetics. , IEEE Transactions. on*, vol. 24, no. 1, pp. 621-630, Jan.1988.